STELLAR RADIAL MIGRATION AND THICK DISKS IN SPIRAL GALAXIES

By

MICHAEL SOLWAY

A dissertation submitted to the

Graduate School—New Brunswick

Rutgers, The State University of New Jersey

in partial fulfillment of the requirements

for the degree of

Doctor of Philosophy

Graduate Program in Physics and Astronomy

written under the direction of

Dr. J. A. Sellwood

and approved by

_____

_____

_____

_____

_____

New Brunswick, New Jersey

October, 2013

ABSTRACT OF THE DISSERTATION

Stellar Radial Migration and Thick Disks in Spiral Galaxies

By MICHAEL SOLWAY

Dissertation Director:

Dr. J. A. Sellwood

We present four studies of radial migration of stars in thickened galactic disks and its relation to the possible internal formation of thick disks. This is an effect caused by transient spirals during which stars that corotate with a spiral gain or lose angular momentum and migrate radially while remaining on nearly circular orbits. The overall angular momentum distribution and surface density of the disk remains unchanged however. Our tools are collisionless N-body simulations that each simulate a single disk galaxy.

First, we study the extent to which radial migration is affected by the vertical motion of stars. We find that rms angular momentum changes are reduced by it, but rather gradually, and the maximum changes are almost as large for thick disk stars as for those in a thin disk. Radial migration is also weaker in disks with greater velocity dispersions and under spirals of lower amplitude or greater number of arms. In barred simulations, it is slightly stronger outside the bar than in comparable cases with just spirals, but the cumulative effect of multiple spiral events still dominates.

In the second study, we determine that vertical actions, and not vertical energies, of stars are conserved on average during radial migration.

Then, we test the hypothesis that bars suppress the outwards radial migration from the inner galactic region that is capable of building a thick disk in the outer regions. If this

works, it can explain why the Milky Way thick disk primarily contains old stars.

First, however, we check whether realistic thick disks form in our simulations by this proposed outwards migration mechanism. We find that they do not, and attribute it to our particle addition prescription and the not strong enough spiral activity.

Nevertheless, we go on to test the above hypothesis, and indeed find that bars significantly reduce this outwards migration. Although small and slow variations of the bar properties allow some trapped particles to escape, new stars that would form inside the bar would be born deep in its potential well, and would remain trapped.

Preface

This thesis begins with a broad introduction to disk galaxies, the effect we call radial migration that we believe occurs in them, how this effect might be responsible for the formation of thick stellar disks, and how the formation of a bar should affect radial migration. It includes summaries about spirals, bars, and thin and thick disks: the features of disk galaxies essential to this work. It also has a description of the N-body simulations we use as tools to study the questions we wish to answer. I close it with an overview of the projects of this thesis presented in the following chapters. It is intended for general audience with some scientific knowledge; although at times, it does get a bit technical, especially in §1.5 where I describe our simulations.

The references I cite, especially in the introduction, are nowhere near complete and exhaustive of the existing literature on the topics. I do not mean to exclude anyone's particular work, but instead use various references, mostly recent and classic ones, as a guide to further reading, examples, and proof of the claims. In the introduction, I heavily cite the two wonderful books (Binney & Merrifield 1998) and (Binney & Tremaine 2008).

Chapters 2 through 5 are technical, and essentially comprise of our published journal paper (Solway et al. 2012, hereafter S12) and another paper that we are close to submitting. Chapters 2 and 3 are from the former paper and 4 and 5 are from the latter.

Chapter 2 is a thorough study of radial migration and how it varies with various stellar disk parameters, most importantly disk thickness. Chapter 3 shows that there is a conserved quantity, the vertical action of a star, that does not change while stars undergo radial migration. However, we find that it is only conserved on average in simulations, and not particle by particle. In 4, we investigate whether thick disk populations form in our simulations by stars radially migrating outwards from the inner galactic region. And in chapter 5, we show that bar formation turns off the ability of younger stars that are born

later inside the bar to migrate outwards, making the thick disk stars in the middle and outer galactic regions at least as old as the bar.

Each of these chapters begins with its own introduction or a continuation tied to the previous chapter, and finishes with a detailed summary section, in which we sometimes suggest possible further projects on the topic. Chapters 4 and 5 are tied, and we present the motivation of the project of chapter 5 and the simulations used for it in chapter 4.

In the main conclusions, I remind why radial migration is important, and again briefly summarize the main findings of our studies. Like the abstract, it serves as a short overview of this entire thesis.

Appendix A discusses how we calculate estimates of the exact vertical actions, which is the appendix from our first paper S12, and connects to chapter 3 in this thesis.

Acknowledgments

First, I thank my advisor, Professor Jerry Sellwood, for guiding and supporting me during my PhD career, and for teaching me galactic dynamics, stellar N-body simulations, some very useful presentation and writing skills, and general aspects of the astrophysics academia. Jerry is a wonderful advisor. I really appreciate his mentoring style of letting me choose my own projects and work on them alone. I also appreciate him taking time to help me solve and debug problems in my research when I got stuck.

I thank my other committee members, Professors Ted Williams, Chuck Keeton, and Karin Rabe, as well for serving as my committee and overlooking my progress. I thank Dr. Victor Debattista, my defense committee member from outside of Rutgers, for flying abroad and participating in my defense. I thank Dr. Ralph Schönrich for collaborating with Jerry and me on my first project, Dr. Rok Roškar for refereeing our paper on it, and the future referee of my second paper to be submitted soon. In addition, I thank Rok and Victor for organizing the amazing conference "Stars Without Border" in Slovenia on radial migration, which allowed me to interact with and learn from the other groups working on radial migration and related topics. I also thank Dr. Jo Bovy for having a very useful discussion during which he suggested to test whether the radial distribution of vertical actions flattens out with time in our simulations.

I thank all the astro faculty for teaching such wonderful astrophysics courses, from which I learned a lot. I also thank them and the postdocs for organizing the astro seminars, which were quite educational and allowed me to practice presenting. I thank the non-astro physics faculty for teaching the general physics courses I took, and all the physics and math faculty for the undergraduate courses I took during my undergraduate years at Rutgers. I thank Professor Harry Kojima for being my undergraduate honors project thesis advisor, and Professor Mike Berger of Indiana University at Bloomington for being my

Dedication

For myself.

I set out to pursue a PhD in physics, and finished it. Yay for me.

Table of Contents

List of Tables

List of Figures

List of Abbreviations

Abbreviated references:

BM98 (Binney & Merrifield 1998)

BT08 (Binney & Tremaine 2008)

SB02 (Sellwood & Binney 2002)

S12 (Solway et al. 2012)

Abbreviated terms:

ΛCDM the standard cosmology with a cosmological constant Λ and cold dark matter

CDM cold dark matter, *i.e.* particles move at non-relativistic speeds

CO carbon monoxide, whose emission from rotational transitions traces molecular gas clouds

CR corotation resonance (§1.2.3.2; BT08, eq. 3.149)

DF distribution function (BT08, p. 275)

GMC giant molecular cloud

H$_2$ molecular hydrogen

HI neutral atomic hydrogen observed by the 21-cm hyperfine transition line

HII ionized hydrogen visible in the Balmer series Hα emission line

ILR inner Lindblad resonance (§1.2.3.2; BT08, eq. 3.150)

MK system developed by Morgan et al. (1943) to classify stars into spectral and luminosity classes (BM98, p. 90)

OLR outer Lindblad resonance (§1.2.3.2; BT08, eq. 3.150)

S0 lenticular galaxies in the Hubble classification system (Hubble 1936)

SoS surface of section (§3.2 & Appendix A; BT08, §3.2.2)

List of Common Symbols

$[\alpha/\text{Fe}]$ abundance of alpha elements of a star

γ growth rate of a mode

Δz vertical spacing of grid planes

ϵ eccentricity of a particle's orbit (§2.3.2)

ε softening length (§1.5.3)

ζ notional vertical amplitude based on epicycle approximation (eq. 2.9; BT08, p. 164)

κ epicycle or radial frequency of a particle on a nearly circular orbit (§1.2.3.2; BT08, eq. 3.79a)

ν vertical frequency of a particle with an orbit whose vertical motion remains close to the midplane (§1.2.3.2; BT08, eq. 3.79b)

$\rho(|z|)$ vertical stellar density

Σ vertically-integrated surface density

Σ_a surface density of a wave or spiral (eq. 2.10 and §2.4.3)

σ_R radial velocity dispersion

σ_z vertical velocity dispersion

τ_0 unit of time

ϕ azimuth (polar angular coordinate)

Φ gravitational potential

Φ_{crt} maximum Φ_{eff} along a bar's major axis, which is achieved at $R_{L_{1,2}}$ (§5.1; BT08, p. 181)

Φ_{eff} effective gravitational potential in a steadily rotating reference frame (§5.1; BT08, eq. 3.114)

ψ phase of a star with respect to a spiral arm: $\psi = m(\phi - \phi_{\text{max}})$, in which ϕ_{max} is the azimuth of the arm and m is the number of arms of the spiral (§2.3.2)

Ψ_0 potential amplitude (§2.4.3)

Ω angular velocity

Ω_b	pattern speed of a bar
Ω_p	pattern speed of a spiral wave
A_m	amplitude of sectoral harmonic m (eq. 2.7)
C_1	coefficient of the first exponential term in vertical profiles (§4.5)
C_2	coefficient of the second exponential term or an additive constant in vertical density profiles (§4.5)
E	specific total energy of a particle
E_J	specific Jacobi integral of a particle (§5.1; BT08, eqs. 3.112 and 3.113)
$E_{z,\mathrm{epi}}$	estimate of specific vertical energy of a particle from epicycle approximation (§3.1; BT08, p. 164 and eq. 3.255)
$E_{z,R}$	specific vertical energy of a particle at instantaneous radius R (eq. 3.1)
$\langle E_{z,R} \rangle$	orbit-averaged specific vertical energy of a particle (§3.1)
E_{z,R_h}	specific vertical energy of a particle at its home radius R_h (§3.1)
f	fraction of active mass of a disk, also distribution function (BT08, p. 275)
[Fe/H]	metallicity of a star
G	Newton's gravitational constant
h_1	scale height of the first exponential term in vertical profiles (§4.5)
h_2	scale height of the second exponential term in vertical profiles (§4.5)
J_R	specific radial action of a particle
J_z	exact specific vertical action of a particle (eq. 3.2; BT08, §3.2 and eq. 3.195)
$J_{z,\mathrm{epi}}$	estimate of specific vertical action of a particle from epicycle approximation (§3.2; BT08, eq. 3.257)
$J_z|_{R,\phi}$	estimate of specific vertical action of a particle at its fixed (R, ϕ) position, *i.e.* from its decoupled vertical motion (§3.2 and eq. 3.3)
k	wavenumber (eq. 2.10)
k_ϕ	azimuthal wavenumber (§2.4)
L_*	angular momentum value of the center of the groove seeded in the angular momentum distribution to grow a spiral wave from the groove mode (eq. 2.6)
L_1 & L_2	Lagrange points of a steadily rotating potential (§5.1; BT08, p. 181)
L_z	specific z-angular momentum of a particle

m	sectoral harmonic or spiral mode
M_d	disk mass
M_h	dark matter halo mass
N	number of particles in a disk
Q	Toomre's dimenssionless parameter measuring the radial velocity dispersion in stellar disks (BT08, eq. 6.71)
R or r	radius
R_0	unit of length
R_a	apo-center of a particle's orbit (maximum radius in the midplane)
R_b	boundary radius (§4.3.1)
R_c	radius of corotation resonance (BT08, eq. 3.149)
R_d	disk scale length
R_h	dark matter halo scale length
R_{home}	home or guiding-center radius of a particle (§1.2.3.2; BT08, eq. 3.72)
$R_{L_{1,2}}$	radial locations of the Lagrange points L_1 and L_2 (§5.1; BT08, p. 181)
R_{max}	maximum radius a particle reaches
R_{min}	minimum radius a particle reaches
R_p	peri-center of a particle's orbit (minimum radius in the midplane)
R_t	truncation radius of a disk
t	time
t_f	final time
t_i	initial time
V_0	unit of velocity
V_c	circular velocity
v_z	vertical velocity of a particle
x	Cartesian x-coordinate
X	ratio of a spiral wave's wavelength $\lambda = 2\pi/k$ to the critical shortest wavelength $\lambda_{crit} = 4\pi G \Sigma \kappa^{-2}$ possible that still can be stabilized by rotation ($X = \lambda/\lambda_{crit}$), which along with the parameter Q determines the gain of the swing amplifier (eq. 2.11; Toomre 1981; BT08, eqs. 6.77 and 6.88)
y	Cartesian y-coordinate

z	polar or Cartesian z-coordinate
z_0	initial vertical scale height of a disk
z_{max}	maximum height a particle reaches

Some less important and not commonly used variables are omitted from this list.

List of Simulation Names

Simulations from §§2 & 3 summarized in Table 2.1:

M2   thin and thick Mestel disks with a single $m = 2$ spiral wave (§2.3)

M2b   variant of M2 with seven extra test particle disks identical to the thick Mestel disk, but with varying initial scale heights (§2.3.4)

M2c   variant of M2 with seven extra test particle disks identical to the thick Mestel disk, but with varying initial radial velocity dispersions (§2.3.4)

M3   thin and thick Mestel disks with a single $m = 3$ spiral wave (§2.4.1)

M4   thin and thick Mestel disks with a single $m = 4$ spiral wave (§2.4.1)

M4b   same as M4, but with half the disk thicknesses (§2.4.2)

T   test simulation identical to M2, but with axisymmetric forces only (§2.3)

TK   variant of M2 with a thick Mestel disk only (§2.3.5)

UC   unconstrained thin and thick Mestel disks with multiple spiral waves (§2.5)

UCB1   unconstrained thin and thick Mestel disks with multiple spiral waves and a bar that forms late from particle noise (§2.5)

UCB2   similar to UCB1, but with a stronger bar (§2.5)

Simulations from §§4 & 5 presented in §4.2 and summarized in Table 4.1:

IB   exponential disk with isothermal halo and an early-formed bar

ISB   exponential disk with isothermal halo that first undergoes a long duration of only spirals, and later forms a bar from particle noise

M2p   variant of M2 from the first list above with an order of magnitude more particles

MB   Mestel disk that forms a bar late from particle noise

MS   Mestel disk with spirals only

MSp   variant of MS with an order of magnitude more particles

NB1   exponential disk with NFW halo and an early-formed bar

NB2   another simulation similar to NB1

NS   exponential disk with NFW halo that contains spirals only

NSp   variant of NS with an order of magnitude more particles

Chapter 1

Introduction

We humans have always been interested in learning how we came to be, as well as how everything around us, from the smallest to the largest, formed and keeps changing. Among these, the origin and evolution of our galaxy and the Sun's trajectory within it are especially intriguing. In this thesis, I present several scientific studies that further our understanding of how disk galaxies, such as the Milky Way, evolve internally due to an important effect called radial migration that stars undergo. This effect implies that the Sun did not necessarily form at its present Galactic radius, but might have migrated from elsewhere in the Galaxy. It also might be responsible for the formation of thick disks, which many disk galaxies, including our own, are believed to harbor in addition to the thin one.

1.1 From the Big Bang to galaxies and stars

Based on our current understanding of observations of our universe, the leading model suggests that it began in a Big Bang about 13.8 billion years ago (Bennett et al. 2012; Planck Collaboration et al. 2013). In the beginning, it expanded rapidly allowing the initial hot and dense state to cool and form simple subatomic particles and eventually neutral hydrogen along with some helium and traces of lithium. Gravity and the ability to radiate away energy forced clouds of this gas to coalesce and form stars and galaxies. Elements heavier than helium, called metals in astrophysics, formed and keep forming through nuclear reactions inside stars and especially during their deaths as explosive supernovae.

1.1.1 Galaxies

There are more than 10^{11} galaxies in the observable universe. They range from dwarfs composed of $\sim 10^7$ stars to giants with as many as $\sim 10^{14}$ stars. In addition to stars, they can contain planets, an interstellar medium of gas and dust, and black holes, including supermassive ones at their centers. Galaxies are classified into four main types according to the Hubble classification system (see §4.1.1 in Binney & Merrifield 1998, hereafter BM98): disks, ellipticals, lenticulars, and irregulars.

Time $\longrightarrow$
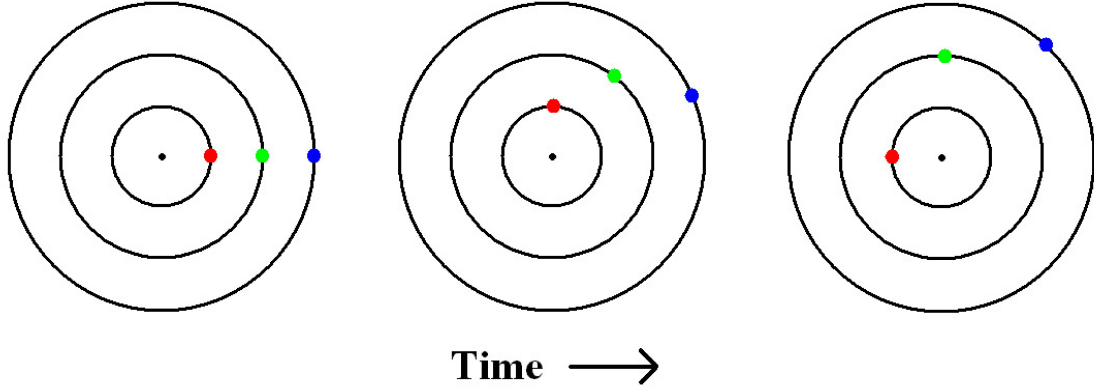
Figure 1.1 Cartoon of differential rotation in a disk galaxy shown face-on. Three blobs of matter (red, green, and blue) lie on circular orbits at three different radii all aligned along one azimuth initially. They orbit at the same constant circular velocity counterclockwise, which is realistic (see §1.1.2). This means that ones at smaller radii have greater angular velocities. Therefore, as time goes on, the closer ones to the galactic center move more rapidly in azimuth, which leads to a differential non-rigid rotation of the disk.

1.1.1.1 Disk galaxies

Roughly two thirds of the luminous galaxies in low-density regions are disk galaxies, such as our own Milky Way. In the high-density regions of cluster centers, however, their fraction can be less than 10%. As the name suggests, they are rotating disks of stars, with usually most or all the stars rotating in the same direction in each disk. See figures 4.6 and 4.7 in BM98 and plates 1, 3, 7, 8-10, 17, 18, and 19 in (Binney & Tremaine 2008, hereafter BT08) for photographs of examples. They do not rotate as rigid bodies, but possess differential rotation (BM98, §9.1), which means that different radial annuli within them rotate at different angular velocities. Fig. 1.1 illustrates this effect for three blobs at different radii. This, as I explain in §1.2, leads to the occurrence of spirals and bars. All disk galaxies, except S0 which are lenticulars, have spirals; so, they are sometimes interchangeably also called spiral galaxies.

Typical nearby disk galaxies have observable radii on the order of $10 - 20$ kpc [I]. The Sun is at a radius of about 8.5 kpc in the Milky Way (*e.g.* Eisenhauer et al. 2003; McMillan 2011). The radial density ρ of stars, or likewise the surface brightness, in each disk follows

---

[I]One kiloparsec is 3.1×10^{19} meters or 3,262 light years.

an approximate declining exponential profile with radius R:

$$\rho(R) \propto \exp^{-R/R_d} \qquad (1.1)$$

where R_d is the scale length (Freeman 1970; de Jong 1996). In some galaxies, the inner density deviates and rises steeper at smaller radii. Also, at the outskirts, the density can either follow the same exponential (Type I profile) or change to a steeper (Type II profile) (Freeman 1970) or more gradual (Type III profile) declining exponential (Erwin et al. 2005).

Even though these galaxies typically contain 10^{11} stars, the distances between nearby stars, not counting binaries, are so large in most of the disk that they do not interact with each other gravitationally. In the solar neighborhood (within ~ 10 pc of the Sun), stars are separated by 2 pc on average, *i.e.* the stellar density is ≈ 0.06 pc^{-3} (*e.g.* Dieterich et al. 2012). Only in the densest regions, which are the galactic centers and the centers of globular clusters introduced below, where the stellar density can be as much as 10^6 (*e.g.* Launhardt et al. 2002; Walcher et al. 2005) and 10^3 (Djorgovski 1993; Pryor & Meylan 1993; Harris 1996) times that of the solar neighborhood respectively, encounters and collisions between stars matter.

Disks contain a lot of cold gas, mostly in the form of molecular (≈ 10 K) and atomic (≈ 120 K) hydrogen (*e.g.* Kalberla & Kerp 2009; Schruba et al. 2011, see also BM98, §8.2). It resides in a superimposed disk that is more extended than the stellar one. The peak of its density, however, occurs at the middle radii of a stellar disk, where the spiral arms are densest and most luminous (*e.g.* Pineda et al. 2013, see also BM98, §9.2.4). Warm atomic and ionized hydrogen (≈ 8000 K) and hot ionized hydrogen ($\approx 10^6$ K) are also present, but reside mostly outside of the disk in much more extended and thicker components with much lower densities than the cold gas in the disk midplane (*e.g.* Petitpas et al. 2005; Trinchieri 2012). Dust, which is composed of $\approx 0.1 \, \mu$m grains of a few molecules of heavier elements, also resides in the disk and traces the spiral arms, but is likewise insignificant making up a mass 1% that of gas (*e.g.* Holwerda et al. 2013). Together, these only comprise $\lesssim 15\%$ of the visible matter by mass (BM98, §8.2.1). Hence, the stars really dictate the mean gravitational field of disk galaxies.

A lot of the cold gas is structured as giant molecular clouds (GMCs), whose average radii are ≈ 10 pc and masses $\gtrsim 10^5 M_\odot$ [II]. There are on the order of a thousand of them in the Milky Way, most lying along the spiral arms (*e.g.* Stark & Lee 2006). GMCs in the nearby Andromeda galaxy follow similar trends (Kirk et al. 2013). Since GMCs are more massive than stars, stars are scattered by them leading to a slow increase in random motion over time (Spitzer & Schwarzschild 1953), *i.e.* increase in the stars' orbit eccentricities and vertical amplitudes. Yet, this scattering plays a minor role (Hänninen & Flynn 2002) compared to scattering by spirals and bars (Sellwood & Carlberg 1984; Binney & Lacey 1988; Sellwood & Binney 2002), which I describe in §1.2.3, and compared to interactions with external nearby galaxies (Helmi et al. 2006; Kazantzidis et al. 2008). Disk galaxies have both old and young stars, which is consistent with the fact that new stars are born from cold molecular gas clouds. The majority of star formation happens in these GMCs in the spirals and at the galactic center, where the stellar and gas densities are greatest. I present more on star formation in §1.1.3.

Most disk galaxies also contain a central bulge (*e.g.* de Vaucouleurs 1948; Boroson 1981), which is a stellar spheroid with a scale radius several times shorter than that of the disk usually rotating in the same direction as the disk. Some bulges, called pseudobulges, are ellipsoidal and resemble thickened disks more compared to the classical bulges (Kormendy & Kennicutt 2004; Athanassoula 2005). In either case, their formation is not well understood yet. They mostly contain older stars, which suggests that they formed early (*e.g.* Peletier et al. 1999; Zoccali et al. 2003). Compared to the disks, they are smooth without filamentary structures like spirals or dust lanes.

The disks themselves, at least in most of the nearby galaxies, are composed of two, thin and thick, concentric disks (*e.g.* Gilmore & Reid 1983; Dalcanton & Bernstein 2002) or of many disk populations with gradually increasing thicknesses (Bovy et al. 2012a). With the exception of one found galaxy that has a counter-rotating thick disk (Yoachim & Dalcanton 2006), most thick disks rotate in the same direction as the thin. Since thick disks are important for this thesis, in §1.4, I present a much more detailed description of thick disks and their differences compared to the thin.

[II]One solar mass ($1 M_\odot$) equals 2.0×10^{30} kg.

Some stars in the Milky Way are assembled into gravitationally bound clusters. Each cluster contains stars roughly of the same age, so they formed from one molecular cloud at the same time. Globular clusters are distributed spherically about the galaxy, contain between 10^5 and 10^7 stars that are very old (10^{10} Gyr), and have diameters between 5 and 30 pc, so they are quite compact spherical objects (BM98, §4.5 & 6.1). About 160 of them are known (Harris 1996). On the other hand, open clusters are not spherically symmetric, are more diffuse, less luminous, and less compact agglomerations of stars that orbit in the plane of the disk, contain $10^2 - 10^3$ stars that are young ($10^6 - 10^9$ Gyr), and have diameters of $1 - 5$ pc (BM98, §6.2). Over a thousand of them have been observed. With time, open clusters get disrupted by gravitational interaction with GMCs in the disk. Other nearby disk galaxies are also observed to contain these two types of clusters (Burkert et al. 2005; Peacock et al. 2010; Larsen 2011). Our bigger disk neighbor Andromeda has about 500 globular clusters (Barmby & Huchra 2001), and some large elliptical galaxies, such as M87, have as many as 10,000 of them (Strom et al. 1981).

Disk galaxies are the focus of this thesis. See van der Kruit & Freeman (2011) for a recent extensive review of disk galaxy observations.

1.1.1.2 Other galaxies

Elliptical galaxies are spheroids or ellipsoids of stars, yet could in addition contain a small stellar disk (BM98, Figs. 4.3 & 4.4; BT08, plate 4). They have very little or no cold gas and dust. Consistently, most of the stars in them are old. Also unlike disk galaxies, they are not rotationally supported, and thus do not have the beautiful spiral and bar features of disks. Elliptical galaxies are preferentially found in clusters and compact groups of galaxies, and more so at the centers of the clusters, where they comprise about 40% of the galaxies. This and dynamical studies suggest that ellipticals are the result of mergers of galaxies of comparable size and mass that have achieved equilibrium (Toomre 1977b; Heyl et al. 1994; Barnes 1996; Schweizer 1998), although mergers in general can lead to many other results. Also, the size and shape similarity between small ellipticals and bulges, supports ideas that both form through similar mechanisms (Kormendy & Kennicutt 2004).

Lenticular galaxies are transitions between disks and ellipticals. They still contain a

rotating disk, a bulge, and sometimes a bar, but are smooth without spirals and have little or no cold gas, and accordingly also no recent star formation (BM98, Fig. 4.5). They also mostly reside at the centers of clusters, and can make up as much as half of the galaxies there (*e.g.* Dressler et al. 1997). They are likely disks from which cold gas has been removed by ram pressure stripping at the cluster centers, heating by hot intra-cluster gas, and/or ejection by their own active galactic nuclei (*e.g.* van Gorkom 2004; van den Bergh 2009).

Lastly, irregular galaxies are ones that have no obvious regular morphology. Their stars, especially young ones, are not organized in spirals or a bulge (BM98, Fig. 4.8; BT08, plate 12). Most of them are dwarfs that surround large disk or elliptical galaxies as satellites, such as the Small Magellanic Cloud of the Milky Way. The Large Magellanic Cloud used to also be considered an irregular, but now is known to contain a bar (Subramaniam & Subramanian 2009, BT08, plate 11). Hence, irregulars are thought to be disks or ellipticals that suffered disruptions and distortions due to neighboring galaxies, or collisions with other galaxies. Most of them are rich in gas, and form stars at rates comparable to those in disks, but have lower abundances of heavy elements (Gallagher & Hunter 1984; Hunter 1997).

Overall, irregulars and disks are more abundant than ellipticals and lenticulars in the universe. However, the smallest least luminous galaxies are irregulars, whereas the largest and most massive ones are ellipticals.

1.1.2 Dark matter

Astrophysicists also have come to realize that there is missing mass in the universe. The earliest evidence of this, and the most important for galactic dynamics, is the inability of visible matter to explain the orbital velocities of stars and gas in most disk galaxies, which follow flat rotation curves [III] out to the largest observable radii (Babcock 1939; Rubin et al. 1970; Bosma 1978; Persic et al. 1996). As shown in the left panel of Fig. 1.2, were it only to the gravitational field of visible ordinary matter, the rotation curves would decline with radius (see also BM98, p. 507).

The leading explanation for the missing mass postulates that it resides in a "dark matter"

[III]A rotation curve is the circular velocity V_c as a function of radius R from the galactic center: $\frac{V_c^2}{R} = \frac{\partial \Phi}{\partial R}$, in which Φ is gravitational potential making the right hand side the central attraction.
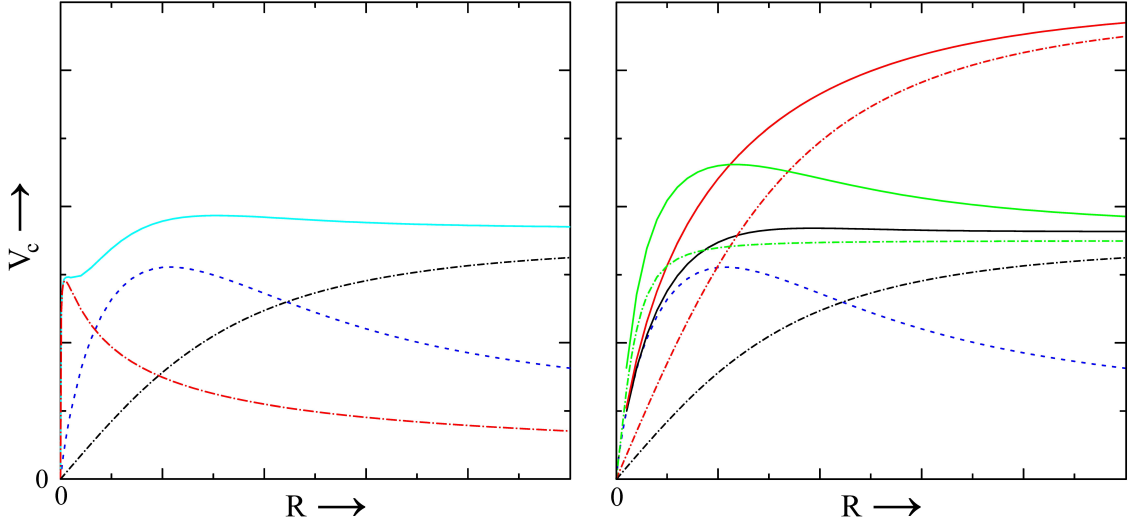
Figure 1.2 In the left plot, the solid cyan is a model (not taken from observations) of a typical rotation curve of stars and gas in a disk galaxy. The short dashed blue curve shows the contribution of an exponential disk, and the short dot-dashed red one that of an $r^{1/4}$ power-law bulge. Whereas the long dot-dashed black curve shows the contribution of a cored isothermal dark matter halo (eq. 4.2) necessary to yield the total cyan rotation curve. On the right, are the same disk and halo, but without the bulge, together giving rise to the solid black rotation curve. The red dot-dashed curve shows a more massive halo, and its composition with the same disk yields the steeper rising total solid red rotation curve. Likewise, the green dot-dashed curve shows a same mass halo as the black one, but with a smaller scale length, and yields the even steeper rising solid green rotation curve. The bar instability is weaker in systems with steeper rising rotation curves. For comparison, the total cyan rotation curve on the left, which includes a bulge, rises much steeper than these three curves; so, that model is much more likely to avoid a linear regime bar.

The cyan rotation curve in the left plot and the black one in the right plot are examples of maximal disks since their halo and/or bulge components contribute much less than the disk at the radii where the disk contribution peaks. The red and green rotation curves in the right plot, on the other hand, are examples of submaximal disks due to their denser inner halos.

that is invisible because it does not interact with electromagnetic waves and, to our current knowledge, only couples to ordinary matter through gravity. It is also believed to be "cold", which means that its particles move at non-relativistic speeds, much lower than the speed of light. The standard model of cosmology estimates that dark matter constitutes about 85% of the total matter in the universe (Planck Collaboration et al. 2013). So, ordinary matter is a minority, and at most 10% of it composes luminous matter in galaxies, whereas $30 - 40\%$ is in gas surrounding the galaxies, and the rest supposedly lies outside of virialized dark matter structures as diffuse gas (Fukugita & Peebles 2004).

Dark matter is believed to encompass disks in extended halos that have some triaxiallity. Furthermore, all galaxies are thought to reside in some dark matter concentrations, but not necessarily at their centers, as is the case for tidal dwarf galaxies. The estimated virial radius (BT08, p. 735) of the dark matter halo in which the Milky Way resides is on the order of 250 kpc, and its virial mass is $\sim 10^{12} M_\odot$ (*e.g.* Xue et al. 2008). The estimate of the circular speed at the Sun is ≈ 240 km s^{-1} (*e.g.* McMillan 2011).

1.1.3 Formation of disk galaxies and stars

Initially, the universe was very homogeneous with no structure. But as it cooled, fluctuations in density grew and formed a cosmic web of filamentary overdensities and voids. Clumps of dark matter merged due to gravity in a hierarchical way, *i.e.* smaller structures formed before larger ones. The densest structures, being the dark matter halos, formed and virialized at the intersections of filaments. In general, these halos were not spherical and had some ellipticity. They rotated and, on average, gained angular momentum over time due to torques from nearby halos caused by random misalignment between these ellipsoids (*e.g.* Efstathiou & Jones 1980). This spin was essential in the production of disk galaxies.

Unlike dark matter, ordinary matter in the form of gas can radiate away its energy through electromagnetic waves and collisions. Therefore, starting at about a redshift of $z \approx 30$ [IV], gas began to condense and fall into these dark matter potential wells, making ordinary matter dominant at the halo centers. Since gas cannot radiate away its angular

---

[IV] z is redshift (BT08, p. 39), which offers a measure of look-back time in the universe. In the modern ΛCDM cosmology, $z = 30, 20, 10, 5, 2, 1, 0.1$ correspond to $13.56, 13.48, 13.18, 12.47, 10.32, 7.73, 1.29$ Gyr ago respectively (Wright 2006).

momentum, it settled in rotating disk structures (Eggen et al. 1962; Mestel 1963; Gott & Thuan 1976; White & Rees 1978; Fall & Efstathiou 1980; Governato et al. 2007). And due to its ability to dissipate energy, it settled onto circular orbits. The earliest known galaxy is more than 13 Gyr years old at $z \approx 10$ (Bouwens et al. 2011).

The disks grew quickly and violently by merging with and consuming smaller galaxies within nearby passing subhalos. Eventually, this process quieted down, but the disks kept growing through the second process of accreting cold gas still residing in the outer halo and intergalactic medium (Brooks et al. 2009). Later accreted gas had more angular momentum on average due to the continued actions of the torques from nearby halos and due to being accreted along filaments (Stewart et al. 2013). Hence, it settled onto circular orbits in the midplane at greater radii, making the disks grow not only in mass, but also in radius. This, as observed in cosmological simulations and supported by theory, yielded the "inside-out" galaxy formation of disks (Fall & Efstathiou 1980; Matteucci & Francois 1989; Governato et al. 2007; Bovy et al. 2012c; Brook et al. 2012; Bird et al. 2013). Simulations also find that, early on, large amounts of gas were dumped onto the disks, whereas at later times, the disks accreted less cold gas (Birnboim & Dekel 2003; Kereš et al. 2005; Dekel & Birnboim 2006; Ocvirk et al. 2008; Brooks et al. 2009).

On smaller scales, the gas cooled to GMCs with temperatures less than 20 K. But it did not keep cooling down endlessly, because at some critical density, clouds became optically thick, meaning that light could not escape from them anymore, which caused further collapse to heat the gas as opposed to cool it. Soon, hydrostatic equilibrium between gravity and radiation pressure was established, and stars formed, although we still have an incomplete understanding of the star formation process.

Early stars released a lot of radiation between $z \approx 20$ and 10 that began reionizing the universe making almost all the gas in the universe ionized by $z \approx 6$ (*e.g.* Becker et al. 2001). This heated the intergalactic medium to temperatures of $\approx 10^4$ K, which made subsequent infall of gas into halos less massive than $\approx 10^8 M_\odot$ impossible (BT08, p. 761). If such halos did not form stars before reionization, they remained dark without stars till present (Dekel & Woo 2003).

Stars form from a small fraction of the gas in their molecular clouds, while most of the

gas gets expelled both mechanically and radiatively into the interstellar medium during the formation process. This ejected energy, called feedback, along with the more powerful ejections from supernovae and active central supermassive black holes, quenches successive star formation. However, it also ejects gas out of the disk, of which some remains in the halo, but the majority quickly settles back onto the disk in cold streams and produces new GMCs and stars (Pettini et al. 2001; Strickland et al. 2004; Governato et al. 2007; Brooks et al. 2009). Thus, the evolution of star formation in disk galaxies heavily depends on the interplay between accretion and feedback.

1.1.4 Stellar ages and abundances of elements

In this subsection, I introduce the three populations, or more properly generations, of stars, which are based on the abundances of elements in their composition. I also describe how astrophysicists estimate the ages of stars.

1.1.4.1 Stellar populations and abundances

The first stars, called population III stars, contained predominantly hydrogen, helium, and traces of primordial lithium from the Big Bang. They must have been massive ($\gtrsim 10 M_\odot$) given the huge amount of ionizing radiation we believe they emitted to reionize the universe. This means that they evolved and died quickly on the timescale of a few million years, because more massive stars have greater pressure acting on their cores, so they burn their hydrogen more rapidly. Consistently, none have been observed yet, *i.e.* all known stars contain some small quantities of heavier elements. Most stars in the immediate present universe, on the other hand, live between one and ten billion years. Yet, some, such as red dwarfs, can be almost as old as the universe, and could last hundreds of billion years. The oldest known star is about 13.2 Gyr old (Frebel et al. 2007).

When the population III stars died, their supernovae produced some metals (elements heavier than helium). The next generation stars were born in the same molecular clouds out of this gas, so they contain some contaminants such as oxygen and carbon. These, still metal-poor stars, are called population II stars, and are observed in the Milky Way. Each further stellar death enriched the environment more and more, so the metallicity grew in

newer generation stars. Therefore, one might expect that it is possible to date stars by spectroscopically observing abundances of metals in their atmospheres. However, newly accreted pristine cold gas from the halo keeps mixing with and diluting the gas already present in the disk, and from it new stars keep forming with lower metallicities. This makes the age-metallicity relation weak and debatable (Edvardsson et al. 1993; Nordström et al. 2004, see also BM98, p. 644). For example, the thick disk of the Milky Way contains some stars that have solar metallicities, but are much older than the Sun (Bensby et al. 2007b).

Astrophysicists usually use observations of iron to quantify stellar metallicity since its absorption lines are easy to measure, and actually measure its ratio to the abundance of hydrogen. Metallicity is a dimensionless quantity denoted as [Fe/H], or sometimes as [Me/H], and follows the formula:

$$[\text{Fe/H}] = \log_{10}\left(\frac{N_{\text{Fe}}}{N_{\text{H}}}\right)_{\text{star}} - \log_{10}\left(\frac{N_{\text{Fe}}}{N_{\text{H}}}\right)_{\text{Sun}}, \tag{1.2}$$

in which each N_{Z} is the number of atoms of species Z per unit volume. The star's measured abundance ratio is compared to that of the Sun, for which $\log_{10}(N_{\text{Fe}}/N_{\text{H}})_{\text{Sun}} = -4.5$ (*e.g.* Grevesse & Sauval 1999).

When spectra are not available, astrophysicists estimate metallicity using photometry since stellar colors have a relative sensitivity to photospheric abundances: absorption lines affect different parts of a stellar spectrum differently. Traditionally, $B - V$ and $U - B$ colors have been used (*e.g.* Roman 1955; Sandage & Eggen 1959; Wallerstein 1962; Carney 1979; Karaali et al. 2011), but recently (Ivezić et al. 2008) used more accurate relations to metallicity in the $u - g$ versus $g - r$ colors plane for F and G dwarfs, which are the most interesting stars as I discuss in §1.1.4.2.

The metallicity in the Galaxy and other nearby disk galaxies declines both with radius in the disk and also with height above and below the midplane (*e.g.* Ivezić et al. 2008; Bovy et al. 2012c). One of the most metal rich stars known to date has triple the metallicity of the Sun (Feltzing & Gonzalez 2001), and the most metal poor, found in the Galactic halo, at least five orders of magnitude less (Caffau et al. 2011).

The youngest metal-rich stars are called population I stars, though they are still primarily made up hydrogen and helium. The Sun for example, which is an intermediate age star, contains about 70% hydrogen, 28% helium, and only 2% metals by mass (BM98, p. 101). They are found preferentially along the spiral arms in disk galaxies, which is why the arms are brighter than the surrounding disk between them, and lie in thinner disks in the Milky Way (*e.g.* Bovy et al. 2012c), which correlates with denser regions, where star formation is more frequent due to more gas and more frequent collisions between molecular clouds. In other words, the thin disk mostly contains population I stars of ages less than 8 Gyr with the very midplane containing the youngest ones, whereas the thick disk stars are primarily population II stars of ages greater than 8 Gyr shown in Fig. 1.3. The bulge also contains old population II stars (*e.g.* Zoccali et al. 2003), except in its dense core and intersection with the disk (*e.g.* van Loon et al. 2003). There are also stars, called halo stars, orbiting on spherical orbits even further from the midplane than the thick disk, and are extremely old population II stars with ages greater than 10 Gyr. Thus, globular clusters also contain the oldest population II stars, while open clusters have population I stars. Other nearby disk galaxies contain similar components (*e.g.* de Vaucouleurs 1959; Yoachim & Dalcanton 2006).

Interestingly, population II stars, despite having lower overall metallicities than population I ones, often have greater ratios of alpha elements [V] relative to iron. The cause is hypothesized to be due to certain supernovae types being more prominent in the earlier universe (Wolfe et al. 2005). Type II supernovae mainly produce the alpha elements, whereas type Ia ones produce iron-peak elements: Sc, Ti, V, Cr, Mn, Fe, Co, Ni, and Cu (BM98, p. 298). Hence, $[\alpha/\text{Fe}]$ has also been used as a rough proxy for stellar age.

1.1.4.2   Estimating stellar age by fitting isochrones

Yet, the most straightforward and reliable way to estimate a star's age is to use the fact that its brightness and surface temperature increase with age in a reasonably determined way while hydrogen fusion dominates its energy production, which is while it lies on the

---

[V]Alpha elements form through the capture of α-particles (^4_2He) beginning with ^{16}O during the alpha process, which is one of the two chains of nuclear fusion reactions in stars (BM98, p. 297). Specifically, they are ^{20}Ne, ^{24}Mg, ^{28}Si, ^{32}S, ^{36}Ar, and ^{40}Ca.
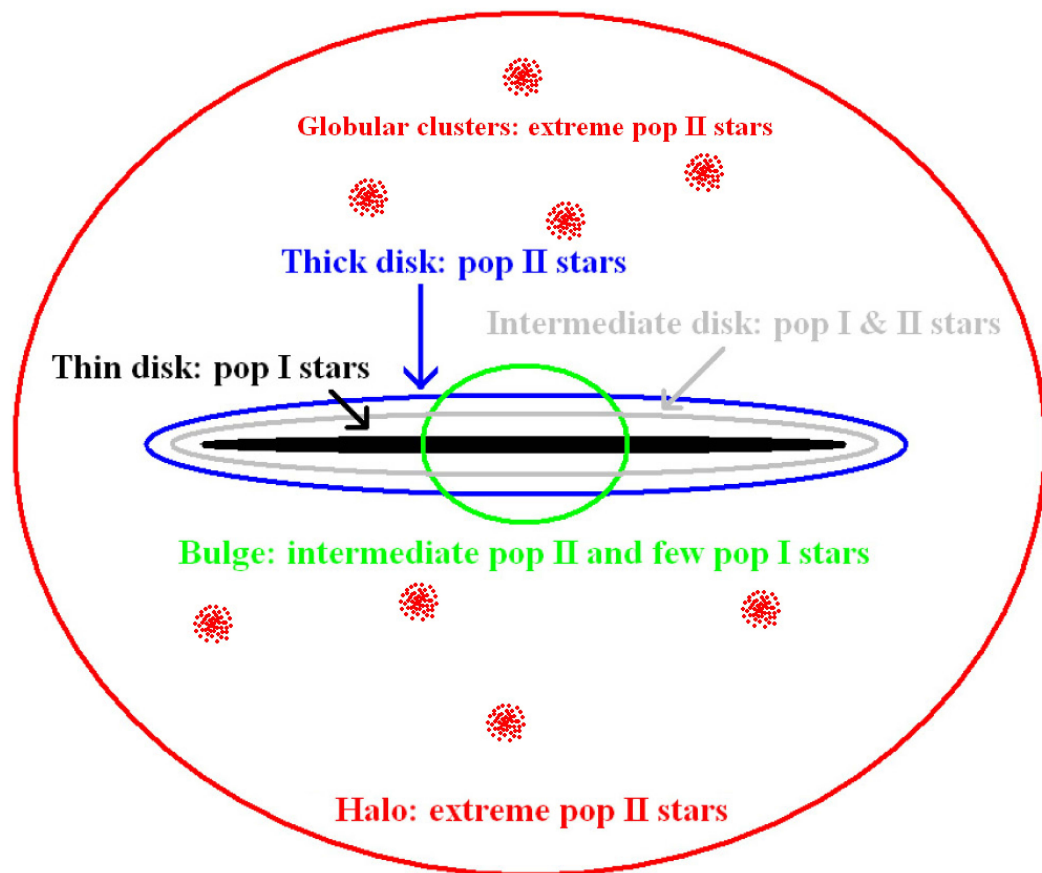
Figure 1.3 Illustration of the Milky Way stellar components and their stellar populations. The thin disk is in black, thick in blue, intermediate disk in gray, bulge in green, and halo and globular clusters in red. This is a qualitative picture with the components' sizes not drawn to scale. The halo represents halo stars, not the dark matter halo that is much more extended.

main sequence in the Hertzsprung-Russel diagram (BM98, pp. 106, 344 & 643). The H-R diagram (BM98, p. 102) plots stellar luminosity versus temperature or color (BM98, p. 52). Redder stars are fainter and colder, while bluer ones are more luminous and hotter. As discussed above, brighter stars burn their fuel faster since they are more massive (see figure 25 in Nordström et al. (2004) for a plot of how stellar mass correlates with age). Therefore, red stars live long, and blue main sequence stars (not white dwarfs) die quickly. Numerical models of the rate of increase in luminosity allow one to determine the age of a star given its mass. These models dictate how isochrones, which are curves in the H-R diagram of populations of stars with identical ages (BM98, p. 340), change with time. Stars are born on the so called zero-age main sequence, and as they evolve and move away from it, one can date them by fitting these isochrones to the stars' current location in the H-R diagram.

This works best for dating star clusters, both open and globular, since each one's members have the same age and metallicity, and therefore trace a single isochrone (BM98, p. 344). In fact, clusters are essential to the method of fitting isochrones, because astrophysicists use them to build the data bank of real observed isochrones. One can also just use the averaged color of a cluster, as opposed to resolving its stars individually, to date it. Newly formed clusters contain stars of a wide range of colors due to their wide range of initial masses. Young clusters are blue because the bluer brighter stars outshine the redder fainter ones. Since the bluer stars die quicker, a cluster's color shifts from blue to red gradually with age.

Given the current age of the universe, this isochrone dating technique works well, although still has some issues (*e.g.* Nordström et al. 2004; Holmberg et al. 2007), for MK (BM98, p. 90) dwarf stars of type G and earlier, because these stars leave the zero-age main sequence within 10 Gyr. F and G dwarfs are the most interesting for studying the formation and evolution histories of the Milky Way and other close disk galaxies since they live comparable to the long galactic evolution time scales.

See Jørgensen & Lindegren (2005) for a Bayesian estimation of ages using theoretical isochrones.

Dating red giants, the later quicker stellar evolution stage when elements heavier than hydrogen become the primary fuel, is much tougher because their evolution models are much less certain. However, one can still place lower bounds on their ages by estimating

their main-sequence lifetimes given their masses.

1.1.4.3   Radial mixing of formation environments

Most stars, and more so GMCs, have circular or nearly circular orbits in the Milky Way (*e.g.* Bond et al. 2010). Were there no mechanism to transport them radially, the environments of radial annuli would not mix with each other, and the stellar metallicity would be correlated with angular velocity, because under a flat rotation curve, angular velocity is $\propto R^{-1}$, and thus decreases monotonically with radius. However, stars in the solar neighborhood have a big range of metallicities (*e.g.* Holmberg et al. 2007; Haywood 2008; Bovy et al. 2012c) that poorly correlate with their angular velocities (Nordström et al. 2004; Ivezić et al. 2008; Bond et al. 2010). Therefore, there must exist a mechanism that mixes formation environments radially while keeping stars and GMCs on nearly circular orbits.

I show in §1.3 that radial migration does exactly that and very effectively. Under its influence, the correlation between metallicity and angular velocity should diminish with stellar age, but still be present for young stars since they did not have time to undergo substantial radial mixing. Some simulations yield exactly this trend when stars are selected in thin height slices (Loebman et al. 2011), and observations (*e.g.* Lee et al. 2011; Yu et al. 2012; Boeche et al. 2013) and chemical Galactic evolution models (Schönrich & Binney 2009a; Wang & Zhao 2013) show it too.

Thus, radial migration erases the star formation history in disk galaxies, and poses one of the biggest challenges to Galactic archeology, the study of the Milky Way's past. By mixing stars radially, it erases radial trends of nearly conserved stellar properties, such as metallicity, more and more with increasing stellar age. In §1.3.2, I describe observational evidence for this. Theory and simulations of disk galaxies reveal that radial migration is always present when spirals exist, and is very hard to stop. This is why radial migration is important and interesting.

1.2 Dynamical features of disk galaxies

Due to differential rotation and large angular momentum, disk galaxies possess much more complex and interesting behavior than ellipticals that have large velocity dispersions and rotate slowly. In addition to a bulge, disks contain spiral structure and sometimes a bar. They may also exhibit less frequent features, such as rings, warps, lenses or ovals, and cartwheels. Yet, we focus on spirals, because their transient nature gives rise to radial migration, and on bars, because theoretically they should stop radial migration within them.

1.2.1 Spirals

Spirals, the most beautiful and magnificent features of disk galaxies, are non-axisymmetric spiral-shaped overdensities of stars, gas, dust, and star formation in the plane of the disk. Hence, they are best seen in face-on disks. See plates 1, 8, 9, 17, 18 & 19 in BT08 for examples. They emanate from inside out radially, but rarely begin at the very center of the disk. Sometimes, however, disks contain secondary very small spirals at their centers. Although spirals are not axisymmetric, they do posses a rough m-fold rotational symmetry if they contain m arms. However, a significant fraction of spiral galaxies are lopsided (*e.g.* Rix & Zaritsky 1995). The ratio of the surface density of an arm to that of the inter-arm region is typically ~ 1.5 (Rix & Zaritsky 1995). The potential of a spiral should decrease with distance away from the midplane, to which we give a simplified explanation in §2.4.

In general, spiral structure comes in many forms. About 10% have grand design spirals, such as M51 on plate 1 in BT08, that have long, symmetric, continuous arms most often occurring as two main ones. On the other end of the spectrum, $\sim 30\%$ have flocculent spirals, which consist of many patchy discontinuous arm segments, like galaxy M63 on plate 9 in BT08. The rest more common spirals have the intermediate state with less regular arms than grand design ones that can branch out, or bifurcate, and more often occur in more than two. An example is M101 on plate 18 in BT08. One armed spirals, such as NGC 4725 (de Vaucouleurs et al. 1991), are quite rare.
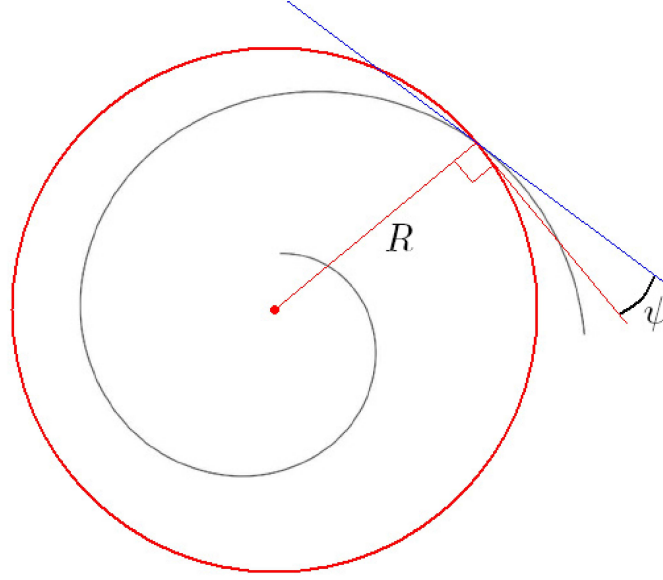
Figure 1.4 Angle ψ shows the pitch angle of the spiral arm at radius R, which by definition is the angle between the circle of radius R (in red) and the tangent (blue line) to the spiral arm (in black) at R.

Each of these types comes in both loosely and tighter wound arms. The Hubble classification system (MB98, §4.1.1) classifies different spirals based upon the degree of winding, or openness. At any radius, the pitch angle ψ of an arm is the angle between the circle of that radius and the tangent to the arm as Fig. 1.4 shows. Usually, the pitch angle barely varies with radius in a spiral arm. In the case that ψ is independent of radius R, the arm traces a logarithmic spiral: $\ln(R) = \tan(\psi)\phi + constant$, in which ϕ is the azimuthal angle. Tighter wound spirals of Hubble type Sa have pitch angles near $\sim 5°$, whereas loosely wound Sc galaxies have angles that range from $\sim 10°$ to $\sim 30°$. Overall, the typical values are between $\sim 10°$ and $\sim 15°$ (*e.g.* Garcia Gomez & Athanassoula 1993). See for example Ma (2002) for how the pitch angles vary between different spiral Hubble types.

Spirals for which the orientation with respect to the direction of the galaxy's rotation has been unambiguously determined are almost always trailing (Hubble 1943; de Vaucouleurs 1959; Pasha 1985), meaning that their outer tips point in the direction opposite to galactic rotation as shown in Fig. 1.5. A few leading spirals, however, have also been observed (Pasha 1985; Buta et al. 1992, 2003).
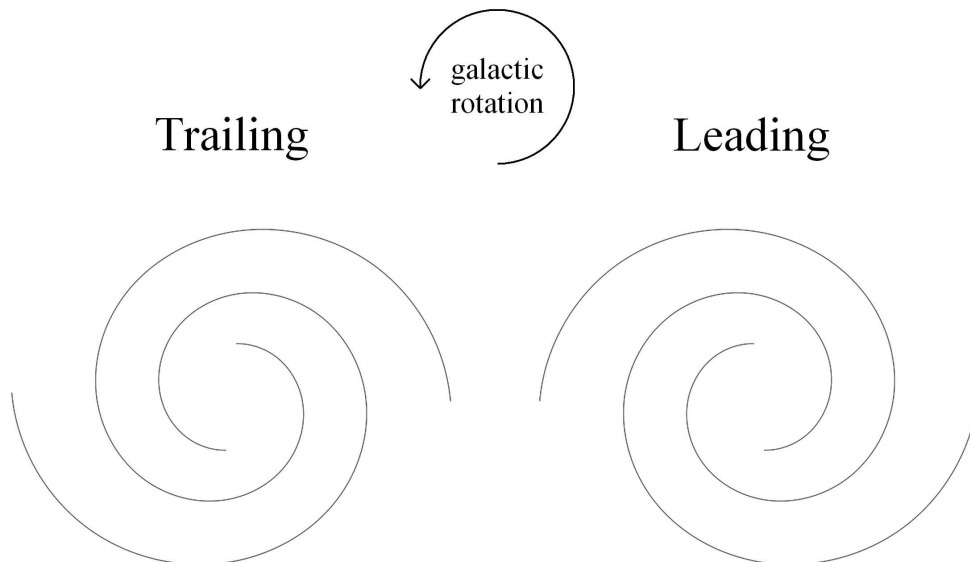
Figure 1.5 Illustration of trailing (left) and leading (right) spiral arms in a disk galaxy that rotates counterclockwise.

1.2.1.1 Origin of spiral structure

The reason why disks tend to form spirals is because this is their way of evolving to lower energy states. In order to do that, they have to contract so that most of the mass concentrates at the center with low angular momentum, while few stars end up on very large orbits carrying most of the angular momentum of the initial system. Hence, it is preferential for them to transfer angular momentum outwards. Momentum conservation does not allow them to contract axisymmetrically. Non-axisymmetric spirals, on the other hand, exert torques on the stars, and exchange angular momentum between them. In §1.2.3.1, I explain that trailing spirals yield an outwards flow of angular momentum (Lynden-Bell & Kalnajs 1972; Lynden-Bell & Pringle 1974). This is why spirals are preferentially trailing. Unlike fluid disks, in which viscous and magnetic stresses can transfer angular momentum, stellar disks have to assemble such overdensities as spirals that can exert torques. However, how efficiently they can form spirals depends on various conditions, especially the degree of random motion.

The presence of gas and the ability to form new stars complicates the picture, but actually strengthens the occurrence of spirals. In fact, whether a disk galaxy contains spirals

highly depends on the presence of cold interstellar gas and young stars. These features exactly distinguish lenticular disks from spiral galaxies (*e.g.* Caldwell et al. 1993; van Gorkom 2004), and only a few gas-poor disks are known that harbor spiral structure, which were probably only recently stripped of their gas (*e.g.* Strom et al. 1976; Yamauchi & Goto 2004). Sellwood & Carlberg (1984) showed that spiral activity fades over time in simulations without gas dissipation, because the spirals themselves raise the velocity dispersion and random motion in the disk making it less responsive. The addition of new stars on circular orbits counteracts this by cooling the disk dynamically (lowers the radial velocity dispersion), and thus can yield indefinite spiral activity. Carlberg & Freedman (1985) and Toomre (1990) further showed that any dynamical cooling of the disk can maintain the recurrence of spirals.

It is hard for dynamically cold enough disks to avoid forming some spirals in the presence of differential rotation. As Fig. 1.1 shows, radial patches of young luminous stars quickly wind up into spiral configurations. However, differential rotation is also a curse, because it winds up material much more quickly than the age of the galaxy. Since very wound up spirals are not observed, large spiral patterns cannot be material arms, meaning that the matter composing them cannot remain in them for their entire lifetime.

One possible solution to this winding problem is that the spirals are composed of young luminous stars that do wind up, but die off quickly (most luminous stars have very short lifetimes of ~ 5 Myr), and constantly ongoing star formation regenerates new patterns. This can explain flocculent spirals, but not grand design ones since, in them, not only young stars but also old ones and most of the mass exhibit the spiral structure. I discuss evidence for this in the next subsection.

Another explanation is that external disturbances from close encounters or satellite galaxies produce temporary spirals. This could likely be the case in the grand design galaxy M51 that has recently had an encounter with NGC 5195 (BT08, plate 1). Toomre & Toomre (1972) explained with a model how the large scale spirals of M51 could arise due to its neighbor. M81 is another example with its companion NGC 3077 (Yun et al. 1994).

Inner bars (§1.2.2) have also been proposed to excite spirals outside of them. The fraction of grand design spirals is much greater in barred galaxies than non-barred ones

(Kormendy & Norman 1979; Elmegreen & Elmegreen 1982). In many barred galaxies, the spirals seem to originate at the ends of the bar, which might suggest that the bars drive them. However, Sellwood & Sparke (1988) found that the spirals have different smaller pattern speeds than the bar in simulations, and observations seem to support this (Seigar et al. 2003; Buta et al. 2009).

Other proposed non-self excitation mechanisms of spirals include substructure in the dark matter halo (*e.g.* Dubinski et al. 2008). Many spiral galaxies do not have companion galaxies nor bars, yet still exhibit large or intermediate-scale spirals. Furthermore, simple collisionless N-body simulations, even two-dimensional ones, of single disks without external perturbers or bars and with no halo or a spherically symmetric rigid one naturally produce spirals (*e.g.* Miller et al. 1970; Hohl 1971; Hockney & Brownrigg 1974; James & Sellwood 1978; Sellwood & Carlberg 1984). Unfortunately, there is still no satisfactory well accepted theory of self-excited spirals.

The preferred leading explanation to the winding problem is that spirals are actually not material, but are density waves in the gravitational potential and density. This idea was invented by Lindblad (1963) and first carefully studied by Lin & Shu (1964) and Lin & Shu (1966).

There are three theories for mechanisms of self-excited spirals. Lindblad (1963), Lin & Shu (1964), and Lin & Shu (1966) originally assumed that spirals are long-lived stationary standing waves. Supposedly, these waves grow from a gravitational instability in the disk and are eventually stabilized by damping due to shocks in interstellar gas. In §1.2.1.3, I go over evidence against this idea. Then, Goldreich & Lynden-Bell (1965) and Toomre (1990) argued that spirals are short-lived transient collective responses to internal fluctuations in density. Finally, Sellwood (2000) agreed that they are transient, but proposed that a cycle of recurrent large-scale instability modes keeps regenerating them, *i.e.* each spiral wave leaves behind an altered distribution function that provokes a new instability. Sellwood & Lin (1989) also reported such cycles earlier in their simulations. All three of these theories portray spirals as density waves. I present a detailed explanation of density waves in §1.2.3.

1.2.1.2 Distribution of different components of ordinary matter in spiral arms

Most of the light in optical observations of spirals comes from luminous young stars and partially ionized hydrogen (HII) regions of recent star formation. Near-infrared, on the other hand, mainly traces old stars that dominate the mass, and thus are more important for the dynamics. In grand design spirals, the spiral structure also exists in the old stars, but constitutes broader and smoother arms, probably due to phase mixing over time (Zwicky 1955; Schweizer 1976; Rix & Zaritsky 1995; Eskridge et al. 2002; Grosbøl et al. 2004; Zibetti et al. 2009). The existence of the spirals in the mass supports the leading hypothesis that spirals are density waves, which I discuss in §1.2.3. Young star and star formation arms are usually found slightly inside the old star arms.

In the well studied grand design spiral galaxy M51 (BT08, plate 1), neutral hydrogen (HI) (Rand & Kulkarni 1990; Rots et al. 1990), which arises by ultraviolet radiation from young stars dissociating molecular hydrogen (H_2) (Tilanus & Allen 1989), and HII (*e.g.* Kennicutt et al. 2003; Shetty et al. 2007), which these young stars ionize, both coincide with the young star arms. Further inside of them, lie arms traced by molecular gas clouds in carbon monoxide (CO) emission (Rand & Kulkarni 1990; Young & Scoville 1991; Regan et al. 2001; Shetty et al. 2007; Egusa et al. 2009), non-thermal radio continuum emission from synchrotron radiation of relativistic electrons spiraling in magnetic fields (Beck et al. 1996; Fletcher et al. 2011), and dust (Lynds 1970; Elmegreen 1980; Rix & Rieke 1993). These correspond to compressed gas, and show where the gas density is highest. Fig. 1.6 shows the locations of all of these components with respect to each other in a spiral arm such as that of M51.

This distribution of different components of ordinary matter about the spiral arms of M51 also fits the density wave theory. As a spiral wave sweeps across the galactic disk, it collects gas and dust due to orbit crowding and gravitational instabilities in its potential well. This enhances the gas density at the crest of the spiral, and leads to enhanced star formation due to the greater amount of gas and the fact that denser gas turns into stars faster. A spiral pattern moves slower than the matter about the galactic center inside its radius of corotation (see §1.2.3.2), which is where the angular velocity of stars equals the

flow of matter
through the spiral

galactic
rotation
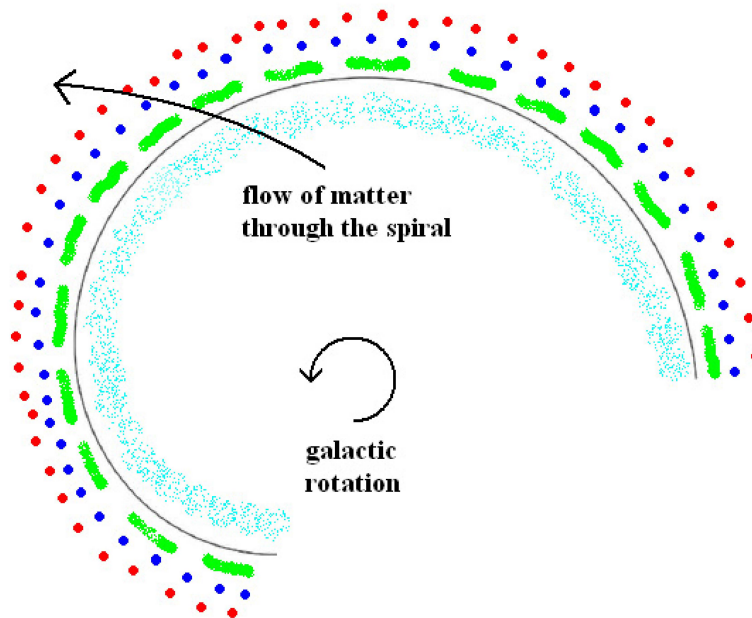
Figure 1.6 Locations of different ordinary matter components in an arm of a trailing grand design spiral such as that of M51. The gray curve shows the crest of the spiral density wave. Just inside it are molecular gas clouds, dark nebulae, and dust lanes, which are shown in cyan. Outside of the crest, first are HII gas regions (green) corresponding to ongoing star formation, then follow young star clusters (blue), and outside them lies the center of the broad older stars arm (red). This distribution, shown here, occurs at radii inside of corotation (§1.2.3.2), where the angular velocity of matter is faster than the pattern speed of the spiral wave. Outside of corotation, the opposite is true, which should yield a flipped distribution.

pattern speed of a spiral. Therefore, stars form and move out ahead of the arm. The displacement between the luminous young stars and molecular gas and dust reflects the time lag between the maximum compression of the gas and star formation (*e.g.* Tamburro et al. 2008; Egusa et al. 2009). Thus, the observed distribution assembles: gas and dust lie inside the spiral crest, HII regions just outside of it, followed by young stars, and further out older stars.

Outside of corotation, on the other hand, gas and stars have smaller angular velocities than the pattern speed of the spiral wave, so this distribution should be exactly flipped about the wave crest. Grand design spirals rarely show this flip, so they supposedly lie inside corotation.

This trend holds in many other grand design and some intermediate-scale spiral galaxies (*e.g.* Kaufman et al. 1989; Knapen & Beckman 1996; Eskridge et al. 2002; Sánchez-Gil et al. 2011), but there are also enough exceptions (*e.g.* Sánchez-Gil et al. 2011), and some disks contain both spiral arms that follow this trend and ones that do not (*e.g.* Humphreys & Sandage 1980). It is also not obvious in many intermediate spirals. Thus, it is far from clear whether this density wave picture can be applied to all such spirals.

In flocculent spirals, on the other hand, there is little or no significant spiral structure in the mass distribution traced by the old stars (Elmegreen & Elmegreen 1984; Thornley 1996). Also, their CO emission is more uniform and less concentrated in arms (*e.g.* Regan et al. 2001). Their short spiral segments are probably local star formation regions that have been sheared out by differential rotation.

1.2.1.3   The transient nature of spirals

The observations discussed in the previous subsection do not necessarily imply that spirals are stationary and survive over many orbital periods. In fact, all simulations show and theory suggests that they are recurring transient features each lasting one to two orbital periods (between 200 and 300 Myr on average) (*e.g.* Goldreich & Lynden-Bell 1965; Julian & Toomre 1966; Miller et al. 1970; Hohl 1971; Hockney & Brownrigg 1974; James & Sellwood 1978; Toomre 1981, 1990; Sellwood & Carlberg 1984; Sellwood & Lin 1989; Sellwood 2000, 2011). Large-scale grand design spirals theoretically redistribute the angular momentum

distribution of the disk on timescales much shorter than the lifetime of the galaxy (BT08, §6.1.5), which implies that these spirals do not live long.

Goldreich & Lynden-Bell (1965) and Julian & Toomre (1966) separately discovered that galactic disks are quite responsive to small disturbances. The former group reported simple simulations of differentially rotating fluid disks in which minor initial disturbances grew, sheared out, and amplified by factors of ten or more. The latter group showed that a massive point particle on a circular orbit produces a strong spiral wave in the stars of a differentially rotating stellar disk. These studies suggest that disks, both fluid and stellar, are very sensitive to even minor disturbances, and respond to them by forming spirals. Since galaxies are frequently subject to such and greater disturbances, single spirals probably do not live long.

Originally, Lindblad (1963), who first envisioned spirals as density waves, hypothesized that they are stationary waves corresponding to neutral quasi-steady global modes of the disk. Analytical studies over the years have supported this idea (*e.g.* Lin & Shu 1964, 1966; Lynden-Bell & Kalnajs 1972; Bertin et al. 1989a,b; Bertin & Lin 1996). Thomasson et al. (1990), Elmegreen & Thomasson (1993), Donner & Thomasson (1994), Zhang (1996), and Zhang (1998) also claimed to have produced long-lived spirals in simulations, but they all failed to provide convincing evidence that these patterns were not a superposition of multiple recurring waves or a growing bar instability. Theory suggests that long-lived spiral waves do not transport angular momentum realistically fast enough. See §6.2.6 in BT08 for a detailed explanation of energy and angular momentum transfer due to spiral waves, and §§6.2.4 & 6.2.5 for the long-wave branch of the dispersion relation that long-lived spirals rely on, but transient ones do not.

The truth about the lifetimes of spirals has proven to be very difficult to tackle observationally, and is still debated.

Some groups (*e.g.* Martínez-García & González-Lópezlira 2013) have incorrectly assumed that the systematic offsets between different components or between stars of different ages in spiral arms discussed in §1.2.1.2 proves that spirals are stationary and long-lived. Short-lived transient spirals equally can give rise to such offsets since most of them are

likewise trailing and contain a substantial region of the disk inside their corotation. Furthermore, estimated ages of the stars that clearly display these angular offsets are $\lesssim 200$ Myr (*e.g.* Tamburro et al. 2008; Egusa et al. 2009; Foyle et al. 2011).

In simulations, decompositions of density into Fourier components show that multiple spiral patterns often coexist at the same time with different pattern speeds and different number of arms. Normally, one wave dominates in amplitude at a given time, but, being transient, it soon declines, and another mode grows to dominance. Similar decomposition methods (Tremaine & Weinberg 1984; Meidt et al. 2008) applied to CO data of some real galaxies reveal the same presence of multiple waves (Meidt et al. 2009). This also does not say much about the lifetimes of the spirals, as in principle multiple stationary ones can coexist.

See Sellwood (2011) for a review of other observational attempts that failed to provide evidence for or against either theory.

To date, truly only one study came close to differentiating between the two theories. Sellwood (2010) showed that the in-plane velocity distribution of solar neighborhood stars (Nordström et al. 2004) carries evidence of scattering by the latest inner Lindblad resonance (see §1.2.3.2), which agrees with the transient spiral picture. The distribution contains a number of different streams and no smooth component (Bovy et al. 2009), which various studies have shown cannot arise from stars possessing similar kinematics (Famaey et al. 2007; Bensby et al. 2007a; Bovy & Hogg 2010).

Our simulations only have short-lived transient spirals. Their transience is the key feature that yields radial migration as I show in §§1.2.3.2 & 1.3, and thus is central to this thesis. The fact that radial migration can explain local trends in relations between stellar metallicity and age and between velocity dispersion and age, which I discuss in §1.3.2, is additional proof that spirals are transient features.

1.2.2 Bars

Although less frequent than spirals, bars are the greatest amplitude dynamical features seen in disks oriented close to or directly face-on towards us. As their name suggests, they are straight cigar-shaped structures of stars, gas, and dust at the centers of disks, although

some are lopsided and are not centered exactly on the galactic center (*e.g.* de Vaucouleurs & Freeman 1972). They can vary from strong luminous elongated ones to weak faint oval looking ones. See Figs. 4.7 & 4.8 in BM98 and plate 10 and Figs. 6.27 & 6.28 in BT08 for examples of barred galaxies. Also see Fig. 4.57 and page 229 in BM98 for an isophotes decomposition of two typical bars showing their internal structure. The Milky Way also contains a bar (*e.g.* Johnson 1957; de Vaucouleurs 1964; Gerhard 2002; Merrifield 2004).

Bars are very common. About a third of spiral galaxies contain strong bars, and if weak bars count, then about two thirds or more are barred (*e.g.* Sellwood & Wilkinson 1993; Eskridge et al. 2000; Menéndez-Delmestre et al. 2007; Barazza et al. 2008; Aguerri et al. 2009; Masters et al. 2011). The fraction of bars has increased since redshift $z \sim 1$ by about a factor of two in intermediate stellar mass galaxies, and stayed about the same in massive ones with masses greater than $10^{11} M_\odot$ (Elmegreen et al. 2004; Jogee et al. 2004; Sheth et al. 2008; Barazza et al. 2009; Nair & Abraham 2010; Cameron et al. 2010). This somewhat suggests that bars live long in real galaxies, which agrees with theory and simulations of isolated disks, in which bars usually persist till the end of the simulations after forming and are hard to destroy. Interactions and mergers with satellite galaxies, however, can destroy bars quickly (*e.g.* Athanassoula & Bosma 2003).

The bar fraction shows a bimodality in galaxy color, with many more bars residing in redder disks (ones with fewer young stars) (*e.g.* Masters et al. 2011; Hoyle et al. 2011). Furthermore, longer bars are preferentially found more in redder disks and shorter ones in bluer ones (Hoyle et al. 2011). Bars also occur more often and are longer in disks with better pronounced bulges (Masters et al. 2011; Hoyle et al. 2011).

Strong bars have bar-interbar contrast ratios of $3 - 5$ (*e.g.* Elmegreen 1996) and contribute about $10 - 30\%$ to the total luminosity (*e.g.* Ohta et al. 1990). Near-infrared observations show that they contain most of the mass of the disk material at the inner radii where the bar lies (*e.g.* Eskridge et al. 2000). So they are mostly composed of old stars, and, in fact, stronger bars are preferentially redder and older (*e.g.* Eskridge et al. 2000; Hoyle et al. 2011), which makes them only appear in near-infrared observations. Furthermore, they are the most elongated triaxial stellar structures known in the universe. Ratios between their major and minor in-plane axes are on average between $2 : 1$ and $5 : 1$, whereas

elliptical galaxies are rarely found with ratios greater than 3 : 1. The shapes of bars are also more rectangular than the elliptical shapes of elliptical galaxies.

Interestingly, barred galaxies do not really differ from non-barred ones in physical and dynamical properties, such as the disk scale length, color of the galaxy, and HI gas properties, except by the presence of a bar (*e.g.* Bosma 1996; Mathewson & Ford 1996; Courteau et al. 2003).

The fact that bars are straight suggests that they rotate at a single well defined pattern speed Ω_b at any given point in time, which simulations support. The speeds are usually reported as the ratio of the bar's radius of corotation (§1.2.3.2) to its semi-major axis. Theory suggests that this ratio, at least for weak bars, can only be greater than unity (Contopoulos 1980, ; BT08, §6.5.2a). Bars are called "fast", if this ratio is close to unity, and "slow" if it is significantly greater. This makes sense in terms of the pattern speed, because angular velocity Ω declines monotonically with increasing radius and corotation occurs when $\Omega = \Omega_b$, so for a given semi-major axis of a bar, this ratio will be greater for greater pattern speeds as illustrated in Fig. 1.7. Although good measurements of pattern speeds and the locations of the corotation resonance are difficult to obtain, observations and simulations show that the majority of bars are fast with ratios between 1 and 1.4 (Sparke & Sellwood 1987; Merrifield & Kuijken 1995; Athanassoula 1992; Weiner & Sellwood 1999; Debattista et al. 2002; Aguerri et al. 2003; Regan & Teuben 2004; Debattista & Williams 2004; Corsini 2008). Theory also supports this (*e.g.* Contopoulos 1980). Yet, very slow bars also exist (Chemin & Hernandez 2009).

Over time, bars slow down due to dynamical friction between them and the dark matter halo (*e.g.* Sellwood 1980; Weinberg 1985; Debattista & Sellwood 1998, 2000). In fact, Debattista & Sellwood (2000) found that they can slow down quite significantly over galactic ages, and argued that halos cannot be very dense at their centers where disks reside, which is in support of maximal disks (§1.5.12), or otherwise we would mostly observe slow bars in the universe. Bars can also slow down or speed up a little by losing or gaining angular momentum to the outer spirals (*e.g.* Sellwood 1981, 2013b). Which one happens depends on the difference in phases between them.

Bars also have vertical structure. It is hard to isolate the bar in edge-on disks, but
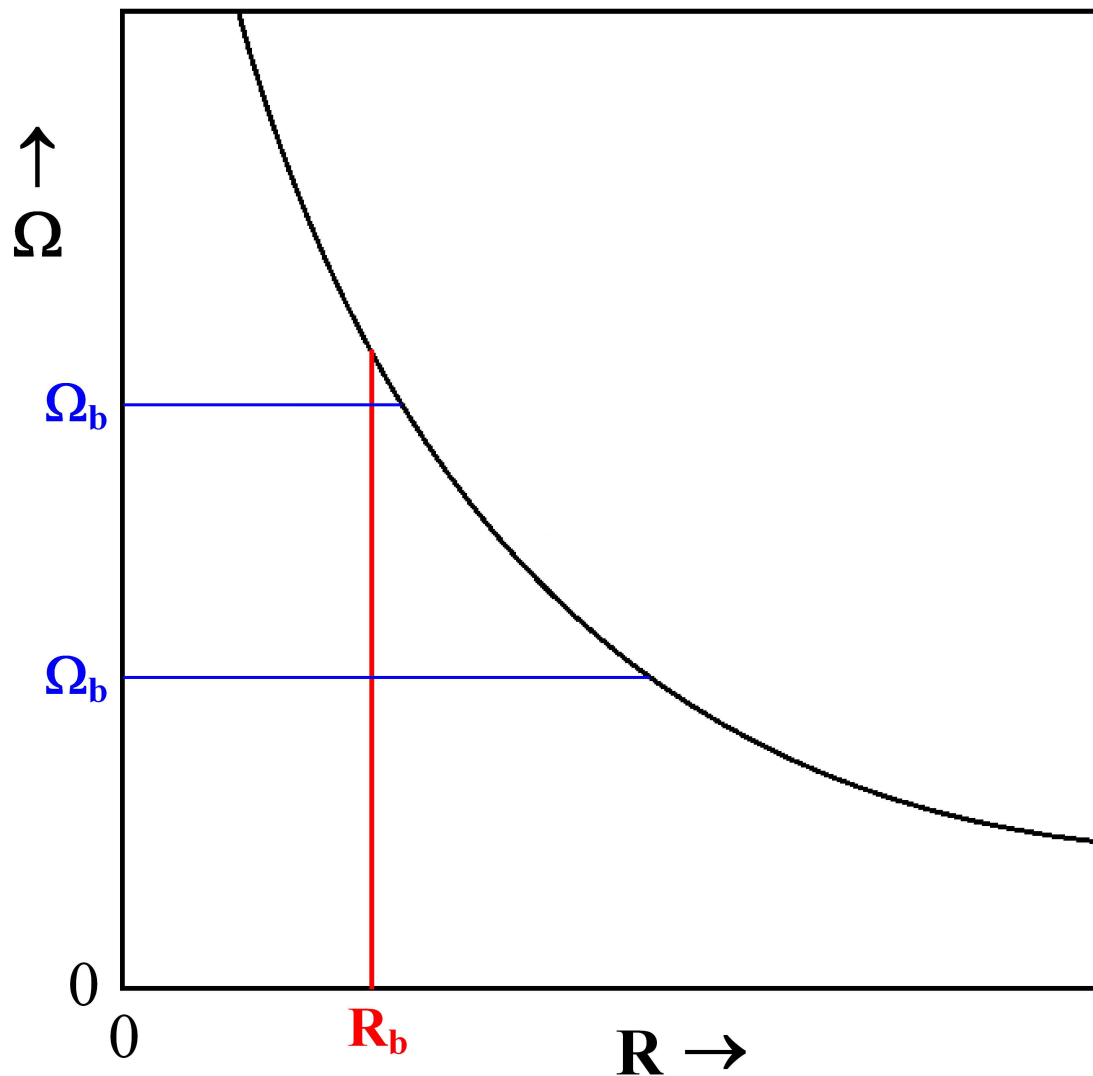
Figure 1.7 The black curve shows a typical radially declining angular speed Ω of stars in a disk. Given a fixed semi-major axis R_b of a bar, shown by the red vertical line, consider two possible bar pattern speeds Ω_b shown by the two blue horizontal lines. Both lines end at the Ω curve where the corotation $(\Omega = \Omega_b)$ radius lies. The ratio of the bar's corotation radius to its semi-major axis is clearly much greater for the slower rotating bar of the lower blue line than that of the faster bar corresponding to the upper blue line.

there is good evidence that bulges with boxy "peanut" shapes that often extend vertically beyond the thickness of the disk and are seen in about half of edge-on disks could be bars (*e.g.* Kuijken & Merrifield 1995; Bureau & Freeman 1999; Kormendy & Kennicutt 2004). See plate 15 for an example and Fig. 6.29 for edge-on isophotes of such a disk in BT08. Some bars could also be oriented along the line of sight in edge-on disks, in which case isophotes do not reveal their presence. Theory suggests that bars should buckle due to the buckling instability (also known as the "fire hose" or corrugation instability) and attain such boxy shapes. See §6.6.2 in BT08 for a detailed description of the buckling instability. Toomre (1966), Fridman & Poliachenko (1984), and Araki (1985) found that thin stellar structures with vertical velocity dispersions less than one third that of the in-plane ones are unstable to buckling. Bars satisfy this criterion due to their eccentric aligned in-plane orbits (Raha et al. 1991). Simulations show that bars do indeed buckle fairly soon after forming (*e.g.* Combes & Sanders 1981; Combes et al. 1990; Raha et al. 1991; Merritt & Hernquist 1991; Skokos et al. 2002).

Bars drive gas along themselves inwards to the galactic center (*e.g.* Weiner et al. 2001). Periodic orbits tend to cross each other and even themselves in a bar potential. Since gas is dissipational, clouds of it collide with each other at such orbit intersections. This forms shocks, which are believed to occur at the linear dust lanes (BT08, plate 10) seen along the leading sides of the bars. When gas passes through these shocks, it loses additional energy. Also, the ahead offset of gas and stellar density from the bar potential exerts torques on the gas that reduce its angular momentum. Hence, the gas flows towards the center. Hydrodynamic simulations confirm this idea (*e.g.* Athanassoula 1992; Combes & Elmegreen 1993), and the fact that barred galaxies are statistically observed to contain more molecular gas at their centers than non-barred ones supports it too (*e.g.* Sakamoto et al. 1999). These dust lanes are not sites of rapid star formation however, because the gas flows along the bar and causes a velocity shear large enough to stabilize the gas gravitationally. Only the tips of the bars often contain HII regions and clusters of young stars that correspond to rapid star formation.

The notion of resonances, as discussed in §1.2.3.2, is ill-defined and does not exist for strong bars. Weak bars, however, could have an inner Lindblad resonance. If it is present,

this gas settles onto circular orbits at this resonance and forms an in-plane ring of a typical radius of a few hundred pc (Athanassoula 1992; Regan & Teuben 2003). The concentration of density leads to abundant star formation in such rings, which have been observed in barred galaxies both traced by young luminous stars (*e.g.* Knapen 1999; Pérez-Ramírez et al. 2000; Benedict et al. 2002) and by molecular gas (*e.g.* Regan et al. 2002), and their locations are proposed estimates of this resonance (*e.g.* Buta & Combes 1996). These rings are called nuclear rings. About one fifth of barred galaxies contain them (Knapen 2005; Comerón et al. 2010).

Barred galaxies could also contain in-plane inner and outer rings, whose formation is also believed to be driven by the bars. See Fig. 4.8 in BM98 for examples of all three types of rings. The inner ones mostly lie at the ends of the bars, while the outer ones at about twice the radii of the bars' major axes (*e.g.* Buta 1995). These rings often have some ellipticity, and the inner ones are generally more elliptical than the outer ones. Some inner ones are even rectangular or hexagonal in shape, like NGC 7020 (Buta 1990). Inner rings are found in about three quarters of SBab-SBc Hubble type galaxies, but rarely in SB0-SBa types (Kormendy 1979; Buta 1986, 1991). Inner lenses, which are flattened ellipsoids of slowly decreasing surface brightness with a sharp outer edge usually ending at and aligned with the bar's major axis, on the other hand occur in most of the SB0-SBa barred galaxies, and are rare in the SBab-SBc ones (*e.g.* Kormendy 1981; Athanassoula et al. 1982; Laurikainen et al. 2009). Outer rings are much less common than inner ones comprising about 10% of barred galaxies (Kormendy 1979; Buta 1986, 1991; Buta & Combes 1996). Some rare galaxies, like NGC 1211 and NGC 2273 (Buta et al. 2007), have two outer rings. Inner and outer rings and inner lenses also likely correspond to resonances (see the end of §1.2.3.2).

In simulations, most disks form bars, and bar formation is very hard to suppress (Sellwood 1981). In §1.5.12 I discuss how to deal with this problem in order to get spirals-only simulations, which we needed in addition to barred ones. Strong bars mostly form early on from a vigorous bi-symmetric instability (*e.g.* Hohl 1971) that is related to the shape of inner rotation curve (Sellwood 1981). The bar instability has been confirmed and studied early on by Shu (1970), Kalnajs (1977), Kalnajs (1978), and Inagaki et al. (1984) for example. In §1.2.3.4, I discuss the most likely mechanism that drives the bar instability. Bars

could also arise later in simulations from particle noise. Lynden-Bell (1979) proposed that bars could form slowly by eccentric orbits aligning with one another, while outer spirals take away angular momentum from these stars to make them more eccentric. This mechanism is more likely to form weak bars. Lastly, interactions with companion galaxies can also generate bars, just like some grand design spirals (*e.g.* Noguchi 2004).

1.2.2.1 Orbits in a steadily rotating potential of a bar

In the steadily rotating potential of a bar with pattern speed Ω_b (BT08, §3.3.2), particles conserve neither their angular momenta $\mathbf{L}$ nor energies E, but instead conserve a quantity called the Jacobi integral: $E_J = E - \mathbf{\Omega_b} \cdot \mathbf{L}$ (BT08, eq. 3.112). It serves as a measure of energy in the effective potential Φ_{eff} of the bar (BT08, eq. 3.114) defined in the frame rotating with the bar. Fig. 3.14 in BT08, which I copy here in Fig. 1.8, shows contours of constant values of Φ_{eff} for a specific logarithmic potential (BT08, eq. 3.103) and specific value for the bar pattern speed. The major axis of the bar lies along the x-axis in this figure. The effective potential contains five Lagrange points (labeled L_1-L_5 in the figure), which are stationary points in the rotating frame at which $\bigtriangledown \Phi_{\mathrm{eff}} = 0$. In other words, stars at these points, except L_3 which is at the very center, are on circular orbits due to the balance between gravity and the centrifugal force, and corotate with the bar. Thus, these four Lagrange points essentially mark the corotation radius (§1.2.3.2) of the bar. L_3 is a minimum of Φ_{eff}, L_4 and L_5 are maxima, and L_1 and L_2 are saddle points.

The saddle points lie along the major axis of the bar, and the equipotential contour running through them marks a critical value Φ_{crt} which serves as the peak of the bar potential well seen by the stars. Stars with $E_J < \Phi_{\mathrm{crt}}$ cannot cross this peak and remain trapped either within it or outside of it, whereas particles with $E_J \geq \Phi_{\mathrm{crt}}$ are not bound, and can move through the radius of this peak.

This trapping of bound orbits along with the non-transient nature of bars suggest that radial migration should not take place within them. Our project in §5 is entirely based on this fact. Outside of a bar, however, particles can get picked up by outer spirals and migrate radially. In fact, the presence of a bar seems to enhance radial migration outside of it a little. I discuss more on this in §1.3.
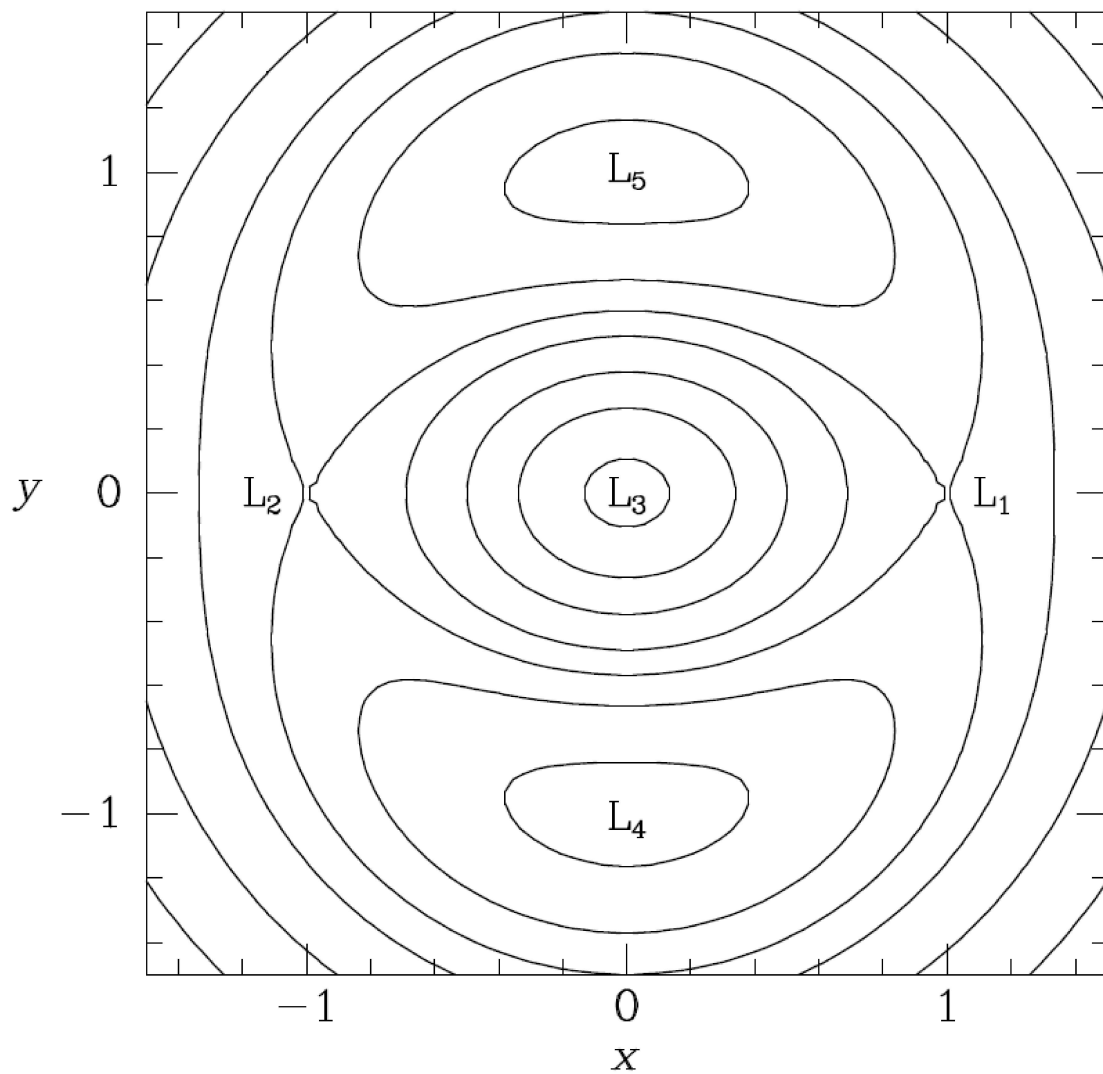
Figure 1.8 (Fig. 3.14 from BT08). In-plane contours of the effective potential in the rotating frame of a bar for a given logarithmic potential. The bar lies along the x-axis, and $L_1 - L_5$ show the locations of the five Lagrange points. See text for more details.

1.2.3   Density waves

As discussed throughout §1.2.1, spirals are believed to be density waves, not material arms, and so are bars. This means that these features are areas of overdensity, through which stars and gas flow as opposed to staying in them. This is somewhat similar to a traffic jam on a highway: cars move through the traffic, but the traffic itself, which is an overdensity of cars, moves much slower, not at all, or even backwards in the frame of the road.

As already mentioned in §1.2.1.3, all the spiral waves ever correctly observed in simulations have been transient and not long-lived. Theory and observational evidence also supports this. In simulations, the waves recur, and often multiple ones coexist together overlapping in time somewhat randomly, as opposed to forming and dying at collective intervals. Each one has a single pattern speed, and can be of mode m, meaning that it has m-fold rotational symmetry, or m number of arms. A typical wave first grows exponentially in amplitude, then saturates to a single peak in amplitude, and finally decays back to zero (Fig. 2.3). The reason why the waves saturate is still not clear, but Sellwood & Binney (2002, hereafter SB02) suggest that the onset of horseshoe orbits (§1.2.3.2) eventually destroys them, for which they and we in §2.4.3 find evidence in simulations. See §1.2.3.2 for more details.

In simple terms, nested closed elliptical orbits systematically varying with radius can crowd in a spiral or bar pattern. To illustrate this, I copy Fig. 6.12 of BT08 in Fig. 1.9, which is based upon similar figures introduced by Kalnajs (1973). This simplified explanation utilizes kinematic density waves that rely on orbits of stars in an axisymmetric potential. In reality, orbits deviate from these paths because the spiral itself produces a non-axisymmetric gravitational field. Yet, this picture offers a good enough motivation for how orbit crowding gives rise to spirals. See §6.2.1 in BT08 for a more detailed explanation.

If the orbits of the stars drift at the same speed while remaining in this varying phase arrangement, the spiral pattern can last a long time. This is not the case in real and simulated spirals. Therefore, even though spirals overcome the material winding problem by being density waves, they are still subject to a similar form of winding. This winding typically occurs at a rate on the order of a factor of five slower than material winding.
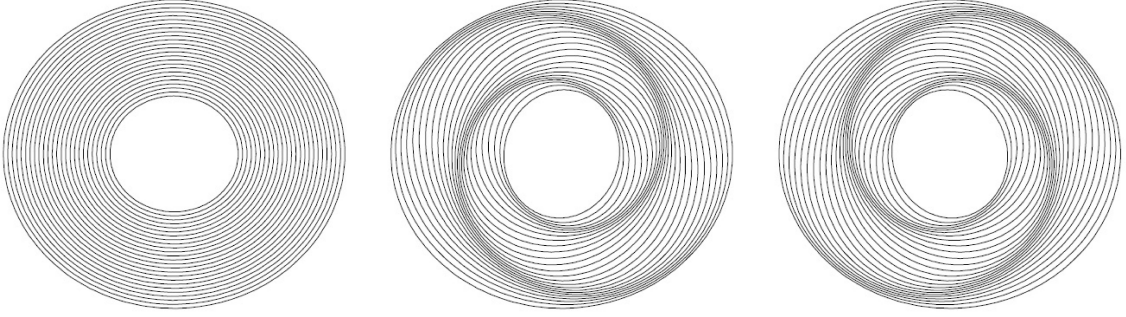
Figure 1.9 (Fig. 6.12 from BT08). Illustration of the simplified picture of how spiral or bar patterns can be organized by nested closed elliptical orbits. The left panel corresponds to a bar pattern, whereas the middle and right ones to spirals of opposite orientations.

Lindblad (1962) noticed a long time ago that the nearly circular and nearly closed orbits that can give rise to an $m = 2$ pattern, actually come close to drifting synchronously at most radii (BT08, §6.2.1 & Fig. 6.11). This makes $m = 2$ waves most resistant to winding. Two-armed large-scale spirals are the most prominent grand designs due to maximal disk masses (§1.5.12), swing amplification (§1.2.3.3), and this fact. These waves are also the most interesting because they give rise to bars.

1.2.3.1   Angular momentum and energy transport

Spirals exert torques on the stars, and therefore redistribute angular momentum from one part of the disk to another. The total angular momentum of the system of course remains conserved during the redistribution. Under trailing spirals, the total averaged torque applied by material inside some radius on the material outside of it is positive (BT08, §6.1.5). Because gravity is a long range force, an outer part of stellar overdensity lying along the spiral arm experiences a torque that mainly is exerted by the vast inner part. Since the inner part of the spiral leads ahead of the outer part in a trailing pattern, this torque is positive. Fig. 1.10 illustrates this. Oppositely, the torque on the inner part is exerted mostly by the outer spiral, which is trailing, so it is negative. Hence, overall, stars in the inner region lose angular momentum, while ones in the outer region gain it, and so trailing spirals transport angular momentum from the inner parts to the outer ones. Leading spirals, on the other hand, do the opposite and transfer angular momentum inwards.

In addition, as waves in dispersive media, like sound in air, transport energy and linear
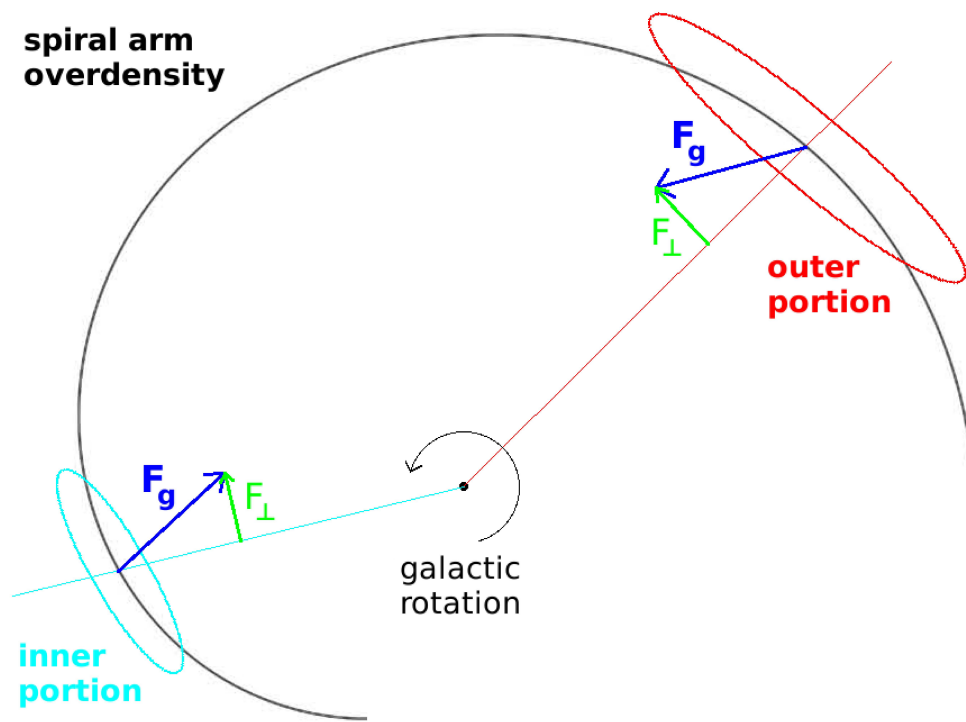
Figure 1.10 Illustration of why trailing spiral arms induce a negative torque on the inner material and a positive one on the outer, redistributing angular momentum outwards. The black curve shows a railing spiral arm. Consider the outer portion of the stellar overdensity inside the red oval. The net gravitational force F_g shown by the blue vector, whose main contribution is exerted by the material in the inner arm, points towards the inner arm, and thus is in the direction of rotation. It has a nonzero component $F_\perp$ (green vector) perpendicular to the lever arm of the outer portion, which lies along the red line connecting the portion to the galactic center. Hence, the net torque on the outer portion is positive, so the portion gains angular momentum. Now consider the inner portion selected by the cyan oval. A similar analysis applies, but this time the net gravitational force exerted on it points in the direction opposite to rotation, because the outer arm exerting the main contribution lags behind the inner portion. Therefore, in this case, the torque the inner portion experiences is negative, so the portion loses angular momentum.

momentum advectively, so do density waves in stellar galactic disks, but instead of linear momentum they transfer angular momentum (Lynden-Bell & Kalnajs 1972, ; BT08, §6.2.6). Normal trailing transient waves transfer angular momentum outwards by convection, just like torques (Toomre 1969). However, this effect is typically weaker than transfer by torques. One can define an angular momentum density in the density waves, and show that advection behaves such that this density is positive outside of corotation (§1.2.3.2) and negative inside it.

The naive interpretation of convection is that, under the action of the density wave, stars normally pick up angular momentum at their pericenters from stars on smaller inner orbits, carry it to their apocenters where they give it up to stars on larger orbits, and return to their pericenters to again collect angular momentum. In the long run, angular momentum gets transported outwards, while the mass distribution remains unchanged under advection. The reality is much more complicated and nonintuitive. Advection really arises due to Reynolds stresses, and the angular momentum is exchanged between stars in a complex way that depends on their radial locations in their orbits. A full derivation requires use of the angular-momentum flux tensor and versions of the Jeans equations that dictate the evolution of the tensor (see Appendix J in BT08).

For stationary long-lived standing waves, the direction of angular momentum transport by advection is reversed and counteracts the action of the torques, because they invoke the long-wave branch (Mark 1977, ; BT08, p. 498) of the dispersion relation of the density waves to stabilize themselves (Sellwood 2013b). This slows down the overall rate of outwards angular momentum transport in such spirals. Transient spirals, on the other hand, do not use the long-wave branch.

In any case and in general, it is tough to compare the convective angular momentum transport to the one caused by torques. The important fact, however, is that the total wave action flows at and in the direction of the group velocity (BT08, §6.2.5).

1.2.3.2   Resonances

Orbits can have natural resonant frequencies, just like springs, when being perturbed by a wave. The most drastic changes in particles' angular momenta and energy take place at

such resonances in the disk, even if the perturbation is weak.

Assuming a spiral wave has the constant pattern speed Ω_p, since the angular velocity Ω of stars normally declines monotonically with increasing radius in a disk, there exists a particular radius at which $\Omega = \Omega_p$. This is called the corotation resonance (CR), because each star at this radius corotates with the spiral, *i.e.* it remains at the same phase with respect to the spiral arms while both rotate at Ω_p. Such stars are said to ride the density wave.

Linear stability theory that assumes an infinitesimal perturbation and an orbital response that is a small deviation from the unperturbed orbit (*e.g.* Kalnajs 1971) does not apply at resonances. Sellwood & Binney (2002) used a different appropriate approach to study the interaction of stars with spirals at corotation (BT08; §3.3.3b). This allowed them to discover what was missed before in the linear regime, namely radial migration.

The exchange of angular momentum between stars and the wave is greatest at corotation due to the accumulation of torque exerted on the stars by the spiral arms. Stars inside corotation rotate faster than the spiral wave about the galactic center. As they approach a spiral arm, they gain angular momentum. In §1.3, I explain that at corotation, the eccentricities of the orbits do not change while the angular momenta of the stars change. This is exactly responsible for radial migration. Thus, the approaching stars move to larger radii, which slows their drift with respect to the wave. This allows positive torque to accumulate and yield a large increase in angular momentum. Eventually, the stars cross corotation and begin to lag the wave. In so doing, they fall behind and move backwards into the adjacent arm in the frame rotating with the spiral. When they come close enough to that arm, its negative torque dominates and causes them to loose angular momentum. So, they migrate to smaller radii, cross corotation again, switch to leading the wave, and eventually star gaining angular momentum again repeating he cycle. Thus, they trace horseshoe orbits in the rotating frame (Fig. 1.11).

§3.3.3b of BT08 shows that this cycle approximately obeys a pendulum equation in a sinusoidally varying potential: $\ddot{\psi} = -p^2 \sin \psi$ with constant frequency p and phase variable $\psi = m(\phi - \phi_{\max})$, in which $\phi_{\max}$ is the azimuth of the peak of the potential and m is the number of arms of the spiral. Stars that obey this equation have an energy invariant
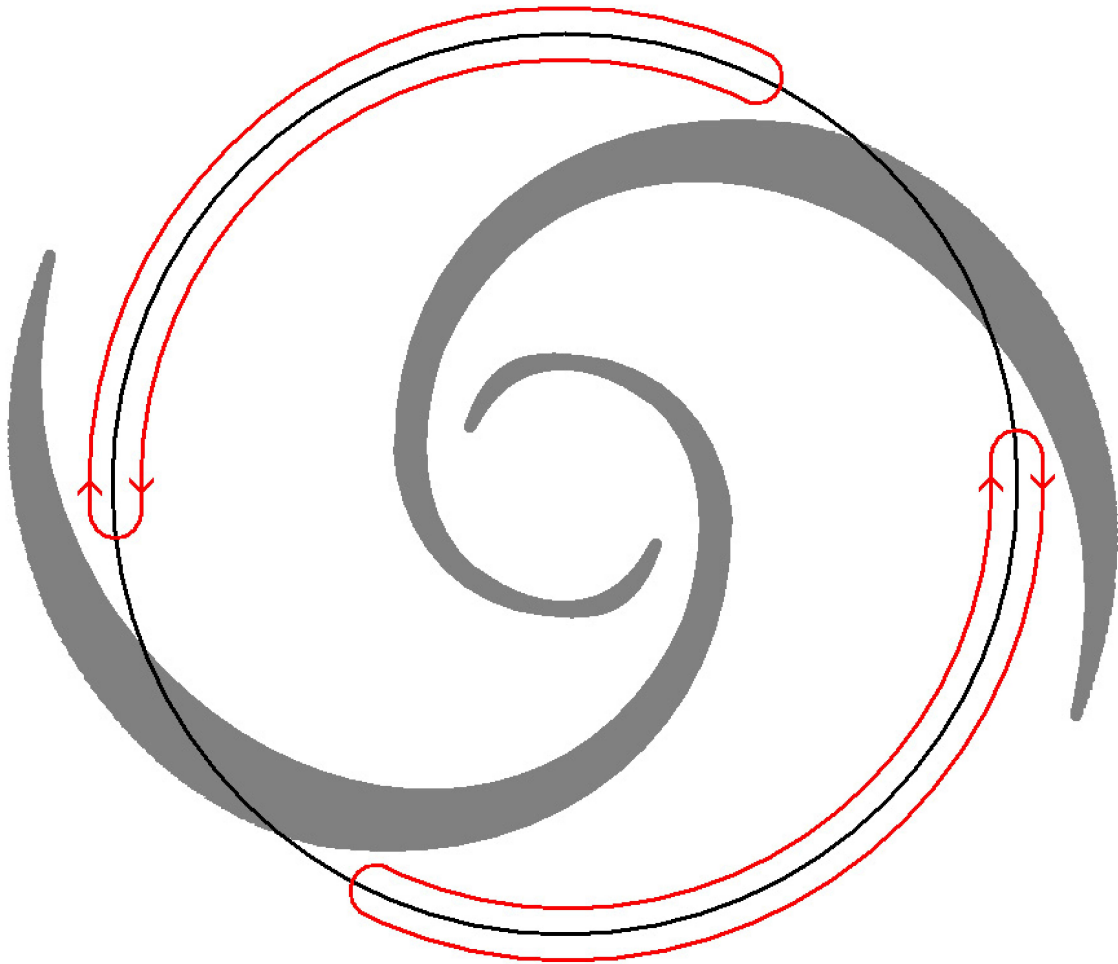
Figure 1.11 This is a face-on view of a disk galaxy with a two-armed spiral (gray) shown in the frame rotating at its pattern speed in the counterclockwise direction; so the arms remain stationary in this frame. The black circle marks the corotation radius. Stars that are trapped at corotation trace horseshoe orbits in this frame, two of which are drawn in red, and the arrows show their directions of motion along the orbits in this frame.

$E_p = \frac{1}{2}\dot{\psi}^2 - p^2\cos\psi$. Ones with $E_p < p^2$ are trapped at corotation in this horseshoe orbit cycle. They are said to "liberate" about the corotation radius at frequency p. Stars with $E_p > p^2$, on the other hand, are not trapped, and simply "circulate" about the galactic center.

In reality, the spiral wave is transient and has a time-varying potential. The disappearing of the wave stops the librating cycle, and allows for non-zero average net changes in angular momenta. Hence, transience of the perturbation is a key property required for radial migration to occur. See eq. 11 in SB02 and the discussion thereafter for the required lifetime duration of the wave that would cause maximum changes.

Sellwood & Binney (2002) explained that every newborn linear wave mode induces some small number of horseshoe orbits about corotation. But as it grows, the periods of the trapped orbits decrease, and the region of horseshoe orbits and the number of trapped stars grow exponentially. These stars reverse their direction of motion in the rotating frame when they reach $\dot{\psi} = 0$. This happens quickly and collectively to many of them, which yields a rapid slow down of growth and a subsequent decay of the wave. Thus, the overall affected corotation region of a single transient spiral has a finite width, as opposed to being a singular radius.

Stars on circular orbits (referring to zero eccentricity as opposed to the shape in the rotating frame) experience maximum angular momentum changes, because they corotate with the spiral most. If the orbit is not circular, only the guiding center corotates with the potential of the wave. The guiding center of a star, also called its home radius R_{home}, is the radius at which it would have a circular orbit with its angular momentum L_z: $L_z^2 = R_{\text{home}}^3|\partial\Phi/\partial R|_{R_{\text{home}}}$. Stars on nearly circular orbits do not deviate away from their home radius much, while more eccentric stars at corotation spend less of their orbits corotating, and thus resonating, with the spiral, because their angular velocity varies more along their orbits, so they spend less time holding station with the steadily rotating wave. Newly formed stars begin on circular orbits, and most stars remain on nearly circular orbits, so the corotation resonance effect is prominent.

There are two other types of resonances that occur for in-plane motion, which are called inner and outer Lindblad resonances after Bertil Lindblad who first described them and

realized that they always lie inside and outside of corotation. Both of them occur when a star encounters successive crests of the wave potential at the same frequency as its radial oscillation.

A general orbit has a radial, azimuthal, and a vertical frequency: $\omega_R \equiv 2\pi/T_R$, $\omega_\phi \equiv 2\pi/T_\phi$, and $\omega_z \equiv 2\pi/T_z$, in which T_R, T_ϕ, and T_z are the radial, azimuthal, and vertical periods. Nearly circular orbits can be approximated by the motion of a radial harmonic oscillator ($\ddot{R} = -\kappa^2 R$) about a circular orbit at the home radius with a constant radial frequency κ and a constant azimuthal, or circular, frequency Ω. If the vertical amplitude of the orbit's motion about the midplane is also small, then the vertical motion can also be approximated by a harmonic oscillator ($\ddot{z} = -\nu^2 z$) with constant vertical frequency ν in the frame rotating at circular frequency Ω. This is called epicycle approximation, and the closed ellipse the in-plane orbit traces in the rotating frame at Ω, demonstrated in Fig. 1.12, is called an epicycle. The radial frequency κ is also more frequently called the epicycle frequency. The three frequencies are related to the disk potential Φ as (BT08, eq. 3.79):

$$\Omega^2(R) = \frac{1}{R}\left(\frac{\partial\Phi}{\partial R}\right)\Bigg|_{R_{\mathrm{home}}} \tag{1.3}$$

$$\kappa^2(R_{\mathrm{home}}) = \left(\frac{\partial^2\Phi}{\partial R^2}\right)\Bigg|_{R_{\mathrm{home}}} + \frac{3}{R_{\mathrm{home}}}\left(\frac{\partial\Phi}{\partial R}\right)\Bigg|_{R_{\mathrm{home}}} \tag{1.4}$$

$$\nu^2(R_{\mathrm{home}}) = \left(\frac{\partial^2\Phi}{\partial z^2}\right)\Bigg|_{R_{\mathrm{home}}} \tag{1.5}$$

In general, $\Omega \lesssim \kappa \lesssim 2\Omega$ (BT08, p. 165).

Lindblad resonances occur when $m(\Omega - \Omega_p) = l\kappa$ for a non-zero integer l and an m-fold spiral wave with pattern speed Ω_p. The left hand side of this equality is the forcing frequency of the wave seen by the star, and the right hand side is a multiple of the star's natural radial frequency. l can also have the value zero, in which case the condition corresponds to the corotation resonance. Inner Lindblad resonances (ILR) correspond to positive l, as they occur when a star encounters the wave crests at a multiple of its resonant frequency κ while overtaking the wave potential. And negative l correspond to outer resonances (OLR), because then the star rotates slower than the potential. Essentially, orbits at these resonances close after l number of turns about the disk center and m radial oscillations.
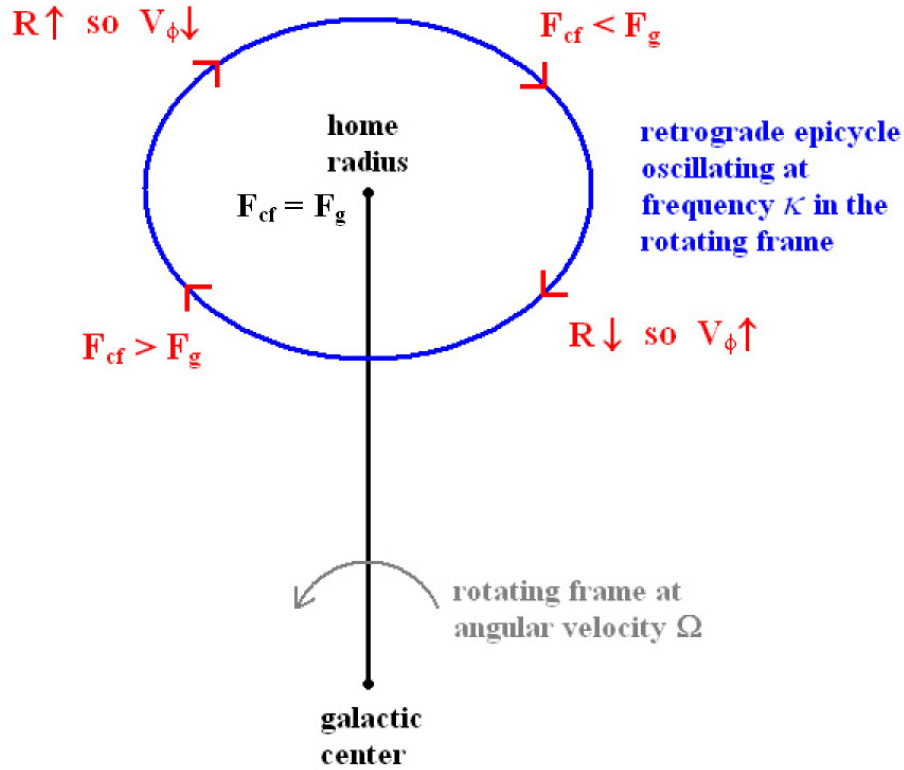
Figure 1.12 In the frame rotating at the angular speed Ω of a star on a nearly circular in-plane orbit, the star traces out an ellipse called its epicycle due to its nearly harmonic oscillator radial motion at frequency κ. If it did not have this radial perturbation, it would appear as a stationary point in this frame exactly at the particle's home radius due to the balance between the radially repulsive centrifugal F_{cf} and attractive gravitational F_g forces. For a nearly circular orbit, the home radius still remains stationary, while the epicycle is centered at it and is retrograde (the star oscillates in the direction opposite to its orbit around the galactic center) due to angular momentum conservation and the interplay in dominance between F_{cf} and F_g, which makes the azimuthal velocity alternate between leading and lagging with respect to the home radius.

Just like corotation, each Lindblad resonance occurs at a certain radius in a differentially rotating disk. Resonances of greater $|l|$ occur at successively smaller radii than the $l = 1$ inner resonance and at greater radii than the $l = -1$ outer one. Usually, there is one outer Lindblad resonance and zero, one, or two inner ones. Fig. 1.13 shows an example of each case for an $m = 2$ wave. Their locations and the number of resonances that exist depend on m, Ω_p, and how the surface density or potential varies with radius in the disk, which determines Ω and κ by eqs. 1.3 & 1.4.

The definition of Lindblad resonances described here is a naive one, because it relies on nearly circular orbits in a weak wave (resonances of strong bars cannot be defined this way). But it can be generalized for any periodic orbits (*e.g.* Contopoulos & Grosbøl 1989). Chaotic orbits are also common in non-axisymmetric potentials. They cannot be easily described in a framework such as epicycles or generalizations, because they fill up all the phase space available to them chaotically, as opposed to regular stable periodic orbits that are confined to orbital tori. The fraction of chaotic orbits present can be large, and seems to increase for stronger bars (Manos & Athanassoula 2011). Interestingly, some chaotic orbits can support features like spirals and bars (Kaufmann & Contopoulos 1996; Patsis 2006; Tsoutsis et al. 2009).

Lindblad resonances also change the angular momenta of resonant stars, but they also add radial energy to their orbits. Therefore, the epicycles, and thus eccentricities, of these stars increase, while their home radii do not change as much as at corotation. See Goldreich & Tremaine (1981) for the dynamics of orbits at Lindblad resonances. This increases random motion and heats up the disk radially, making it less responsive to further collective waves. Hence, density waves can only survive in between the inner and outer Lindblad resonances of $l = \pm 1$ (Lin & Shu 1964). When waves encounter these resonances, they get absorbed. This is confirmed in simulations (*e.g.* Sellwood 1989), and, supposedly, the spiral arms observed in real disks lie between these resonances too. Although there are also smaller nuclear spirals found inside the inner Lindblad resonance (*e.g.* Martini et al. 2003), but they rarely connect to the outer main spirals or bar (*e.g.* Regan & Mulchaey 1999). Obtaining measurements of the pattern speeds of real spirals and locations of the resonances is quite difficult. The main difficulty in measuring the former is the problem that impairs all studies of galactic
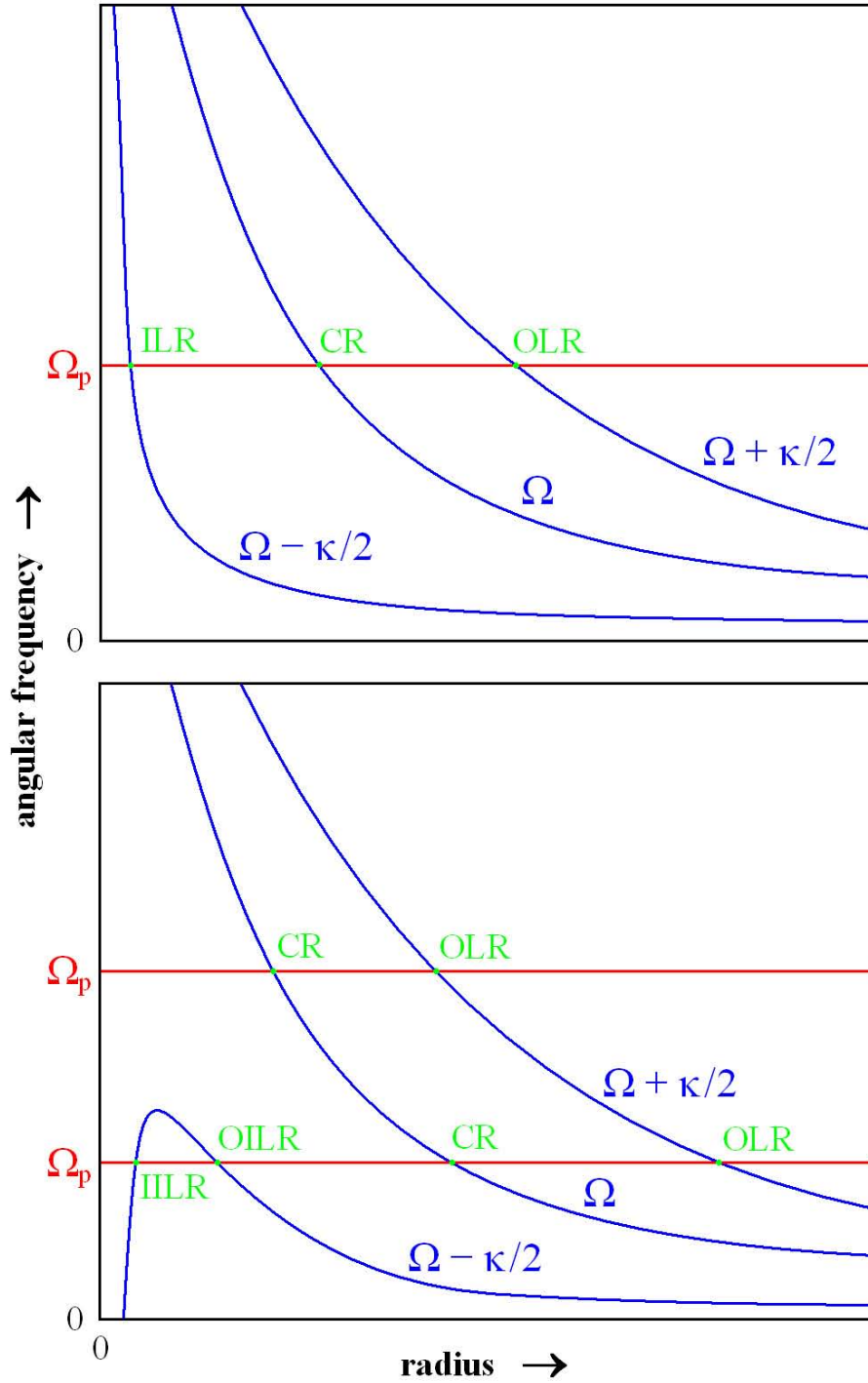
Figure 1.13 Blue curves show the Ω, $\Omega + \kappa/2$, and $\Omega - \kappa/2$ frequencies of stars as a function of radius in two different realistic disk potentials. In the top plot, a wave of mode $m = 2$ with pattern speed Ω_p (red) has one of each resonance: ILR, CR, and OLR (green). Whereas in the bottom plot, the wave with the upper faster pattern speed has no ILR, while the one with the slower speed has two inner Lindblad resonances, which are called the inner inner and the outer inner Lindblad resonances.

dynamics, namely the fact that we humans have not existed even nearly long enough to observe substantial changes in stellar orbits, except at the very center of our Galaxy. Thus, the most important resonances are the $l = \pm 1, 0$ ones.

If there are no inner Lindblad resonances, then density waves can pass through the galactic center and emerge as outwards propagating leading waves. I discuss the importance of this in §1.2.3.4. The existence of strong bars requires the waves' ability to get to and pass through the center. Strong bars form with pattern speeds that exceed the maximum value of $\Omega - \kappa/2$, so that no ILR exists for them. Simulations confirm this fact (Sellwood 1981; Sparke & Sellwood 1987). One can destroy, suppress, or not allow a bar to form by having a dense enough core, which would yield an $\Omega - \kappa/2$ great enough for ILRs to exist for all pattern speeds (Toomre 1981). See §1.5.12 for other ways to suppress bars. Weak bars could have an ILR however.

The CR is also quite important for bars. Theory suggests that bars end at radii smaller than their CR (Contopoulos 1980, see also §6.5.2a in BT08 for an explanation). Furthermore, as already mentioned in §1.2.2, rings are thought to form at the resonances of the bar, although this is far from certain. Nuclear rings supposedly form at the ILR of weak bars from gas flowing inwards along them and accumulating on circular orbits at the ILR. Some have associated outer rings with the OLRs of the bars (Schwarz 1981; Kalnajs 1991). And inner rings and lenses are believed to lie at the bar's CR, $m = 4$ Lindblad resonance, or the $m = 2$ ultraharmonic resonance caused by nonlinear effects (*e.g.* Patsis et al. 2003).

One can interpret these changes at the resonances in terms of different orbit families. The resonances mark transitions and intersections between them that lead to orbit crossing. For example, if an ILR exists in a barred potential, then it marks the transition of the orientation of periodic orbits from lying parallel to perpendicular with respect to the major axis of the bar (*e.g.* Contopoulos & Grosbøl 1989). Since perpendicular orbits weaken the bar, this provides another interpretation of why ILRs are bad for bars. Refer to §3.3.2 & Fig. 3.18 in BT08 for details about different orbit families.

Finally, vertical resonances are also possible. These are very similar to the Lindblad ones, but occur in the vertical direction. At them, the forcing frequency of the wave equals a multiple of the vertical frequency of a star: $m(\Omega - \Omega_p) = l\nu$, in which l again can be either

positive or negative corresponding to inner or outer (in the radial direction) resonances respectively.

In real disks, ν is significantly greater than κ, so the inner vertical resonances lie at radii inside corresponding ILRs and the outer ones at radii outside of OLRs. In simulations, as I discuss in §4.4, the vertical frequency can be closer to the radial epicycle one, in which case the vertical resonances lie closer to the radial Lindblad ones, but ν still remains quite large. Theoretically, vertical resonances and buckling instabilities are the only mechanisms known through which spirals and bars can heat the disk vertically. Since spirals mainly exist between the ILR and OLR, vertical resonances should barely affect the disk. Yet, real vertical motions, especially in thick disks, can extend further away from the midplane than the harmonic region, and the vertical frequency can vary greatly between the peri- and apocenters of a star's orbit. These complicate the simple epicycle approximation picture, and could make vertical resonance somewhat significant.

1.2.3.3 Swing amplification

There are two more known important effects in the dynamics of density waves. The first is called swing amplification. As I mentioned in §1.2.1.3, Goldreich & Lynden-Bell (1965) and Julian & Toomre (1966) separately discovered, in gas and stellar disks respectively, that small perturbations create spiral disturbances that amplify in amplitude and then die out over time. Toomre (1981) studied this effect in detail, and found that a leading tightly wound spiral wave of small amplitude unwinds, grows reaching a peak in amplitude about the time the arms are most open, switches to trailing, and continues winding while decreasing in amplitude eventually becoming tightly wound trailing and disappearing (BT08, Fig. 6.19). The growth in amplitude is the swing amplification.

The unwinding from leading and winding to trailing arms is due to shear caused by differential rotation as discussed in §1.2.3. Swing amplification is caused by the change in the rotation rate of the spiral wave. When tightly wound, it rotates slowly. But as it unwinds, the rotation rate increases and reaches a maximum exactly when the wave changes from leading to trailing. The maximum rate is comparable to the stars' epicycle frequency κ, and the unwinding happens in the same retrograde direction as the epicycle
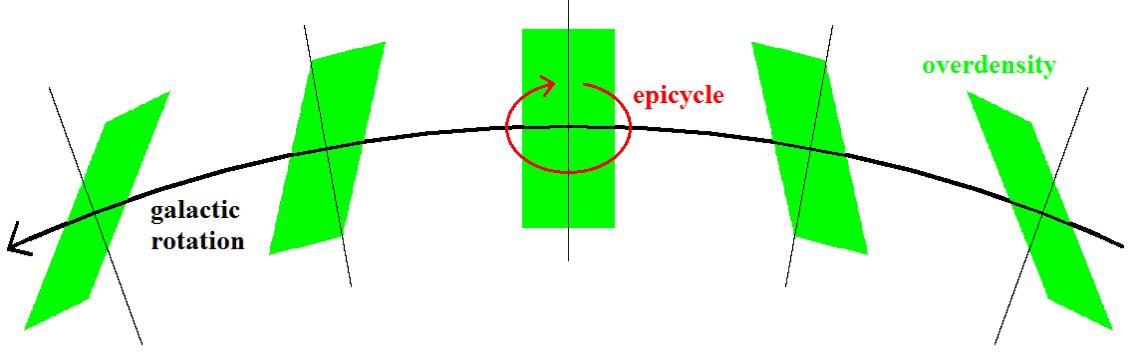
Figure 1.14 While the disk rotates counterclockwise (black), a leading overdensity (green) unwinds clockwise due to shearing by differential rotation and switches to trailing. The epicycles (red) of typical stars also rotate clockwise. Since both the perturbation and the epicycles rotate in the same direction, stars stay longer in the overdensity, and amplify the spiral.

rotation. Fig. 1.14 illustrates this matching (see also Fig. 6.20 in BT08). This temporary matching enhances the gravitational force from the spiral on the stars and the stars' self gravity, which leads to a rapid growth of the spiral's amplitude. In other words, the stars remain in the spiral overdensity for a significant enough fraction of their epicycle period. This effect is essentially a form of the Jeans instability (Jeans 1902, ; BT08, §§5.2.1–5.2.4), which rotation and epicycle motion normally suppress. In this case, however, the stabilizing nature of rotation enhances it.

The gain of the swing amplifier depends on the two parameters Q (eq. 2.3) and X (eq. 2.11). The former is a dimensionless measure of the random motion in the disk, and the latter is the ratio of the wave's wavelength to the critical shortest wavelength ($\lambda_{crit} = 4\pi G\Sigma\kappa^{-2}$ with Σ being the surface density) possible that rotation can still stabilize. Swing amplification is effective when the disk is stable ($Q > 1$) and responds strongly to gravitational perturbations (best when $Q \approx 1.2$, whereas $Q > 2$ is already bad), while $1 \lesssim X \lesssim 3$ (BT08, §6.3.2 & Fig. 6.21). For more details about swing amplification see Mark (1976), Goldreich & Tremaine (1978), Toomre (1981), Athanassoula (1984), and Fuchs (2001).

In simulations, and supposedly in real galaxies, Poissonian particle noise creates a Fourier spectrum of plane waves of all pitch angles, both leading and trailing. Differential rotation winds the trailing waves more, and when they meet the ILR, they get destroyed never

having the chance to grow in amplitude. The leading ones, on the other hand, unwind and become trailing, while their amplitudes increase due to swing amplification, making them the prominent trailing spirals seen. Yet, they too keep winding up and disappear after a few galactic rotations, which is why spirals are transient.

1.2.3.4 Feedback loops

The second important effect is the possibility of certain disks to form positive feedback in the density waves. This coupled with the swing amplifier can lead to an instability, just like audio feedback.

If the disk contains no inner Lindblad resonances, trailing density waves will propagate to the center of the disk, pass through it, and emerge as outgoing leading waves. See Fig. 6.22 in BT08 for a depicted explanation of why they become leading after passing through the center. Then, they will shear and unwind, the swing amplifier will boost their amplitudes, they will switch to trailing, wind up more, pass again through the center, and the cycle will continue (Toomre 1981; Sygnet et al. 1988; Fuchs et al. 2005). This will create a feedback loop, and lead to an instability.

This instability is supposedly responsible for the growth of global bar instabilities and the formation of bars (Toomre 1981). Although simulations and theory support this idea, there is still no convincing explanation for how bars formed in real galaxies (Sellwood 2013b).

1.2.3.5 Excitation of waves by gravitational instabilities

Swing amplification is not the only mechanism capable of producing prominent spiral patterns. Substantial radial changes in surface density over radial distances shorter than the critical wavelength λ_{crit}, introduced in §1.2.3.3, will yield significant perturbations in the potential, because small distortions caused by shearing will move material from the high density regions to the low density ones, and the disk will respond to the change by forming a wake (Julian & Toomre 1966) that itself shears into a spiral. Examples are edges or narrow grooves and ridges in the surface density, or likewise steps, reductions, or accesses in the angular momentum distribution.

Toomre (1989) studied the edge mode, in which the surface density drops by an order of magnitude or more at some radius with the low density being on the outside. In this case, a half-wake forms inside in the denser disk (outside of the edge there is not enough material to form a significant outer half of the wake). It leads the potential disturbance, and its unbalanced gravitational attraction exerts a torque that can make the high density material at the edge gain angular momentum. If it does, this material, and thus the edge, will move further out, which will increase the potential and density disturbance, and could lead to a run-away instability. Toomre (1989) showed that the corotation resonance of the spiral wake lies just outside of the edge in the low density region.

Lovelace & Hohlfeld (1978) first studied grooves, but Sellwood & Kahn (1991) first discovered that grooves and ridges lead to spiral instabilities. Both modes can be thought of as two nearby adjacent edge modes. In either case, a full wake forms with an inner and an outer half about the groove or ridge. A runaway does not occur in this case, but the instability grows more vigorously due to the supporting response of the disk.

Sellwood (2000) suggests that groove modes can generate a recurrent cycle of spirals, in which resonant stars from each wave seed a similar instability for the next spiral. The velocity distributions of stars in the solar neighborhood have a lot of substructure that supposedly corresponds to resonant scattering by recurring transient spirals and supports this idea (Sellwood 2010).

In our simulations for §§2 & 3, we place a groove in the initial angular momentum distribution of the disk in order to make it grow a strong predictable spiral density wave.

For more details on density waves and their dispersion relations in fluid and stellar disks see §§6.2–6.4 in BT08.

1.3   Radial migration

In §1.2.3.2, I stated that a spiral wave scatters resonant stars at its corotation such that they gain or lose angular momentum while remaining on nearly circular orbits without increases in their eccentricities. This obviously leads to changes in the home radii of the stars, and causes them to migrate either inwards or outwards radially. At Lindblad resonances,

resonant stars also gain or lose angular momentum, but their eccentricities change in the process, mostly increasing, which heats the disk (raises the radial velocity dispersion) and does not yield as large changes in the home radii. Following Sellwood & Binney (2002), I now prove these claims.

I introduced the invariant Jacobi integral $E_J = E - \Omega_p L_z$ (BT08, eq. 3.112) of a star in a potential rotating at pattern speed Ω_p in §1.2.2.1. It also remains conserved in the frame rotating with a steady spiral pattern. This implies that changes in energy and angular momentum relate by

$$\Delta E = \Omega_p \Delta L_z \ . \tag{1.6}$$

As a star gains ΔE, some of it will go towards changing the circular motion, while the rest will contribute to random motion. This can be expressed as

$$dE = \frac{\partial E}{\partial J_R} dJ_R + \frac{\partial E}{\partial L_z} dL_z \ , \tag{1.7}$$

in which J_R is a parameter that quantifies the radial kinetic energy of the star. Choosing J_R to be the radial action sets the partial derivatives in the above expression to the radial ω_R (κ in the epicycle approximation) and azimuthal Ω frequencies respectively:

$$dE = \omega_R dJ_R + \Omega dL_z \ . \tag{1.8}$$

Plugging in eq. 1.6 on the left hand side gives:

$$\Omega_p \Delta L_z = \omega_R \Delta J_R + \Omega \Delta L_z \ , \tag{1.9}$$

which can be rearranged to:

$$\Delta J_R = \frac{\Omega_p - \Omega}{\omega_R} \Delta L_z \ . \tag{1.10}$$

It follows that changes in angular momentum at corotation ($\Omega = \Omega_p$) do not induce changes in the radial action, but do so away from corotation. In fact, at Lindblad resonances ($m(\Omega - \Omega_p) = \pm l\omega_R$ for a wave of mode m and a positive integer l), the action would

change according to:

$$\Delta J_R = \mp \frac{l}{m} \Delta L_z \qquad (1.11)$$

with the upper minus sign corresponding to the ILR and the bottom plus one to OLR. This relation is approximate for not nearly circular orbits, but the important point is that random motion increases at Lindblad resonances, and very little if at all at the CR.

I also reproduce the classic Lindblad diagram of Fig. 1 in SB02 here in Fig. 1.15, which illustrates the physics of eq. 1.10. Orbits cannot lie in the gray shaded lower right region. The solid black curve that marks the boundary of the shaded region is the locus of circular orbits. The dashed red line shows the tangent to this curve at CR, which has the slope Ω_p. Stars move on lines with this slope in the $E - L_z$ plane when getting scattered by a steadily rotating spiral, as stated by eq. 1.6. The radial action J_R is a measure of distance away from the locus of circular orbits in this plot. As seen, J_R does not increase only at CR when stars on circular orbits get scattered by the spiral (green double arrow). Away from CR, they preferentially gain random motion (green single arrows), and the amount of increase in J_R increases further away from CR.

Sellwood & Binney (2002) dubbed the effect of stars gaining or losing angular momentum without gaining random motion at the corotation resonance "churning", and the scattering at radii substantially away from CR, especially at the Lindblad resonances, which increases eccentricities, "blurring".

This is only part of the story for successful radial migration to take place. The second important property needed is for the scattering wave to be transient. I mentioned this already in §1.2.3.2, and described the librating oscillation of stars trapped at corotation. They migrate radially near CR, but as they do, they eventually cross to a region at which the torque exerted by the spiral arms on them changes sign and forces them to migrate backwards. Such changes in phase occur both for outwards and inwards migrators at two locations usually somewhere on either side of corotation. Therefore, if the disturbance lasts a long time, stars will continue oscillating in radius, and will come back to their initial radii on average. This is not radial migration, and theoretically should happen for stars at the outer tip of a steady bar since it is a long-lived feature. However, if the perturbation is
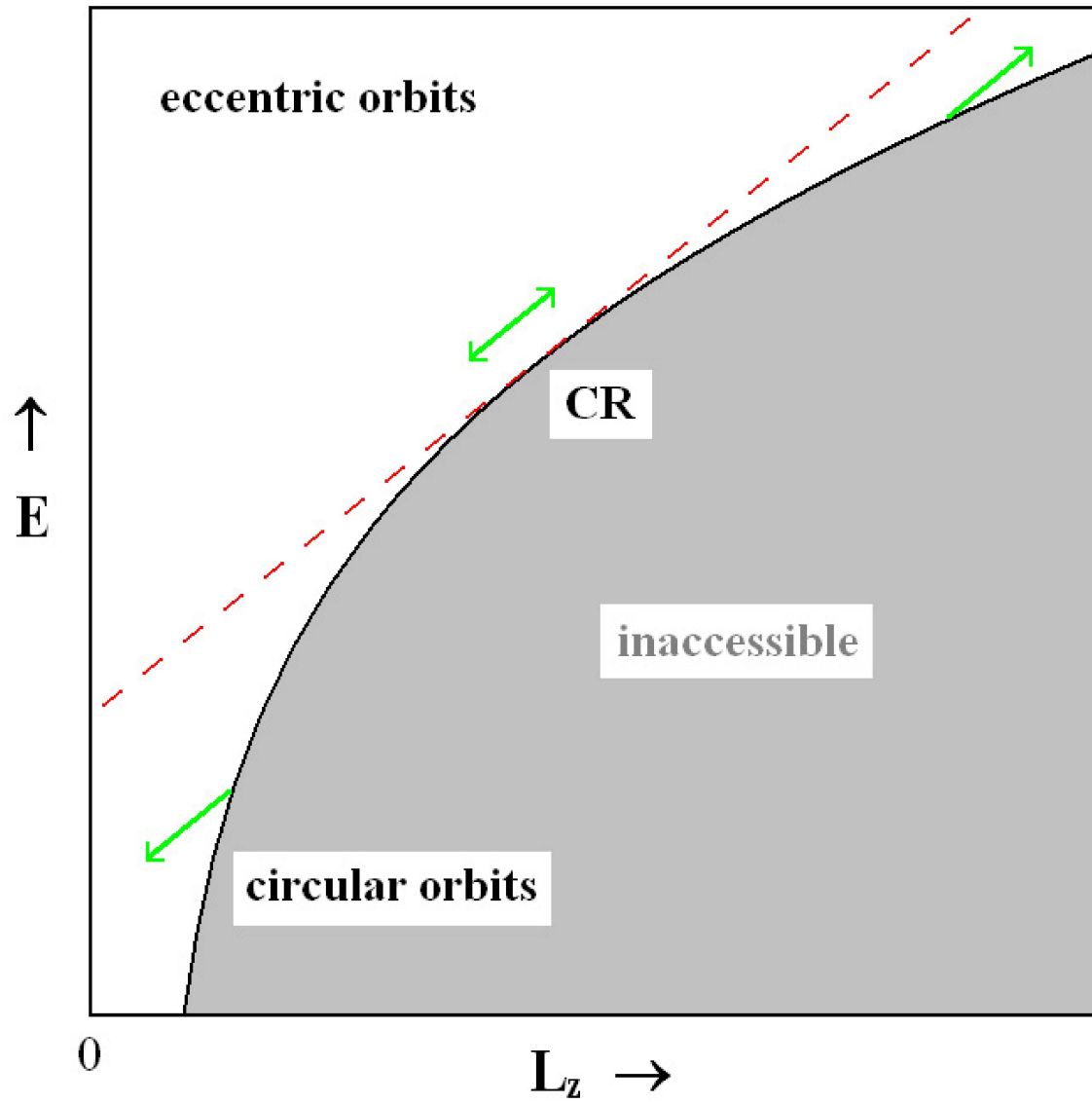
Figure 1.15 (Reproduction of Fig. 1 from SB02). Energies versus angular momenta of stars in a steadily rotating potential. See text for details.

transient, resonant stars have the chance to migrate significantly by the time the wave dies.

Sellwood & Binney (2002) discovered and first tested radial migration by churning in collisionless N-body simulations. They found, that indeed a single transient spiral, which on average lasts between two to three galactic rotations, successfully scatters particles by average radial distances of ~ 1 kpc and as much as 2 kpc while leaving them on nearly circular orbits. Interestingly, the average particle migrates to the opposite side of corotation by the same distance it was from it before the spiral formed. But there are also ones that migrate further away from CR, as theory predicts. So, Sellwood & Binney (2002) found that the spiral churns particles in an annulus of width ~ 2 kpc centered at CR. This shows that particles even migrate if they are partially resonating near corotation. Furthermore, as discussed in §1.2.3.2, corotation itself is broadened. They also found that most of the induced changes in angular momenta take place when the spiral wave saturated around its peak amplitude.

Thus, Sellwood & Binney (2002) showed that radial migration works and is significant in simulated disks with transient spirals. Since spirals in real disks are likely transient as well, which I discuss in §1.2.1.3, it should occur in real galaxies too. They called this effect "radial migration" or interchangeably "churning".

We refer to it mostly as radial migration until §§4 & 5, in which we use churning for it and radial migration to refer to any internal secular effect that causes changes in the particles' home radii. Many other groups also use radial migration to refer to other effects than churning.

Sellwood & Binney (2002) also observed that radial migration barely changes the overall angular momentum and surface density distributions around corotation. Basically, there are nearly as many particles that begin inside corotation and migrate to outside of it as there are ones that begin outside and migrate inwards. Others noticed this earlier, which is why effects at corotation were thought to be uninteresting and were ignored. This is another important property characteristic only to changes at corotation. This result is a bit surprising, because the surface density is not constant across CR and declines with radius in normal disks.

They also ran simulations with multiple transient spirals, and found that radial migration leads to a significant radial mixing in the disk, because each spiral's CR occurs at a different radius, so particles end up essentially random walking in radius. Given the migration distances caused by a single spiral, extreme migrators could traverse the entire disk in a duration as short as a Gyr. This makes radial migration a very important effect that affects the evolution of spiral disk galaxies. Sellwood & Binney (2002) also showed that scattering by molecular clouds yields much weaker radial changes than radial migration. On a related note, radial migration should affect GMCs just as stars in the disk.

Thus, during radial migration, stars near corotation suffer changes in angular momentum that contribute only to changes in home radii without increase in eccentricities. Transience of the perturber is very important for a net nonzero migration effect. Radial migration leaves the surface density and the overall angular momentum distribution practically unchanged. And, multiple recurring transient spirals cause major radial mixing in almost the entire disk, except for the very inner and outer regions where corotation rarely occurs.

1.3.1   Other effects distinct from churning that yield migration

There are a number of effects other than radial migration that can cause changes in home radii. I already mentioned two of these in the previous subsection, namely the similar scattering near the corotation of a bar, which supposedly should yield a small net migration because of its non-transient nature, and blurring, which takes place away from corotation, but yields smaller angular momentum changes and heats and spreads the disk.

Actually, bars combined with outer spirals cause greater angular momentum changes than only spirals (Friedli et al. 1994; Raboud et al. 1998; Grenon 1999; Debattista et al. 2006; Minchev et al. 2011; Brunetti et al. 2011; Bird et al. 2012; Di Matteo et al. 2013). But this is likely because they are stronger amplitude features, and because they couple with the effect of the outer spirals that can pick up stars at the edges of the bars and scatter them outwards further. Also, bar formation changes the radial distribution of angular momentum, and therefore also the surface density profile of the disk, and it adds a substantial amount of radial motion (Hohl 1971). Although a bar may subsequently settle, grow, and/or slow down over time, the main changes associated with its formation probably occur only once

in a galaxy's lifetime (for a dissenting view see Bournaud & Combes 2002), whereas spirals seem to recur indefinitely as long as gas and star formation sustain the responsiveness of the disk. Hence, angular momentum changes in the outer disk beyond the bar should ultimately be dominated by the effects of radial mixing by dynamically-unrelated transient spirals.

Another effect distinct from radial migration is the overlap between resonances of bars and outer spirals, which Minchev & Famaey (2010) and Minchev et al. (2011) claim enhances migration. Minchev & Famaey (2010) used steadily rotating potentials to represent a bar and spiral, and therefore did not address possible mixing by transient spirals in a barred galaxy model.

Finally, external sources can also cause a form of radial migration. Both Quillen et al. (2009) and Bird et al. (2012) find that external bombardment of the disk can enhance radial motion through the increase in the central attraction and also through possible angular momentum changes. However, the importance of bombardment is unclear since satellites may be dissolved by tidal shocking (D'Onghia et al. 2010) before they settle, and furthermore satellite accretion to the inner Milky Way over the past ~ 10 Gyr is strongly constrained by the dominant old age of thick disk stars (*e.g.* Wyse 2009).

1.3.2 Evidence of radial migration

The distributions of metallicities, ages, and angular velocities of stars in the solar neighborhood contain evidence for radial migration. As I explained in §§1.1.4.3 & 1.3, radial mixing from multiple transient spirals by churning should mix formation environments and flatten the radial metallicity gradient with time. Simulations (Loebman et al. 2011) and Galactic chemical evolution models (Schönrich & Binney 2009a; Wang & Zhao 2013) with analytically prescribed radial migration yield this trend. And, more importantly, observations of nearby stars possess it as well (Lee et al. 2011; Yu et al. 2012; Boeche et al. 2013): while young stars exhibit a declining metallicity gradient with radius, this gradient gets flatter for older stellar groups. Likewise, correlation between angular velocity and metallicity disappears with age (Nordström et al. 2004; Haywood 2008; Ivezić et al. 2008; Bond et al. 2010).

Moreover, radial migration naturally explains the high metallicity dispersion in the age-metallicity distribution of solar neighborhood stars (*e.g.* Haywood 2008; Casagrande et al. 2011). In simple terms, the ability of stars to migrate radially over $2 - 3$ kpc in a Gyr or less explains how a young metal poor star with [Fe/H]$= -0.4$ and age $2 - 3$ Gyr can reach the solar neighborhood.

In §3, we find that the vertical action of stars is conserved on average as they undergo radial migration. This implies that radial migration should mix the radial distribution of vertical actions in a disk galaxy just as it mixes metallicities. Therefore, the distribution should be flatter for older stars since those would have had more time to undergo radial migration and hence mixing. Jo Bovy intends to use this idea as another observational test for the presence of radial migration in the Milky Way. Preliminary results from our simulations indeed show that the radial distribution of vertical actions, which is initially a monotonically declining function with increasing radius, flattens out in the middle and outer regions of the disk with time.

Roškar et al. (2008b,c) showed using simulations that radial migration can explain breaks in the outer radial surface density profiles (Types II and III, see §1.1.1.1) of observed disks (*e.g.* van der Kruit 1979, 1987; Pohlen et al. 2002; Bland-Hawthorn et al. 2005; Erwin et al. 2005). They found that particles comprising the final profiles outside of the breaks are mainly ones that migrated from the inner regions. The edge-on disk galaxies NGC 4244 (de Jong et al. 2007; Roškar et al. 2008b), NGC 2684, 6155, and 7437 (Yoachim et al. 2012), and NGC 7793 (Radburn-Smith et al. 2012) have increasing mean stellar age beyond the break. Yoachim et al. (2012), however, also observed three other galaxies that do not contain such breaks, so they concluded evidence for radial migration only in their former three.

The ability of outwards radial migration to form realistic thick disks (Schönrich & Binney 2009b; Loebman et al. 2011), which I discuss in the next section and in §1.4.4, also adds to the indirect evidence for the presence of radial migration.

1.3.3 Radial migration in simulations and models of other groups

Sellwood & Binney (2002) studied radial migration in 2D simulations. Since then, it has

been studied with numerical computations of equations of motion (Lépine et al. 2003) and also shown to occur in fully 3D simulations that included gas and star formation (*e.g.* Roškar et al. 2008b,a; Loebman et al. 2011). These groups found the same qualitative in-plane results and consequences of radial migration.

Schönrich & Binney (2009a) first presented a model for Galactic chemical evolution that included radial mixing, and found (Schönrich & Binney 2009a,b; Scannapieco et al. 2011; Schönrich & Binney 2012) that it naturally gave rise to both a thin and a thick disk, under the assumption that thick disk stars experience a similar radial churning. This assumption needed to be tested, which was the main motivation for our projects in §§2 & 3.

Loebman et al. (2011) and Brook et al. (2012) showed that extensive spiral activity in their simulations also caused a thick disk to develop, and presented a detailed comparison with data (Ivezić et al. 2008) from SDSS (York et al. 2000). However, Bird et al. (2012), Minchev et al. (2012a), and Minchev et al. (2012b) reported that no significant thick disks developed in their simulations.

We, in §2, use controlled simulations to study how radial migration varies with vertical motion in detail, and extend the study of Sellwood & Binney (2002) to thickened 3D disks.

In §3, we search for a quantity of motion that remains conserved for stars when they undergo radial migration. Theoretically, it should be the vertical action, because it is an adiabatic invariant when a star's vertical oscillation is significantly faster than the radial one, which is the case in disk galaxies. Around the same time that we were working on this, Minchev et al. (2012a) showed preliminary simulation results that suggest its conservation using the naive epicycle approximation. We, on the other hand, attempt to estimate exact vertical actions for the particles in our simulations. We also test vertical energy since Schönrich & Binney (2009a) assumed that it is conserved during radial migration. This assumption implies that the radial and vertical motions are decoupled, which is likely not true.

1.4 Thin and thick stellar galactic disks

The Milky Way (*e.g.* Gilmore & Reid 1983; Munn et al. 2004; Jurić et al. 2008; Adibekyan et al. 2013) and many other nearby disk galaxies (Schwarzkopf & Dettmar 2000; Dalcanton & Bernstein 2002; Seth et al. 2005; Yoachim & Dalcanton 2006; Collins et al. 2011; Comerón et al. 2012) are observed to have both a thin and a thick stellar disk.

1.4.1 Thick disk of the Milky Way

Gilmore & Reid (1983) found the first evidence in the vertical stellar density profile of the solar neighborhood, which they derived from estimated distances and luminosities of $\sim$ 12,500 dwarf stars extending to heights of 5 *kpc*. Their Fig. 6 shows that the density is not a single declining exponential with increasing height above and below the midplane, but can be fitted with a sum of two exponentials, with the second having a greater scale height and a lower total mass. See the top right panel of Fig. 4.9 in this thesis for an example of a thin+thick disks vertical profile from our simulations. Also see Fig. 15 by Jurić et al. (2008) for a more recent vertical profile from $\sim$ 48 million stars up to a height of 20 kpc. Actually, the tails of their profile show a third thicker non-exponential component, which is associated with halo stars that have been known earlier (*e.g.* Gilmore & Wyse 1985). More recently, Carollo et al. (2010) and de Jong et al. (2010), for example, studied the interface between thick disk and halo stars in more detail.

The interpretation of the thick disk stars, whether a true distinct component (*e.g.* Rose 1985; Wyse & Gilmore 1986), or a tail of a continuous thin disk distribution (*e.g.* Bahcall & Soneira 1984), has been debated for many years. In the late 90s, Fuhrmann (1998) and Gratton et al. (2000) confirmed the former distinct thick disk hypothesis by showing that the two populations have significantly different abundances. Since then, thick disk stars in the solar neighborhood have been studied extensively from their positions, velocities, velocity dispersions, and chemical abundances (*e.g.* Majewski 1993; Chiba & Beers 2000; Munn et al. 2004; Fuhrmann 2008; Haywood 2008; Jurić et al. 2008; Ivezić et al. 2008; Bond et al. 2010; Navarro et al. 2011; Lee et al. 2011; Cheng et al. 2012; Pasetto et al. 2012; Jayaraman et al. 2013; Adibekyan et al. 2013), including with red giant stars (*e.g.* Moni Bidin et al.

2009; Alves-Brito et al. 2010; Ruchti et al. 2011; Casetti-Dinescu et al. 2011; Moni Bidin et al. 2012). Various groups have divided stars into the two populations using various different spatial, kinematic, or chemical abundance criteria making the assignment to a population not clear cut. Furthermore, selecting these criteria has been difficult, because thick disk stars have properties in between the thin disk and halo populations and often contain overlaps.

These studies and many others find that the Milky Way thick disk has a higher velocity dispersion and lags in its net rotational velocity compared to the thin disk (see for example Bond et al. 2010). The commonly reported rotational lag of the thick disk with respect to the local standard of rest is $40 - 50$ km s^{-1}.

The most extensive study ($\sim$ 48 million stars) by Jurić et al. (2008) reported scale heights of 300 pc and 900 pc and scale lengths of 2600 pc and 3600 pc for the thin and thick disks respectively, but with up to 20% errors due to uncertainties in the photometric parallax used to estimate distances and to the poorly constrained fraction of binary stars. They also reported a local normalization of thick to thin disk densities of 12% with up to 10% errors. Other groups were able to constrain these numbers slightly better, but with fewer stars, and they found roughly the same results (*e.g.* de Jong et al. 2010).

Most importantly, the thick disk is primarily composed of older stars ($\gtrsim$ 8 Gyr old) (Gilmore et al. 1995; Bensby et al. 2003; Nordström et al. 2004; Reddy et al. 2006; Ivezić et al. 2008; Bensby & Feltzing 2012; Haywood et al. 2013). Compared to the thin disk, it also has enhanced [α/Fe] ratios (Bensby et al. 2005; Reddy et al. 2006; Fuhrmann 2008; Ruchti et al. 2011; Schlesinger et al. 2012; Liu & van de Ven 2012) and lower metallicities ([Fe/H]≤ -0.4) on average (*e.g.* Majewski 1993), although some of its stars have solar and even supersolar abundances (*e.g.* Bensby et al. 2007b; Casagrande et al. 2011). See Fig. 2 in Lee et al. (2011) for example, for a plot of [α/Fe] versus [Fe/H] of solar neighborhood stars cut into the thin and thick populations.

It is not very well known yet if these properties, including the disk thickness, vary significantly with radius outside of the solar neighborhood. Observations of external galaxies (*e.g.* Yoachim & Dalcanton 2006; Comerón et al. 2012) suggest roughly constant thicknesses across the disks, but they average the vertical profiles over large annuli.

1.4.2 Continuum of mono-abundance sub-population disks

Various groups have argued, however, that there could be more than one thick disk component (Chiba & Beers 2000; Gilmore et al. 2002; Karaali et al. 2004; Schuster et al. 2006; Girard et al. 2006; Cabrera-Lavers et al. 2007). Vallenari et al. (2006), for example, also found that the thin disk itself is composed of groups of stars with increasing scale heights and velocity dispersions. Bovy et al. (2012a), Bovy et al. (2012c), and Bovy et al. (2012b), who properly corrected for observed versus actual stellar number density, showed more decisively that fine subdivision into [Fe/H] and [α/Fe] yields a continuum of mono-abundance sub-populations that are each nearly isothermal in σ_z and have increasing scale heights and decreasing scale lengths with increasing age.

Notice that their finding of decreasing scale lengths with increasing scale heights is in sharp contradiction with studies that report two components and average over all of their stars' abundances, which find a greater scale length for the thick disk. Cheng et al. (2012), however, found a shorter scale length for thick disk stars with high [α/Fe] ratios compared to the thin disk and the low [α/Fe] thick disk stars.

The trend found by Bovy et al. (2012c) can be interpreted as an "inside-out" and "upside-down" galaxy formation. Bird et al. (2013), Roškar et al. (2013), and Stinson et al. (2013) have reproduced such mono-abundance sub-populations in simulations. This view contradicts the thin and thick disk dichotomy, but nevertheless supports the existence of thick disk populations and that the thickest only contain old stars.

1.4.3 Thick disks in other galaxies

Our neighbor Andromeda also has a thick disk that is more metal-poor, lags rotationally, and has a greater velocity dispersion compared to its thin one (Ibata et al. 2005; Collins et al. 2011). It is the only other disk galaxy astrophysicists were able to resolve stars in so far, and measure their element abundances. However, the presence of thick disks has been detected in other nearby edge-on spiral galaxies by averaging over stars (Schwarzkopf & Dettmar 2000; Dalcanton & Bernstein 2002; Seth et al. 2005; Yoachim & Dalcanton 2006, 2008a,b; Comerón et al. 2012). Yoachim & Dalcanton (2008b) studied nine disks and found

that all of their thick disks are older than the thin ones. In the low mass ones, Yoachim &
Dalcanton (2008a) also observed rotationally lagging and one counter-rotating thick disks.
Some earlier studies found thick-disk-like characteristics in external galaxies, but they were
not recognized as distinct thick disks yet (Burstein 1979; van der Kruit & Searle 1981).
Thus, the existence of a thick disk is not special to the Milky Way among spiral galaxies.

1.4.4   Formation scenarios of thick disks

How these thick disk populations formed has been an important question that is still unan-
swered and debated. It is important because the answer will shed light on how disk galaxies
form and whether our current cosmological theory of galaxy formation is correct. Since the
thick disks are old, their formation will tell us something about these galaxies' early states.
The main question is whether they formed through secular internal evolution, or from exter-
nal interactions and sources reminiscent of the early violent merging and accretion history
disk galaxies are believed to have undergone.

Several formation scenarios have been proposed for the thick disk populations. Accretion
of stars from disrupted satellites (Abadi et al. 2003), thickening of an early thin disk by
minor mergers (Quinn et al. 1993; Kazantzidis et al. 2008; Villalobos & A. 2008; Bird
et al. 2013), and star formation triggered by gas rich mergers at early times (Brook et al.
2004; Bournaud et al. 2009) all require external sources. Whereas star formation from a
turbulent clumpy early disk (Bournaud et al. 2009; Förster Schreiber et al. 2009), massive
star clusters adding kinematically hot components by massive stars and supernovae blowing
out gas from these clusters that reach large enough heights (Kroupa 2002; Assmann et al.
2011), and radial migration (Schönrich & Binney 2009b; Loebman et al. 2011) rely only on
internal processes.

In the radial migration model, stars migrate outwards from the inner region of a galaxy
to the outer regions where they experience a weaker vertical restoring force. Due to the
difference in the vertical restoring force, and because stars conserve their vertical actions on
average during radial migration (Minchev et al. 2012a; Solway et al. 2012; Minchev et al.
2012c), their vertical amplitudes increase as they migrate outwards, and they form the thick
disk. We focus on this scenario in §§4 & 5. Likely, it is not the sole mechanism responsible

for thick disk formation. It especially cannot explain the retrograde thick disk found by Yoachim & Dalcanton (2008a) in one of their galaxies. Yet, we expect the presence of radial migration in every spiral galaxy.

Sales et al. (2009) attempted to discern the first three formation mechanisms that rely on external sources and radial migration by studying the distribution of orbital eccentricities a simulation of each mechanism yields. They found that each mechanism generated somewhat different distributions. Wilson et al. (2011) compared these distributions with that of a sample of thick disk stars in the solar neighborhood, which is peaked at low eccentricities and falls of steeply but smoothly to high eccentricities. They found that it is inconsistent with the satellite accretion scenario, does not favor the particular heating by mergers simulated result, but could in principle if the perturber is oriented at a different angle, and is consistent with both gas rich mergers and radial migration, but favors gas rich mergers most.

Bovy et al. (2012b) also argued that the continuous distribution of vertical temperatures of the mono-abundance sub-populations they found is in disagreement with a massive satellite infall being the dominant disk heating mechanism, and that their continuous spatial and kinematic trends overall suggest an internal mechanism, although they could not rule out multiple minor mergers. The turbulent disk scenario requires the disk to have remained turbulent over a large fraction of its history for it to work (Forbes et al. 2012). Radial migration, however, seems likely to explain these trends.

Both the winds from massive clusters and radial migration scenarios suffer from the problem of not being able to explain why the thick disk primarily contains old stars at present without some additional mechanism that turned these effects off in the past. If radial migration from the Galactic center continued till present, young stars forming in the center should have continued to migrate outwards and populate the thick disk. Likewise, feedback from new clusters should have kept adding new material to thick disk heights. In this case, it is hard to think of a mechanism that can shut off this feedback. Whereas in the radial migration case, theory suggests and we show proof in §5 that the formation of a bar naturally shuts the outwards migration from inside the bar off and does not allow any stars younger than the bar to populate the thick disk.

Furthermore, it is not clear whether the gas expelled from the massive clusters forms

stars at large heights before settling back onto the midplane. In cosmological simulations, Pettini et al. (2001), Strickland et al. (2004), Governato et al. (2007), and Brooks et al. (2009), for example, found that most of the blown out gas settles back onto the disk fairly quickly and produces stars in the midplane.

Both the Milky Way (de Vaucouleurs 1964; Kerr 1967; Nakai 1992; Hammersley et al. 1994; Calbet et al. 1995; Bissantz & Gerhard 2002; Benjamin et al. 2005; López-Corredoira et al. 2007; Cabrera-Lavers et al. 2008; González-Fernández et al. 2012) and Andromeda (Athanassoula & Beaton 2006; Beaton et al. 2007) have a bar, which is already consistent with our proposed suppression of outwards radial migration of young stars by bar formation.

The ability of outwards radial migration to build a thick disk with just spirals is still not settled however. Schönrich & Binney (2009a,b), Loebman et al. (2011), and Brook et al. (2012) found that it is, whereas Minchev et al. (2012a) and Minchev et al. (2012b) reported that radial migration does not thicken the disk enough in general, but they analyzed a shorter duration of only a few Gyr of evolution in their simulations, and their models might have been initially unstable yielding rapid heating as Roškar et al. (2013) pointed out. Bird et al. (2012, 2013) also reported that, although radial migration influences the final state of each age cohort, it does little to thicken and spread the disk sub-populations compared to the trends established during formation. In §4, we test whether our simulations with only spirals produce thick disk populations.

1.5 Collisionless N-body simulations

We use N-body simulations as the main tool to study the galactic dynamic questions posed in this thesis. These simulations run on a computer simulating a single isolated disk galaxy as N point particles that each represent a collisionless fluid element in that galaxy. At each step, the program numerically computes the gravitational force on each particle, and then advances the particles one step forward in time. N-body simulations include the collective effects of the dynamics of collisionless stellar systems, which are very hard, if not impossible, to calculate by hand. Thus, N-body simulations allow the study of the evolution of a galaxy, and have contributed significantly to the understanding of galactic dynamics.

In our simulations, we only simulate stars, and do not include gas or dust that is present in real galaxies. This is an approximation, but a valid one, because, as stated in §1.1.1.1, gas and dust make up at most 15% of the mass in disk galaxies, and thus barely matter in the secular dynamics of disks, especially in relation to radial migration, which Sellwood & Binney (2002) showed causes much greater changes in the angular momenta of stars compared to in-plane scattering by GMCs. Furthermore, other groups (*e.g.* Loebman et al. 2011) who include gas physics in their simulations get qualitatively similar results on radial migration to ours and that of Sellwood & Binney (2002), who used two-dimensional disks without gas. Nevertheless, our neglect of gas is a simplification, and we comment throughout the thesis where applicable on how our results could differ were we to include it.

We also do not include live dark matter halos and bulges represented by additional collections of particles as other groups do. Instead, we make these components rigid, meaning that we represent each with a fixed spherical gravitational potential. The only important effect our simulations miss with this approximation is dynamical friction between a bar and the halo, which is known to slow the bar down (Debattista & Sellwood 2000). This is relevant only to our last project in §5. Theoretically, it should not affect the bar's ability to shut off outwards radial migration from the center, for which only the non-transient nature matters. Yet, we do analyze some simulations that have slowing down bars, caused by transfer of angular momentum to the outer spirals, to confirm this.

We use the halos to get realistic flat rotation curves and/or stabilize the disks against bar or all instabilities where desired. The gravitational force, therefore, arises from all the particles plus the rigid halo and any other rigid components. Aside from the halo and bulge, another rigid spherical component we include is a supplementary force accounting for various corrections described in §1.5.10.

In §§4 & 5, we present simulations in which we add particles to the disk as they progress. We add them in the midplane with zero vertical velocities, on circular orbits, and at an average radius that increases with time. This prescription mimics realistic cold gas accretion with later-accreted gas having greater average angular momentum, which settles into gas

clouds on circular orbits in the midplane, out of which new stars form yielding the "inside-out" galaxy formation discussed in §1.1.3. Groups that include cold gas in their simulations prescribe star formation by replacing clouds with new stars when they reach a big enough density. They are only starting to resolve giant molecular clouds by reaching high enough grid resolutions (*e.g.* Roškar et al. 2008a; House et al. 2011). Their prescription mostly yields the same qualitative picture of star addition we use.

The only significant portion of star formation that we do not include is the one in the center of a galaxy, where inward flows of cold gas and more dying stars, caused by the high stellar density, provide more gas to make more new stars. The locations of central star formation differ between barred and non-barred disks. As explained in §1.2.2, stars barely form in a bar due to the strong radial shearing motion. In barred galaxies, most of the star formation takes place at the tips of the bar and at the inner ring at a weak bar's ILR, if it exists. On the other hand, in disks with only spirals, the central star formation occupies a continuous roughly axisymmetric distribution, as opposed to lying in a couple of rings. Due to this reason, in order to compare our barred simulation with the spirals-only ones of §4 as fairly as possible, we omit such central particle addition in all of our simulations. We comment in §§4.3 & 4.4 on possible consequences of excluding it.

1.5.1 Number of particles

Typical disk galaxies contain at least 10^{10} stars. Modern computers are still not powerful enough to handle this many particles in a reasonable amount of time. Using available computing resources, we are only able to simulate up to $\sim 10^7$ particles. Even so, we mostly utilize lower resolutions of only 10^5 particles, because they are much more computationally cost effective allowing for many runs, and the dynamics in such simulations differ little from higher resolution ones.

The only important effect that depends on particle number is heating due to two-body relaxation, which affects the vertical structure, but reduces for larger N (Sellwood 2013a). In §4, we report greater N simulations to study whether this is so in our simulations. Higher resolution simulations are also useful for better statistics and producing plots with finer bins, which we also present in §4.

1.5.2 Collisionless systems and two-body relaxation

Spherical systems of stars are collisionless, meaning that stars do not come close to each other and do not affect each other's trajectories much, because the distances between them are immense. Instead, the mean force field generated by the whole system dictates the smooth trajectories of the stars. The collisionless Boltzmann equation (BT08, eq. 4.6) governs the dynamics in such systems.

Disk galaxies have also been considered to be collisionless. Recently, however, Sellwood (2013a) showed that two-body scattering is significant in simulations with moderate numbers of particles for reasons pointed out long ago by Rybicki (1972). The effect reduces with increasing number of particles, and is supposedly negligible in real galaxies.

1.5.3 Gravitational softening

The Newtonian gravitational force between two point masses becomes very large when they come close to one another. To integrate their motions accurately, the integrator would need to proceed at very small time steps making the simulation unrealistically time consuming. To solve this problem, N-body codes use softening (BT08, p. 123), in which a force softening kernel function S_F replaces $|\mathbf{r}_\beta - \mathbf{r}_\alpha|^{-2}$ in the total gravitational force on a particle α from all the other particles (BT08, eq. 2.224):

$$\mathbf{F}_\alpha = \sum_{\beta \neq \alpha} G m_\beta S_F(|\mathbf{r}_\beta - \mathbf{r}_\alpha|) \frac{\mathbf{r}_\beta - \mathbf{r}_\alpha}{|\mathbf{r}_\beta - \mathbf{r}_\alpha|}. \tag{1.12}$$

S_F tends to $|\mathbf{r}_\beta - \mathbf{r}_\alpha|^{-2}$ for separations greater than a characteristic softening length ε, and tends smoothly to zero for separations less than ε. Softening also helps by making simulated disks more collisionless, which is realistic since, as just discussed in §1.5.2, real galaxies are nearly collisionless over most radii.

The softening kernel most commonly used in 2D simulations of razor-thin disks is the spherical Plummer rule of scale length ε (BT08, eq. 2.226), which weakens inter-particle forces on all scales, and hence mimics the effect of disk thickness. Due to this, it is unsuitable for 3D simulations of thickened disks. Instead we use the cubic spline softening rule recommended by Monaghan (1992), which yields the full attraction of a point mass at

distances greater than two softening lengths (2ε).

We take great care in choosing the softening length in order to minimize both noise and systematic bias (Sellwood 1987). Very small ε cause the potential to be too grainy, while values too large make the potential too smooth yielding a poor resolution of density gradients. We also choose a value that exceeds the vertical grid spacing in order to minimize the grid dependence of the inter-particle forces.

1.5.4 Particle-mesh code

Direct summation of the total force on each particle from all the other particles results in an $O(N^2)$ computation. This is too costly even for 10^4 particles. The most commonly used tree codes (*e.g.* Barnes 1986) reduce the computation cost to $O(NlogN)$ by approximating each group of distant particles as a single imaginary particle located at their center of mass and having their total mass. This technique does not dependent on geometry, and works well for moderate N. Yet, particle-mesh codes, or "grid" codes, are even faster at $O(N + N_g log N_g)$ when the number of grid cells N_g is significantly less than the number of particles N.

Particle mesh codes work by placing a lattice of a fixed volume and a fixed number of cells over the N-body system. For best results, the geometry of the lattice should match that of the system: spherical for spheres or ellipsoids, and polar for disks. The code first assigns the masses of the particles to the cells. Then, it solves Poisson's equation (BT08, eq. 2.10) to get the gravitational potential and force field on the centers of the cells. Lastly, it calculates the acceleration on each particle by interpolating between nearby cell centers. In order to conserve the total linear momentum of the system, it uses the same method for both assigning the mass to the grid and interpolating from it (BT08, p. 134).

We use the particle-mesh code developed by Professor Jerry Sellwood that has been tested with many different simulations over the years. It employs the cloud in cell mass-assignment scheme and interpolation (BT08, p. 129), in which it distributes each particle's mass to the surrounding cube of nearby eight grid points (cell centers) and interpolates the three components of acceleration on the particle linearly from the same eight points.

1.5.5 3D polar grid

We use a polar 3D grid composed of logarithmically spaced radial annuli, linearly spaced azimuthal spokes, and linearly spaced vertical planes. Sellwood & Valluri (1997) describe it in detail. Initially, we make the centers of the disk and the spherical rigid components coincide with each other and the grid center. The logarithmic spacing and the polar geometry gives better spatial resolution at the center, which is desirable because there the particle density is greatest.

The Poisson solver uses fast Fourier transforms (FFTs) in the azimuthal and vertical directions and direct convolution in the radial direction to compute the potential and the three components of acceleration separately. Thus, the solver expands the force field in azimuthal Fourier components, or sectoral harmonics. This is very useful, because it allows us to control various aspects of the simulations by restricting the forces to a specific set of these harmonics.

We work with sectoral harmonics up to $m = 8$, but omit the $m = 1$ harmonic in order to avoid imbalanced forces from a possibly asymmetric distribution of particles in a rigid halo with a fixed center. In §§2 & 3, we present controlled simulations with a single two, three, or four-armed spiral wave. In order to achieve this, we eliminate all the non-axisymmetric forces except $m = 2$, $m = 3$, or $m = 4$ respectively. In other words, for example in the first case, only harmonics $m = 0$ and $m = 2$ are active. We also run a test simulation in which we only have the axisymmetric $m = 0$ mode active in order to suppress all spiral activity and test whether radial migration does not occur in it as theory predicts.

Our code is unable to compute forces from particles that leave the grid, but keeps them free streaming at their exit velocities in order to conserve the total energy and linear and angular momenta of the system. The typical fraction of particles that escape the grid by the end of our simulations is $\lesssim 1\%$.

1.5.6 Time step, guard radii, and time zones

We evaluate forces from the particles at intervals of $0.02\tau_0$, where τ_0 is our unit of time described in §1.5.11. However, we step forward only some of the particles at each evaluation.

Particles span a wide range of orbital periods. In order to maintain a good accuracy of orbit integration, we use smaller integration time steps at smaller radii where the periods are shorter and accelerations are greater due to the greater concentration of mass. In our older simulations that use Mestel disks, we simply subdivide the time step by a factor of 2 for every factor of 2 decrease in radius without updating forces. These simulations contain five such subdivisions called "guard radii" (Shen & Sellwood 2004). In other words, particles on longer sub-time steps wait while the ones on shorter steps move until their steps coincide. The code calculates forces only at the main time steps, while the integrator uses the same previous main time step's force on a particle that is within a guard radius when moving it at the sub-time steps. When a particle crosses a guard radius, its orbit proceeds at the new zone's sub-time step.

In the newer more realistic exponential disk simulations, we actually calculate the locations of the guard radii where the period halves using the potential of the initial setup, and half the time step at these calculated guard radii. We fix their locations for the entire durations of the simulations even though the addition of particles and redistribution of mass due to internal dynamics may change where the orbital period halves. We find that the important condition for good orbit accuracy is to integrate every particle's full orbit period with at least ≈ 200 time steps, and our guard radii prescription achieves this in excess. We use between one to eight such radii depending on the setup: simulations with rigid bulges require more subdivisions due to the greater central mass concentrations, and so do ones with NFW halos as opposed to cored isothermal halos since the former have more massive cores (see §1.5.8).

To save computing time, we also double the time step for every factor of 2 increase in radius in the Mestel disks and at radii where the orbital period doubles in the exponential ones for two to five such "time zones" (Sellwood 1985). So, the integrator moves particles in these zones at the longer power-of-two multiples of the main time step using the forces calculated at these longer steps.

Tests with shorter main time steps than $0.02\tau_0$ yield similar results.
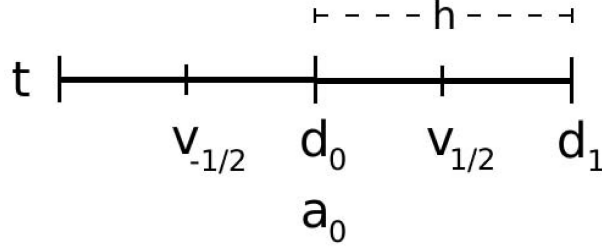
Figure 1.16 Helpful illustration for understanding how our leapfrog integrator works. See text in §1.5.7 for explanation and variable definitions.

1.5.7 Time-centered leapfrog integrator

Orbits of stars cannot be computed analytically in most stellar systems, including the ones we use in this thesis. Therefore, our simulations use a numerical orbit integrator. Specifically, we use a (non-standard) leapfrog integrator that, at each main step, uses the acceleration $\mathbf{a_0}$ on a particle along with the velocity $\mathbf{v_{-1/2}}$ at half a time step $h/2$ before the main step to get the velocity at half a step ahead:

$$\mathbf{v_{1/2}} = \mathbf{v_{-1/2}} + h\mathbf{a_0}, \tag{1.13}$$

and then uses this forwards velocity to get the new position at a full step ahead of the main step:

$$\mathbf{d_1} = \mathbf{d_0} + h\mathbf{v_{1/2}}, \tag{1.14}$$

which we illustrate in Fig. 1.16. It calculates

$$\mathbf{v_{-1/2}} = \mathbf{v_0} - \frac{1}{2}h\mathbf{a_0} \tag{1.15}$$

only in the beginning from the initial velocities and accelerations, and stores each $\mathbf{v_{1/2}}$ in memory to be used as the following $\mathbf{v_{-1/2}}$ for subsequent steps. Compared to standard leapfrog integrators (BT08, p. 200), this integrator allows us to have different time zones while the forces are calculated at discrete times with the fixed main time step.

1.5.8 Disk, halo, and bulge models

In the projects of S12, we use Mestel disks (BT08, p. 99). This model has a constant circular velocity at all radii; so, adding a halo is not needed to get a realistic rotation curve. A Mestel disk with half of its mass active (represented by particles) and the other half held rigid is the only stable disk model known against global instabilities such as spirals and bars (Zang 1976; Toomre 1981; Evans & Read 1998). Hence, we use this model to get controlled simulations, in which we seed a specific spiral disturbance of predictable behavior by adding a groove in angular momentum at a certain radius. The rigid half of the mass resides in a rigid halo that has the same radial potential as the Mestel disk, but is spherically distributed. This ensures that the total central attraction in the midplane corresponds to a total mass razor-thin Mestel disk.

Real disks, however, have approximately exponential density profiles (our Mestel disks are actually close to exponential at intermediate radii). Hence, we also use exponential disks (BT08, p. 100) in the last two projects. As the disks evolve in the simulations, their surface densities change due to spirals, bars, and more so due to the addition of particles. At intermediate radii, they always remain nearly exponential, but their scale lengths increase due to the added mass. Whereas at small radii, the surface densities deviate to a much steeper profile with a small scale length. And at large radii, the disks either follow the same intermediate exponential profile (Type I profile), or truncate more rapidly by deviating again to a steeper exponential (Type II profile).

To get a flat rotation curve, we add a rigid spherical halo to our exponential disks. We use two halo profiles: NFW (BT08, p. 70) and cored isothermal (eq. 4.2). The former is a generic result in CDM cosmological simulations of halos that undergo dissipationless collapse (Navarro et al. 1997). It contains a steep core that rises as $\rho(r) \propto r^{-1}$, which does not have strong support from observations of rotation curves (Moore 1994; de Blok et al. 1996; Côté et al. 2000; McGaugh et al. 2001) and velocity dispersions (*e.g.* Spano et al. 2008). Profiles, like the latter simpler one, that do not have a cuspy core seem to fit the inner disks well in these observations.

Although we end up not using any simulation with a rigid bulge, we did initially add

bulges to the exponential disks in order to weaken and shorten the bars that would form in them (see §1.5.12). We tried the observationally motivated $r^{1/4}$ power-law bulge profile (de Vaucouleurs 1948, BT08, p. 21), but also the Hernquist (BT08, p. 70) and Plummer sphere (BT08, p. 65) profiles.

The density of stars also declines exponentially in the vertical direction away from the midplane in disks (BT08, eq. 1.10). A disk with a velocity dispersion that is independent of height z above or below the midplane has a $\rho(z) \propto \mathrm{sech}^2 z$ vertical profile (Spitzer 1942). This profile approaches an exponential one for greater heights, but deviates from it at small heights. Unlike the exponential profile, it has a harmonic core, $i.e.$ the derivative of the density ρ with respect to z at $z = 0$ is zero, which is a desirable feature for setting up initial conditions in simulations. Observations of both the Milky Way ($e.g.$ Gilmore & Reid 1983; Jurić et al. 2008) and external galaxies ($e.g.$ de Grijs et al. 1997) suggest that the most common vertical profile is intermediate between the exponential and the $\mathrm{sech}^2 z$ ones, and is even closer to the exponential than a $\mathrm{sech} z$ profile. We use our own intermediate profile given in eq. (2.5) that also has a harmonic core and approaches the exponential profile faster than $\mathrm{sech}^2 z$.

1.5.9   Initial coordinates

Setting up initial positions of the particles so that the disk has a desired profile is not difficult. However, then assigning their initial velocities so that the disk remains in equilibrium and keeps the initial profile is very difficult. Most profiles do not have a distribution function (DF), from which suitable velocities can be chosen (BT08, p. 275).

Such a DF exists for a razor-thin Mestel disk (Zang 1976), but not for a thick one, nor for the more realistic exponential disk. Thus, for our Mestel disks, we set up the midplane velocities using the Zang DF, and then assign the vertical velocities using the one-dimensional Jeans equation (BT08, eq. 4.271), which yields the vertical velocity mean and dispersion necessary for vertical equilibrium in a specified potential. This approximation works adequately with a low radial velocity dispersion. In §2.2.1, we present the vertical changes our disks undergo in the beginning of the simulations due to their realistic radial velocity dispersions.

As for our exponential disks, we essentially use the full Jeans equations (BT08, eq. 4.222) to obtain the initial velocity means and dispersions given the gravitational fields of both the particles and the rigid halo and/or bulge components. First, we calculate the radial velocity dispersion for a given Toomre Q value (eq. 2.3; BT08, eq. 6.71) while neglecting disk thickness and softening corrections. Then, we use epicycle approximation (BT08, p. 164) to estimate the azimuthal velocity dispersion. Then, we compute the mean orbital velocity using the Jeans equation that accounts for asymmetric drift in axisymmetric systems in the midplane (BT08, eq. 4.226). Finally, we again use the 1D Jeans equation to set up the vertical balance.

1.5.10 Supplementary force

The radial gravitational potential gradient in the midplane of our disks is less than that of razor-thin infinite disks due to finite thickness, truncation, and gravitational softening. In our Mestel disk models, it is also due to the seeded angular momentum groove and the angular momentum tapers described in §2.2.1. We use a distribution function that corresponds to the razor-thin infinite Mestel disk to set up the initial velocities of the particles. Therefore, in order to maintain equilibrium, we add a supplementary rigid spherical central attraction necessary to correct for these effects. Throughout the simulation, we add the same supplementary force that we calculate and tabulate in the beginning. Since we use a different more approximate approach, as opposed to a distribution function, to set up initial conditions in our exponential disk simulations, it is unnecessary to add such corrections in them. Yet, we decided to use a supplementary force in those simulations as well.

1.5.11 Choice of units

Our code uses parameters without physical units. The initial circular velocity V_0 is constant over most radii, especially for the Mestel disk setup. Thus, to make sense of the variables, it is most sensible to choose it to be the unit of velocity and some meaningful radial parameter R_0 to be the unit of length. Then, the unit of time will correspond to the dynamical time $\tau_0 = R_0/V_0$, the unit of mass will be $M_0 = V_0^2 R_0/G$, and that of angular momentum $L_0 = R_0 V_0$.

To limit the radial extent of our Mestel disks, we taper them with inner and outer angular momentum tapers described in §2.2.1. The inner one sets a radial scale R_i, which we choose to be 1.0 in the code units. So, we set $R_0 = R_i$. We also make the circular velocity $V_0 = 1.0$, which makes all the units simple to follow.

For our exponential disks, we choose R_0 to be their initial radial length scale, which is also 1.0. Each simulation, however, has a different initial circular velocity; so, the units for each one have to be interpreted accordingly. Furthermore, their inner rotation curves rise from smaller circular velocities than the flat V_0 they asymptote to. And, the addition of particles slowly raises their circular velocity.

These units are still not physical ones. The power of such code is that now one can choose any desired scaling to physical units. Reasonable scalings would fit some observable physical parameters, such as the circular velocity in the solar neighborhood or in some external disk galaxies, the dynamical mass, or the present exponential scale length of the disk. One possible scaling we suggest is to choose $R_0 = 0.75$ kpc and $\tau_0 = 3.0$ Myr, which leads to $V_0 = 244$ km s^{-1} and $M_0 = 1.04 \times 10^{10}$ M$_\odot$. But there are many other realistic scalings.

Throughout the thesis, we express all the variables in terms of R_0, τ_0, and V_0 without adopting a specific scaling to physical units.

1.5.12 Difficulty suppressing bars in simulations

To test our hypotheses in this thesis, especially ones in §§4 & 5, we need various specific disk galaxies: some that have spirals, but do not form a bar, and others that do form a bar, but one that is realistically small. Such simulations, especially bar-free ones, are not easy to generate. We simulated many test galaxies until finding suitable ones. We also sought realistic final disk thicknesses and radial scale lengths, but these were minor requirements.

It is a known problem that N-body simulations of disk galaxies naturally produce bars that are hard to suppress (Sellwood 1981). Yet, about a third of the observed real disk galaxies do not contain a bar. We still do not know exactly how nature produces non-barred galaxies, but there are various ways to do that in simulations.

As mentioned before in §1.2.3.3, bars are believed to arise due to a feedback loop in

the swing amplifier caused by density waves passing through the center of the galaxy. And as mentioned in §1.2.3.2, one way to shut off this feedback is to place a dense enough concentration of mass in the center, such as a bulge (Toomre 1981). This increases the maximum $\Omega - \kappa/2$, and allows the ILR to exist for all pattern speeds. An ILR absorbs the inwards traveling density waves. One can also use this method to obtain a weaker and shorter bar by using a less massive and/or less concentrated bulge than is required to completely suppress it (Hasan et al. 1993; Sellwood & Moore 1999; Shen & Sellwood 2004). Another related method is to make the halo more concentrated (Sellwood 1981). These methods essentially translate to the bar instability being weaker in disks with faster rising rotation curves, which I illustrate in Fig. 1.2.

Some methods of bar suppression are unrelated to the inner rotation curve. Sellwood (1981) also found that increasing the softening length weakens the bar perturbing potential leading to weaker bars. Another way is to increase the radial velocity dispersion in the central region, which damps the in-going waves. Finally, one unrealistic way is to omit the $m = 2$ sectoral harmonic, which would also suppress two-armed spirals. But then, the disk can form a pattern of three straight arms, which is not observed in nature.

These methods work against bars predicted by the linear theory of swing amplification: ones that form early on in simulations out of a bar instability "seeded" in the initial conditions. However, bars can also be born out of particle noise, which does not depend on the mass concentration at the center. One can stabilize the disk against such bars, and also the linear regime kind, by decreasing the active mass of the disk that is represented by particles, *i.e.* increasing the mass of the halo (red curves in the right plot of Fig. 1.2). This works (Ostriker & Peebles 1973) by decreasing the gain of the swing amplifier, and also has implications on the rotation curve. This method also weakens the spiral activity, whereas we need strong spirals without a bar. Our addition of particles, however, comes to the rescue because we place them in the midplane on circular orbits, which cools the disk (reduces the velocity dispersion) where the particles are added making it more susceptible to spiral activity. Furthermore, particle addition increases the active disk mass over time, and eventually makes it more prone to these instabilities.

Suppressing bars with less massive disks may lead to the use of unrealistically massive

halos. Various lines of evidence suggest that galactic disks are maximal, meaning that the halo contribution to the rotation curve is substantially smaller than that of the disk at the radii where the disk matters. Fig. 1.2 shows examples of both maximal and submaximal disks as described in its caption. See Sellwood & Moore (1999) and §6.3.3 in BT08 for good summaries of evidence for maximal disks. However, in a simulation with particles being added constantly, one can begin with a submaximal disk and end up with a maximal one due to the addition of active mass over time.

In practice, stochasticity makes finding suitable simulations worse, especially when dealing with a bar born out of particle noise. Two simulations with exactly the same setup but different random number generator seeds for the initial positions and velocities can yield very different simulations. A bar can arise from particle noise early or very late in the simulation. So, we had to run many test simulations with different random seeds to get a simulation that has only spirals for a long time and then forms a bar.

The reason why disk galaxies, both simulated and real, are stochastic on a macroscopic level is because they tend to develop vigorous collective responses to small disturbances from particle noise (Goldreich & Lynden-Bell 1965; Julian & Toomre 1966; Toomre 1981). These responses die out quickly due to differential rotation and transience, but they change the distribution function of the system macroscopically. Such changes lead to divergence in results of similar systems with different initial random noise, or of identical systems simulated with different codes or machine precision. Sellwood & Debattista (2009) showed that this stochastic and chaotic behavior is a real effect in disks that does not decrease for greater number of particles. However, it does not stop, or much affect, the growth of global instabilities, such as a vigorous global bar instability, seeded in the initial disk.

We also ran many simulations with different particle addition rules to get the desirable disk behavior. Particle addition influences the radial disk surface density distribution and the spiral activity as discussed above.

Once bars form, they can get weakened or even destroyed by outer spirals if the beating between the bar and the spiral arm phases occurs in a specific manner. When the spiral arms originate just ahead of the bar in phase, gravitational stresses of the spirals onto the bar can cause the bar to gain angular momentum from the spirals making it weaker

Sellwood (2013b). However, strong bars rarely undergo such weakening, and almost never get destroyed in simulations. Weak bars get destroyed sometimes, but often are shortly followed by the formation of a new bar mode. More often than weakening, bars grow by aligning more orbits along them and by losing angular momentum to the outer particles and spirals, which makes the orbits along the bar more elongated. The persistence of bars agrees with observations of the bar fraction evolution mentioned in §1.2.2.

1.6 Projects of this thesis

In our first project, presented in §2, we extend the study of radial migration of Sellwood & Binney (2002) to three-dimensional stellar disks using controlled simulations of the stable half-mass Mestel disk. We investigate how the strength of radial migration varies with disk thickness, radial velocity dispersion, and the number of spiral arms all tested under the influence of a single spiral wave. We show that the results of these tests are motivated by theory. We also study how radial migration affects the vertical structure of the disk. Then, we compare these results to similar simulations with multiple transient spirals, both with and without the presence of a bar. The main motivation for this project was the assumption made by Schönrich & Binney (2009a) in their Galactic chemical evolution model that radial migration affects both thin and thick disks equally. They asked us to test this assumption with simulations; and so we did, collaborating with Ralph Schönrich on this and the following project. As theory suggests, we find that radial migration weakens with increasing disk thickness.

In §3, we present the second project, which is really a continuation of the first since we analyze the same simulations and published both in S12. In it, we seek a quantity describing a star's orbit that remains conserved while the star undergoes radial migration. If such a quantity exists, one can use this fact along with the other known properties of radial migration to prescribe radial migration in galactic evolution models. We test various estimates of two quantities that come to mind, namely vertical energy and vertical action. As mentioned in §1.3.3, theory suggests that the vertical action should be conserved, and not vertical energy. Indeed, we find that this is the case, but the vertical action is only conserved on average, not particle by particle.

We go on to test the idea of explaining why the thick disk of the Milky Way contains primarily old stars assuming it formed through the radial migration scenario. As presented in §§1.2.3.2 & 1.3, theoretically, radial migration should not take place in the inner galactic region when a bar is present. Hence, bar formation should prevent newly formed stars in the inner region from populating the thick disk in the solar neighborhood, thus leaving the thick disk deficient of young stars. In §5, we test this idea using our previous Mestel disk setup and more realistic exponential disks. Before we do that, however, we check, in §4, whether realistic thick disks form via radial migration in our simulations in the first place.

Chapter 2

Detailed study of radial migration in galactic disks

2.1 Introduction

In §1.3, I introduced the effect called radial migration, which Sellwood & Binney (2002) discovered and first studied in collisionless N-body simulations. In §§1.1.4.3 & 1.3.2, I explained that radial migration is important, because multiple transient spirals cause substantial radial mixing of stars that mixes formation environments and erases the history of a disk galaxy. Theory and simulations suggest that this effect is unavoidable when transient spirals are present.

Schönrich & Binney (2009b) proposed that outwards radial migration of stars from the inner galactic region could build a thick disk (see §1.4.4). Their Galactic chemical evolution model with prescribed radial migration produced a realistic thick disk this way (Schönrich & Binney 2009a,b). In their model, they assumed that radial migration affects thin and thick populations equally. Thus, it became important to test how the strength of radial migration varies with distance away from the disk midplane, which we do in this chapter.

Loebman et al. (2011) and Brook et al. (2012) showed that realistic thick disks also form in simulations through this mechanism. While Loebman et al. (2011) presented circumstantial evidence for radial migration in the thick disk, they did not show explicitly that it was occurring, neither did they attempt to quantify the extent to which it may be reduced by the weakened responses of thick disk stars to spiral waves in the thin disk. Bird et al. (2012) found that mixing is more extensive when spiral activity is invigorated by star formation, although the level of spiral activity is strongly dependent on the "gastrophysical" prescription adopted. They showed that mixing persists even for particles with large oscillations about the mid-plane, and they determined migration probabilities from their simulations.

In this chapter, we set ourselves the limited goal of determining the extent of radial migration in isolated, collisionless disks with various thicknesses and radial velocity dispersions that are subject to transient spiral perturbations. Following Sellwood & Binney (2002), we first present controlled simulations of two-component disks constructed so as to support an isolated, large-amplitude spiral wave, in order to study the detailed mechanism of migration in the separate thin and thick disks. We also report the responses of two-component disks to multiple spiral patterns, both with and without a bar.

2.2 Description of the simulations

All our models use the constant velocity disk known as the Mestel disk (BT08). Linear stability analysis by Toomre (1981, see also Zang 1976 and Evans & Read 1998) revealed that this disk with moderate random motion lacks any global instabilities whatsoever when half its mass is held rigid and the center of the remainder is cut out with a sufficiently gentle taper.[I] We therefore adopt this stable model for the thin disk, and superimpose a thick disk of active particles that has 10% of the mass of the thin disk. The remaining mass is in the form of a rigid halo, set up to ensure that the total central attraction in the midplane is that of the razor-thin, full-mass, untapered Mestel disk.

2.2.1 Disk setup

Ideally, we would like to select particles from a distribution function (DF) for a thickened Mestel disk. Toomre (1982) found a family of flattened models that are generalizations of the razor-thin Zang disks that have the isothermal $\text{sech}^2 z$ vertical density profile (Spitzer 1942; Camm 1950). Unfortunately, these two-integral models have equal velocity dispersions in the radial direction and normal to the disk plane (see BT08), whereas we would like to set up models with flattened velocity ellipsoids.

Since no three-integral DF for a realistic disk galaxy model is known, as far as we are aware, we start from the two-integral DF for the razor-thin disk (Zang 1976; Toomre 1977a):

$$f_{\text{Zang}}(E, L_z) \propto L_z^q e^{-E/\sigma_R^2}, \tag{2.1}$$

where E is a particle's specific energy and L_z its specific z-angular momentum. The free parameter q is related to the nominal radial component of the velocity dispersion through

$$\sigma_R = V_0(1 + q)^{-1/2}, \tag{2.2}$$

with V_0 being the circular orbital speed at all radii. The value of Toomre's local stability

---

[I]Sellwood (2012) found that particle realizations of this disk are not completely stable, but on a long time scale when N is large.

parameter for a single component, razor-thin Mestel disk would be

$$Q \equiv \frac{\sigma_R}{\sigma_{R,\mathrm{min}}} = \frac{2^{3/2}\pi}{3.36 f (1+q)^{1/2}},$$

(2.3)

where f is the active fraction of mass in the component; note that these expressions for both σ_R and Q are independent of radius. A composite model having two thickened disks, such as we employ here, will have some effective Q that is not so easily expressed. We choose different values of σ_R for the thin and thick disks, given in Table 2.1, in order that the thick disk has a greater radial velocity dispersion, as observed for the Milky Way.

We limit the radial extent of the disks by inner and outer tapers

$$f_0(E, L_z) = \frac{f_{\mathrm{Zang}}}{[1 + (L_i/L_z)^4][1 + (L_z/L_o)^6]},$$

(2.4)

where L_i and L_o are the central angular momentum values of the inner and outer tapers respectively. The exponents are chosen so as not to provoke instabilities (Toomre, private communication). We employ the same taper function for both disks and choose $L_o = 15 L_i$. We further restrict the extent of the disk by eliminating all particles whose orbits would take them beyond $25 R_0$, where $R_0 = L_i/V_0$ is the central radius of the inner taper. This additional truncation is sufficiently far out that the active mass density is already substantially reduced by the outer taper.

We thicken these disk models by giving each the scaled vertical density profile

$$\rho(\tilde{z}) \propto \frac{1}{\left(e^{|\tilde{z}|/2} + 0.2 e^{-5|\tilde{z}|/2}\right)^2},$$

(2.5)

where $\tilde{z} = z/z_0$ with z_0 independent of R. While both this function and the usual $\mathrm{sech}^2 z$ function have harmonic cores, we prefer eq. (2.5) because it approaches $\rho \propto e^{-|\tilde{z}|}$ more rapidly, as suggested by data (*e.g.* Kregel et al. 2002); z_0 is therefore the exponential scale height when $z \gg z_0$. We set the vertical scale height of the thick disk to be three times that of the thin disk, as suggested for the Milky Way (Jurić et al. 2008).

We estimate the equilibrium vertical velocity dispersion at each z-height by integrating the 1D Jeans equation (BT08, eq. 4.271) in our numerically-determined potential. This
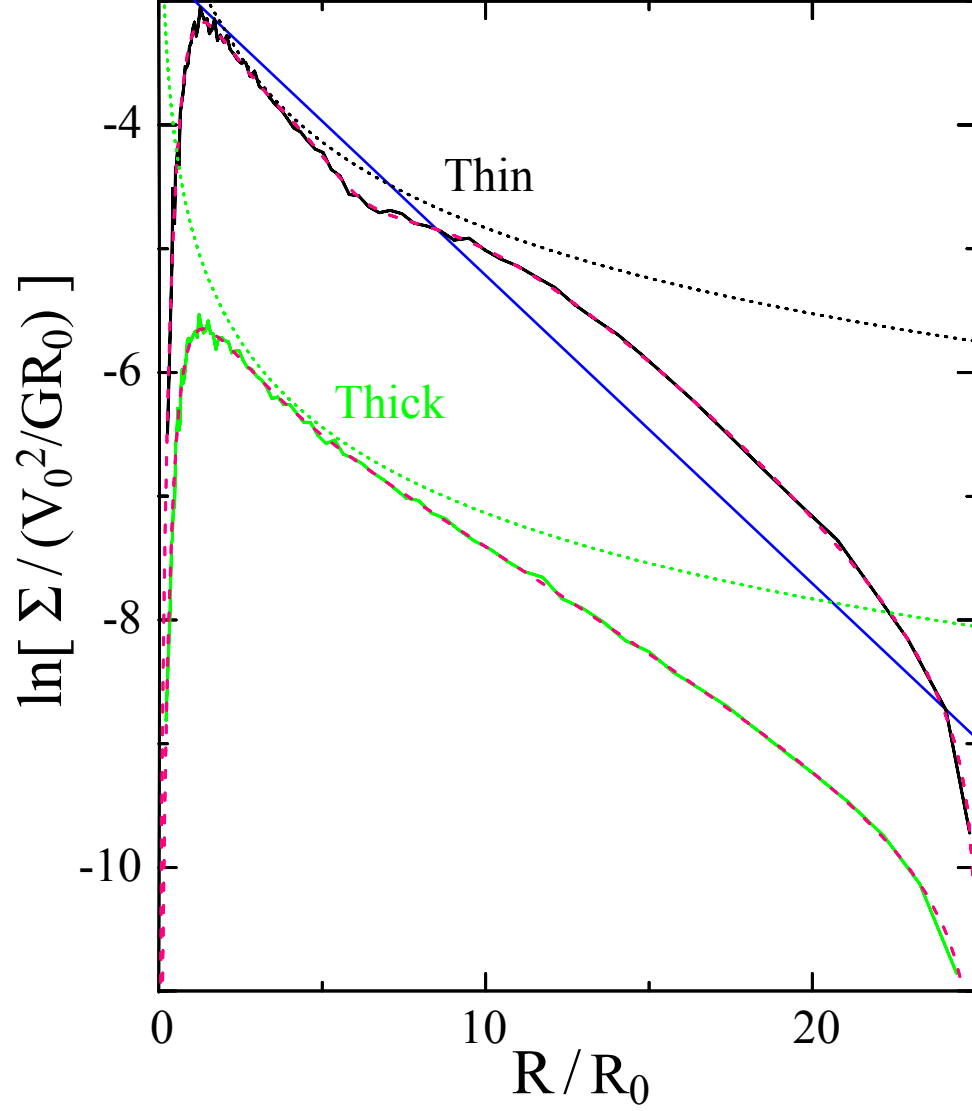
Figure 2.1 Initial surface density profiles of the tapered thin (top black curves) and thick (bottom green curves) Mestel disks in simulation M2 (solid curves) measured from the particles. The dashed red curves, which are almost perfectly overlaid by the solid curves, show the expected surface density of the tapered disks from integrating the DF over all velocities, while the dotted curves indicate the density profiles of the corresponding non-tapered disks. The groove in the thin disk is centered on $R = 6.5R_0$ and is broadened by epicycle excursions. The blue line of slope -0.25 indicates the adopted exponential profile of the thin disk.

procedure is adequate when the radial velocity dispersion is low, but the vertical balance degrades in populations having larger initial radial motions, which flare outwards as the model relaxes from initial conditions, as shown below.

The tapered thin Mestel disk has a surface density that declines with radius as shown in Fig. 2.1. While there is no radial range that is closely exponential, we estimate an approximately equivalent exponential radial scale length $R_d = 4.0R_0$ as shown by the blue line. Accordingly, we choose $z_0 = 0.4R_0$ for the thin disk so that the ratio R_d/z_0 is similar to that of the Milky Way and the average volume-corrected ratio of $7.3 \pm 2.2(1\sigma)$ found by Kregel et al. (2002) for 34 nearby galaxies. The values we adopt for each model are given in Table 2.1.

The radial gravitational potential gradient in the midplane of our model is less than that of the full-mass, razor-thin, infinite Mestel disk as a result of the reduced disk surface density, the angular momentum tapers, the finite thickness of the disks, and gravitational force softening. In order to create an approximate equilibrium, we therefore add a rigid central attraction to the self-consistent forces from the particles in the disks at each step. We tabulate the supplementary central attraction needed at the initial moment to yield a radial force per unit mass of $-V_0^2/R$ in the midplane, and apply this unchanging extra term as a spherically symmetric, rigid central attraction.

We find that our model is close to equilibrium, with an initial virial ratio of the particles of ≈ 0.52. This value adjusts quickly to reach a steady virial ratio of 0.50 within the first 32 dynamical times (defined below). As noted above, the initial imbalance seems to arise mostly from the vertical velocity structure, for which we adopted the 1D Jeans equation. The adjustment of the model to equilibrium is illustrated in Fig. 2.2; the bottom left panel shows that thicknesses of both disks change as the system relaxes, increasing in the outer parts and decreasing in the inner parts – notice that the change in thickness is least over the radius range $2R_0 \lesssim R \lesssim 10R_0$, where the surface mass density is closest to its untapered value (dotted curves in Fig. 2.1). The changes, which are larger for the radially-hotter thick disk, result from the radial excursions of the particles, which may take them far from their initial radii for which the vertical velocity was set. However, neither the radial balance (top left panel) nor the vertical velocity dispersion (right panel) of the thick disk change

Table 2.1 Parameters of all the simulations from §§2 & 3

Sim.	Disk	f	$\frac{z_0}{R_0}$	$\frac{\sigma_R}{V_0}$	N	m	$\frac{\Delta z}{R_0}$	$\frac{\varepsilon}{R_0}$	Grid Size
M2	thin	0.5	0.4	0.283	1.2M	0, 2	0.1	0.15	120×128×243
	thick	0.05	1.2	0.567	1.8M				
T	thin	0.5	0.4	0.283	1.2M	0	0.1	0.15	120×128×243
	thick	0.05	1.2	0.567	1.8M				
M3	thin	0.3333	0.4	0.189	1.2M	0, 3	0.1	0.15	120×128×243
	thick	0.0333	1.2	0.378	1.8M				
M4	thin	0.25	0.4	0.142	1.2M	0, 4	0.1	0.15	120×128×243
	thick	0.025	1.2	0.283	1.8M				
M4b	thin	0.25	0.2	0.142	1.2M	0, 4	0.05	0.075	120×128×405
	thick	0.025	0.6	0.283	1.8M				
	massless thick	0	1.2	0.283	1.8M				
M2b	thin	0.5	0.4	0.283	480k	0, 2	0.1	0.15	75×80×625
	thick	0.05	1.2	0.567	240k				
	massless 1	0	0.5	0.567	240k				
	massless 2	0	0.6	0.567	240k				
	massless 3	0	0.7	0.567	240k				
	massless 4	0	0.8	0.567	240k				
	massless 5	0	1.6	0.567	240k				
	massless 6	0	2.0	0.567	240k				
	massless 7	0	2.4	0.567	240k				
M2c	thin	0.5	0.4	0.283	480k	0, 2	0.1	0.15	75×80×243
	thick	0.05	1.2	0.567	240k				
	massless 1	0	1.2	0.378	240k				
	massless 2	0	1.2	0.454	240k				
	massless 3	0	1.2	0.680	240k				
	massless 4	0	1.2	0.794	240k				
	massless 5	0	1.2	0.907	240k				
	massless 6	0	1.2	1.021	240k				
	massless 7	0	1.2	1.134	240k				
TK	thick	0.5	1.2	0.283	1.8M	0, 2	0.1	0.15	120×128×243
UC, UCB1, UCB2	thin	0.4	0.4	0.227	200k	≤8, ≠1	0.2	0.3	75×80×125
	thick	0.04	1.2	0.454	300k				

The first column gives the simulation designation. The next five columns give the properties of each disk: f is the mass fraction, z_0 its vertical scale height, σ_R is the nominal radial velocity dispersion, and N is the number of particles in the disk. The final four columns give m, the active sectoral harmonic(s), Δz the vertical spacing of the grid planes, ε the softening length, and the grid size in terms of the number of rings×spokes×planes. The "massless" disks of simulations M4b, M2b, and M2c describe massless thick disks composed of test particles. z_0, Δz, and ε are in terms of R_0, and σ_R is in terms of V_0. Simulations UC, UCB1, and UCB2 all have the same parameters listed in last two rows.
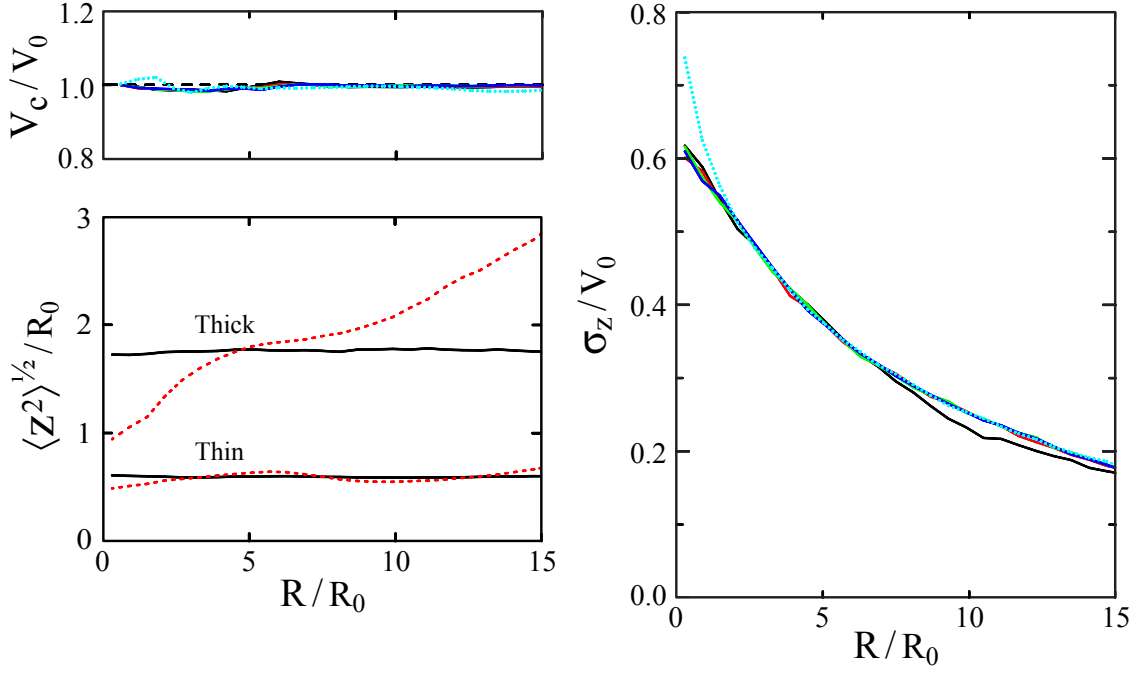
Figure 2.2 The circular velocity in disk midplane (top left) and vertical velocity dispersion of the thick disk particles (right) at five equally spaced times during simulation M2. The times, which include the initial and final moments of the simulation, are color coded in temporal order by solid black, red, green, blue, and dotted cyan respectively. The dashed horizontal line in the top left panel shows the theoretical circular velocity $V_0 = 1$. The bottom left panel shows the initial $\langle z^2 \rangle^{1/2}$ of the thin (bottom curves) and thick (top curves) disks (solid black) compared to that at $t = 32\tau_0$ (dashed red).

significantly from their initial values. After this initial relaxation from initial conditions, we do not observe any significant flaring. A negligibly small fraction ($< 1\%$) of particles escape from our grid by the end of the simulation, and most particle loss takes place as the model settles.

Following Sellwood & Binney (2002), we seed a vigorously unstable spiral mode by adding a Lorentzian groove in angular momentum to the DF of the thin disk only:

$$f(E, L_z) = f_0(E, L_z) \left[1 + \frac{\beta w_L^2}{(L_z - L_*)^2 + w_L^2} \right].$$

(2.6)

Here β, a negative quantity, is the depth of the groove, w_L is its width, and L_* is the angular momentum of the groove center. This change to the DF seeds a predictable spiral instability (Sellwood & Kahn 1991). The groove in the thin disk has the parameters $\beta = -0.9$, $w_L = 0.3 R_0 V_0$, and $L_* = 6.5 R_0 V_0$. We find that a deeper and wider groove is needed than that used by Sellwood & Binney (2002) in order to excite a strong spiral in our thickened disk.

Since a groove of this kind will provoke instabilities at many sectoral harmonics, m, we restrict disturbance forces from the particles to a single non-axisymmetric sectoral harmonic to prevent other modes from growing. Corotation for a global spiral mode excited by this groove is at a radius somewhat greater than L_*/V_0, where local theory would predict. A large-scale mode is not symmetric about the groove center due to the geometric variation of surface area with radius – an effect that is neglected in local theory. However, the radius of corotation approaches the local theory prediction for modes of smaller spatial scale, *i.e.* as $m \to \infty$.

As in SB02, we choose the circular velocity V_0 to be our unit of velocity, R_0 our unit of length, the time unit or dynamical time is $\tau_0 = \tau_0$, our mass unit is $M_0 = V_0^2 R_0/G$, and L_i is our unit of angular momentum. One possible scaling to physical units is to choose $R_0 = 0.75$ kpc, with $R_d = 4.0 R_0$ being the equivalent scale length of the thin disk, and $\tau_0 = 3.0$ Myr, leading to $V_0 = 244$ km s^{-1} and $M_0 = 1.04 \times 10^{10}$ M$_\odot$.

2.2.2 Numerical procedure

We use the 3D polar grid described in Sellwood & Valluri (1997) to determine the gravitational field of the particles. This "old-fashioned" method is not only well suited to the problem, but also has the advantage of being tens of times faster than the "modern" methods recently reviewed by Dehnen & Read (2011). We employ a grid having 120 rings, 128 spokes, and 243 vertical planes, and adopt the cubic spline softening rule recommended by Monaghan (1992), which yields the full attraction of a point mass at distances greater than two softening lengths (2ε). The Plummer rule used in SB02 is suited for razor-thin disks where it mimics the effect of disk thickness but, because it weakens inter-particle forces on all scales, it is unsuited for 3D simulations where disk thickness is already included in the particle distribution. The value of ε, given in Table 2.1, exceeds the vertical grid spacing in order to minimize the grid dependence of the inter-particle forces.

In the simulations described in §§2.3 & 2.4, we use quiet starts (Sellwood & Athanassoula 1986) for both disks to reduce the initial amplitude of the seeded unstable spiral mode far below that expected from shot noise. In 3D, this requires many image particles for each fundamental particle: we place two at each (R, ϕ, z) position with oppositely directed z-velocities and two more reflected about the midplane at the point $(R, \phi, -z)$. We then place images of these four particles at equal intervals in ϕ, each set having identical velocity components in cylindrical polar coordinates. For these simulations, the thin disk has 1,200,000 particles and the thick disk 1,800,000. All the particles in a single population have equal mass, but particle masses differ between populations in order to create the desired ratio of disk surface densities.

We evaluate forces from the particles at intervals of $0.02\tau_0$, and step forward some of the particles at each evaluation. Since the orbital periods of particles span a wide range, we integrate their motion when $R > 2R_0$ using longer time steps in a series of five zones with the step doubling in length for each factor 2 in radius (Sellwood 1985). We also subdivide the time step for particles within $R = 0.5R_0$ without updating forces, with further decreases by a factor of 2 for every factor of 2 decrease in radius (Shen & Sellwood 2004). Note that very few particles have $R < 0.5R_0$, which is well within the inner taper where the rigid

component of the force dominates. Tests with shorter time steps yielded similar results.

2.2.3   List of simulations

For convenience, we summarize the parameters of all the simulations presented in §§2 & 3 in Table 2.1. Simulation T is constrained to remain axisymmetric, while all those whose identifier begins with 'M' are highly controlled experiments designed to support a single spiral instability. We first present, in §2.3, a detailed description of M2, which supports a bisymmetric spiral, and briefly compare it to simulation T. Variants of M2, with many populations of test particles are presented in §2.3.4, while simulation TK, which has a thick disk only, is described in §2.3.5. Simulations that support a single spiral of higher angular periodicity are motivated and described in §2.4. The last three simulations in the Table, with identifier beginning with 'U', are uncontrolled experiments presented in §2.5 that explore the consequences of multiple spirals, with and without a bar.

2.3   A single bisymmetric spiral

Our first objective is to study radial migration in both the thick and thin disks due to a single spiral disturbance. We therefore present simulation M2, which is designed to support an isolated $m = 2$ spiral instability.

We measure

$$A_m(t) = 2\pi \int_{R_1}^{R_2} \Sigma(R, \phi, t) e^{im\phi} \, dR, \tag{2.7}$$

where $\Sigma(R, \phi, t)$ is the vertically-integrated mass surface density of the particles at time t, and we generally choose $R_1 = 1.5R_0$ and $R_2 = 19R_0$.

The top panel of Fig. 2.3 shows the time evolution of A_2/A_0, revealing that the mode grows exponentially, peaks, and then decays non-exponentially to a trough. The peak is 2.55 times higher than the minimum of the following trough. Continued evolution reveals that the amplitude rises again due to the growth of a secondary wave. In order to isolate the single initial spiral, we stop the simulation at the trough and compare quantities, such as the specific angular momenta of particles, at this final time with those at the initial time $t = 0.0\tau_0$. The bottom panel plots the same quantity from simulation T in which
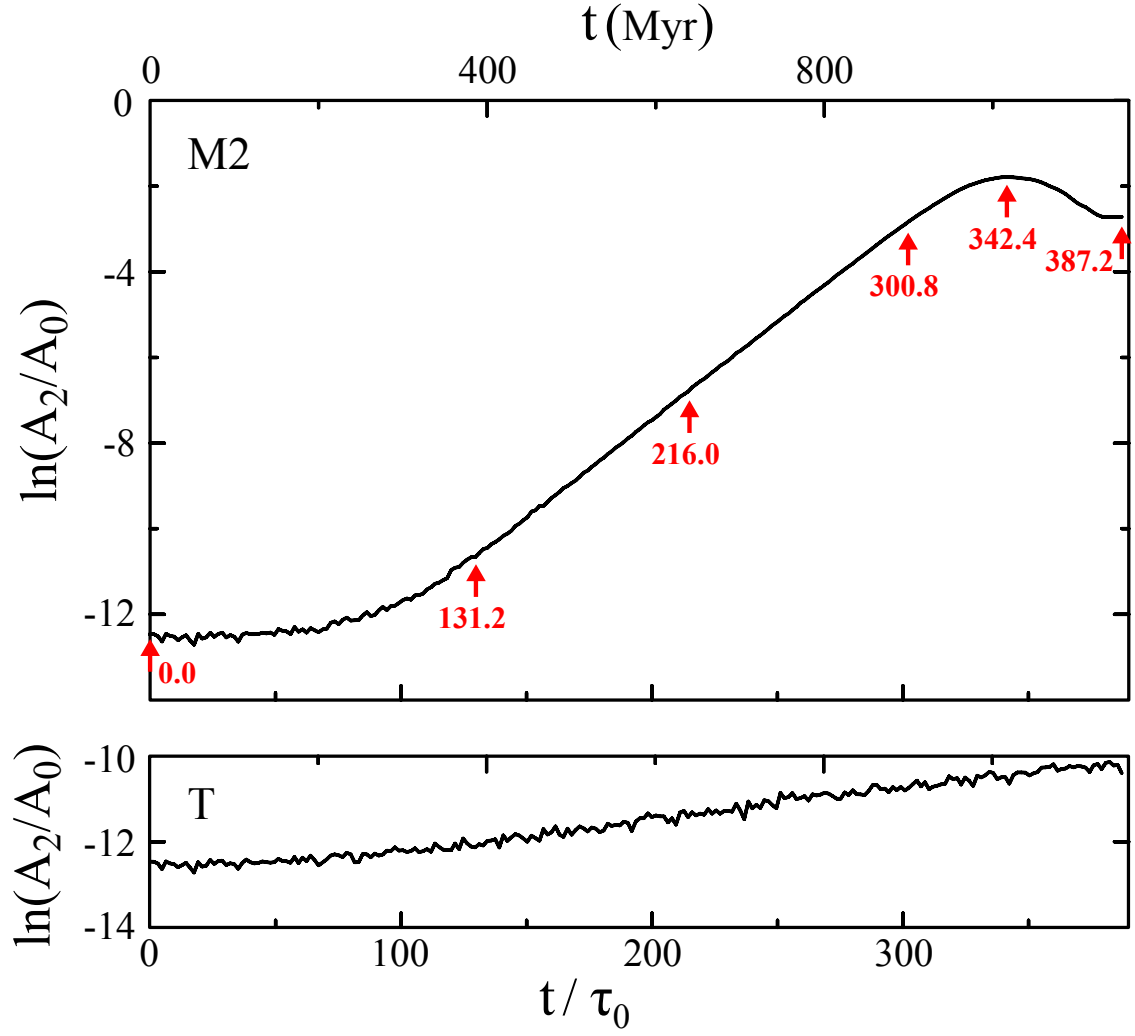
Figure 2.3 The time evolution of A_2/A_0 in simulations M2 (top) and T (bottom). Note the difference in the vertical scales. The numbered arrows in the top plot mark the six times of M2 at which the snapshots of the disks are shown in Fig. 2.4. The top axis shows time scaled to physical units using the adopted scaling at the end of §2.2.1.

Table 2.2 Measured values from fits to the spiral modes.

	m	$\Omega_p/\frac{V_0}{R_0}$	γ	$\frac{R_c}{R_0}$	$\left(\frac{A_m}{A_0}\right)_{\text{peak}}$	P/T	$t_p/\frac{R_0}{V_0}$, (Myr)
M2	2	0.138	0.0454	7.24	0.168	2.55	73.5 , 221
M3	3	0.147	0.0417	6.81	0.099	2.15	76.9 , 231
M4	4	0.150	0.0361	6.67	0.063	1.80	76.3 , 229
M4b	4	0.151	0.0465	6.63	0.083	3.07	81.3 , 244
M2b	2	0.138	0.0457	7.25	0.166	2.52	72.1 , 216
M2c	2	0.138	0.0456	7.25	0.166	2.52	74.4 , 223
TK	2	0.135	0.0180	7.40	0.064	1.68	149 , 446

The second column gives the angular periodicity of the spiral or the greatest active sectoral harmonic m in the simulation. The next three columns give the pattern speed Ω_p, growth rate γ, and the corotation radius R_c of the spiral obtained by fitting it's exponential growth using the method in Sellwood & Athanassoula (1986). The next two columns provide the spiral's peak amplitude and $\left(\frac{A_m}{A_0}\right)_{\text{peak}} / \left(\frac{A_m}{A_0}\right)_{\text{trough}}$. And the last column gives the duration of the peak amplitude, which we measure between the moment the amplitude reaches the trough and the moment preceding the peak at which the amplitude is at the same level as the trough amplitude. The second number in the peak duration column is the time in physical units using the adopted scaling at the end of §2.2.1.

disturbance forces from the particles were restricted to the axisymmetric ($m = 0$) term; the very slow rise is caused by the gradual degradation of the quiet start.

Fig. 2.4 shows snapshots of the thin and thick disks of M2 at six different times of the simulation that are marked by the red arrows in Fig. 2.3.

We find the period of exponential growth can be very well fitted by a single mode, using the apparatus described in Sellwood & Athanassoula (1986). Table 2.2 reports the fitted pattern speed Ω_p and growth rate γ, together with other parameters of the spiral in M2. Furthermore, the non-linear evolution visible in Fig. 2.4 shows no evidence of a bar. Thus, the selected time period of the simulation M2 presents the opportunity to study radial migration due to a single, well isolated spiral wave. Note that the spiral pattern makes a full rotation every $2\pi/\Omega_p \simeq 45.5\tau_0$.

2.3.1 Angular momentum changes

Fig. 2.5 shows the change in the specific z-angular momenta ΔL_z of the particles in the thin disk (top) and the thick disk (middle) of simulation M2 against their initial L_z. The
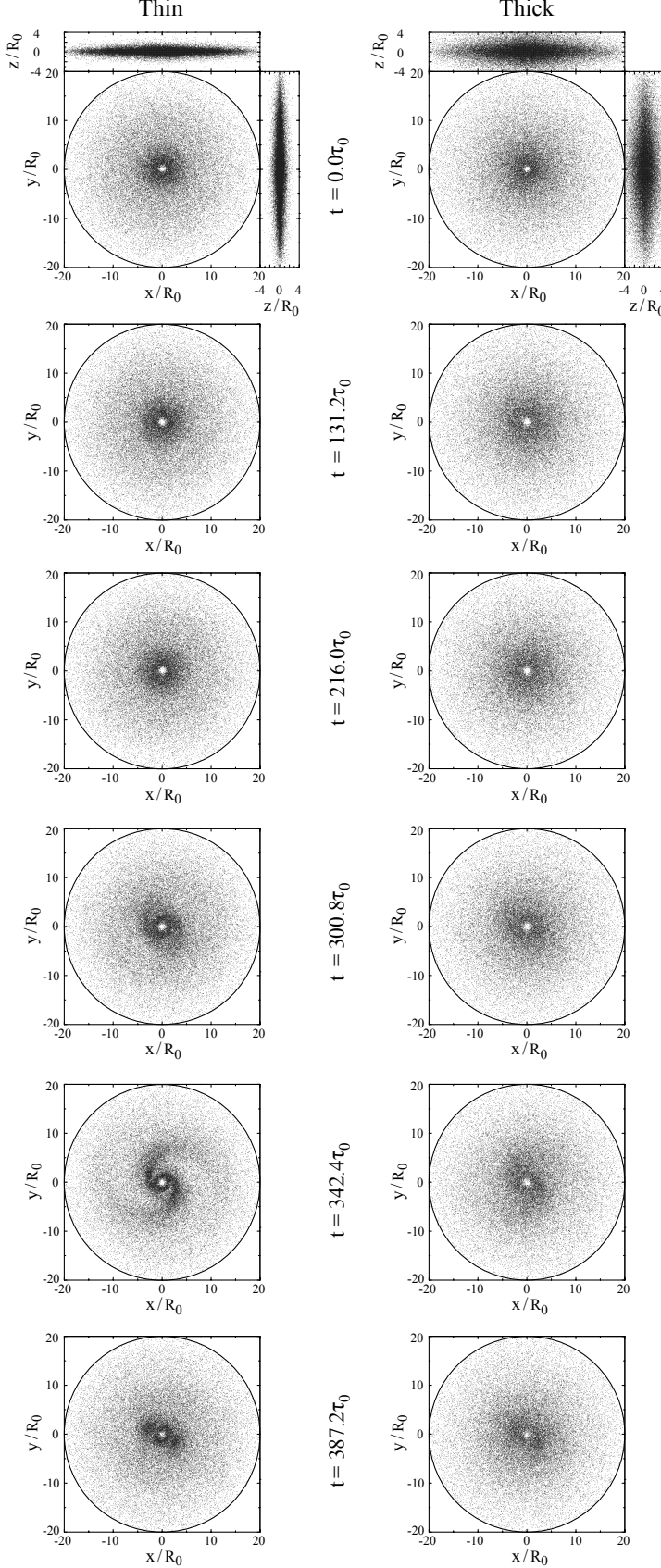
Figure 2.4 Snapshots of the thin (left column) and thick (right column) disks in simulation M2 at the six times marked in Fig. 2.3. One in every 24 particles is plotted for the thin disk, and one in every 36 for the thick. The side views are shown only at the initial time because they change little throughout the simulation.
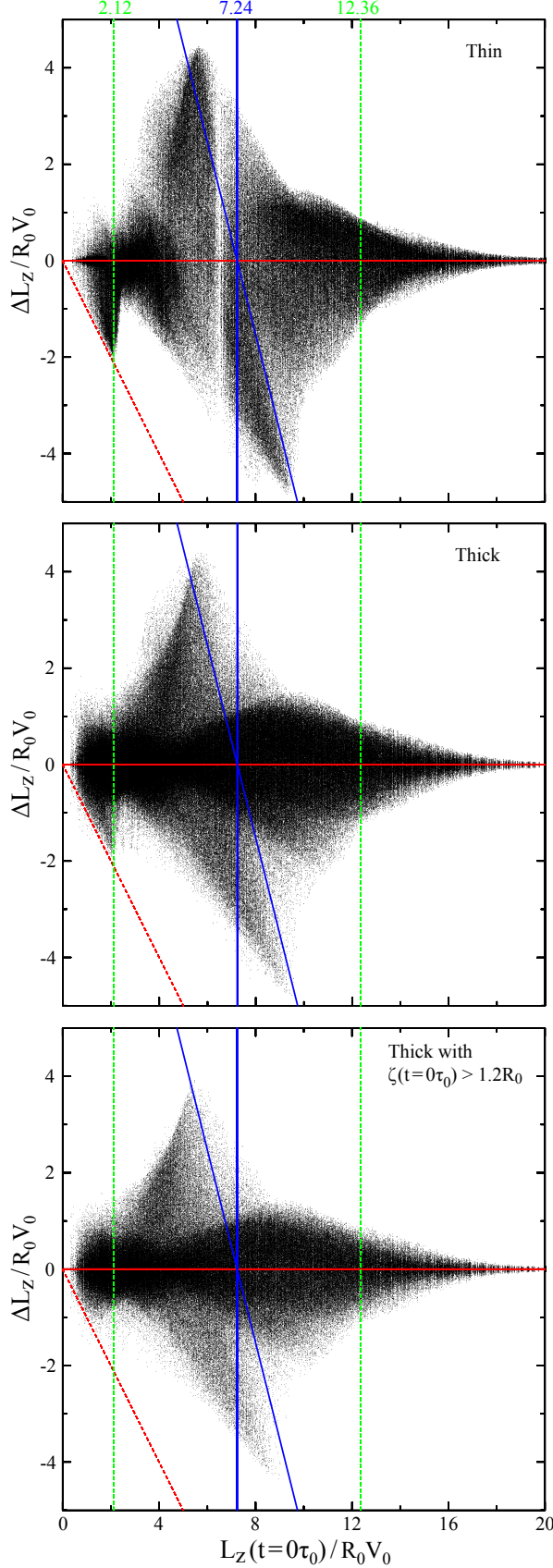
Figure 2.5 Angular momentum changes of particles in M2 as a function of their initial angular momenta. The top panel is for thin disk particles, the middle for all thick disk particles, and the bottom for thick disk particles having notional vertical amplitude $\zeta > 1.2R_0$. The horizontal red line denotes zero change. The vertical lines mark the Lindblad resonances (dashed green) and corotation (solid blue). The solid blue line with a slope of -2 illustrates the locus of particles whose changes would be symmetric about corotation. The dashed red line of slope -1 shows the $\Delta L_z = -L_z(t = 0)$ locus below which particles end up on retrograde orbits.

deficiency of particles at $L_z(t = 0) = L_* = 6.5R_0V_0$ in the top panel is due to the groove in the thin disk. The vertical lines show the locations of the corotation (solid blue) and the Lindblad resonances (dashed green) for nearly circular orbits.

The maximum changes in angular momentum occur near corotation, and lie close to the solid blues line of slope -2; these particles cross corotation, in both directions, to about the same radial distance away from it as they were initially. As for the razor-thin disk, we find that large angular momentum changes occur only around the time that the spiral saturates, for reasons explained by Sellwood & Binney (2002). While many particles near the inner Lindblad resonance lose angular momentum, only a tiny fraction end up on retrograde orbits. Note also that $\langle (\Delta L_z)^2 \rangle^{1/2} \approx 9.0 \times 10^{-6} R_0 V_0$ in simulation T, where non-axisymmetric forces were eliminated, showing that changes in L_z due to orbit integration and noise errors are tiny in comparison to those caused by the spiral.

For each particle, we determine the initial value of

$$Z = \frac{1}{2}v_z^2 + \frac{1}{2}\nu^2 z^2, \tag{2.8}$$

where v_z is the vertical velocity component at distance z from the midplane and ν is the vertical frequency measured in the midplane at the particle's initial radius R. For particles whose vertical and radial oscillations are small enough to satisfy the epicycle approximation, $Z = E_{z,\mathrm{epi}}$ the energy of its vertical oscillation; the vertical potential is roughly harmonic for $|z| \lesssim 0.4R_0$. Even though the epicycle approximation is not satisfied for the majority of particles, we compute an initial notional vertical amplitude

$$\zeta = \left(\frac{2Z}{\nu^2} \right)^{1/2}, \tag{2.9}$$

for them all. The value of ζ defined in this way, i.e. at the initial moment only, yields a convenient approximate ranking of the vertical oscillation amplitudes of the particles, although it is clear that in most cases $\zeta < z_{\mathrm{max}}$, the maximum height a particle may reach. Note that since each disk component in our models has an initial thickness that is independent of radius, the distribution of ζ is independent of $L_z(t = 0)$.

Notice from Fig. 2.5 that changes for the thick disk particles are only slightly smaller
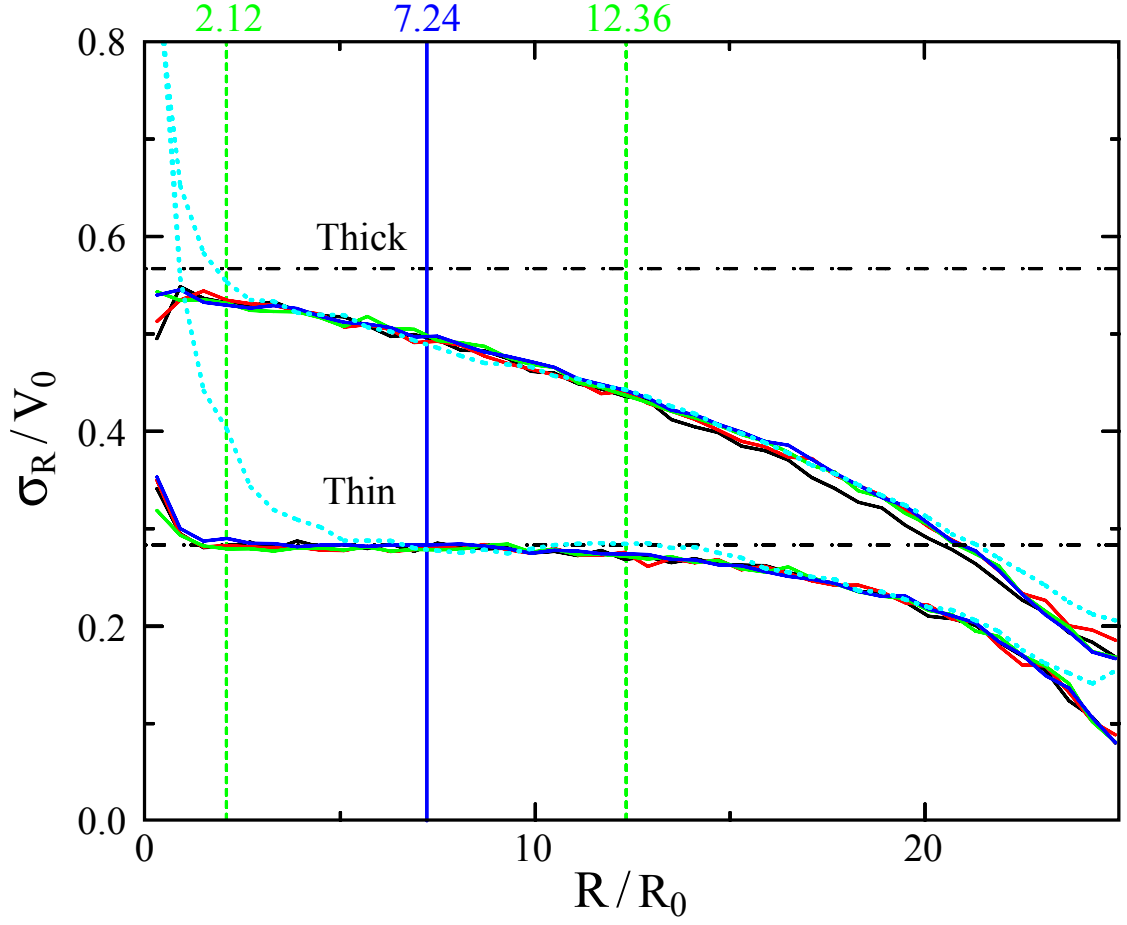
Figure 2.6 The radial variations of σ_R in the thin (bottom curves) and thick (top curves) disks of M2 at the same five different times as used in the top left and right panels of Fig. 2.2 with the same line color and style coding. The horizontal dot-dashed curves show the theoretical initial dispersions from the untapered disks, while the vertical lines mark the principal resonances of the spiral, color and style coded as in Fig. 2.5.

than those for thin disk particles. In order to emphasize this point, the bottom panel displays only those thick disk particles for which $\zeta > 1.2R_0$, or one scale height of the thick disk, revealing that even for these particles changes can be almost as large as those in the thin disk.

Fig. 2.6 shows the evolution of the radial velocity dispersion for the thin and thick disks. As expected (SB02), the large angular momentum changes near corotation cause little heating. Some heating occurs near the Lindblad resonances, and is greater near the inner resonance, again as expected.

2.3.2 Distribution of angular momentum change

Table 2.3 lists the root mean square, maximum positive, and maximum negative changes in angular momentum for both all the particles and only those that satisfy $\zeta > z_0$ in each disk.

Fig. 2.7 shows the 5th and 95th percentile values of the changes in angular momentum as a function of initial notional vertical amplitude, ζ (eq. 2.9), using bin widths of $0.3R_0$. The affect of radial migration seems to decrease almost linearly with increasing ζ.

Radial migration should also be weaker for particles having larger radial oscillations or epicycles of large amplitude. As reasoned by Sellwood & Binney (2002), particles on more eccentric orbits cannot hold station with a steadily rotating spiral, because their angular velocities vary significantly as they oscillate radially. Fig. 2.8, which is for only those particles in the angular momentum range $2.5R_0V_0 \leq L_z(t = 64) \leq 10.0R_0V_0$, confirms that the largest angular momentum changes occur among particles having the least eccentric orbits. [II] It shows angular momentum changes from, and eccentricities at, time $t = 64\tau_0$, which is after the model has settled from its mild initial imbalance, but before any substantial angular momentum changes have occurred. We define eccentricity as $\epsilon = (R_a - R_p)/(R_a + R_p)$, in which R_a and R_p are respectively the initial apocenter and pericenter distance of the orbit of a particle having the same L_z, but whose motion is confined to the midplane of the axisymmetric potential.

[II] The energy cut-off we apply (see after eq. 4) eliminates the most eccentric orbits from this plot.
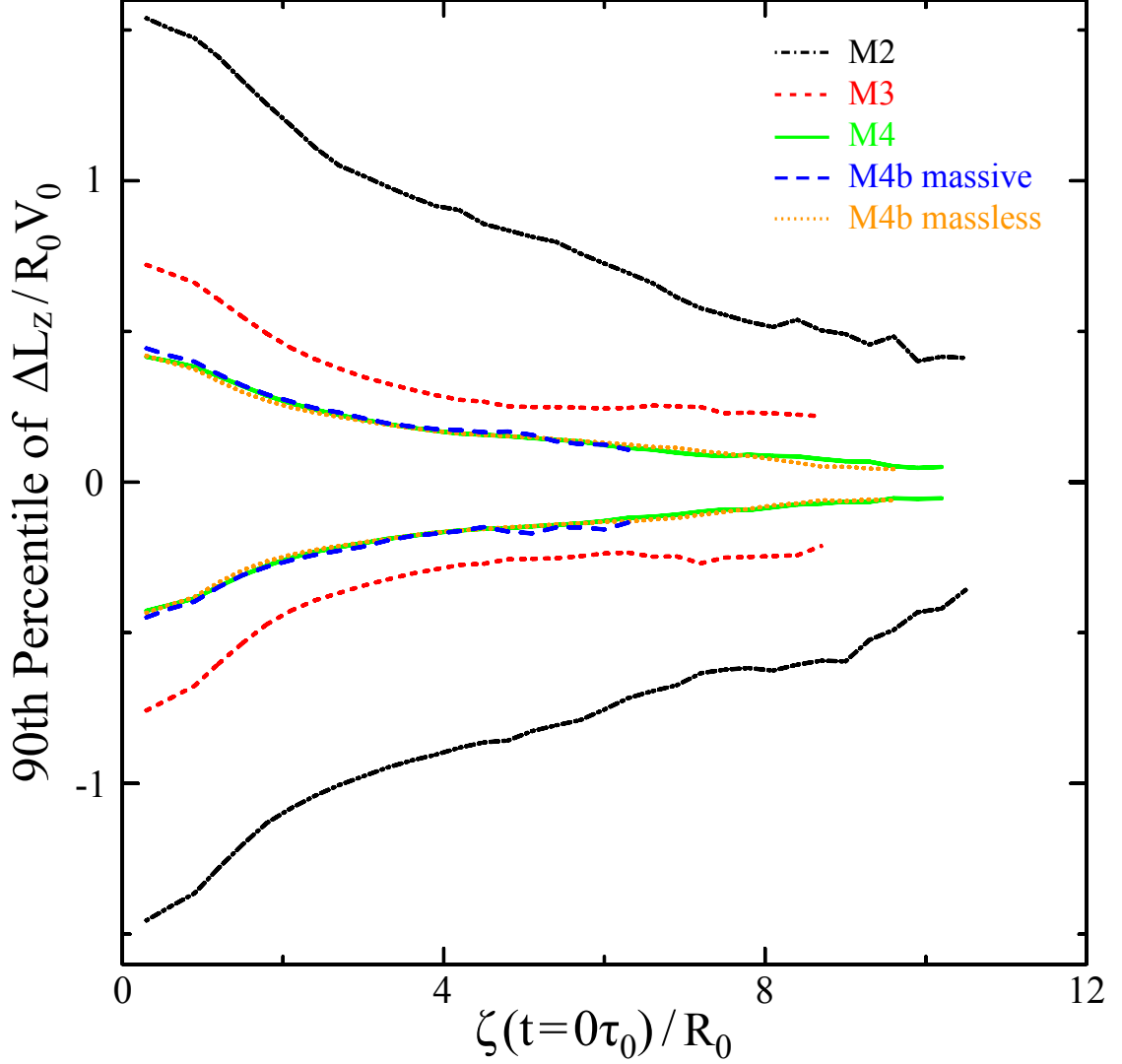
Figure 2.7 The 5th and 95th percentiles of the angular momentum changes in the thick disks of simulations M2 (dot-dashed black), M3 (short-dashed red), M4 (solid green), the massive thick disk of M4b (long-dashed blue), and the massless thick disk of M4b (dotted orange) as a function of notional vertical amplitude ζ. Although we have smoothed the curves, the rising noise with increasing ζ is caused by the decrease in the number of particles per bin. The curves stop when the number of particles per bin drops below twenty.
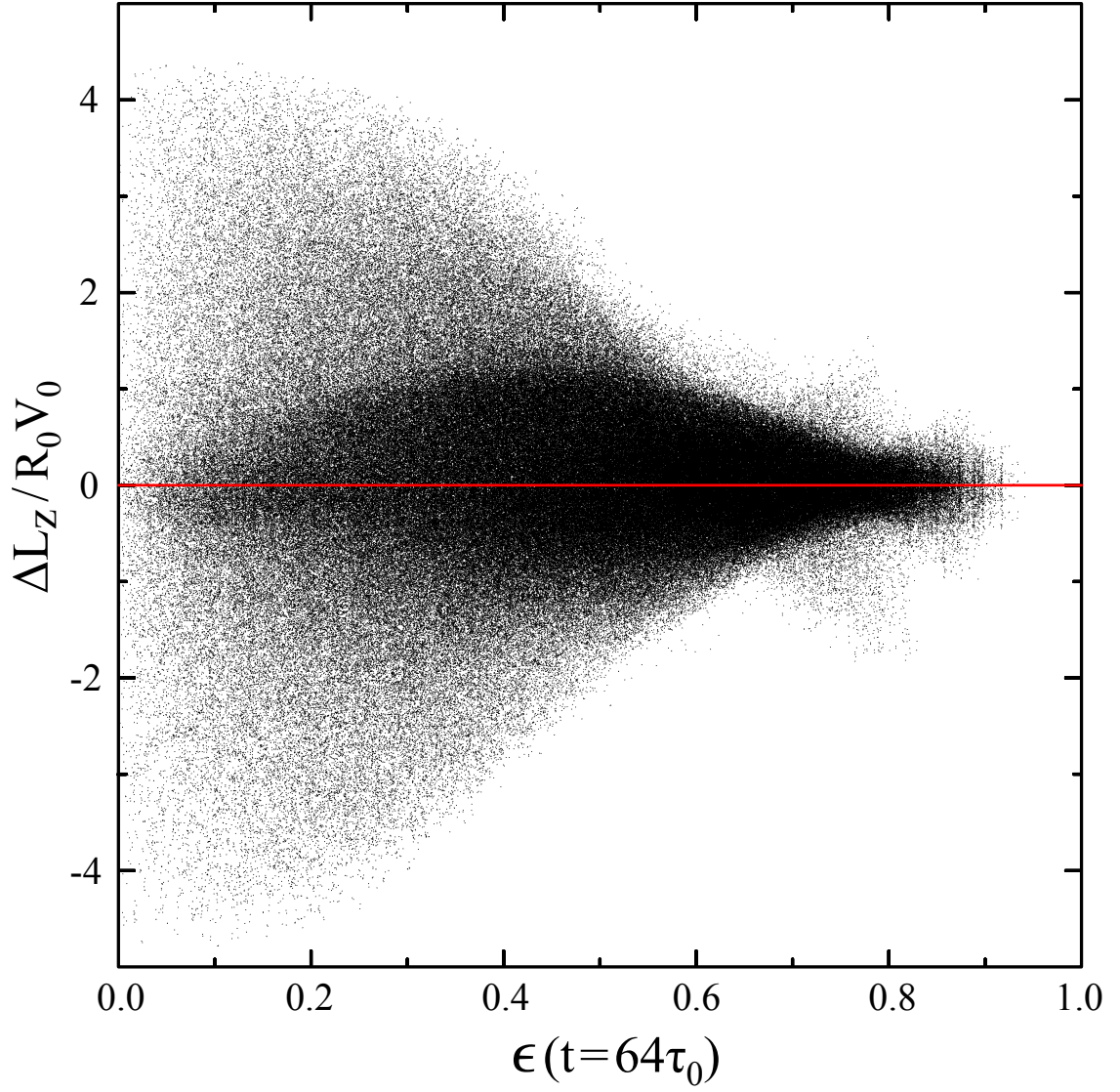
Figure 2.8 Angular momentum changes of thick disk particles between the final time and $t = 64\tau_0$ having $2.5R_0V_0 \leq L_z(t = 64) \leq 10.0R_0V_0$ in simulation M2 as a function of their eccentricities at $t = 64\tau_0$. The plot for the thin disk is quite similar. The red horizontal line shows zero angular momentum change.

Table 2.3 Changes in angular momentum resulting from the spirals and bar.

	Disk	$\frac{\left\langle(\Delta L_z)^2\right\rangle^{1/2}}{R_0V_0}$	$\frac{\text{Max }\Delta L_z}{R_0V_0}$	$\frac{\text{Max -}\Delta L_z}{R_0V_0}$
M2	thin	1.59 , 1.56	4.44 , 4.37	-4.83 , -4.79
	thick	0.97 , 0.85	4.38 , 3.91	-4.78 , -4.46
M3	thin	0.92 , 0.89	2.79 , 2.72	-2.67 , -2.61
	thick	0.54 , 0.43	2.76 , 2.22	-2.60 , -2.12
M4	thin	0.62 , 0.60	2.03 , 1.97	-2.11 , -2.02
	thick	0.37 , 0.30	1.93 , 1.65	-1.99 , -1.59
M4b	thin	0.80 , 0.78	2.25 , 2.18	-2.17 , -2.08
	thick	0.47 , 0.40	2.21 , 1.84	-2.09 , -1.83
	massless	0.38 , 0.27	2.17 , 1.43	-2.05 , -1.48
M2b	thin	1.58 , 1.54	4.45 , 4.36	-4.57 , -4.43
	thick	0.95 , 0.84	4.33 , 3.76	-4.52 , -4.02
	massless 1	1.08 , 1.06	4.42 , 4.32	-4.43 , -4.43
	massless 2	1.06 , 1.02	4.41 , 4.19	-4.54 , -4.22
	massless 3	1.04 , 0.98	4.41 , 4.08	-4.47 , -4.27
	massless 4	1.02 , 0.95	4.48 , 4.11	-4.43 , -4.15
	massless 5	0.89 , 0.72	4.35 , 3.46	-4.40 , -3.67
	massless 6	0.83 , 0.64	4.39 , 3.11	-4.29 , -3.64
	massless 7	0.79 , 0.58	4.05 , 3.06	-4.30 , -3.37
M2c	thin	1.57 , 1.53	4.46 , 4.35	-4.58 , -4.44
	thick	0.96 , 0.85	4.33 , 3.76	-4.50 , -4.03
	massless 1	1.19 , 1.06	4.37 , 3.75	-4.42 , -4.11
	massless 2	1.08 , 0.95	4.37 , 3.81	-4.46 , -4.01
	massless 3	0.86 , 0.76	4.37 , 3.66	-4.49 , -4.09
	massless 4	0.80 , 0.72	4.35 , 3.70	-4.28 , -4.09
	massless 5	0.75 , 0.68	4.22 , 3.79	-4.33 , -3.89
	massless 6	0.72 , 0.65	4.18 , 3.56	-4.51 , -3.81
	massless 7	0.69 , 0.63	4.21 , 3.51	-4.29 , -3.81
TK	thick	0.78 , 0.75	3.37 , 3.26	-2.88 , -2.77
UC	thin	2.65 , 2.31	13.97 , 11.60	-10.43 , -9.48
	thick	1.95 , 1.75	12.71 , 10.33	-10.15 , -10.04
UCB1	thin	3.15 , 2.76	16.42 , 12.41	-13.22 , -11.12
	thick	2.34 , 2.10	16.00 , 13.80	-12.00 , -10.92
UCB2	thin	3.53 , 3.46	19.23 , 19.14	-16.74 , -16.74
	thick	2.54 , 2.28	19.31 , 17.40	-15.83 , -13.63

The first values in the third, fourth, and fifth columns give the rms, maximum positive, and maximum negative changes in L_z respectively. We calculate these for all the particles except those that escaped the grid for which the initial L_z lies in an interval of the spiral's main influence around its corotation. This interval, in values in terms of R_0V_0, is $[2.5, 10]$ for simulations M2, M2b, and M2c, $[4.5, 9.5]$ for M3, $[5.0, 8.5]$ for M4 and M4b, and $[3.5, 9.5]$ for TK. We do not confine $L_z(t = 0)$ to such an interval for simulations UC, UCB1, and UCB2 since the influence of their spirals and bar span almost the entire range. The second values in the last three columns give the same results but only for particles having $\zeta > z_0$.

2.3.3 Effect of radial migration on vertical oscillations

We have just shown how the particles' angular momentum changes vary with initial amplitude of vertical motion. Here, we present the converse: how the vertical oscillations are affected by the radial excursions.

Since the notional amplitude of vertical motion ζ (eq. 2.9) is accurate only in the epicycle approximation, we determine a particle's actual maximum vertical excursion, $z_{\max}$, by integrating its motion in a frozen, azimuthally-averaged potential for many radial periods. We do this twice for each particle in simulation M2, at time $t = 64\tau_0$ starting from the particle's phase space coordinates in the frozen potential at that moment and again at the final time $t = 387.2\tau_0$.

Fig. 2.9 shows that, on average, the vertical excursions of particles increase for those that move radially outwards and decrease for those that move inwards. This is expected, because restoring forces to the mid-plane are weaker at larger radii. For both disks, the mean (solid green) and median (dashed blue) curves show a roughly constant $\Delta z_{\max}$ for a wide range of ΔL_z. For the thick disk, this constant $\Delta z_{\max}$ is about twice as great as that for the thin.

While the large majority of the particles lie in the contoured region, the outliers exhibit significant substructure. The dense group of points near a line of slope of -1 in the second quadrant are particles with initial home radii within and near the inner $m = 2$ vertical resonance[III], which lies at the radius $2.23R_0$, not far from the radial inner Lindblad resonance at $2.12R_0$. Usually $\nu \gg \kappa$, which causes vertical resonances to be found significantly farther from corotation than the radial resonances, but in our case the inner taper reduces the inner surface density so that $\nu \sim \kappa$ in this part of the disk. Thus, these particles are scattered vertically at the inner vertical resonance at the same time as they lose angular momentum at the radial inner Lindblad resonance. Another outlying group can be seen in the first quadrant, with large $\Delta z_{\max}$ for small ΔL_z; these particles have quite eccentric initial orbits that have particular radial phases just before the spiral saturates. Either they are at their pericenters and lie near corotation just trailing either spiral arm, or they are at their

---

[III]Vertical resonances occur when $m(\Omega - \Omega_p) = \pm\nu$

apocenters and surround the outer ends of the spiral arms. Being at these special locations when the spiral wave is strongest, gives them instantaneous angular frequencies about the center that cause them to experience more nearly steady, and not oscillatory, torques from the perturbation, leading to some angular momentum gain. Thus these particles move onto even more eccentric orbits and their increased z_{max} occurs at their new larger apocenters.

2.3.4 Effects of disk thickness and radial velocity dispersion

Our somewhat surprising finding from simulation M2 is that angular momentum changes in the thick disk are only slightly smaller than those in the thin, and also in the razor-thin disk of SB02. Despite the fact that thick disk particles both rise to greater z heights and have larger epicycles, on average, than do thin disk particles, we observe only a mild decrease in their response to spiral forcing. This finding suggests that the potential variations of a spiral having a large spatial scale, such as the $m = 2$ spiral mode in simulation M2, couple well to particles having large vertical motions and epicycle sizes.

To provide more detailed information about how the extent of angular momentum changes vary with disk thickness, we added seven test particle populations to some simulations. In M2b, all test particle populations have the same initial radial velocity dispersion as the massive thick disks, but have scale heights in the range $0.5R_0 \leq z_0 \leq 2.4R_0$. Simulation, M2c, employs seven test particle populations having the same scale height $(z_0 = 1.2R_0)$ as the massive thick disk, but with differing σ_R.

Being test particles, they do not affect the dynamics of the spiral instability, but merely respond to the potential variations that arise from the instability in the massive components. These simulations have identically the same physical properties as M2 but lower numerical resolution as summarized in Table 2.1; the reduced numerical resolution remains adequate since the fitted spiral mode is little changed from that in simulation M2 (Table 2.2).

Variations of $\langle (\Delta L_z)^2 \rangle^{1/2}$ with both disk thickness, at fixed radial velocity dispersion, and of radial dispersion at fixed thickness, are displayed in Fig. 2.10. The decrease is somewhat more rapid in subpopulations of particles that start with a notional vertical amplitude $\zeta > z_0$, as seems reasonable. The fitted line indicates that $\langle (\Delta L_z)^2 \rangle^{1/2}$ decays approximately exponentially with disk thickness with a scale that can be related to theory
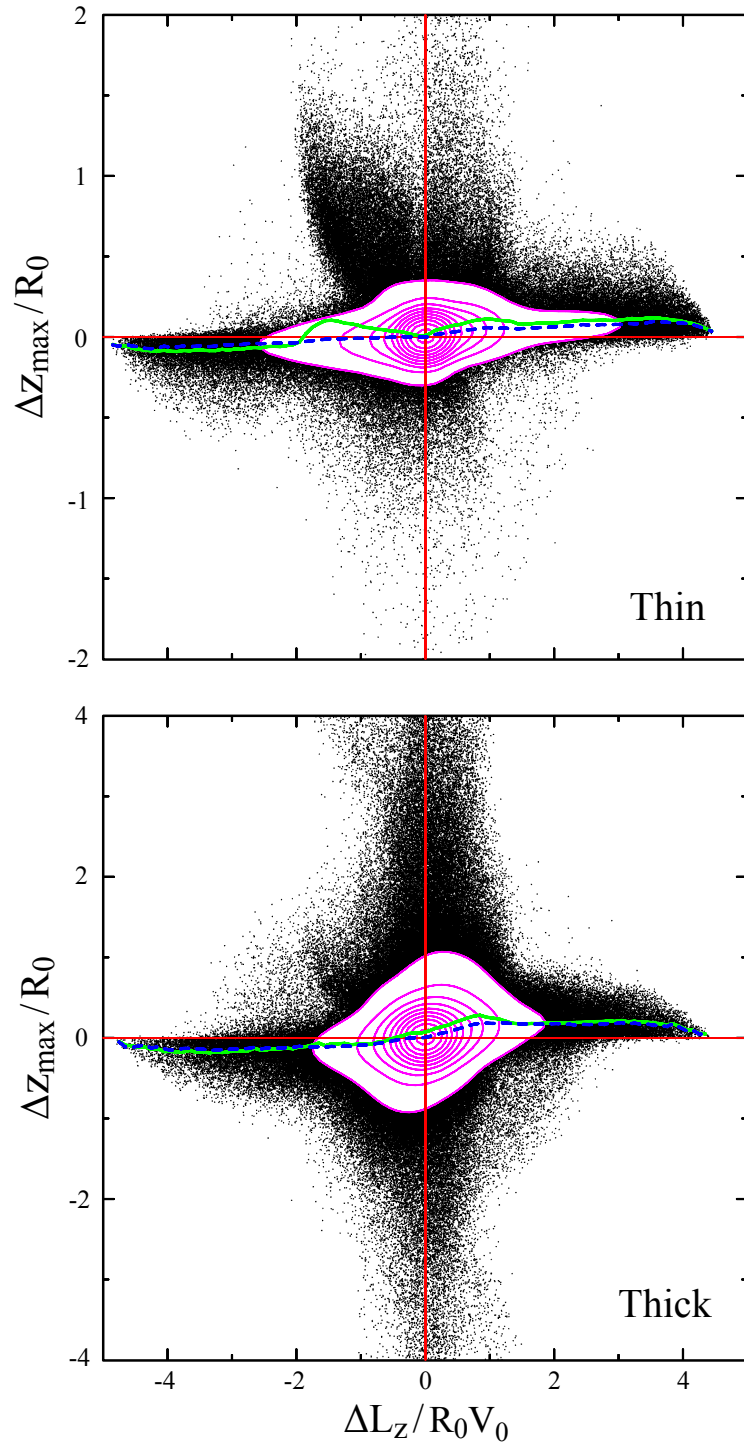
Figure 2.9 Changes in maximum vertical excursions of particles in the thin (top) and thick (bottom) disks of M2 versus changes in their angular momenta. Contours are linearly spaced in number density and we plot only those points that lie outside the lowest contour. The mean (solid green) and median (dashed blue) show systematic variations, as expected. Note that the vertical scales differ in the two plots.
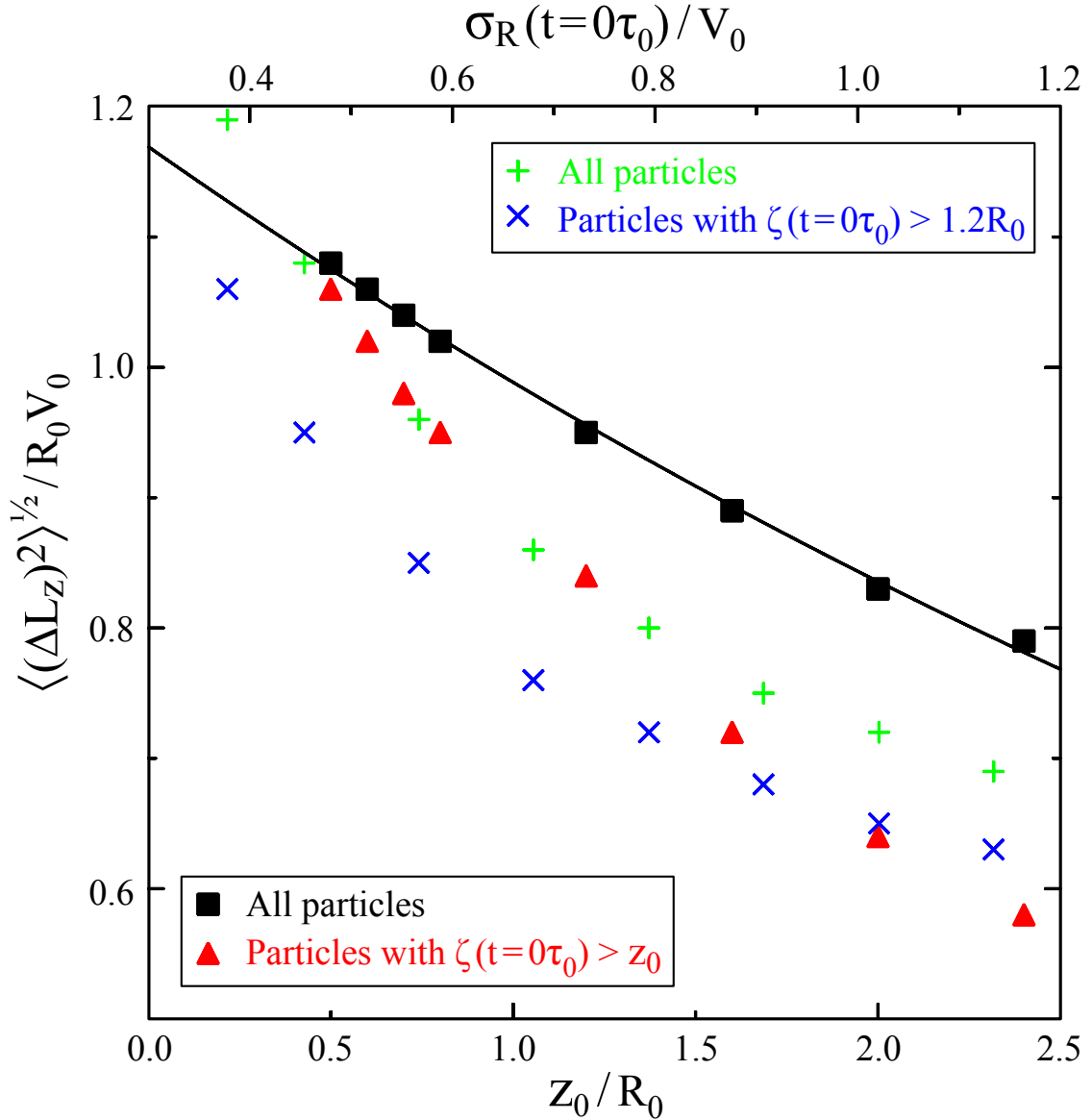
Figure 2.10 The filled symbols show $\left\langle (\Delta L_z)^2 \right\rangle^{1/2}$ as a function of vertical thickness (bottom axis) of particle populations of simulation M2b. The black squares are for all the particles in the angular momentum range $2.5 R_0 V_0 \leq L_z(t = 0) \leq 10.0 R_0 V_0$, while the red triangles are for only those particles having $\zeta > z_0$. The line is a least-squares fit to the black squares of the form $\left\langle (\Delta L_z)^2 \right\rangle^{1/2} \propto e^{-z_0/5.95 R_0}$. The green plus symbols show the variation of $\left\langle (\Delta L_z)^2 \right\rangle^{1/2}$ with initial radial velocity dispersion (top axis) of all the particles in the same $L_z(t = 0)$ range from populations in simulation M2c. The blue crosses are for only those with $\zeta > z_0 = 1.2 R_0$.

– see §2.4.3. Table 2.3 gives both the plotted root mean square, as well as the maximum positive, and maximum negative ΔL_z for all the particles of each population and separately for those with $\zeta > z_0$ of each disk.

We caution that the information in Table 2.3 and in Fig. 2.10 quantifies how the *responsiveness* of a test particle population scales when subject to a fixed perturbation. Self-consistent spiral perturbations may differ in strength, spatial scale, and/or time dependence causing quite different angular momentum changes.

2.3.5 Thick disk only

For completeness, we also present simulation TK, which has a single, half-mass active disk with a substantial thickness. We inserted the same initial groove, and restricted forces to $m = 2$ only.

It is interesting that a groove in the thick disk still creates a spiral instability, but one that grows less rapidly and saturates at a lower amplitude than we found in M2. As a consequence, the spread in $\left\langle (\Delta L_z)^2 \right\rangle^{1/2}$ is about 1/2 as large as in M2. Again we find that the radial migration is reduced by increasing disk thickness, but not inhibited entirely.

2.4 Other simulations

The potential of a plane wave disturbance in a thin sheet having a sinusoidal variation of surface density Σ_a in the x-direction is

$$\Phi_a(x, z) = -\frac{2\pi G \Sigma_a}{|k|} e^{ikx} e^{-|kz|} \tag{2.10}$$

where k is the wavenumber (BT08, eq. 5.161). The exponential decay away from the disk plane is steeper for waves of smaller spatial scale, *i.e.* larger $|k|$. While spirals are not simple plane waves in a razor-thin sheet, this formula suggests that we should expect radial migration to be weakened more by disk thickness for spirals of smaller spatial scale or higher angular periodicity – note that the azimuthal wavenumber, $k_\phi = m/R$. The simulations in this section study the effect of changing this parameter.

2.4.1 Spirals of different angular periodicities

We wish to create spiral disturbances that are similar to that in M2, but have higher angular periodicities. Since we expect migration to depend not only on the spatial scale relative to the disk thickness, but also the peak amplitude, Σ_a, and perhaps also the time dependence, we try to keep as many factors unchanged as possible.

The mechanics of the instability seeded by a groove depends strongly on the supporting response of the surrounding disk (Sellwood & Kahn 1991), which in turn, according to local theory, depends on the vigor of the swing amplifier (Toomre 1981). Thus to generate a similar spiral disturbance with $m > 2$, we need to hold the key parameters X and Q at similar values. For an m-armed disturbance in a thin, single component Mestel disk with active mass fraction f, the locally-defined parameter

$$X = \frac{2}{fm} \tag{2.11}$$

is independent of radius. We therefore scale the active mass fractions in both components as $f \propto m^{-1}$ – recall that we used a half-mass disk for $m = 2$. In order to preserve the same Q value (eq. 2.3), the radial velocity dispersion of the particles also has to be reduced as $\sigma_R \propto f$.

Simulations M3 and M4 therefore have lower surface densities and smaller velocity dispersions in order to support similarly growing spiral modes of sectoral harmonic $m = 3$ and 4 respectively. A further simulation M4b is described below. These models are all seeded with a groove of the same form (eq. 2.6) and parameters as that in M2.

Note that the instability typically extends between the Lindblad resonances, which move closer to corotation as m is increased. In the Mestel disk, the radial extent of the mode varies as

$$\frac{R_{\mathrm{OLR}}}{R_{\mathrm{ILR}}} = \frac{m + \sqrt{2}}{m - \sqrt{2}}, \tag{2.12}$$

i.e. $R_{\mathrm{OLR}}/R_{\mathrm{ILR}} \approx 5.8$, 2.8 & 2.1, for $m = 2$, 3 & 4 respectively. Since we have also decreased the in-plane random motion in proportion to the surface density decrease, the decreased size of the in-plane epicycles somewhat compensates for the smaller scale of the

mode, although the ratio is not exactly preserved.

2.4.2   Results for $m > 2$

Table 2.2 gives our estimates of the spiral properties in each simulation; uncertainties in the measured frequencies are typically $\lesssim 2\%$ (Sellwood & Athanassoula 1986). The pattern speeds of these instabilities do not change much with m, except that we find the radius of corotation lies closer to the groove center $L_*/V_0 = 6.5R_0$, as expected. The table also gives the time during which the amplitude of the wave is equal to or greater than that at the post-peak trough, which again does not vary much with angular periodicity. However, both the growth rates and the peak amplitudes of the modes decrease from M2, to M3 and M4.

Table 2.3 includes the root mean square, maximum positive, and maximum negative angular momentum changes for M3, M4, and M4b, measured in each case to the moment at which A_m passes through the first minimum after the mode has saturated. Comparison with M2 reveals that increasing m causes a roughly proportionate decrease in the angular momentum changes, in part because the saturation amplitude is lower, but perhaps also because the spatial scale is reduced. Note that again some thick disk particles in both M3 and M4 have ΔL_z values almost as large as the greatest in the thin disk, as was also the case for M2.

Fig. 2.7 shows 5th and 95th percentile values of ΔL_z versus initial notional vertical amplitude ζ for simulations M3, M4, and M4b. Compared to the curve of M2, the ΔL_z values are smaller for greater m – *i.e.* the extent of radial mixing is substantially lessened. Note that this difference could have a variety of causes, such as the lower limiting amplitude of the mode, or possibly the different growth rate of the mode, and/or the different disk thickness relative to the spatial scale of the mode.

This last factor is one we are able to eliminate. The thickness of the disks of simulations M2, M3, and M4 were held fixed as we increased m and reduced the surface density. In order to eliminate a change in the ratio of disk thickness to spatial scale of the mode, we ran a further simulation M4b with the same in-plane parameters as in M4, but with half the disk thickness. We also halved the gravity softening length and the vertical spacing of the grid planes.

This change restores the growth-rate of the mode in run M4b to a value quite comparable to that in simulation M2 (Table 2.2). The saturation amplitude, while larger than in simulation M4, is still about half that in M2. In addition, we added a test particle population to simulation M4b that has parameters identical to those of the massive thick disk, including σ_R or q, except its vertical scale height z_0 is that of the thick disk of M2, M3, and M4. Again as expected, Table 2.3 reveals that $\left\langle (\Delta L_z)^2 \right\rangle^{1/2}$ is substantially lower in the massless disk than in the thinner, massive disk.

2.4.3 Comparison with theory

In order to make sense of these results, we here compare with the theoretical picture developed by Sellwood & Binney (2002).

First, we eliminate the possibility that the spiral in the simulations with higher m is "on" for too long for optimal migration. Sellwood & Binney (2002) argue that efficient mixing by the spiral requires the duration of the peak amplitude be less than half the period of a horseshoe orbit, so that each particle experiences only a single scattering. They show that the minimum period of a horseshoe orbit varies as $|\Psi_0|^{-1/2}$, where the potential amplitude of the spiral perturbation at corotation varies with the spiral density amplitude, Σ_a, and sectoral harmonic as $|\Psi_0| \propto \Sigma_a/m$ (eq. 2.10). Thus the weaker density amplitude that we find with higher m implies that the minimum periods of the horseshoe orbits are greater, and the condition for efficient mixing is more strongly fulfilled for $m > 2$.

Theory also suggests that an m-dependence of the peak amplitude is unavoidable if the spiral saturates due to the onset of many horseshoe orbits, as was argued in SB02. In their notation, orbits librate – *i.e.* are horseshoes – when $E_p < p^2$, where the frequency $p \propto m|\Psi_0|^{1/2}$. Since $|\Psi_0| \propto \Sigma_a/m$ (eq. 2.10), we see that $p^2 \propto m\Sigma_a$, suggesting that as m increases, horseshoe orbits become important at a lower peak density. Comparing M2 with M4b, we find (Table 2.2) the relative limiting amplitudes $\Sigma_a \propto m^{-1}$, which is consistent with the idea that the spiral instability saturates when the importance of horseshoe orbits reaches very nearly the same level. The fixed thickness and softening length used in M2, M3 and M4 disproportionately weakens the potential of the spiral as m rises, and spoils this exact scaling.

Note also that both $\left\langle (\Delta L_z)^2 \right\rangle^{1/2}$ and the extreme values measured from M4b are almost exactly half those in M2, which is also consistent with the horseshoe orbit theory developed by Sellwood & Binney (2002). Since they showed that the maximum $\Delta L_z \propto |\Psi_0|^{1/2}$, the relations in the previous paragraph require $\Delta L_{z,\mathrm{max}} \propto m^{-1}$ as we observe. As the rms value also scales in the same way, it would seem the entire distribution of ΔL_z scales with m in the same way. Again, the constant disk thickness prevents this prediction from working perfectly for M3 and M4.

We stress that this scaling holds because we took some care to ensure the key dynamical properties of the disk were adjusted appropriately. Spirals in a disk having a different responsiveness would have both a different growth rate and probably also peak amplitude, and the behavior would not have manifested a simple m-dependence.

Finally, we motivate the exponential fit to the variation of $\left\langle (\Delta L_z)^2 \right\rangle^{1/2}$ with z_0, for the same $m = 2$ spiral disturbance. We have already shown that $\left\langle (\Delta L_z)^2 \right\rangle^{1/2} \propto |\Psi_0|^{1/2}$, and have argued that the spiral potential decays away from the mid-plane as $e^{-|kz|}$ (eq. 2.10), with $k_\phi = m/R$. Naïvely, we could set $z = z_0$, $k = k_\phi = m/R$, $m = 2$, and $R = R_c$, since angular momentum changes are centered on corotation, leading to $\left\langle (\Delta L_z)^2 \right\rangle^{1/2} \propto e^{-z_0/R_c}$. The fitted scale is $5.95 R_0$, which is somewhat smaller than $R_c = 7.24 R_0$. The dominant cause of this discrepancy is probably that spiral is not a plane wave, curvature is important for $m = 2$, and that its wavenumber is larger than k_ϕ because the spiral ridges are inclined to the radial direction; we should therefore expect the potential to decay away from the mid-plane rather more rapidly, in the sense that we measure.

We conclude that angular momentum changes scale with spiral amplitude in the manner predicted in SB02 and, furthermore, the limiting amplitude itself is determined by their theory. The variation with disk thickness is also in the sense expected from the theory, but the quantitative prediction is not exact.

2.5 Unconstrained Simulations

Having studied at length the effects of a single spiral wave, we now wish to illustrate the effects of multiple spirals. We present three simulations, UC, UCB1, and UCB2, that have

no initial groove and the initial positions of the particles are random (*i.e.* not a quiet start) since we wish spirals to develop quickly from random fluctuations. We include gravitational disturbance forces from all sectoral harmonics $0 \leq m \leq 8$, except $m = 1$, which we omit in order to avoid imbalanced forces from a possibly asymmetric distribution of particles in a rigid halo with a fixed center.

All the many simulations of this type that we have run have ultimately developed a strong bar at the center. We here compare radial migration in three separate cases: simulation UC avoids a bar for a long period and supports many transient spirals, while simulations UCB1 and UCB2 have identical numerical parameters but form a bar quite early. In all three cases, the combined thin and thick disks have a smaller active mass fraction, $f = 0.44$, compared with $f = 0.55$ for simulation M2. A smaller active mass and a larger gravitational softening length help to delay bar formation but also weaken the $m = 2$ spiral amplitudes somewhat. The numerical parameters of these simulations are also listed in Table 2.1. Since bar formation in these models is stochastic (*e.g.* Sellwood & Debattista 2009), the different bar-formation times simply arise from different initial random seeds.

2.5.1   Multiple spirals only

The black curve in Fig. 2.11 shows the evolution of A_2/A_0 in simulation UC. The spiral amplitudes rise to the point at which significant particle scattering begins by $t \sim 1{,}500\tau_0$ and we present the behavior up to time $3{,}500\tau_0$ shortly before a bar begins to form. The period $1{,}500\tau_0 < t < 3{,}500\tau_0$ during which particles are scattered by spiral activity corresponds to ~ 6.0 Gyr with our adopted scaling.

Fig. 2.12 illustrates the $m = 2$ power spectrum of disturbances. Each horizontally extended peak indicates a spiral of a particular pattern speed. Some 20 transient spirals of significant amplitude occur during this period spanning a wide range of angular frequencies and corotation radii.

Since there are numerous disturbances with well scattered Lindblad resonances, random motion rises generally over the disk, as reported in Fig. 2.13, in contrast to Fig. 2.6 which shows the localized heating at the ILR of the single spiral case.
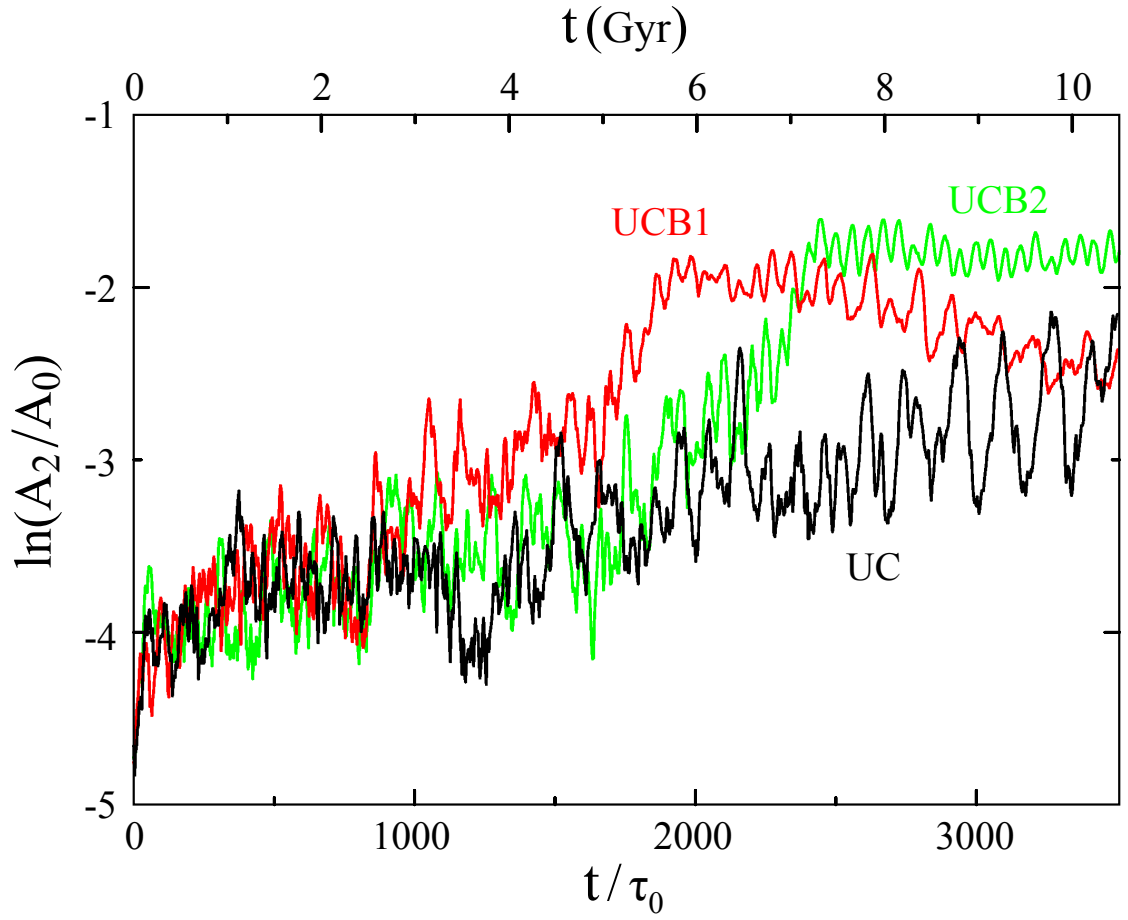
Figure 2.11 The time evolution of A_2/A_0 in simulations UC (black), UCB1 (red), and UCB2 (green). The top axis shows time scaled to physical units using the adopted scaling.
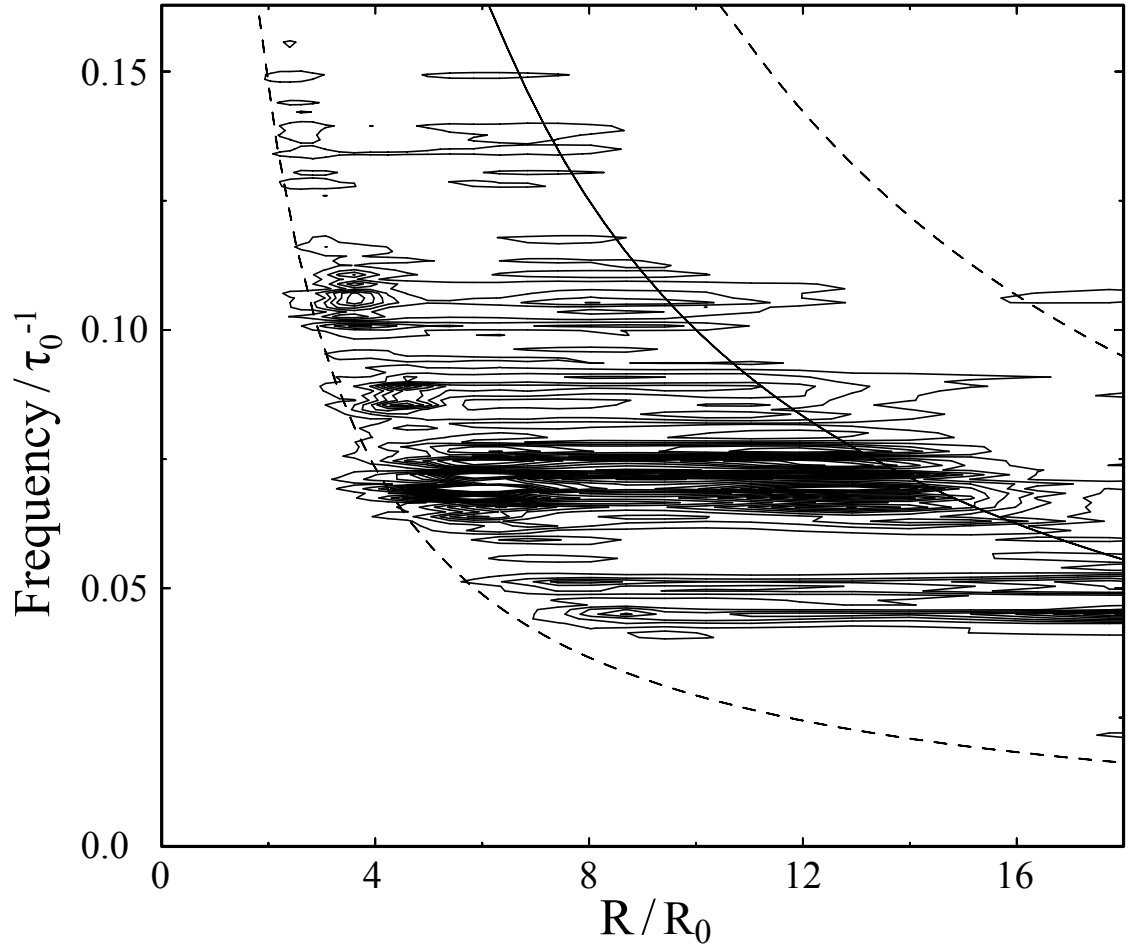
Figure 2.12 The power spectrum of $m = 2$ density variations in simulation UC. The solid curve indicates the radius of corotation for the given frequency, while the dashed curves show the radii of the Lindblad resonances.
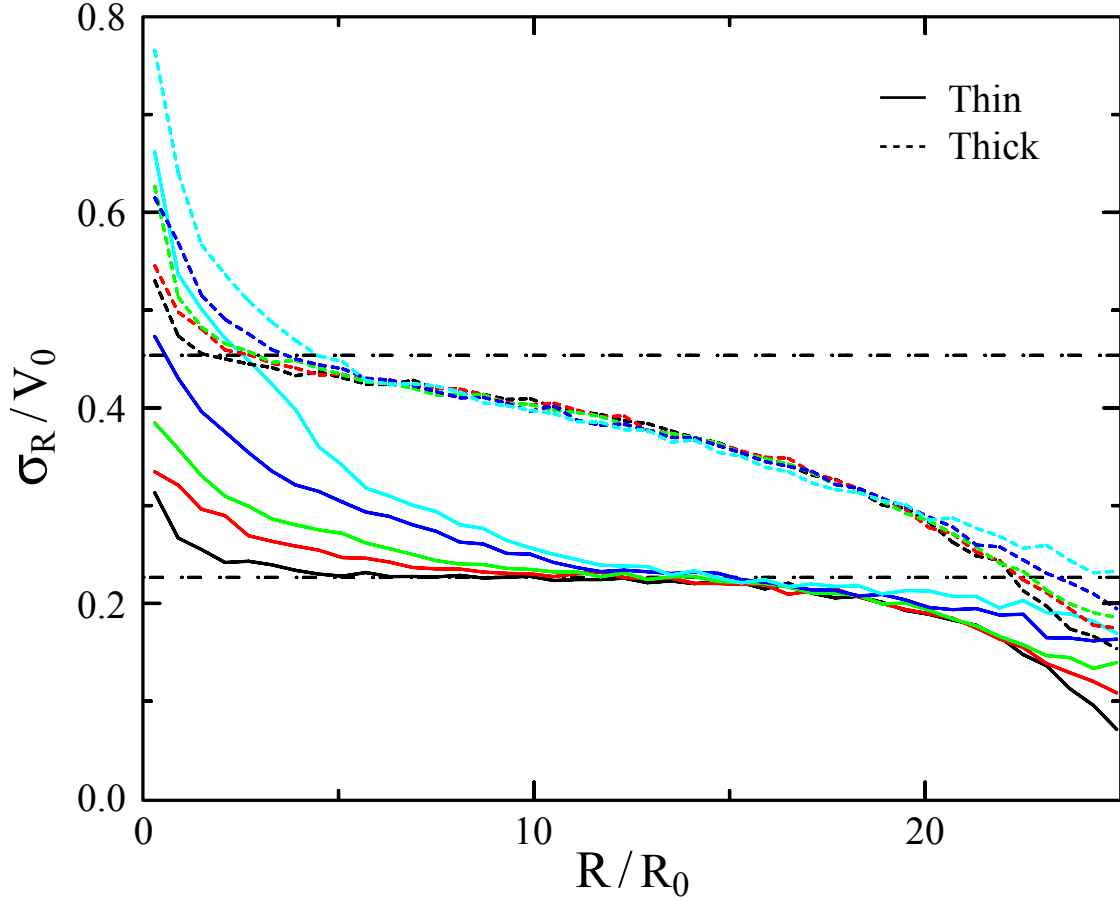
Figure 2.13 Radial variations of σ_R in simulation UC for the thin (solid) and thick (dashed) disks. The curves are drawn at equal time intervals and σ_R rises monotonically in the inner and outer disks.

The larger changes in L_z than those for the single spiral case are evident from the dot-dashed black curves of Fig. 2.14, which show the 5th and 95th percentiles of ΔL_z versus initial notional vertical amplitude ζ. Although the shapes of these curves are similar to those in Fig. 2.7, they are asymmetric about zero indicating that gains are larger than losses.

The angular momentum changes illustrated in Fig. 2.15 reflect mostly the effects of the latest spirals that developed in the simulation in each $L_z(t = 0)$ region. Contours of changes to the distribution of home radii for the particles (dotted black and solid green in Fig. 2.16) reveal that particles from all initial radii can move to new home radii, but that the changes are greatest around the mid range of initial radii where corotation resonances are more likely. Some 0.003% of the particles in the thin disk and 0.03% in the thick end
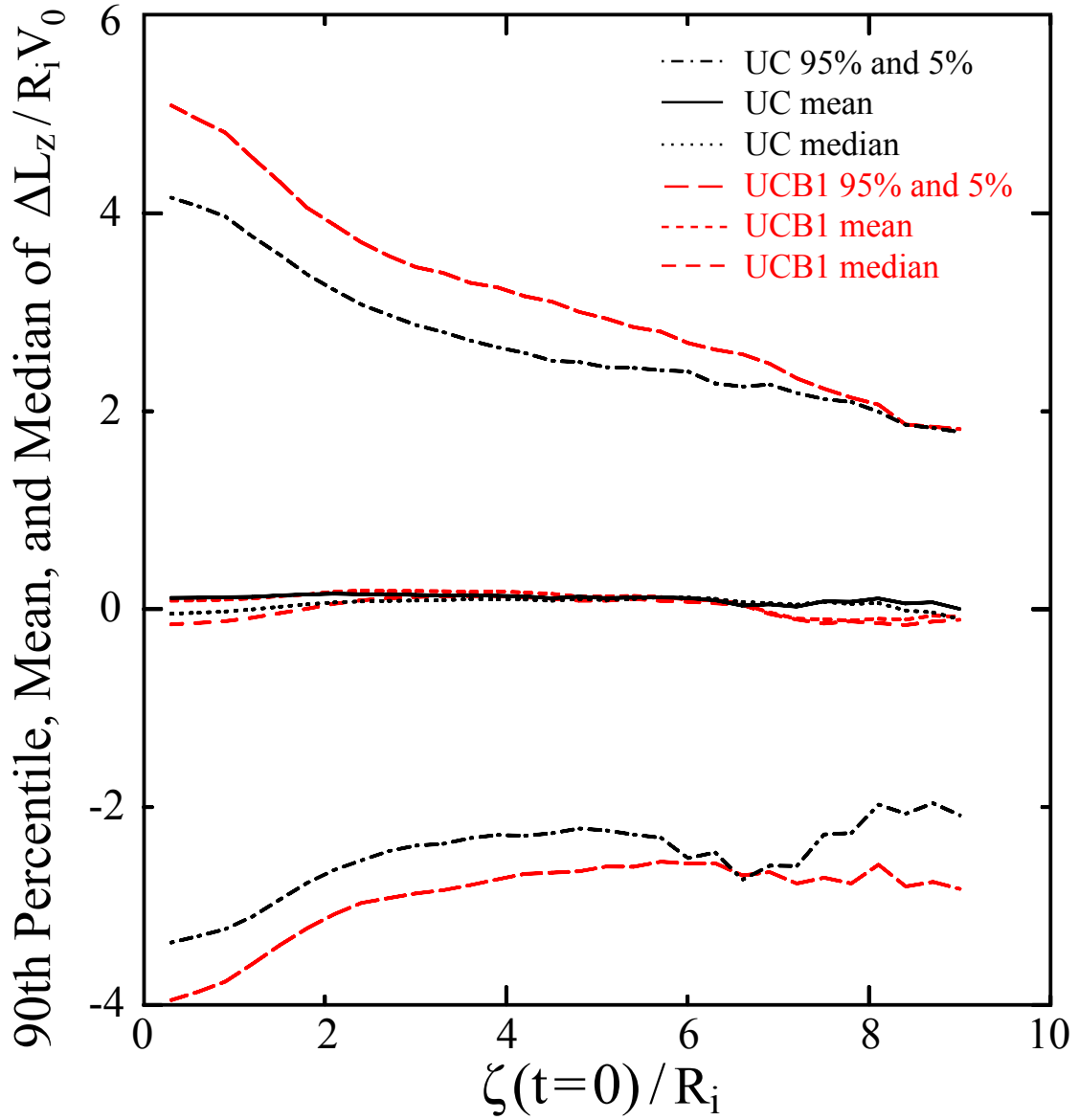
Figure 2.14 Same as Fig. 2.7 for simulations UC (dot-dashed black) and UCB1 (long-dashed red). The solid black and short-dashed red curves show the average angular momentum changes for UC and UCB1 respectively, and the dotted black and medium-dashed red ones show the median changes.

up on retrograde orbits.

Taken together with the results from the single spiral simulations described above, we again find that the changes in angular momenta and home radii are almost as great in the thick disk as in the thin. That is, radial migration is weakened only slightly by disk thickness.

The top row of Fig. 2.17 shows changes in the UC particles' maximum vertical excursions versus changes in their angular momenta. We find that, on average, $z_{\max}$ increases except for the greatest losses in angular momentum. This is different from the single spiral case, in which the contours and the mean and median curves are centered on the origin (Fig. 2.9). This overall extra increase in vertical amplitude probably comes from the net heating by vertical resonances that the multiple transient spirals induce by the end of the simulation. Nevertheless, the trend of the mean and median with ΔL_z remains as in M2. An exception is again the group of points along the slope of -1 in the second quadrant. It is much more pronounced for the thin disk than in M2. The particles contributing to this feature are still initially from the inner region of the disk, but this region is more extended in UC since the inner vertical resonances occur at various radii for the numerous transient spirals. As in M2, changes in $z_{\max}$ remain about twice as great for the thick disk particles as for those of the thin for the same ΔL_z.

Although the scale height of outward migrating particles does increase somewhat, as expected, the changes are not substantial enough to cause the thickness of outward migrating thin-disk particles to approach the scale height of the thick disk. The changes in the vertical motion of inward migrating particles are more minor than those for outward migrators. Thus we do not observe much of a tendency in our models for evolution to cause a significant degree of blurring between the separate populations.

2.5.2 Multiple spirals with a bar

We here study radial migration in two simulations, UCB1 and UCB2, that formed bars at an early stage of their evolution and compare them with simulation UC that did not form a bar for a long period. As noted in the introduction, it has long been known that bar formation causes some of the largest changes to the distribution of angular momentum within a disk.
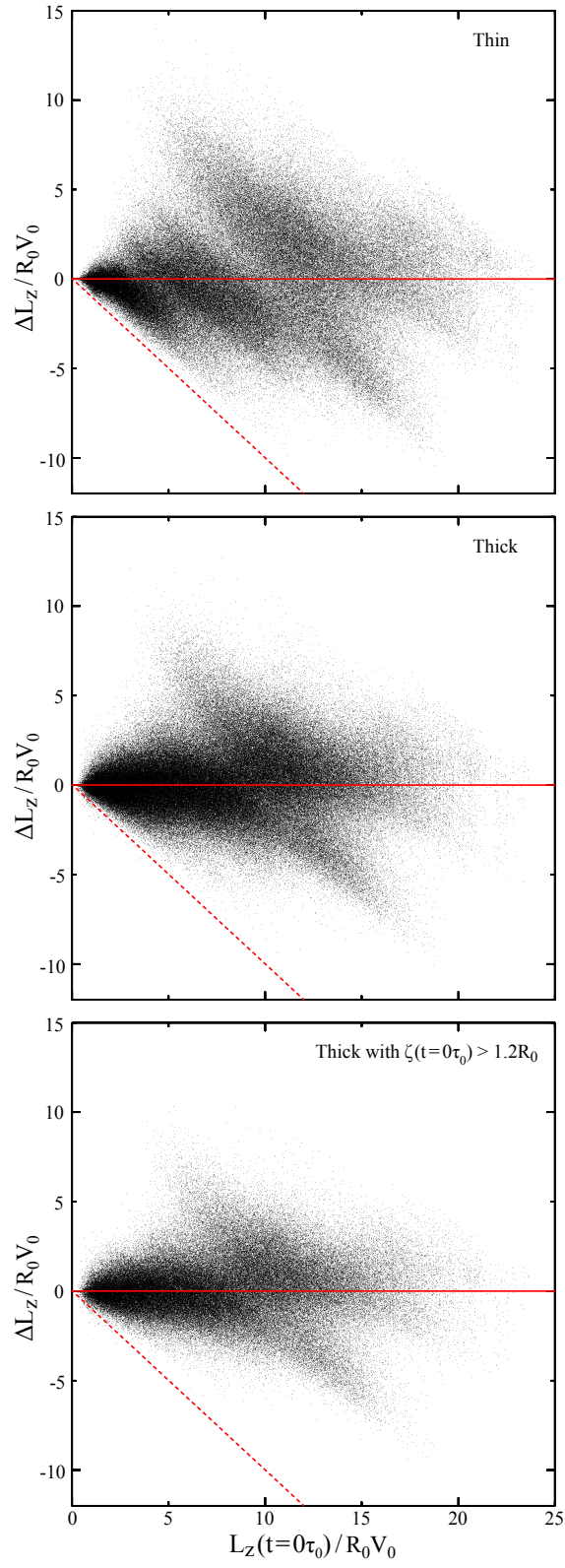
Figure 2.15 Same as Fig. 2.5 for simulation UC.
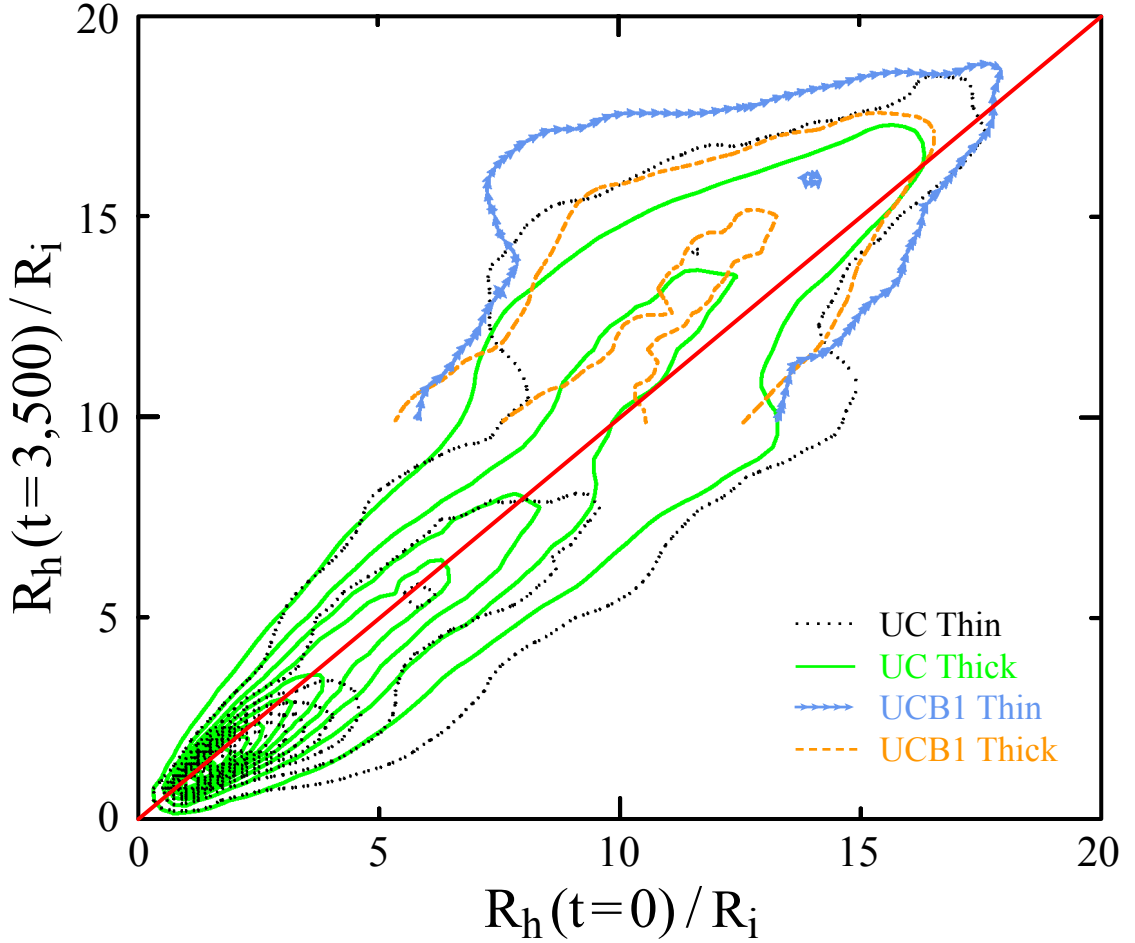
Figure 2.16 The distributions of final home radii versus initial home radii for all the particles in simulation UC. The particle density in this plane is estimated using an adaptive kernel, the dotted black and solid green contours represent the thin and thick disks respectively, and the red line shows zero change in R_{home}. Contour levels are chosen every 10% of the thick disk's maximum value from 5% to 95% for both thin and thick disks. The arrow light blue and dashed orange contours represent the same for the thin and thick disks of UCB1 respectively. The region inside the bar ($R_{\mathrm{home}}(t = 3500) < 10R_0$) is omitted.
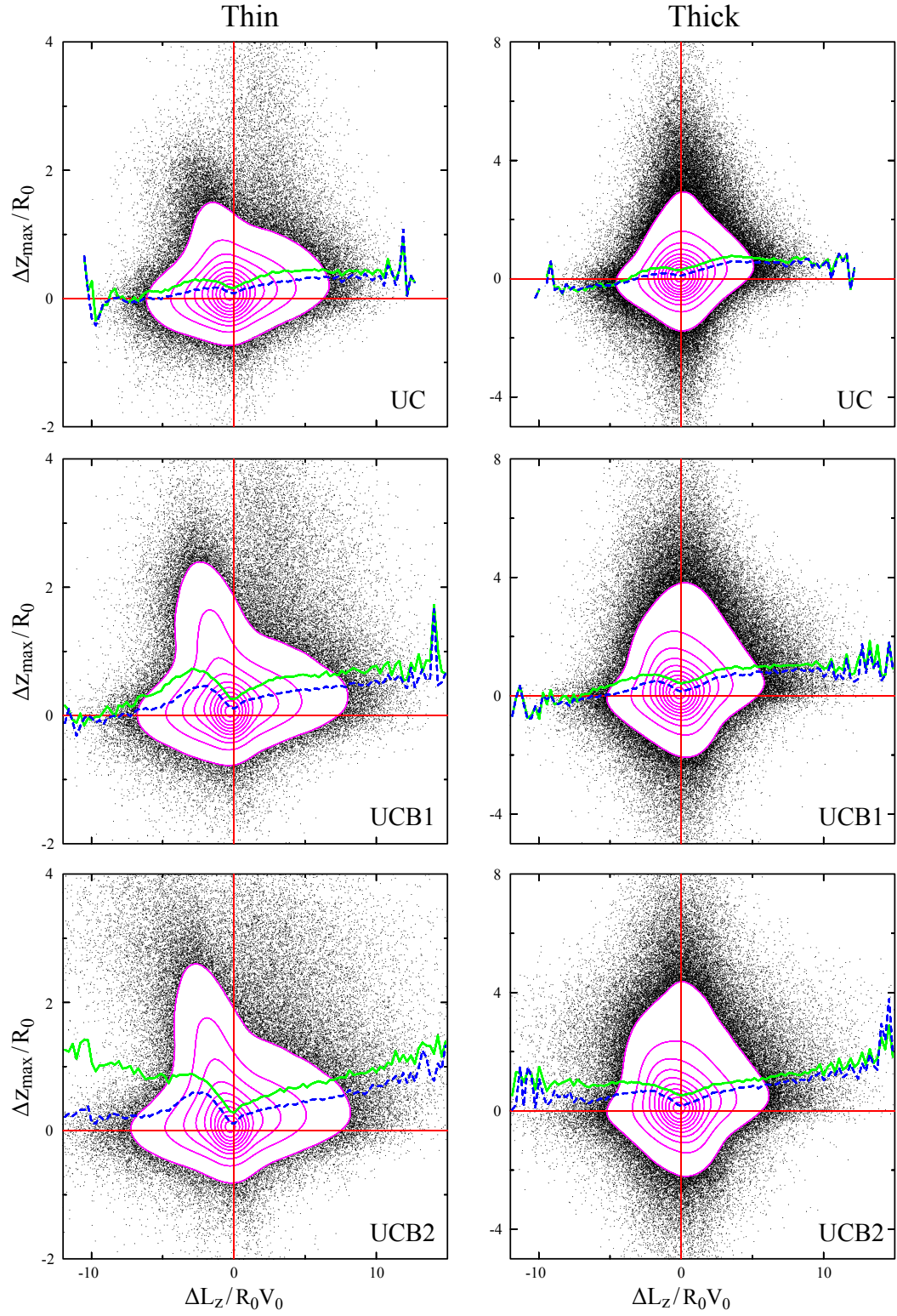
Figure 2.17 Same as Fig. 2.9 for simulations UC (top row), UCB1 (middle row), and UCB2 (bottom row). The left column shows $\Delta z_{\max}$ as a function of ΔL_z for the thin disks and the right for the thick.

Here our focus is on the consequences of continued transient spiral behavior in the outer disk long after the bar formed, which has not previously received much attention, as far as we are aware.

The red curve of Fig. 2.11 shows the evolution of A_2/A_0 in UCB1. The spirals become significant around the time $\sim 1,000\tau_0$, the bar forms around $\sim 2,000\tau_0$, and we stop the simulation at the same final time $t = 3,500\tau_0$ as UC. Thus, the time interval of significant scattering is roughly $2,500\tau_0$ in length with a bar being present for the last $\sim 1,500\tau_0$, which correspond to 7.5 Gyr and 4.5 Gyr respectively. With our suggested scaling, the bar has a pattern speed of 31.8 km s^{-1} kpc^{-1} and corotation $R_c \sim 7.5$ kpc. This scaling makes the bar substantially larger than that in the Milky Way.

The long-dashed red curves in Fig. 2.14 show that the bar enhances the changes in L_z somewhat over those that arise due to spirals alone. Note that we measure the instantaneous value of L_z of each particle and it should be borne in mind that it changes continuously in the strongly non-axisymmetric potential of this model, especially so for particles in or near the bar.

For this reason, we cannot extend the light blue (marked with arrow heads) and dashed orange contours in Fig. 2.16 to small home radii at the later time in the strongly non-axisymmetric potential of the bar. However, a clear asymmetry can be seen; the distribution is biased above the zero change red line, indicating a systematic outward migration in the outer disk. A similar asymmetry can be seen without a bar in UC (dotted black and solid green contours), but the formation of the bar makes it more pronounced. Since total angular momentum is conserved in these simulations, there is a corresponding inward migration in the inner regions (see Fig. 2.5).

Aside from the bar region, where systematic non-circular streaming biases the rms radial velocities, Fig. 2.18 shows that the bar does not appear to cause much extra heating over that in the non-barred case.

Fig. 2.19 again illustrates that changes in L_z in the outer disk are more substantial in this barred model than in the non-barred case (Fig. 2.15), but the larger spread in ΔL_z in the inner disk is partly an artifact of using the instantaneous values of L_z at later times. Because we use the instantaneous L_z in the barred potential in this Figure, a particle in
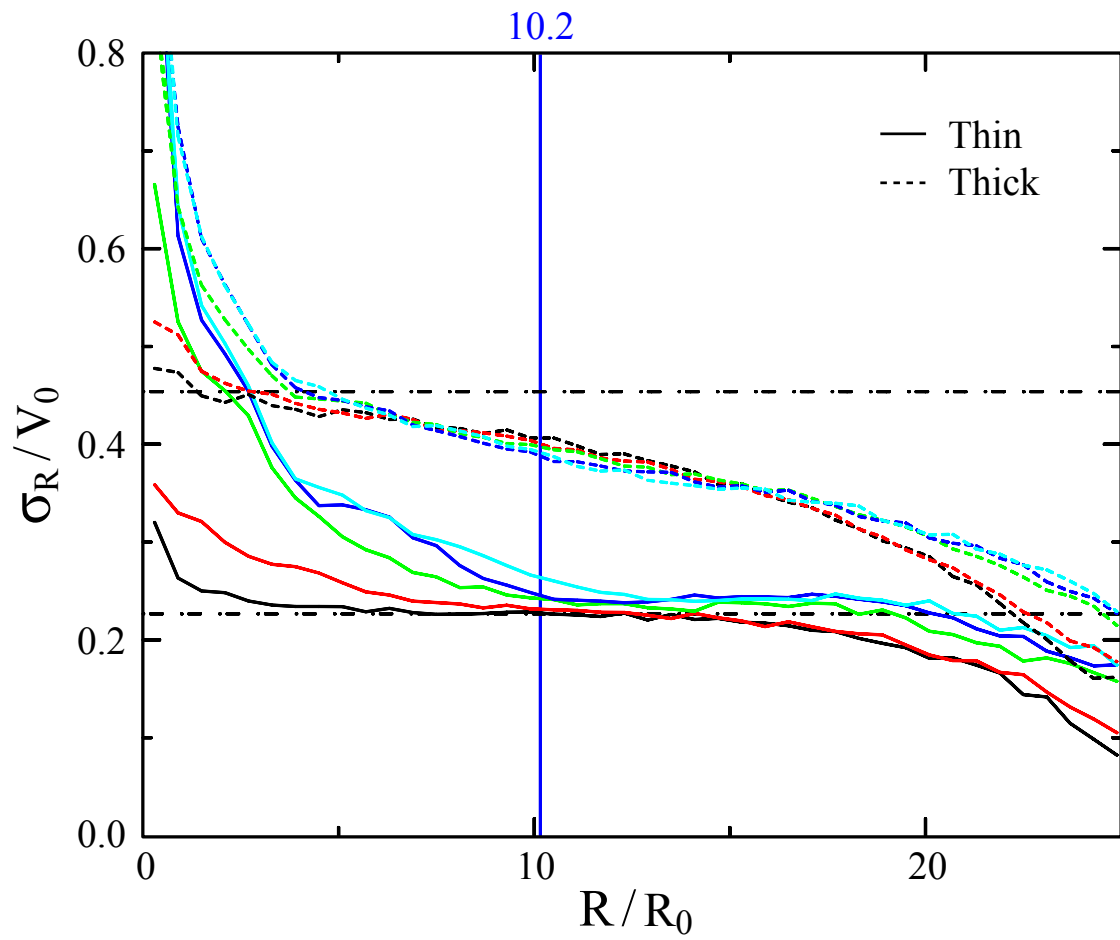
Figure 2.18 Same as Fig. 2.13 for UCB1.

the region where $\Delta L_z < -L_z$ need not necessarily have been changed to a fully retrograde orbit.

The asymmetries in Figs. 2.16 & 2.19 about the red lines of zero change are not caused by bar-formation alone, as the distributions (not shown) are approximately symmetric immediately after this event. Rather, we find they appear to be caused by multiple migrations of the same particles by separate events.

Our second barred simulation, UCB2, again differs from UCB1 and UC only by the initial random seed. It formed a stronger bar, but a little later than in UCB1, as shown by the green curve of Fig. 2.11. Significant scattering occurs for the last $\sim 1,800\tau_0$ time units (5.4 Gyr) of which the bar is present for the last $\sim 1,100\tau_0$ (3.3 Gyr). The pattern speed (33.6 km s^{-1} kpc^{-1}) and corotation radius (~ 7.3 kpc) for our adopted scaling, are similar to the values in UCB1.

We find the extent of radial migration (bottom two rows of Table 2.3) is further increased by the stronger bar, but not by much. Variants of Figs. 2.19 & 2.16 (not shown) are qualitatively similar with slightly larger changes, but the outer disk is again dominated by scattering due to the latest few spirals.

In both these models, therefore, we see that the formation of a bar does indeed increase the net angular momentum changes. However the overall behavior is similar to that of scattering by transient spirals without a bar. This is different from the effect found by Brunetti et al. (2011), in which essentially all the angular momentum changes occurred during bar formation.

The lower two rows of Fig. 2.17 show Δz_{max} versus ΔL_z for UCB1 and UCB2 respectively. The presence of a bar yields a much denser and more extended feature in the second quadrant, which is also visible in for thick disk. For UCB2, its contribution is so great that the mean Δz_{max} keeps increasing with greater angular momentum loss. This extra apparent vertical heating is probably caused by the buckling of the bar. Unlike for M2, UC, and UCB1, we find that for positive ΔL_z in UCB2, the mean and median curves keep rising for larger ΔL_z.
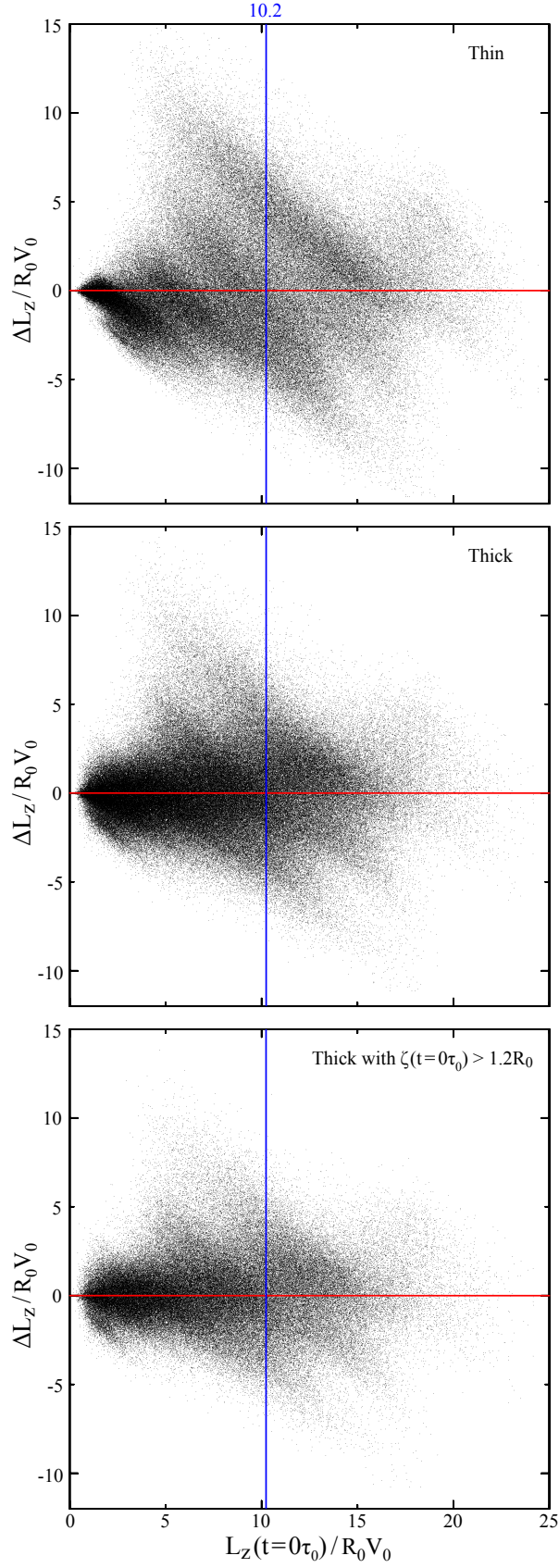
Figure 2.19 Same as Fig. 2.15 for simulation UCB1. The vertical blue line marks the approximate corotation resonance of the bar.

2.6 Summary of radial migration in 3D galactic disks

We have presented a quantitative study of the extent of radial migration in both thin and thick disks in response to a single spiral wave. We find angular momentum changes in the thick disk are generally smaller than those in the thin, although the tail to the largest changes in each population is almost equally extensive.

We have introduced populations of test particles into a number of our simulations in order to determine how changes in L_z vary with disk thickness and with radial velocity dispersion when subject to the same spiral wave, finding an exponential decrease in $\left\langle (\Delta L_z)^2 \right\rangle^{1/2}$, as shown in Fig. 2.10.

We find that spirals of smaller spatial scale cause smaller changes. When we were careful to change all the properties of the model by the appropriate factors, we were able to account for smaller changes to $\left\langle (\Delta L_z)^2 \right\rangle^{1/2}$ as being due to a combination of the weakened spiral amplitude near corotation and the change in the value of m. Furthermore, we found evidence that the saturation amplitude scales inversely as m, in line with the theory developed by Sellwood & Binney (2002). Note the simple scaling holds true only when the principal dynamical properties, such as Q, X, thickness, and gravity softening, are held fixed relative to the scale of the mode. Nevertheless, it seems reasonable to expect smaller changes to $\left\langle (\Delta L_z)^2 \right\rangle^{1/2}$ in general for spirals higher m. The exponential decrease of $\left\langle (\Delta L_z)^2 \right\rangle^{1/2}$ with increasing disk thickness applies only for different populations subject to the same spiral perturbation.

We have also run slightly more realistic simulations to follow the extent of churning in both thick and thin disks that are subject to large numbers of transient spiral waves having a variety of rotational symmetries. Fig. 2.16 shows that changes in the home radii of thick disk particles are smaller on average than those of the thin disk, but again the tails of the distributions in both populations are almost co-extensive. As found in previous work (Friedli et al. 1994; Raboud et al. 1998; Grenon 1999; Debattista et al. 2006; Minchev et al. 2011; Bird et al. 2012), the formation of a bar also causes substantial angular momentum changes within a disk, but we find that the churning effect from multiple spiral patterns still dominates changes in the outer disk after the bar has formed.

Chapter 3

Conservation of vertical action during radial migration

Radial migration results from angular momentum changes near corotation, which we have shown to be somewhat weakened by increased vertical motion. Schönrich & Binney (2009a), in their model of radial mixing in thin and thick disks, assumed that vertical and radial motions are decoupled and that vertical energy is conserved as stars migrate radially. We here try to identify a conserved quantity that can be used to predict vertical motion when particles suffer large changes in L_z, by comparing various measures of vertical amplitude at the initial and final times in simulations with a single spiral. Note that the "initial" value of each quantity we discuss in this chapter is measured at $t = 64\tau_0$, which avoids possible effects of the settling of the model from its mild initial imbalance. Also, all quantities are computed in an azimuthally averaged potential, to eliminate variations with spiral phase, which remain significant at the final time.

We focus on particles whose initial home radii lie in an annulus of width $6.0R_0$ centered at corotation of the spiral in M2, and measure quantities for only one particle per quiet start ring, meaning one in every twelve. This results in $\sim 40,000$ particles from the thin disk and $\sim 73,000$ from the thick. Although the entire thick disk is represented by just 50% more particles than is the thin, the effects of the inner and outer tapers, together with the groove in the thin disk cause the number of particles in the range $4.0R_0 \leq R_{\text{home}}(t = 64) \leq 10.0R_0$ to be some 82% larger for the thick disk than for the thin. While we endeavor to measure each quantity in this chapter for the same set of particles, from both simulations M2 and T, we have been able to estimate some quantities for only a subset of these particles, as noted below.

3.1 Vertical energies

We have tried a number of different way to estimate the energy of vertical motion. A simple definition might be

$$E_{z,R} = \frac{1}{2}v_z^2 + \Phi(R, z) - \Phi(R, 0),$$ (3.1)

with R being the instantaneous radius of the particle. However, Fig. 3.1 shows that $E_{z,R}$ defined this way varies by some 30% as a particle oscillates in both radius and vertically in a static axisymmetric potential. The orbit of this particle is multiply periodic and
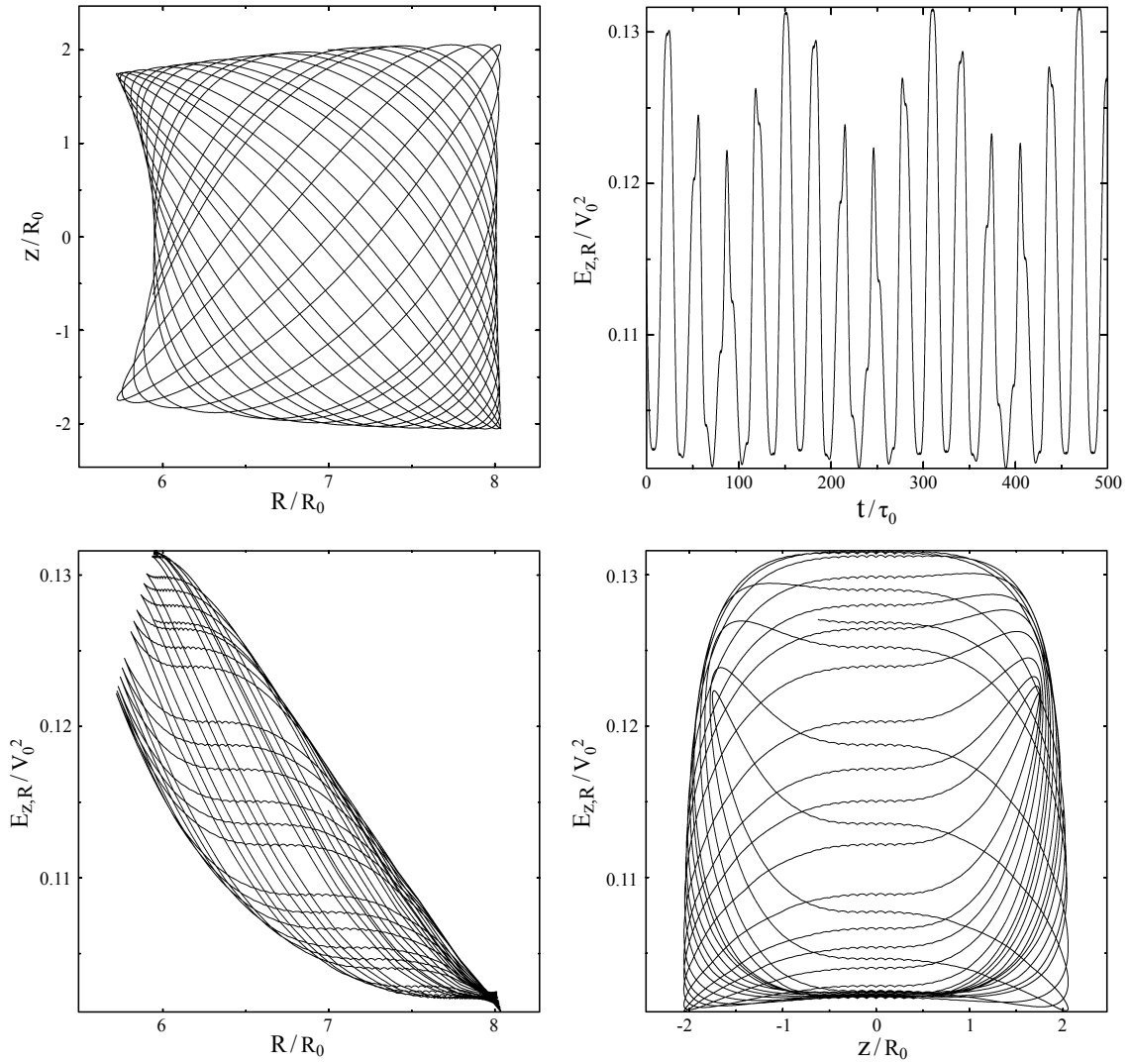
Figure 3.1 The top left panel shows a typical thick disk orbit in the meridional plane, and the other three panels show how $E_{z,R}$ varies with time (top right), radius (bottom left), and z-height (bottom right). The particle, which has a home radius of $6.5R_0$, a total energy of $-2.0V_0^2$, a midplane eccentricity of 0.15, and a vertical excursion of $2.1R_0$, is integrated in the frozen initial axisymmetric potential of simulation M2.

clearly respects three integrals (as we will confirm below), in common with many orbits in axisymmetric potentials (BT08, §3.2). Although such orbits can be described by action-angle variables, which imply three decoupled oscillations, the *energy* of vertical motion is clearly not decoupled from that of the radial part of the motion. In particular, the bottom left panel shows that $E_{z,R}$ varies systematically with radius, which reflects in part the weakening of the vertical restoring force with the outwardly declining surface density of the disk. This behavior considerably complicates our attempts to compare the vertical energies at two different times in the same simulation.

The epicycle approximation (BT08, p. 164) holds for stars whose orbits depart only slightly from circular motion in the midplane. In this approximation, when a star pursues a near-circular orbit near the mid-plane of an axisymmetric potential, the vertical and radial parts of the motion are separate, decoupled oscillations, and the vertical energy is $E_{z,\mathrm{epi}}$ ($= Z$ eq. 2.8) is constant. However, the epicycle approximation is a poor description of the motion of most particles, for which the radial and vertical oscillations are neither harmonic nor are the energies of the two oscillations decoupled.

Table 3.1 gives the rms values of $[Y(t_{\mathrm{final}}) - Y(t_{\mathrm{initial}})]/Y(t_{\mathrm{initial}})$ for particles in both the thin and the thick disks of simulations M2 and T.[I] Here Y represents one of several possible vertical integrals. The first rows give the fractional changes in the epicyclic approximation, $Y = E_{z,\mathrm{epi}}$, that are substantial. Furthermore, they are almost as large in simulation T, which was constrained to remain axisymmetric, as those in M2 in which substantial radial migration occurred, suggesting that the changes are mostly caused by the inadequacy of the approximation.

The second rows in Table 3.1 show the rms fractional changes in the instantaneous values of $E_{z,R}$. While these values are slightly smaller than for the epicyclic estimate, they are again large for the thin disk and still greater for the thick. This is hardly surprising, as the particles in the simulation have random orbit phases at the two measured times.

Particles on eccentric orbits generally spend more time at radii $R > R_{\mathrm{home}}$ than inside this radius, which biases the instantaneous measure to a lower value, as shown in the third

---

[I]For all quantities in this table, we use the biweight estimator of the standard deviation (Beers et al. 1990), which ignores heavy tails. We also discard a few particles with initial values $< 10^{-4}$ in order to avoid excessive amplification of errors caused by small denominators.

Table 3.1 Biweight standard deviation of fractional changes in various estimates of vertical energy and action.

Simulation	Disk	Variable Y	$\sigma(\Delta Y/Y_{\text{initial}})$	
M2	Thin	$E_{z,\text{epi}}$	30.7%	28.9%
		$E_{z,R}$	28.3%	27.2%
		$E_{z,R_{\text{home}}}$	25.0%	26.1%
		$\langle E_{z,R} \rangle$		23.6%
		$J_{z,\text{epi}}$	22.7%	20.7%
		$J_z\|_{R,\phi}$	16.5%	16.0%
		J_z		15.6%
	Thick	$E_{z,\text{epi}}$	59.4%	39.4%
		$E_{z,R}$	47.6%	31.5%
		$E_{z,R_{\text{home}}}$	34.9%	26.0%
		$\langle E_{z,R} \rangle$		22.3%
		$J_{z,\text{epi}}$	55.7%	34.9%
		$J_z\|_{R,\phi}$	35.0%	19.7%
		J_z		15.4%
T	Thin	$E_{z,\text{epi}}$	22.5%	19.5%
		$E_{z,R}$	17.9%	15.4%
		$E_{z,R_{\text{home}}}$	10.0%	8.8%
		$\langle E_{z,R} \rangle$		5.8%
		$J_{z,\text{epi}}$	16.5%	13.8%
		$J_z\|_{R,\phi}$	9.4%	8.2%
		J_z		6.1%
	Thick	$E_{z,\text{epi}}$	53.6%	34.3%
		$E_{z,R}$	40.8%	22.8%
		$E_{z,R_{\text{home}}}$	23.3%	11.4%
		$\langle E_{z,R} \rangle$		3.0%
		$J_{z,\text{epi}}$	47.5%	27.8%
		$J_z\|_{R,\phi}$	24.8%	11.0%
		J_z		3.4%

The biweight estimated standard deviation of the fractional change in variable Y listed in the third column for both the thin and thick disks in simulations M2 and T. We give two values for the standard deviation in some rows: the value in the fourth column is measured from all the particles, that in the fifth column is from only the 48% (in M2) of particles for which ΔJ_z is calculable.

panel of Fig. 3.1. To eliminate this bias, and to reduce the random variations, we evaluate $E_{z,R_{\mathrm{home}}}$ from eq. (3.1) at the home radius of each particle, which requires us to integrate the motion of each particle in the frozen potential of the appropriate time until the particle reaches its home radius. A tiny fraction, ~ 500 of the $\sim 113{,}000$ sample particles, never cross $R = R_{\mathrm{home}}$ at the initial time and ~ 200 more at the final time; these particles rise to large heights above the mid-plane and have meridional orbits resembling that shown in the top right of Fig. A.2, but appear to be confined to $R > R_{\mathrm{home}}$. The fact that this is possible seems consistent with the description of vertical oscillations developed by Schönrich & Binney (2012). The third rows of Table 3.1 give the fractional rms changes in $E_{z,R_{\mathrm{home}}}$ for all the remaining particles; the changes in simulation M2 are a little smaller than those of the instantaneous values and significantly so in simulation T.

Since $E_{z,R}$ is multiply periodic (Fig. 3.1), we have also estimated an orbit-averaged value, $\langle E_{z,R} \rangle$, by integrating the motion for many periods until the time average changed by $< 0.1\%$ when the integration is extended for an additional radial period. The fourth rows of Table 3.1 give the rms changes in $\langle E_{z,R} \rangle$, which are still considerable. Note that we did not compute this time-consuming estimate for all the particles, but for only the subset used for other values in the fifth column of this table. The choice of this subset is described below.

Generally, we find that none of these estimates of the vertical energy is even approximately conserved, except for the orbit-averaged energy when the simulation is constrained to remain axisymmetric (simulation T). In this case, the potential at the two times differs slightly due to radial variations in the mass distribution – values of this orbit-averaged quantity in an unchanged potential would be independent of the moment at which the integration begins.

In all cases, changes are larger in simulation M2 where significant radial migration occurs. Fig. 3.2 illustrates that the changes in the estimated vertical energy correlate with ΔL_z. The excesses of particles in the second and fourth quadrants indicate that changes have a tendency to be negative for outwards migrating particles and positive for inwards migrating particles. The significance of this trend is discussed below.
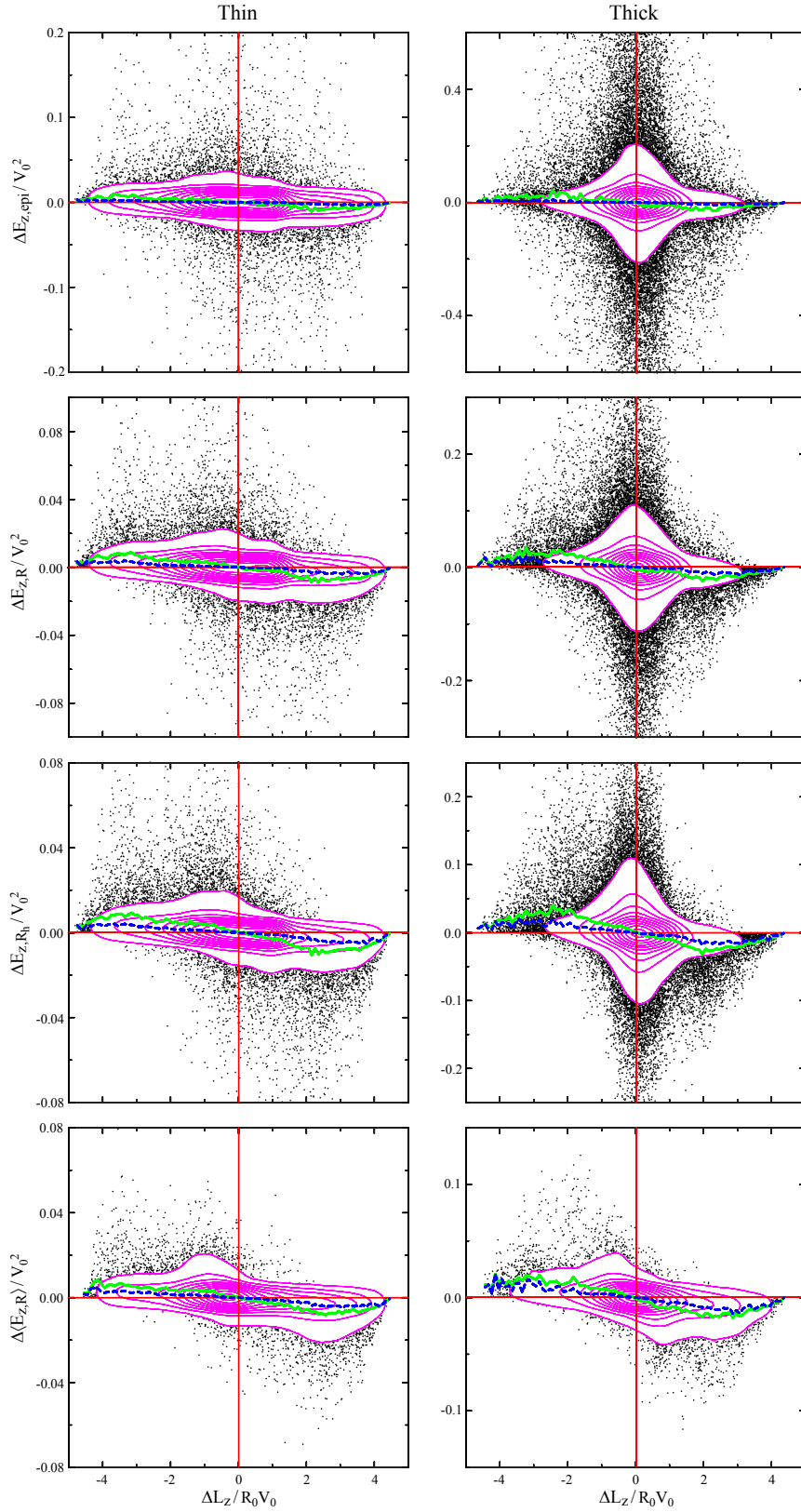
Figure 3.2 Changes in $E_{z,\mathrm{epi}}$ (first row), $E_{z,R}$ (second row), $E_{z,R_{\mathrm{home}}}$ (third row), and $\langle E_{z,R}\rangle$ (fourth row) versus ΔL_z for the thin (left column) and thick (right column) disks of simulation M2. Just as in Fig. 2.9, the horizontal and vertical red lines show zero changes, the linearly spaced magenta contours show number density, and the bold solid green and dashed blue curves show the mean and median changes in each ordinate respectively. Note that the vertical scales differ in each plot.

3.2 Vertical actions

The various actions of a regular orbit in a steady potential are defined to be $(2\pi)^{-1}$ times the appropriate cross-sectional area of the orbit torus (BT08, pp. 211–215). One advantage of actions is that they are the conserved quantities of an orbit when the potential changes slowly – *i.e.* they are adiabatic invariants under conditions that are defined more carefully in BT08 (pp. 237–238).

The vertical action is defined as

$$J_z \equiv \frac{1}{2\pi} \oint \dot{z}dz, \tag{3.2}$$

where z and $\dot{z}$ are measured in some suitable plane that intersects the orbit torus. Since L_z ($\equiv J_\phi$) is conserved in a steady axisymmetric potential, the orbit can be followed in the meridional plane (BT08, p. 159) in which it oscillates both radially and vertically, as illustrated in the first panel of Fig. 3.1. To estimate J_z, we need to integrate the orbit of a particle in a simulation from its current position in the frozen, azimuthally averaged potential at that instant and construct the $(z, \dot{z})$ surface of section (SoS) as the particle crosses R_{home} with $\dot{R} > 0$, say. The integral in eq. (3.2) is the area enclosed by an invariant curve in this plane.

Before embarking on this elaborate procedure, we consider two possible approximations. When the epicycle approximation holds, the vertical action is $J_{z,\text{epi}} = E_{z,\text{epi}}/\nu$ (BT08 p. 232). The fifth rows of Table 3.1 for each disk show that changes in this quantity are large and again they are similar to those in simulation T, confirming once again that the epicycle approximation is inadequate.

Since most orbits reach beyond the harmonic region ($|z| \lesssim 0.4R_0$) of the vertical potential, an improved local approximation is to calculate

$$J_z|_{R,\phi} = (2\pi)^{-1} \oint \dot{z}dz \bigg|_{R,\phi} \tag{3.3}$$

at the particle's fixed position in the disk. This local estimate still ignores the particle's radial motion, but gives a useful estimate for the average vertical action that is also used
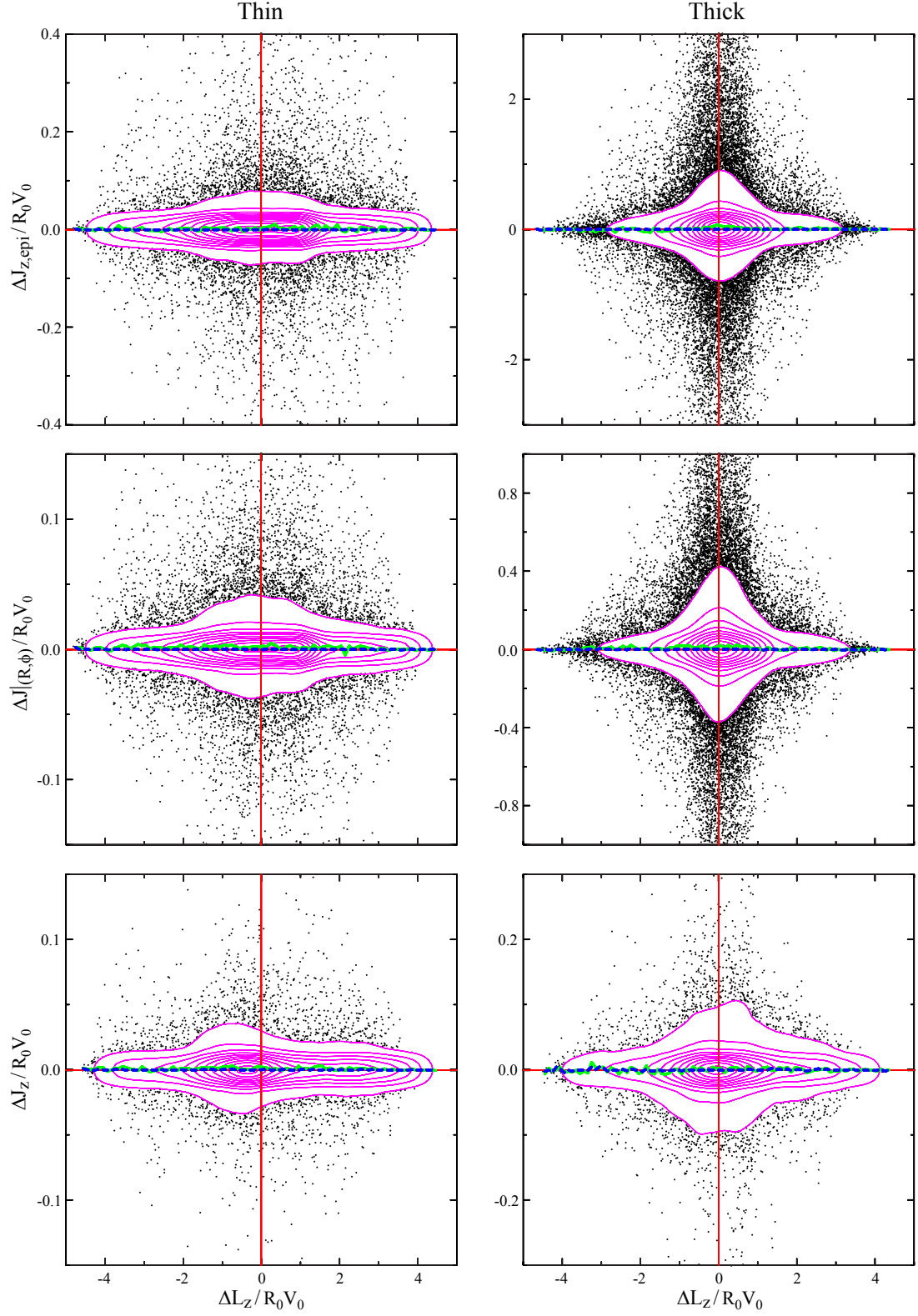
Figure 3.3 Same as Fig. 3.2 for changes in $J_{z,\mathrm{epi}}$ (first row), $J_z|_{R,\phi}$ (second row), and J_z (third row) of the particles in M2.

in analytic disk modeling (Binney 2010). The function $\dot{z}(z)$ at this fixed point is simply determined by the vertical variation of $\Phi(R, \phi, z)$, and the area is easily found. We evaluate $J_z|_{R,\phi}$ at the particle's instantaneous position at the initial and final times using the corresponding azimuthally averaged frozen potential. The rms variation of $\Delta J_z|_{R,\phi}$ is given in the sixth rows of Table 3.1 for each disk. We find that $\Delta J_z|_{R,\phi}$ in the thin disks of both M2 and T are small, suggesting that this estimate of vertical action is more nearly conserved. However, the changes for the thick disks are still large, and we conclude that this local estimate is still too approximate.

We therefore turn to an exact evaluation of eq. (3.2) using the procedure described in Appendix A. Unfortunately, we can evaluate ΔJ_z only if the consequents in the SoS form a simple invariant curve that allows J_z to be estimated at both times. We find that only 48% of the $\sim 113,000$ particles have closed, concave invariant curves at the initial time and only 73% of those retain these properties at the final time. Although the thick disk contains more particles than the thin, we are able to calculate ΔJ_z for a smaller fraction: we succeed with $\sim 26,000$ in the thin disk but only $\sim 13,000$ in the thick.

Column five of Table 3.1 gives the rms changes of all estimates of vertical energy and action for only these particles. While the fractional rms values of the different energy estimates remain large, they are generally smaller than those for all the particles given in the fourth column, but only slightly so for $J_z|_{R,\phi}$. Thus the orbits for which ΔJ_z can be computed are not a random subset, but are biased to those for which energy changes are smaller on average.

The seventh (final) rows of Table 3.1 for each disk list the rms values of the fractional change in ΔJ_z. They are just a few percent for particles in simulation T, in which the disk is constrained to remain axisymmetric, and are smaller than for any other tabulated quantity in the disks perturbed by a spiral. The small scatter about the red line of unit slope in Fig. 3.4 indicates that differences in the final and initial values of J_z in both disks for M2 are indeed small.

Fig. 3.3 shows that changes in all three estimators of the vertical actions are uncorrelated with ΔL_z, and that the mean and median changes are close to zero. Comparison with the systematic changes in Fig. 3.2 suggest that J_z is, in fact, conserved. To see this, note that
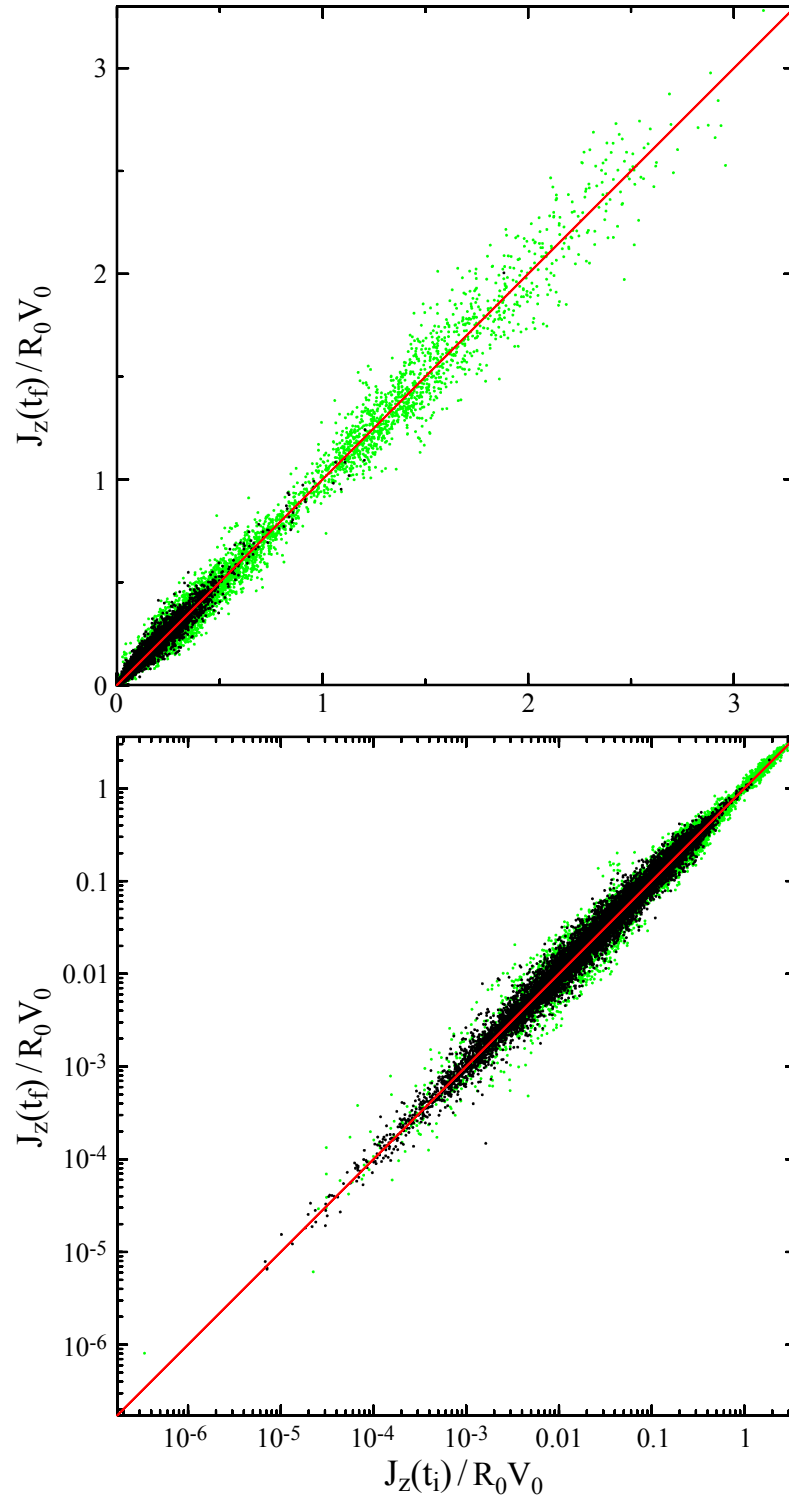
Figure 3.4 Comparison of J_z for $\sim 40{,}000$ particles from simulation M2 at the initial and final times. Values are calculated from eq. (3.2). The top panel is on a linear scale, the bottom on a log scale to reveal the behavior for very small actions. The red line has unit slope. Thin disk particles are marked in black, thick disk in green.

changes in L_z shift the home radius of each particle to a region where the average vertical restoring force differs, the amplitudes of the vertical oscillations increase due to the weaker average restoring force when $\Delta L_z > 0$, and conversely decrease for $\Delta L_z < 0$. Thus, if an estimator of vertical motion is not conserved, we should expect a systematic variation with ΔL_z, as we observe for all the energy estimators in Fig. 3.2. The fact that there is no systematic variation of the median or mean change in vertical action suggest that it is conserved.

If J_z is a conserved quantity, it may seem puzzling that the rms changes in our measurements are not smaller. Both $J_{z,\text{epi}}$ and $J_z|_{R,\phi}$ are approximate, which could be responsible for apparent substantial changes, but changes in the "exact" estimate of J_z remain significant, even for simulation T. It is possible that our estimate of ΔJ_z is inaccurate. For example, we must eliminate non-axisymmetric structure from the potential to compute J_z, introducing small errors when the potential is mildly non-axisymmetric. Larger differences could arise, however, if the invariant curve changes its character, especially since entering or leaving a trapped area in phase space is not an adiabatic change. It is possible an orbit that appears to be unaffected by resonant islands in phase space at the initial and final times could have experienced trapping about resonant islands for some of the intermediate evolution, allowing J_z to change even when changes to the potential are indeed slow.

We have verified that J_z is conserved to a part in 10^4 in a further simulation with a frozen, axisymmetric potential. Note this is not a totally trivial test, since we use the N-body integrator and the grid-determined accelerations to advance the motion for ~ 350 dynamical times before making our second estimate. Therefore the non-zero changes in simulation T are indeed caused by changes to the potential. Even though the potential variations are small, substantial action changes indicate that changes to the orbit were non-adiabatic, which can happen for the reason given in the previous paragraph. Our "initial" J_z values are estimated at $t = 64\tau_0$, when we believe the model has relaxed from the initial set up; we therefore suspect that the small potential variations are more probably driven by particle noise, which can be enhanced by collective modes (Weinberg 1998). This hypothesis is supported by our finding variations in J_z that were about ten times greater than in simulation T when we employed 100 times fewer particles.

3.3 Summary of vertical action conservation during radial migration

We find that vertical action is conserved during radial migration, despite the fact that relative changes in our estimated J_z, which can be measured for only about half the particles, are as large as $\sim 15\%$. Because the vertical restoring force to the mid-plane decreases outwards, an increased (decreased) home radius causes the particle to experience a systematically weaker (stronger) vertical restoring force, making it impossible for both vertical energy and action to be conserved. We find a clear systematic variation of the vertical energy with ΔL_z, but none with ΔJ_z leading us to conclude that vertical action is the conserved quantity. The residual scatter in our measured values of ΔJ_z could be caused by trapping and escape from multiply-periodic resonant islands in phase space, as well as numerical jitter in the N-body potential, as we discuss at the end of §3.2. In the absence of these complications, we believe that the vertical action is conserved.

Thus conservation of vertical action, and not of vertical energy, should be used to prescribe the changes to vertical motion in models of chemo-dynamic evolution. It would be especially useful to obtain diffusion coefficients that include the effects of radial migration as functions of radius and height due to a transient spiral or a combination of consecutive spirals with various corotation radii. We leave this work to a future paper.

Chapter 4

Thick disk formation through outwards radial migration

4.1   Introduction

In §1.4, I introduced the existence and properties of thick disk populations of the Milky Way and nearby spiral galaxies. I presented the current suggested models of how the thick disks might have formed in §1.4.4, including that by outwards radial migration of stars from the galactic center (Schönrich & Binney 2009b; Loebman et al. 2011). While it is likely that no single mechanism plays a unique role in their formation, our focus in this chapter is on this radial migration scenario.

This model cannot explain why the Galactic thick disk primarily contains old stars at present (Gilmore et al. 1995; Bensby et al. 2003; Nordström et al. 2004; Reddy et al. 2006; Ivezić et al. 2008; Bensby & Feltzing 2012; Haywood et al. 2013). If outwards radial migration from the inner central region of the Milky Way continued till present, young stars should have continued to populate the thick disk. Roškar et al. (2013) found that internal heating thickened coeval stellar populations by as much as radial migration did in 10 Gyr of their isolated disk simulation. However, stars can migrate from the inner to the outer region of a disk in a duration of a few transient spirals (~ 1 Gyr) and contribute to the greatest vertical excursions of the thick disk (SB02, S12). The amount of thickening radial migration contributes is limited by the maximum net radial distance stars can travel, i.e. slightly less than the disk size, whereas the amount internal heating contributes is limited by time, *i.e.* stellar age. Stars usually form in the midplane with very small vertical amplitudes. Ones formed in the middle and outer regions of a galaxy would take a much longer time to join the thick disk through heating than those that migrate from the inner region. Thus, having this outwards migration turn off at some point in the past is sufficient to explain the α-enhanced old thick disk (Bensby et al. 2005; Reddy et al. 2006; Fuhrmann 2008; Ruchti et al. 2011; Schlesinger et al. 2012; Liu & van de Ven 2012). But what mechanism shut it off?

In §§1.2.2.1, 1.2.3.2, & 1.3, I explained that we expect radial migration to be suppressed inside a bar, because it is not transient, it has a much greater amplitude than the outer transient spirals, so they cannot penetrate into it, and because it traps stars that are not energetic enough to escape the peak of its potential well at the Lagrange points L_1 and

L_2. Both the Milky Way (de Vaucouleurs 1964; Kerr 1967; Nakai 1992; Hammersley et al. 1994; Calbet et al. 1995; Bissantz & Gerhard 2002; Benjamin et al. 2005; López-Corredoira et al. 2007; Cabrera-Lavers et al. 2008; González-Fernández et al. 2012) and Andromeda (Athanassoula & Beaton 2006; Beaton et al. 2007) have a bar. Hence, this offers a natural solution to the question above: the formation of their bars should have shut off the outwards radial migration and the supply of stars younger than the bar from the galactic center, which would explain why their thick disks only contains old stars at present. In §5, we test this hypothesis using N-body simulations of isolated collisionless disks.

We use the word "churning" to describe solely the process described by Sellwood & Binney (2002), and "radial migration" for any type of secular mechanism that induces changes in the stars' home radii, which includes the effects of a bar, overlap of resonances, Lindblad resonances, blurring, etc., but excludes ones from external perturbers or mergers since our disks are isolated. Hence, we are answering the question of whether bar formation can suppress all internal types of radial migration from the center, not just churning.

Whether radial migration from the inner region with just spirals is strong enough to form the thick disk in the first place is debatable as I explained in §1.4.4. Thus, first, we use our simulations to also test this more important question.

4.2 Simulations

Three of our simulations: MS, MSp, and MB contain Mestel disks and are described in §2.2. MS is exactly UC and MB is very similar to UCB2 from from §2, whereas MSp is similar to MS but has five times as many particles and only contains a single thin disk. The setups of MS and MB only differ by the random seeds of the initial coordinates, but yield different results with MS containing only spirals for a much longer time, while MB forms a bar from particle noise earlier. Although these simulations contain both a thin and a thick disk, we focus our analysis only on the thin one, because we wish to test whether thick populations can arise from the thin disk through radial migration.

4.2.1 Search for more-realistic bars

Simulation MB forms a bar that is too large compared to the ~ 1.5 disk scale lengths Milky Way bar (*e.g.* Bissantz & Gerhard 2002; López-Corredoira et al. 2007). Furthermore, many barred galaxies have small bars, some being smaller than one disk scale length (Gadotti 2011). We spent a long time searching for simulations that form smaller more-realistic bars. The solution that ended up working for us is gradually growing the disk by adding extra particles at its outer regions during the simulation. As the disk grew, its scale length increased while the bar length remained the same. In the long run, we obtained simulations with long-lived bars that ended up being even less than one final disk scale length in size.

We began with disks that are more realistic than the Mestel setup: we used exponential disks surrounded by rigid spherical NFW (BT08, p. 70) or cored isothermal halos. The density profile of the NFW halo is

$$\rho(r) = \rho_s \frac{R_h^3}{r(r + R_h)^2} \tag{4.1}$$

with characteristic constant density ρ_s and core radius R_h (Navarro et al. 1997). And that of the cored isothermal halo we use is:

$$\rho(r) = \frac{V_c^2}{4\pi G} \frac{3R_h^2 + r^2}{(R_h^2 + r^2)^2} \ , \tag{4.2}$$

in which we use $G = 1$, R_h is again a core radius, and V_c is the constant value the circular veloity asymptotes to at large radii (see Fig. 1.2):

$$V_{\text{circ}}^2(r) = V_c^2 \frac{r^2}{R_h^2 + r^2} \ . \tag{4.3}$$

The mass interior to radius r in this cored isothermal profile is

$$M(r) = \frac{V_c^2}{G} \frac{r^3}{R_h^2 + r^2} \ . \tag{4.4}$$

We added particles on circular orbits in the midplane, with zero vertical velocity, at random azimuths, and with home radii chosen from a Gaussian distribution in angular

momentum whose mean L_z increased linearly as time went on. This prescription mimics realistic cold gas accretion with later-accreted gas having greater average angular momentum, which settles into gas clouds on circular orbits in the midplane, out of which new stars form yielding the "inside-out" galaxy formation (Eggen et al. 1962; Fall & Efstathiou 1980; Matteucci & Francois 1989; Bovy et al. 2012c; Brook et al. 2012; Bird et al. 2013).

We did not add particles in rings at the tips of the bar, because we also ran non-barred simulations, in which realistic central star formation would be distributed continuously instead of in rings as mentioned in §1.5, and we wanted to compare barred and non-barred simulations as fairly as possible. Hence, our simulations do not include star formation at the center of the disk. We comment in §§4.3 & 4.4 on possible consequences of omitting this feature.

We wanted to have strong spirals in our simulations. Strong bars heat up the disk quickly making it unresponsive to spiral instabilities. By design, adding cold particles in the outer disk cools the disk down and allows spirals to form. However, we found that, at least in the beginning, we had to add a substantial number of particles to cool down the disk enough to have strong spiral activity. We ended up gradually decreasing the number of added particles as the simulation progressed, which somewhat resembles the cold gas accretion evolution seen in cosmological galaxy formation simulations, in which a large amount of gas is dumped onto the disk early on, and later the disk accretes less cold gas (Birnboim & Dekel 2003; Kereš et al. 2005; Dekel & Birnboim 2006; Ocvirk et al. 2008; Brooks et al. 2009).

The strong spirals that form outside of the bar from the cold accretion can slowly weaken or destroy the bar if the beating between the bar and the spirals phases is unfortunate. Furthermore, due to stochasticity, two simulations with identical parameters except for different random seeds of the initial particle conditions can yield very different results. In addition, two simulations with the same setup and initial seed, but different rules for adding particles (different starting $\langle L_z \rangle$ of the Gaussian distribution, number of particles to add, and/or different rates of adding them) can yield different results. Thus, we spent a long time testing different parameters and random seeds to find the successful simulations presented below.

4.2.2   New simulations

In addition to the three old-type Mestel disk simulations MS, MSp, and MB, we present six new simulations of the more realistic setup: NS, NSp, NB1, NB2, IB, and ISB. Each of these contains a live, thin, fully-massive, exponential disk. The first four have NFW rigid halos, whereas the last two have cored isothermal rigid halos. Table 4.1 summarizes the disk, halo, and grid parameters of all nine simulations, and Table 4.2 gives the parameters of adding particles in the six new exponential disk simulations.

We also present simulation M2p, which is similar to M2 in §§2 & 3, but has an order of magnitude more particles and contains only a thin disk. In §4.4.1, we use this controlled simulation with a single seeded $m = 2$ spiral among other simulations to study vertical heating.

Simulations NB1, NB2, and IB form a bar quite early from a strong global bar instability present in the initial conditions. To achieve our first task of testing the efficiency of radial migration to form a thick disk with only spirals, we need simulations which do not form a bar for a long time. We already have simulation MS and MSp, but we also want spirals-only simulations with the more realistic setup. We weaken the initial bar instability by increasing the initial Toomre's Q parameter of the inner disk and obtain simulations NS, NSp, and ISB.

To do so, we gradually add small radial velocity kicks to the particles in the inner disk while running the simulation with axisymmetric forces only ($m = 0$ was only active) for about 25,000 steps resulting in an inner Q of ~ 2.5 that gradually declines to an outer Q of 1.5 by a cubic spline of width $1R_0$ centered at radius $1.5R_0$. This reduces the surface density of the disk slightly inside radius $1.5R_0$ and raises it slightly between $1.5R_0$ and $3R_0$ because the apocenters of the heated particles increase. Also, the disks extend a little beyond the initial truncation radius listed in Table 4.1 during this procedure. We use these resulting disks as the initial disks in the actual simulations.

The disks of simulations MS, MSp, MB, and NB1 have more or less constant Q of 1.5, and the ones of NB2 and IB have Q of 1.2.

Table 4.1 Parameters of all the simulations from §§4 & 5

Sim.	Thin Disk					Rigid Halo				3D Polar Grid			
	type	$\frac{M_d}{M_0}$	$\frac{R_t}{R_0}$	$\frac{z_0}{R_0}$	N	type	$\frac{M_h}{M_0}$	$\frac{V_c}{V_0}$	$\frac{R_h}{R_0}$	$\frac{\Delta z}{R_0}$	$\frac{\varepsilon}{R_0}$	grid size	m
M2p	Mestel	0.5	25	0.4	12M	Mestel	0.5	1.0	1	0.08	0.2	116×128×243	0, 2
MS	Mestel	0.4	25	0.4	200k	Mestel	0.56	1.0	1	0.2	0.3	75×80×125	$\leq 8, \neq 1$
MSp	Mestel	0.4	25	0.4	1M	Mestel	0.56	1.0	1	0.2	0.3	75×80×125	$\leq 8, \neq 1$
MB	Mestel	0.4	25	0.4	200k	Mestel	0.56	1.0	1	0.2	0.3	75×80×125	$\leq 8, \neq 1$
NS	exp	1.0	6	0.1	100k	NFW	28	0.8	10	0.04	0.07	87×90×225	$\leq 8, \neq 1$
NSp	exp	1.0	6	0.1	1M	NFW	28	0.8	10	0.04	0.07	87×90×225	$\leq 8, \neq 1$
NB1	exp	1.0	4	0.1	100k	NFW	28	0.8	10	0.04	0.07	87×90×225	$\leq 8, \neq 1$
NB2	exp	1.0	6	0.1	100k	NFW	14	0.6	10	0.04	0.07	116×120×225	$\leq 12, \neq 1$
IB	exp	1.0	6	0.1	100k	isoth		0.6	5	0.04	0.07	116×120×225	$\leq 12, \neq 1$
ISB	exp	1.0	6	0.1	100k	isoth		1.1	5	0.04	0.07	116×120×225	$\leq 12, \neq 1$

The first column gives the simulation designation. The next five columns give the properties of each thin disk: the disk type, its mass M_d, its initial truncation radius R_t, vertical scale height z_0, and the initial number of particles in the disk N. All the disks have the same scale length $R_0 = 1$. Note that we only list the thin disks of simulations MS and MB (see Table 2.1 for parameters of their thick disks). The next four columns specify the rigid halo: its type, mass M_h, its contribution to circular velocity at large radii V_c, and its scale length R_h. For the NFW halo, the halo mass is $M_h = 4\pi\rho_s R_h^3$ (see eq. 4.1 for the function form of the density ρ). And for cored isothermal halos, we do not provide a mass since V_c specifies the profile (see eq. 4.2). The next four columns give the 3D polar grid parameters: Δz the vertical spacing, ε the softening length, the grid size in the form of the number of rings×spokes×planes, and m the active sectoral harmonics starting from mode $m = 0$.

The greater inner Q is enough to suppress the bar in NS and NSp, but we need an additional mechanism to weaken the bar instability further in ISB. Raising the inner Q further with the above procedure changes the surface density profile too drastically and raises the outer Q beyond useful values due to very eccentric particles whose home radii still reside in the inner part.

Instead, we use a more massive rigid halo, or equivalently a halo that yields a greater asymptotic circular velocity, making the disk more stable. This, along with a greater inner Q, gives a long period of only spirals in ISB, but a weak bar forms around time $6{,}000\tau_0$ from particle noise, just like in MB. Simulations NS and NSp do not produce a bar during the integrated time. We find that, on average, the cored isothermal halo gives slightly more bar-unstable models than the NFW one. To obtain a strong bar in the NFW case, we decrease the halo mass in simulation NB2 compared to NB1 by the same principle.

We use the Jeans equations to estimate the initial equilibrium radial velocity dispersion for the exponential disks. We calculate the azimuthal velocity dispersion assuming the epicycle approximation and estimating the mean orbital velocity by eq. 4.226 in BT08. Then, we use the same rounded-off exponential profile (eq. 2.5) for the vertical component and set up the vertical velocity dispersion using the 1D Jeans equation (BT08, eq. 4.271). This is adequate when the radial velocity dispersion is low. The virial ratios of the disks oscillate within 0.5 ± 0.01 with the greatest oscillations occurring during bar formation and/or strongest spirals. The disks undergo mild changes in the beginning mostly due to imbalances in the vertical structure, but settle by $t \sim 32\tau_0$ just like the models in §§2 & 3.

We choose the initial radial length scale of the disk $R_0 = 1.0$ to be our unit of length (the radius of the inner angular momentum taper for the Mestel disk simulations MS, MSp, MB, and M2p) and the initial circular velocity $V_0 = 1.0$ our unit of velocity. Then the unit of time or dynamical time is $\tau_0 = R_0/V_0$, the mass unit is $M_0 = V_0^2 R_0/G$, and the unit of angular momentum is $L_0 = R_0 V_0$. We suggested a scaling to physical units in §§1.5.11 & 2.2.1. Note that our simulations have different initial circular velocities V_c as listed in the ninth column of Table 4.1.

Table 4.2 Particle addition parameters

Sim.	t_i/τ_0	(ptcls/steps)$_i$	t_m/τ_0	(ptcls/steps)$_m$	$\langle L_z \rangle_i /L_0$	σ/L_0	$\gamma/L_0\tau_0^{-1}$
NS	0	16/16			3.5	0.5	0.0025
NSp	0	160/16			3.5	0.5	0.0025
NB1	0	16/16			3.5	0.5	0.0025
NB2	320	4/1	1,600	1/1	4.0	0.5	0.003
IB	160	4/1	800	1/1	5.0	0.5	0.003
ISB	0	4/1	2,400	1/1	4.0	0.5	0.003

The second column gives the time t_i at which the addition of particles begins. The third column specifies the number of particles added after each number of specified steps in the beginning. The accretion rate remains constant in simulations NS and NB1, whereas in ISB, IB, and NB2 it linearly decreases to the rate given in column five at an intermediate time t_m (column four), after which it remains constant at the final rate. The sixth column gives the starting mean $\langle L_z \rangle_i$ of the Gaussian distribution in L_z from which a generator chooses initial home radii for the added particles, and σ in column seven is the non-changing standard deviation of the distribution. Finally, γ in column eight is the linear growth rate of $\langle L_z \rangle$ with time.

4.2.3   Numerical procedure

We use the same numerical procedure as in §2.2.2. The size of the 3D polar grid and the cubic spline softening length vary between the simulations as listed in Table 4.1. We do not use quiet starts and we include gravitational disturbance forces from all sectoral harmonics $0 \leq m \leq 8$ or 12, except $m = 1$ to avoid imbalanced forces from a possibly asymmetric distribution of particles in a rigid halo with a fixed center. We add a supplementary rigid central attraction to the forces from the particles at every step, just as in §2.2.1. It corrects the razor-thin infinite exponential disk for reduced surface density, finite thickness, and gravitational force softening. This is optional, however, because we use the Jeans equations, not a distribution function, to set up initial velocities in approximate equilibrium.

We also use the same time step of $0.02\tau_0$ for evaluating forces and moving particles, double the time step every radius at which the orbital period doubles starting with R_0 in a series of five outer zones, and half the time step where the orbital period halves in five successive inner zones.

In the exponential disk simulations, added particles have the same mass as the initial particles. As these simulations progress, the total masses of their disks increase accordingly.

Table 4.3 Disk radial profile parameters

Sim.	$\frac{t_f}{\tau_0}$	$\frac{M_{d_f}}{M_{d_i}}$	$\frac{R_{d_{In}}}{R_0}$	$\frac{R_{d_{Mid}}}{R_0}$	$\frac{R_{d_{Out}}}{R_0}$	$\frac{R_{b_{In,Mid}}}{R_0}$	$\frac{R_{b_{Mid,Out}}}{R_0}$	$\frac{R_{t_f}}{R_0}$
MS	3,500	1.0	2.1	6.4	3.4	4.0	16.1	26
MSp	3,200	1.0	2.1	5.8	3.2	3.6	16.2	27
MB	4,000	1.0	2.5	6.5	4.7	6.1	9.5	32
NS	6,080	3.04	1.0	8.8	1.9	3.3	20.0	28
NSp	4,320	2.16	1.0	5.6	1.2	2.7	13.7	21
NB1	5,500	2.75	0.7	7.9	2.7	3.3	17.2	27
NB2	3,520	3.24	0.6	8.4	3.0	3.0	17.1	27
IB	3,680	3.08	0.5	7.5	3.6	3.1	18.4	30
ISB	4,640	4.52	1.3	5.0	1.0	2.1	14.3	18
ISB	10,880	7.64	1.0	7.0	2.3	2.5	27.7	36

The second column gives the final time of the simulation, and the third gives the ratio of the final mass of the disk to the initial one. The second to last row, however, gives the values at the intermediate time of ISB just before the bar forms. The next three columns give estimates for the radial length scales of each of the three sections (inner, middle, and outer) of the disk surface density, and the following two give the rough break radii between these sections at the times of column two. The last column gives the rough truncation radii of the disks at the same times.

4.2.4 Simulation results

We run simulations MS, MSp, NS, and NSp until they form a bar, and use a final time just before it forms for analysis of a long duration with only spirals. The other simulations we stop when the number of escapers from the grid reaches about 1%. Table 4.3 lists the final times of the simulations in column two, and by how much the masses of the disks have increased by final time in column three.

As particles are added and the disk grows in a new simulation, various properties of the disk, such as circular velocity and vertically-integrated mass surface density, gradually change as shown in Fig. 4.1 for simulation NB1 for example. The other simulations have a similar behavior.

At the final time, each disk's surface density is composed of three somewhat exponential sections with different scale lengths. The middle section has a greater scale length than the inner and outer ones, so these are all Type II disks (§1.1.1.1). Columns four through eight in Table 4.3 give approximate scale lengths for each of the three sections and the break

radii between them at the final time. The last column gives a disk's rough final truncation radius. The same profile arises in the thin disks of MS and MB, in which the spirals and/or bar affect the radial distribution without addition of particles. In addition to the final time of simulation ISB, we report these parameters for its disk at the intermediate time $4{,}640\tau_0$ just before the bar forms in the second to last row.

In a test simulation (not shown) that is identical to NB1 except has no non-axisymmetric forces (only $m = 0$ active), the added particles build a broad bump in the middle section of the surface density that grows and moves outwards with time. In NB1 and other unconstrained simulations, however, the spirals and bar smear this bump out over time (top middle plot of Fig. 4.1). Circular velocity also shows evidence of the smearing out of a corresponding feature over time. Sellwood & Moore (1999) and Sellwood (2013b) found similar behavior in their simulations.

The interesting scale lengths of the middle sections do not change much during the exponential disk simulations. The particle addition parameters basically set their values and how fast the disks grow. A greater linear growth rate of $\langle L_z \rangle$ of the added particles or a lesser number of particles added at each step would yield smaller more realistic middle scale lengths. However, we find that disks with such conditions have much weaker spiral activity.

To illustrate when the bars form, how their amplitudes evolve, and to compare with the non-barred simulations, we show A_2/A_0 as a function of time in Fig. 4.2 (A_m is defined in eq. 2.7). We use $R_1 = 0.5R_0$ and $R_2 = 8.0R_0$ for MS, MSp, and MB and $R_1 = 0.2R_0$ and $R_2 = 2.5R_0$ for the exponential disk simulations to focus on the bar region. The bars form roughly at times $2{,}400\tau_0$, $200\tau_0$, $50\tau_0$, $50\tau_0$, and $6{,}000\tau_0$ in simulations MB, NB1, NB2, IB, and ISB respectively. If run further, simulations MS, MSp, NS, and NSp form bars shortly after as well. The bar amplitudes in NB1, NB2, and IB change drastically at some times. In §5.3, we show how other bar parameters change with time and answer the interesting question of how many particles remain trapped by the bar when it undergoes such changes.
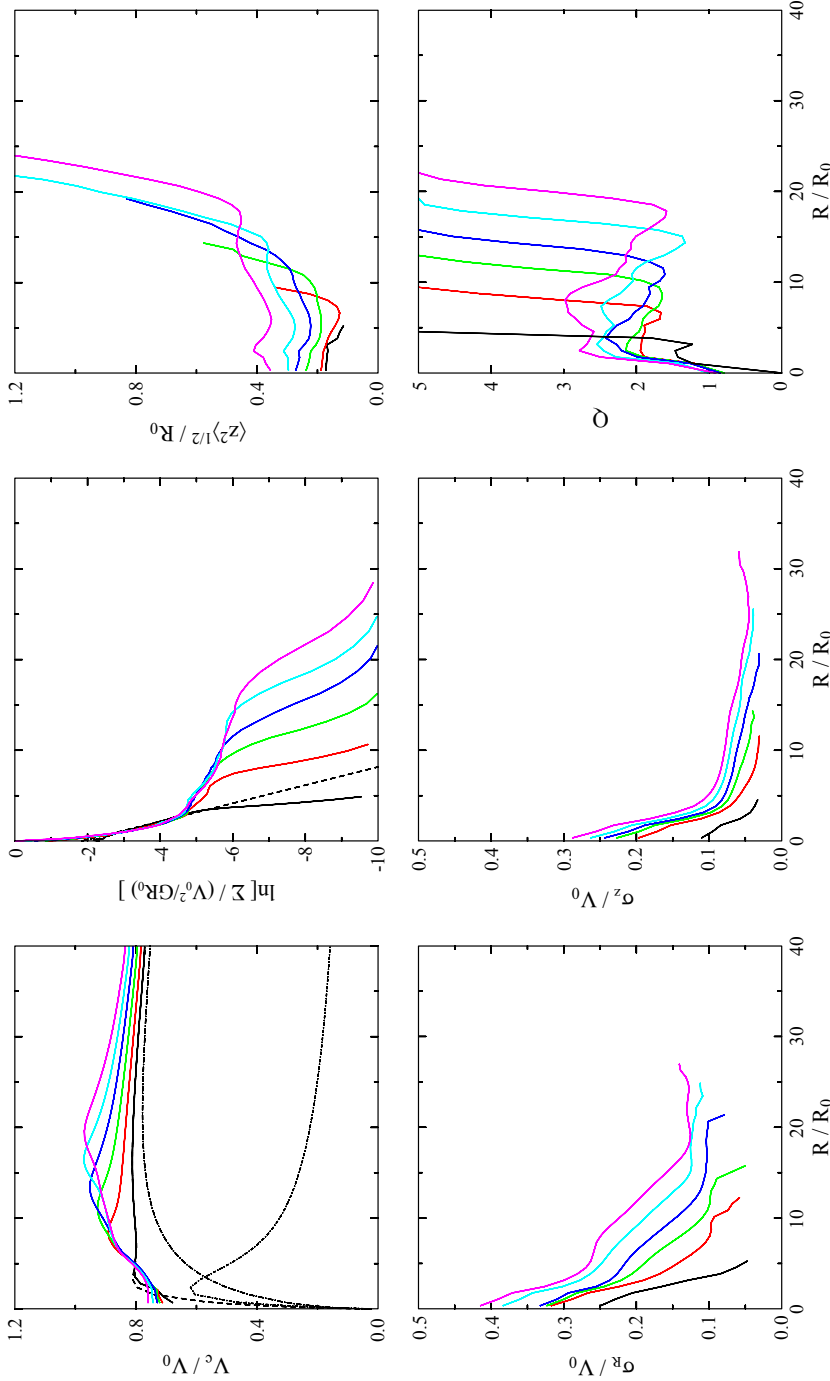
Figure 4.1 Temporal evolution of circular velocity (top left), natural log surface density (top middle), root-mean-square height (top right), radial velocity dispersion (bottom left), vertical velocity dispersion (bottom middle), and Toomre's Q parameter (bottom right) versus radius of the disk in simulation NB1. Colors show incrementing time with constant time step 1,097.6τ_0 (roughly one fifth the final time at a constant interval at which we saved particle data) starting at $t = 0\tau_0$ in the order: black, red, green, blue, cyan, and magenta. The curves shift to the right with time. In the top left plot, the short dot-dashed black curve shows the initial theoretical contribution from the non-truncated disk, the long dot-dashed one from the halo, and the dashed black curve shows their sum. And in the top middle plot, the dashed line shows the theoretical initial surface density of the non-truncated exponential disk.

We chose to present all these different simulations because their bars and spirals have different types of behaviors. MB has a large bar, whereas NB1, NB2, IB, and ISB have small bars by final time. ISB has a slow bar, while the other bars are fast. NB1 has an elongated bar, MB has a somewhat elongated bar, NB2 has a fatter one, IB an even fatter one, and ISB has a very fat weak oval-like bar. The Mestel disk simulations MS, MSp, and MB all have somewhat weak spirals, simulation ISB has weak to medium spirals, NS and NSp have strong ones, NB2 and IB begin with strong spirals but they progressively get weaker to medium strength by the end, and NB1 has very strong spiral activity.

Fig. 4.3 shows particle position snapshots at different times in simulation NB1. Here, and in all our exponential disk simulations, spiral modes of $m = 4 - 6$ dominate the disk. This is no surprise, because the disks are low-mass, which are known to yield spirals with greater number of arms (Sellwood & Carlberg 1984). As we showed in §2.4, such spirals cause weaker radial migration than $m = 2$ ones.

4.3 Outwards radial migration from the inner disk with spirals only

Our first task is to test whether spirals in our simulations cause an outwards radial migration from the inner regions powerful enough to build the thickest disk component in the solar neighborhood. To do so, stars must migrate outwards as far as possible to the solar neighborhood. We use simulations MS, MSp, NS, NSp, and the first half of ISB (up to time $4{,}640\tau_0$), which do not contain a bar.

4.3.1 Ability of particles to migrate out of the inner disk

We choose an inner region for each disk defined by a boundary radius R_b, and count how many particles initially in that region end up outside of it. For simulations MS and MSp, to later compare to the barred-simulation, we choose $R_b = 8R_0$, which corresponds to the $L_{1,2}$ Lagrange points of the bar in MB. For simulations NS, NSp, and ISB, a similar prescription would yield $R_b = 2.5R_0$, which we decided is too small; so, for these simulations, we choose $R_b = 5R_0$ instead, which is slightly less than one final disk scale length. Note that, since the initial exponential disks were truncated at $R = 6R_0$, the number of particles in this inner
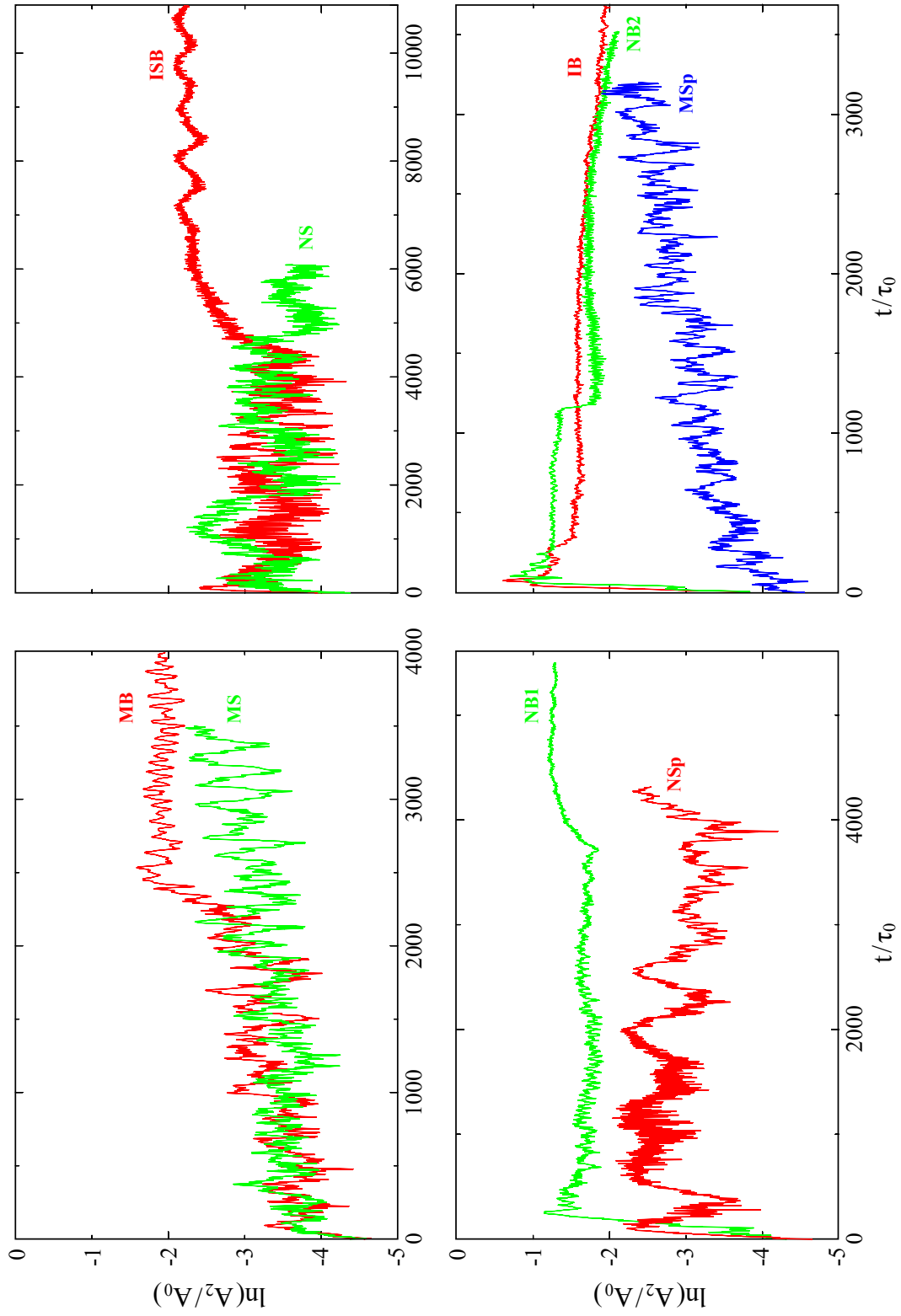
Figure 4.2 A_2/A_0 as a function of time on a natural log scale as measured by eq. 2.7 for all the simulations. Note that the horizontal time axes have different scales.
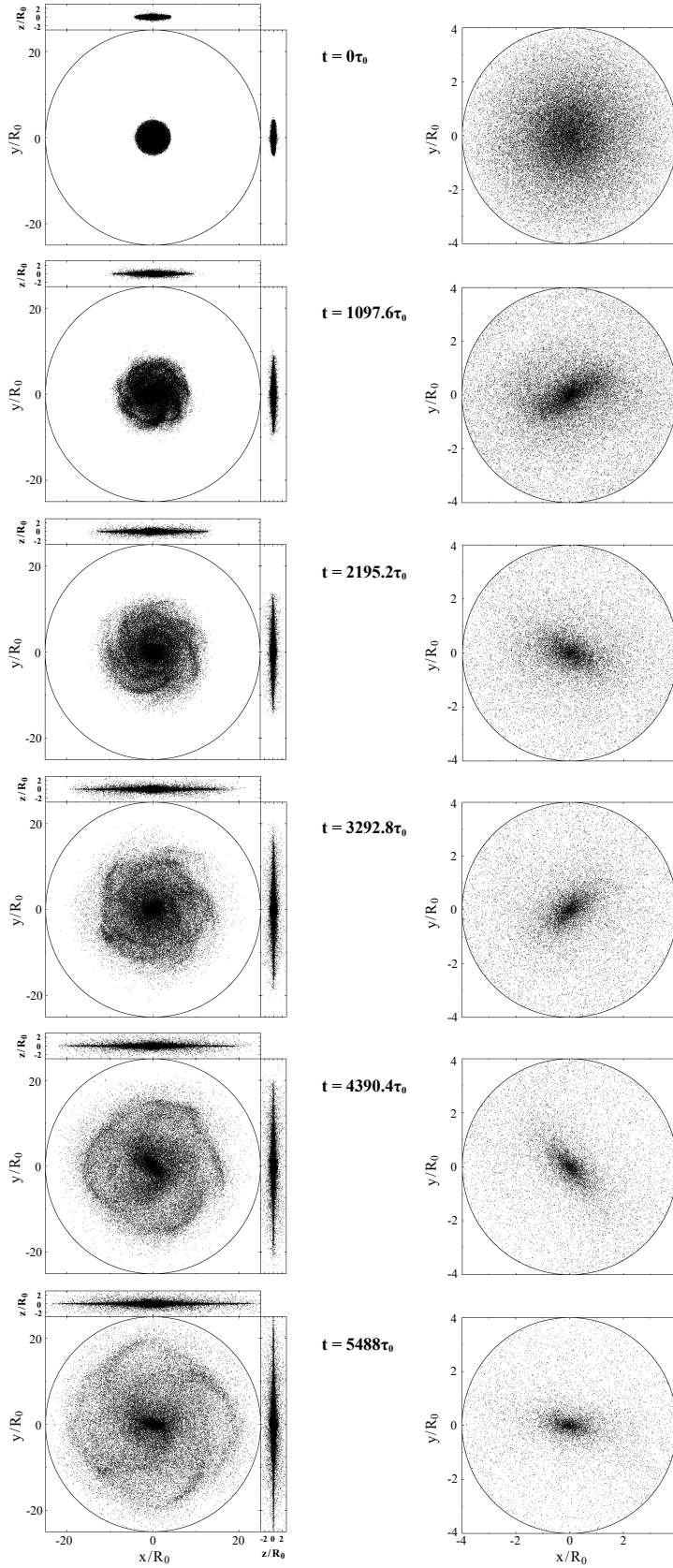
Figure 4.3 Snapshots of the disk in simulation NB1 at the six times presented in Fig. 4.1 from top to bottom in the left column. The right column shows the same snapshots zoomed-in. Only ~ 50 k representative particles are plotted in every left snapshot, while all the particles that fit the zoomed frame are plotted in the right snapshots.

Table 4.4 Percentage of outwards migration due to spirals only

Sim.	Mig.	% of Total	rms z/R_0 at t_i	rms z/R_0 at t_f
MS	I→I	83.6%	0.58	0.69
	I→II	3.5%	0.51	0.75
	I→III	12.9%	0.58	0.70
	II→II		0.60	0.88
MSp	I→I	86.7%	0.58	0.62
	I→II	2.0%	0.50	0.65
	I→III	11.3%	0.57	0.65
	II→II		0.60	0.75
NS	I→I	84.6%	0.23	0.29
	I→II	5.9%	0.15	0.41
	I→III	9.5%	0.16	0.32
	II→II		0.15	0.45
NSp	I→I	85.3%	0.23	0.26
	I→II	4.7%	0.14	0.34
	I→III	10.0%	0.15	0.31
	II→II		0.15	0.43
ISB	I→I	79.6%	0.25	0.33
	I→II	7.3%	0.15	0.38
	I→III	13.1%	0.16	0.35
	II→II		0.14	0.38

The third column gives the percentage of particles of the total that begin in region I and end up in the final region specified by column two for the five spirals-only simulations specified in the first column. Columns four and five give the initial and final root-mean-square absolute vertical positions of just the particles that undergo the corresponding migration of each row. The forth row of each simulation reports these for particles that begin and end up in the outer region II.

region is $\approx 97\%$ of all the particles initially. At the initial time $t = 0\tau_0$, we integrate each particle's orbit in the frozen initial potential for about fifty full radial periods, and estimate its minimum $R_{\min}$ and maximum $R_{\max}$ radial excursions, even though the orbit might be chaotic. We define three different regions with respect to R_b: a particle is in region I if its $R_{\max} \leq R_b$, in region II if $R_{\min} > R_b$, and in region III if $R_{\min} \leq R_b$ and $R_{\max} > R_b$. Thus, particles in region I spend their entire orbits in region I in a non-changing potential. Then, we determine which region each particle ends up in at final time by integrating its orbit in the frozen potential of the final time starting from the particle's coordinates at final time.

Table 4.4 lists the percentage of particles that begin in the inner region I and end up in each region. About 15% to 20% of the particles migrate outside of region I by the end

of each simulation or by time $4,640\tau_0$ for simulation ISB, but the fraction of these that end up in II is small. Nevertheless, outwards migration from the inner region exists in our simulations. Note that this analysis involves the original particles only and none of the added ones since they do not exist at $t = 0\tau_0$.

This tests only the particles' ability to migrate out of the inner region. Next, we report how many of them actually migrate to the solar neighborhood and beyond.

4.3.2 Fraction of extreme outwards migrators that make it to the solar neighborhood

Fig. 4.4 shows histograms of the fraction of particles in each initial home radius bin that migrate to outside of radius $12R_0$ by the final time of each of the three simulations, meaning that their final home radii are greater than $12R_0$ (we do not use $R_{\min}$ and $R_{\max}$ as above). These include all the new particles that are added before the final time in the exponential disk simulations, but they barely contribute to the inner region as they are added mostly outside of it. We choose this radius as a rough inner boundary of a solar neighborhood analogue: about two final disk scale lengths.

Many, including Roškar et al. (2008a), Schönrich & Binney (2009b), Minchev & Famaey (2010), Minchev et al. (2011), Loebman et al. (2011), Brunetti et al. (2011), Roškar et al. (2011), Bird et al. (2012), Minchev et al. (2012a), Curir et al. (2012), Brook et al. (2012), Roškar et al. (2012), and Minchev et al. (2012b), reported similar histograms, but for particles that end up in a solar annulus as opposed to our stronger case of anywhere beyond the inner edge of the solar neighborhood. The majority of their histograms are similar to ours for MS, MSp, NS, and NSp: a fraction of about 0.05 migrate from the home radius of one final disk scale length ($6R_0$-$7R_0$) to the solar neighborhood or beyond. However, at the smallest radii, our fractions are on the low end. The fractions of simulation ISB are much lower overall likely due to its much weaker spiral activity, and only rise a little by the final time $10,880\tau_0$ that includes the bar.

Many of these authors' simulations contain gas physics including cold flows in the inner disk that lead to star formation in the inner regions, whereas ours do not. Since such stars are more prone to form in the midplane and radial migration affects thinner populations
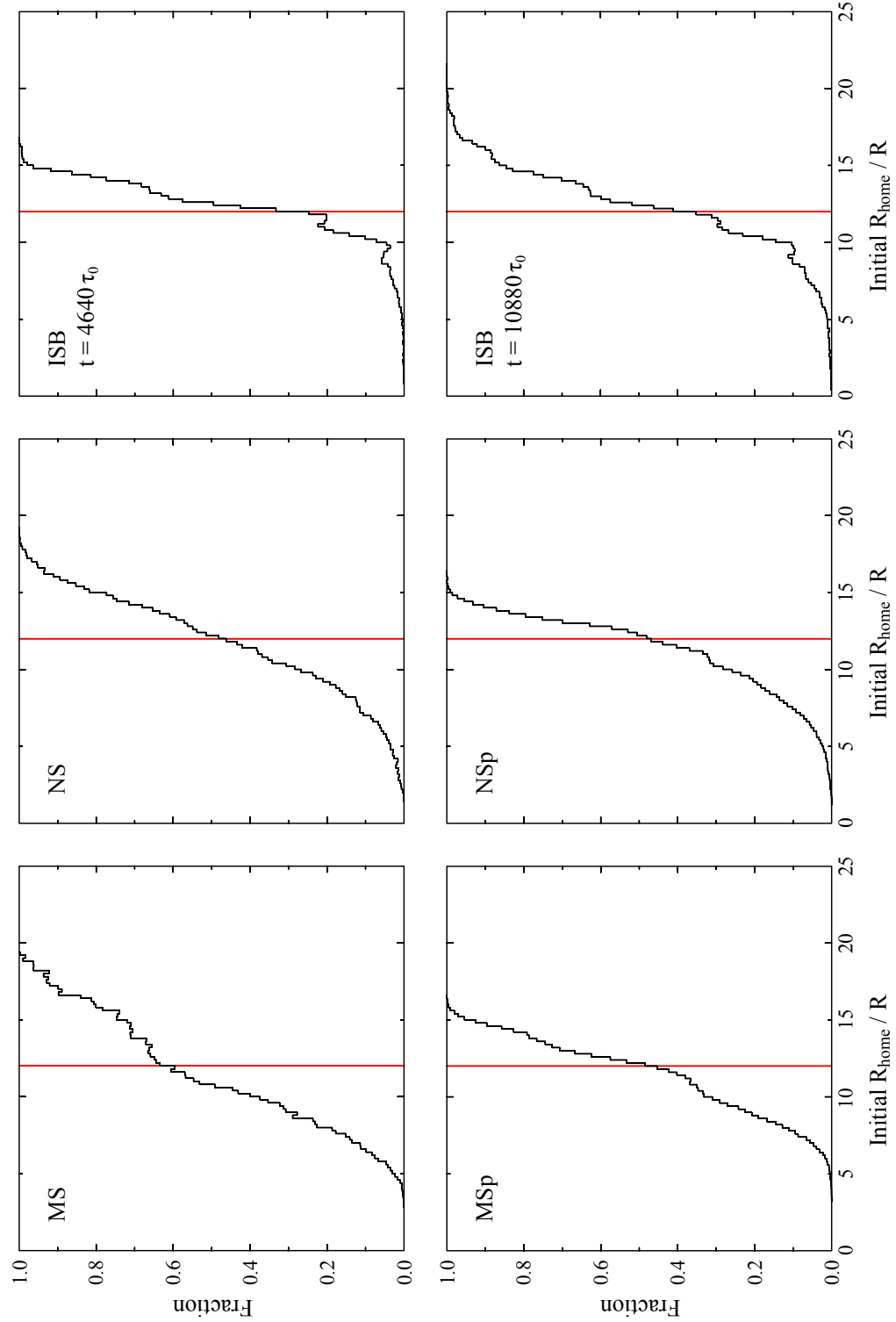
Figure 4.4 Histograms of the fraction of particles in each initial home radius bin that migrate to outside of radius $12R_0$ (final $R_{home} > 12R_0$) by the ends of simulations MS, MSp, NS, and NSp and by the intermediate time $4{,}640\tau_0$ for simulation ISB just before its bar forms as well as at its final time $10{,}880\tau_0$, which includes the effect of the bar. The red vertical line marks this $12R_0$ radius.
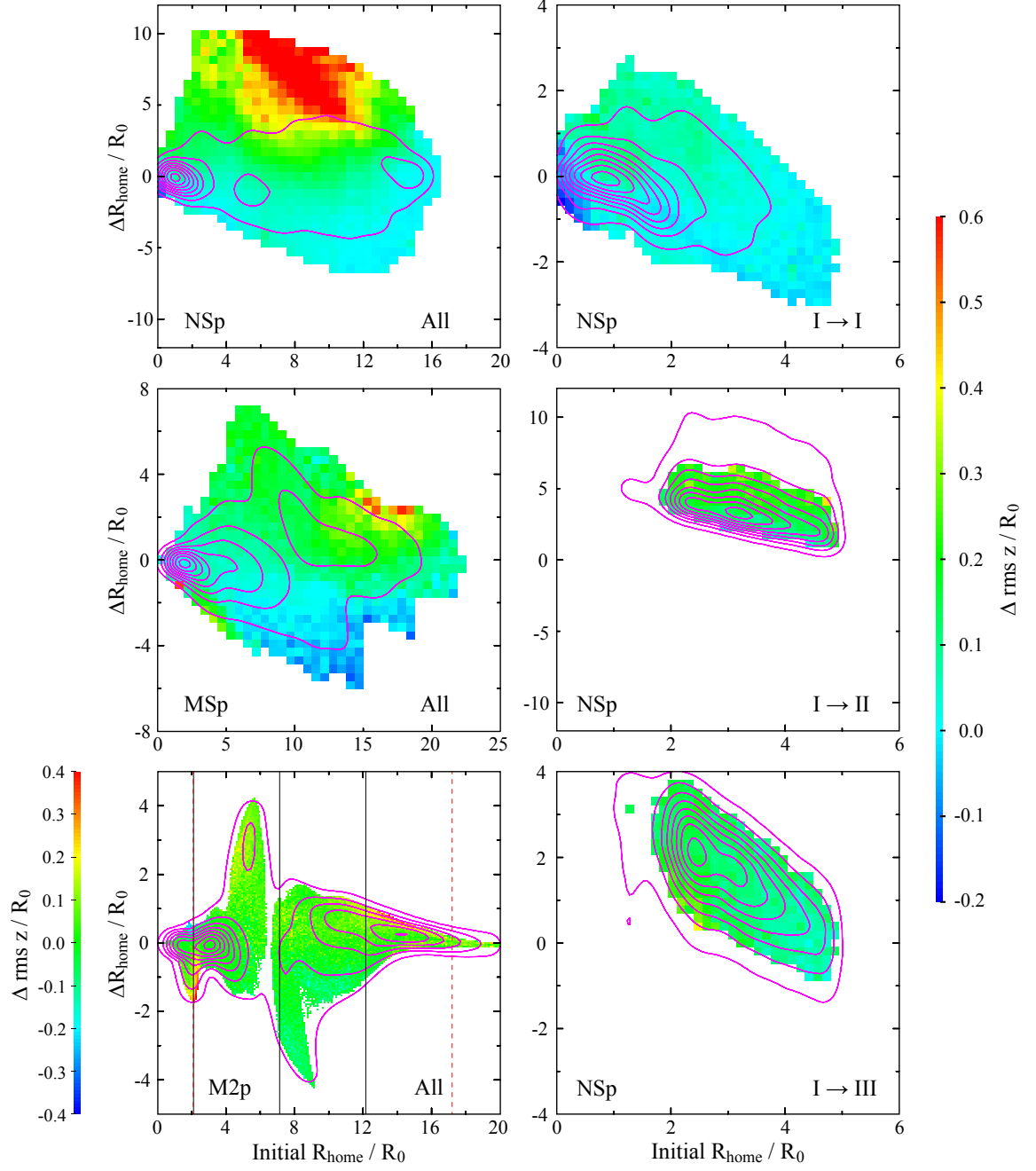
Figure 4.5 (Caption next page.)

Figure 4.5 (Previous page.) Color gradient shows changes in rms z (rms $z_{\text{final}}-$ rms z_{form}) of bins in initial home radii and changes in home radii. The left column contains plots for all the particles for simulations NSp (top), MSp (middle), and M2p (bottom) including the added ones in the case of NSp. The right column contains plots for particles in NSp that originate in region I and by final time remain there (top), migrate to region II (middle), or to III (bottom). We ignore bins with less than hundred particles and less than four hundred in the plot of M2p since it contains an order of magnitude more particles, for which reason we also use much smaller bins in it. Magenta contours denote particle number density and are linearly spaced at 95%, 85%, and so on. The few bins at the smallest initial R_{home} and negative ΔR_{home} in the top two plots correspond to particles that end up on retrograde orbits: we assign negative home radii to particles that have negative angular momenta. In the bottom left plot of M2p, the vertical black lines mark the locations of corotation and inner and outer Lindblad resonances, whereas the red dashed vertical ones mark the inner and outer $m = 2$ vertical resonances. The inner $m = 2$ vertical resonance lies almost on top slightly inside the inner Lindblad resonance. The initial time for M2p is not $0\tau_0$ as it is for the other simulations, but is $80\tau_0$, which we choose in order to ignore the mild effects of the disk initially settling to equilibrium described in §2.2.1. Note that the initial and changes in R_{home} scales vary between the plots, and the Δ rms z color scale is different for M2p with a zero at green instead of cyan.

more than thicker ones (§2.3), including this star formation would likely increase the fractions of far outwards migrators from the smallest radii in our simulations making them agree more with others' findings.

Furthermore, as stated before, our simulations contain spirals with greater number of arms, which cause weaker radial migration. In addition, the spiral activity declines in the inner disks at later times, because the addition of particles, which cools the disk and allows for stronger spirals, moves outward. The fraction of outwards migrators should have also increased were we to move the addition of particles outward at a slower rate, add them in a broader distribution, or begin adding them closer to the center.

4.3.3   Changes in root mean squared height

Many authors found that such small fractions of outwards migrators can still give rise to a thick disk (*e.g.* Loebman et al. 2011). Thus, our small fractions and the $\sim 15\%$ of migrators from the inner regions could be doing the same. To test this, we check what happens to the vertical amplitudes of the particles that escape the inner region bound by R_b. Columns four and five and seven and eight of Table 4.4 show that their root-mean-square heights increase by final time. Notice that the particles that migrate outwards furthest (from region I to

II) have the smallest initial rms z, which agrees with the fact that radial migration affects thinner populations more (§2.3.4).

Fig. 4.5 shows more detail plotting changes in rms z as a color gradient versus initial home radii and changes in home radii for the simulations with more particles MSp and NSp. Simulations MS, NS, and ISB with less particles have similar plots except the rms z changes are slightly greater overall, which we comment on below. Also, a plot for ISB at its final time $10{,}880\tau_0$, which includes the presence of a bar, is similar to the one ending at $4{,}640\tau_0$ just before the bar forms. The affect of radial migration on vertical amplitudes is evident: in the left column plots for all the particles, ones that migrate outwards experience increases in rms z, and, to some degree, those that migrate further have greater increases, while those particles that migrate inward mostly experience either zero or negative changes in rms z. An exception in MSp are particles at small initial home radii that migrate inwards to the very center. Their amplitudes increase because the Mestel disk has a hole in the center (inner angular momentum taper as described in §2.2.1); so just near the center, the disk is less massive making the vertical restoring force weaker. Likewise in the right column plots, particles that migrate from the inner region I to regions II and III have greater rms z changes than the particles that remain in region I. The middle plot for migration from I to II shows a small vertical color gradient with bins of greater ΔR_{home} having greater Δ rms z. But in the bottom plot of particles that end up in region III, a few bins at the smallest initial R_{home} and slightly positive ΔR_{home} have the greatest increase in rms z. The main point of plots in this figure is show the nontrivial dependence of Δ rms z on initial R_{home} in our simulations.

The top left plot for NSp clearly shows that outwards migrators beginning and ending up in the outer region II have the greatest rms z increases, not the ones that begin in the inner region I and migrate outwards to II. The same is evident from the forth rows of Table 4.4: while both groups have similar initial rms z, the former group has greater final rms z in simulations MS, MSp, NS, and NSp, and the same final rms z in ISB. Thus, although the small number of particles that migrate outwards from the inner region do thicken up a little and might contribute to thick disk populations in the middle and outer galactic regions, the thickest populations are composed of particles that originate in region II.
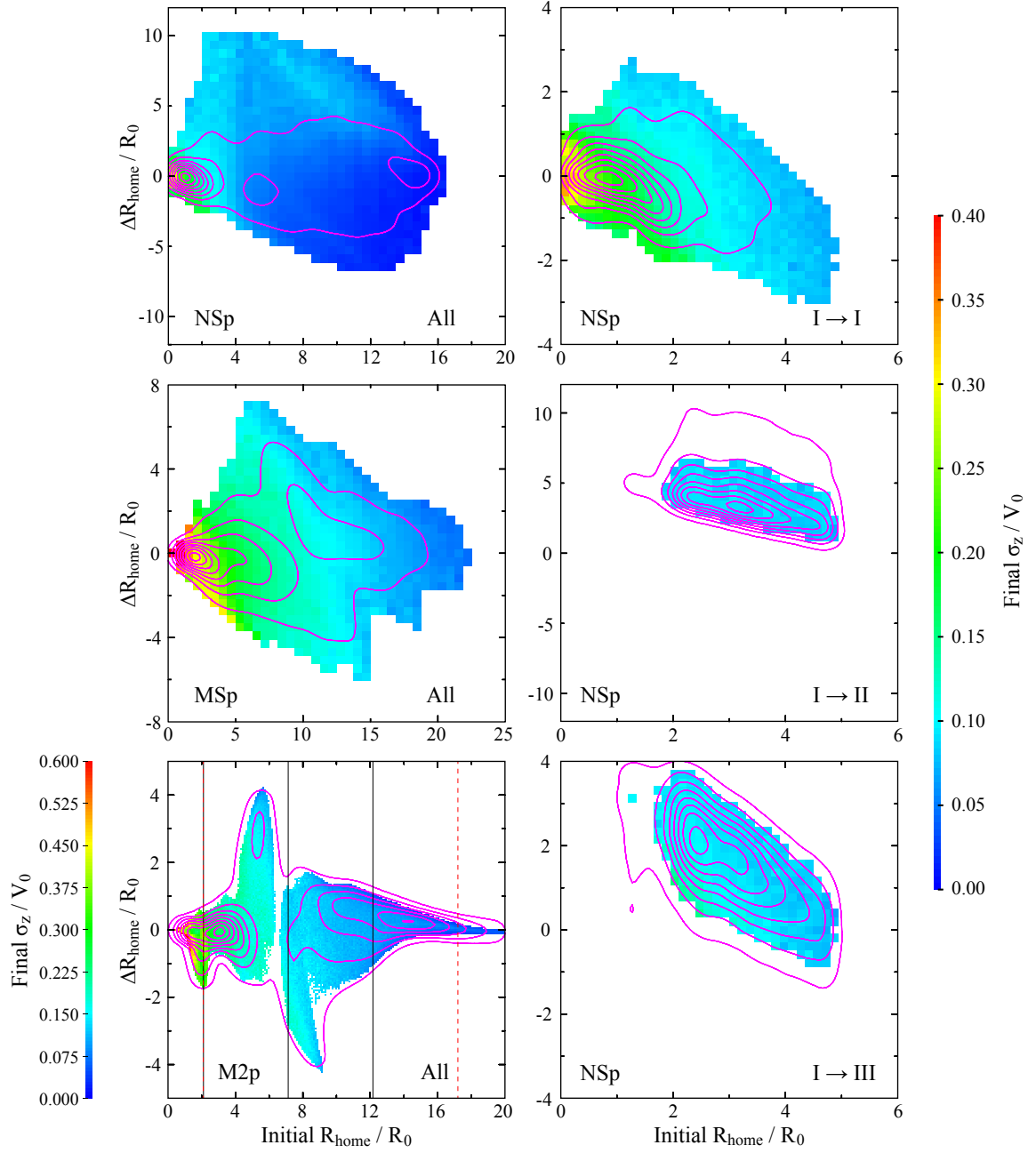
Figure 4.6 Same as Fig. 4.5, but the color gradient shows final vertical velocity dispersions. Again, the color scale for M2p differs.

4.3.4 Final vertical velocity dispersion

Fig. 4.6 shows corresponding vertical velocity dispersions at the final time. These plots indicate that, for the most part, the original trend of a declining σ_z with increasing radius remains. So, as expected, σ_z declines for particles that migrate outwards, which Minchev et al. (2012b) and Roškar et al. (2013) also found. An exception is the former group of particles from the previous paragraph with the greatest rms z increases in NSp that lie along a line roughly of slope -1 that connects with initial $R_{\text{home}} \approx 15R_0$ at $\Delta R_{\text{home}} = 0R_0$. Their final vertical velocity dispersion is slightly greater than the surrounding bins. Interestingly, these particles all migrate to roughly the break radius between the middle and outer radial exponential portions of the disk as listed in second-to-last column of Table 4.3 by the final time. They seem to contribute to some disk flaring at this radius.

4.3.5 Are the rms height increases enough to constitute a realistic thick disk?

To investigate further, we present Fig. 4.7, in which we show how the root mean square height varies with radius for particles that begin in a specific radial annulus and by final time migrate either outwards or inwards to other annuli based upon their instantaneous radii (not home radii). We present these plots for the two simulations MSp and NSp with greater number of particles for better statistics; their lower particle number variants have similar plots, and ISB is also similar to NSp. Overall, these plots again show the affect of radial migration on the particles' vertical amplitudes: rms z increases for outwards migrators, and decreases for inner ones. However, there is a clear difference for particles that begin in the inner most annuli between the Mestel and exponential disk simulations. In the Mestel ones, all groups of particles experience increases in rms z after migrating outwards, and the ones from the inner annuli thicken up most per radial distance migrated, as one would expect. In the exponential ones, on the other hand, the inner annulus particles barely thicken after migrating outwards.

This difference is due to the addition of new particles in the exponential disk simulations, and has nothing to do with differences between the Mestel and exponential disk profiles. The new particles add mass and, especially being placed in the midplane, increase the vertical
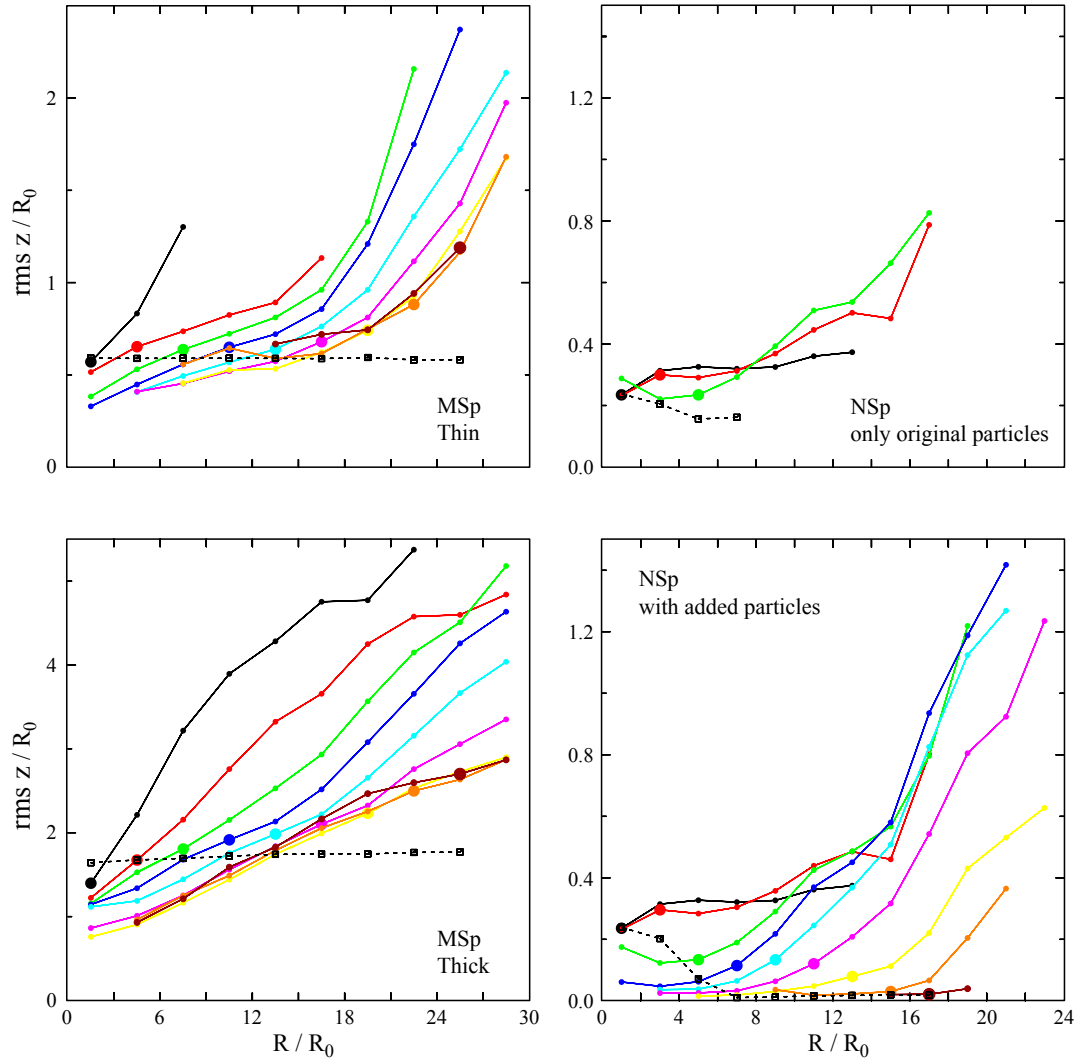
Figure 4.7 The open black squares connected by dashed lines show the initial rms z in each radial annulus of the disk. The big dots show the final rms z of those particles that begin in each dot's corresponding annulus and remain in it at final time (instantaneous radii determine membership to annuli). Whereas, the small dots of the same color connected by solid lines to the big dot show final rms z of particles that began in the same annulus but migrated either outwards (to the right) or inwards (to the left) to their small dot's corresponding annuli. Groups of particles grouped by their initial annulus vary in color from the inner most initial annulus to the outer most one in black, red, green, blue, cyan, magenta, yellow, orange, and brown. We ignore annuli, both initial or final, with less than fifty particles. The left two plots are for the Mestel disk simulation MSp, with the top for its thin disk and the bottom one for the thick. Whereas, the right plots are for the exponential disk simulation NSp, with only the original particles in the top plot and all the particles including the added ones in the bottom one. Hence, the black open squares trace the initial rms z versus radius at time $t = 0\tau_0$ in each disk except in the bottom right plot, in which the added particles contribute from many formation times to each initial annulus. Note that the vertical scales, sizes of the radial annuli, and the maximum radius vary between the left and right plots. The annulus sizes are $3R_0$ and $2R_0$ for MSp and NSp respectively.

restoring force in the middle and outer sections of the disk. Thus, the vertical amplitudes of particles that migrate outwards from the inner region do not increase as much. The right plots in Fig. 4.7 clearly show that the resulting thickest populations beyond $R = 12R_0$ formed at annuli greater than the inner one. The thickening overall is weak compared to in MSp, and only strengthens beyond $R = 14R_0$, which is the transition radius from the intermediate exponential to the steeper declining outer exponential of the radial surface density profile of the NSp disk; so the restoring force drops significantly beyond it. The group of particles that stand out in Figs. 4.5 & 4.6 with the greatest increases in rms z correspond to these thickened populations beyond $R = 14R_0$.

Realistic disks do grow and gain mass over time due to the continuing inflow of cold gas from the halo. Our particle addition prescription could be a bit excessive since the disk of NSp triples in mass by final time. Loebman et al. (2011) presented a simulation of a disk in which outwards migrators from the inner region did form a realistic thick disk in the solar neighborhood. They included gas physics and cold gas inflows, so their disk grew in mass as well. The major difference between our simulations and theirs is that we do not include ongoing star formation in the inner region of the disk. This realistic addition of mass in the inner region is likely the key, because it makes the vertical restoring force increase more uniformly over the entire disk as opposed to just in the outer regions, and could even make the force grow more rapidly in the inner region. To test this, we are planning to run more simulations in the future with a secondary particle addition in the inner disk, and also ones with a much broader Gaussian angular momentum distribution for adding particles with an increasing mean over time.

Given the similar final radial length scales of the disks in MSB and NSp tabulated in Table 4.3, the fact that the scale height of the Galactic thick disk is roughly three times as large as that of the thin in the solar neighborhood, and a rough ratio of 9 between the Galactic thin disk's scale length and scale height, realistic final scale heights for thin and thick disks in both simulations are roughly $0.6R_0$ and $1.8R_0$ respectively. Corresponding rms heights should be comparable (the fitted final scale heights of the thin components at $R = 14 - 16R_0$ are about $0.5R_0$ and $0.3R_0$ for MSp and NSp respectively as seen in Fig. 4.10). This means that, based upon Fig. 4.7, NSp did not produce anything near a

thick disk in the solar neighborhood ($R \approx 15R_0$), while outwards migrators of the thin disk of MSp did build a thick population, but not thick enough. In MSp, the particles that begin in the inner most annulus and migrate outwards furthest thicken up significantly, but they do not reach the solar neighborhood. We expect that, in a simulation with stronger spirals and greater number of particles, so that annuli of further migrators would have better representation, these particles would have made it to the solar neighborhood and beyond, and would have built a realistic thick disk.

4.4 Vertical heating

The facts that most of the final rms z are greater than the initial ones for particles that remain in their original annuli (big dots are above the open squares in Fig. 4.7) and that most of the changes in rms z are nonnegative in Fig. 4.5 suggest that vertical heating is also present and increases the particles' vertical amplitudes in addition to radial migration. Table 4.4 also shows that rms z still increases for particles that remain in region I and do not migrate much.

How much vertical heating contributes to disk thickening compared to radial migration is not very certain. Roškar et al. (2013) were able to somewhat separate the two effects and found that both contribute about equally. House et al. (2011) also studied heating of disks in various hydrodynamic cosmological simulations with and without mergers. We follow Roškar et al. (2013) attempting to separate the contribution of each effect in our simulations, but do not study the thickening changes of nearly circular versus eccentric orbits.

In Fig. 4.8, we present variants of figures 2 and 3 of Roškar et al. (2013) for our simulations NS, NSp, and ISB, in which ages of the added particles correspond to when they are added to the disk. Here we also include corresponding plots at the final time of ISB, which includes the presence of the weak bar. The left column shows changes in rms z and the right shows final vertical velocity dispersions against age and changes in home radii. The very top strip of ΔR_{home} bins mostly comprises of the original particles, whereas the other strips contain only added ones. Younger strips are essentially cuts in initial home

radii since we add the particles in a narrow Gaussian in angular momentum with a mean L_z that increases gradually as time goes on.

Purely horizontal color gradients would correspond to only radial migration being responsible for thickening, and purely vertical ones would correspond to only heating contributing. Just as Roškar et al. (2013) found, Δ rms z increases somewhat diagonally to the right and upwards, so vertical amplitudes increase both due to radial migration and heating. The slope of this diagonal increase varies between our simulations however. In NS, it is much closer to horizontal. Whether this suggests that radial migration plays a bigger role is not certain, because our plots have very few bins with negative rms z changes, suggesting that some amount of rms z increase is present in all the bins.

Of the right plots for final σ_z, only the two for ISB show the trend Roškar et al. (2013) found in their simulations: σ_z increases diagonally to the left and upwards. For simulations NS and NSp, this trend is contaminated by the group of outwards migrators that end up beyond $R \approx 14R_0$ where the surface density drops drastically giving them significantly greater increases in rms z. They fill in the majority of the positive ΔR_{home} bins.

Overall, Fig. 4.8 shows that our simulations do not yield the same gradual trends found by Roškar et al. (2013). Figs. 4.5, 4.6, & 4.7 along with this figure show that both vertical heating and radial migration affect thickening non-uniformly between different groups of particles and different radial regions of the disk.

4.4.1 Sources of vertical heating

A problem with the vertical heating is that we do not really expect its presence in fully collisionless simulations. Theoretically, at Lindblad resonances, spirals heat the disk only in its plane, not vertically. They can cause vertical heating only at vertical resonances: $m(\Omega - \Omega_p) = \pm\nu$. The vertical resonances should lie quite outside of the radial outer Lindblad resonance and inside the inner Lindblad resonance, because the vertical frequency is greater than the radial one. However, gravitational softening reduces the vertical frequency in our simulations making them lie closer to the Lindblad resonances and affect a bigger portion of the disk. Instead of tracking the vertical resonances of multiple recurring transient spirals, we show the results of simulation M2p, which is very similar to M2 in §§2 & 3 and contains

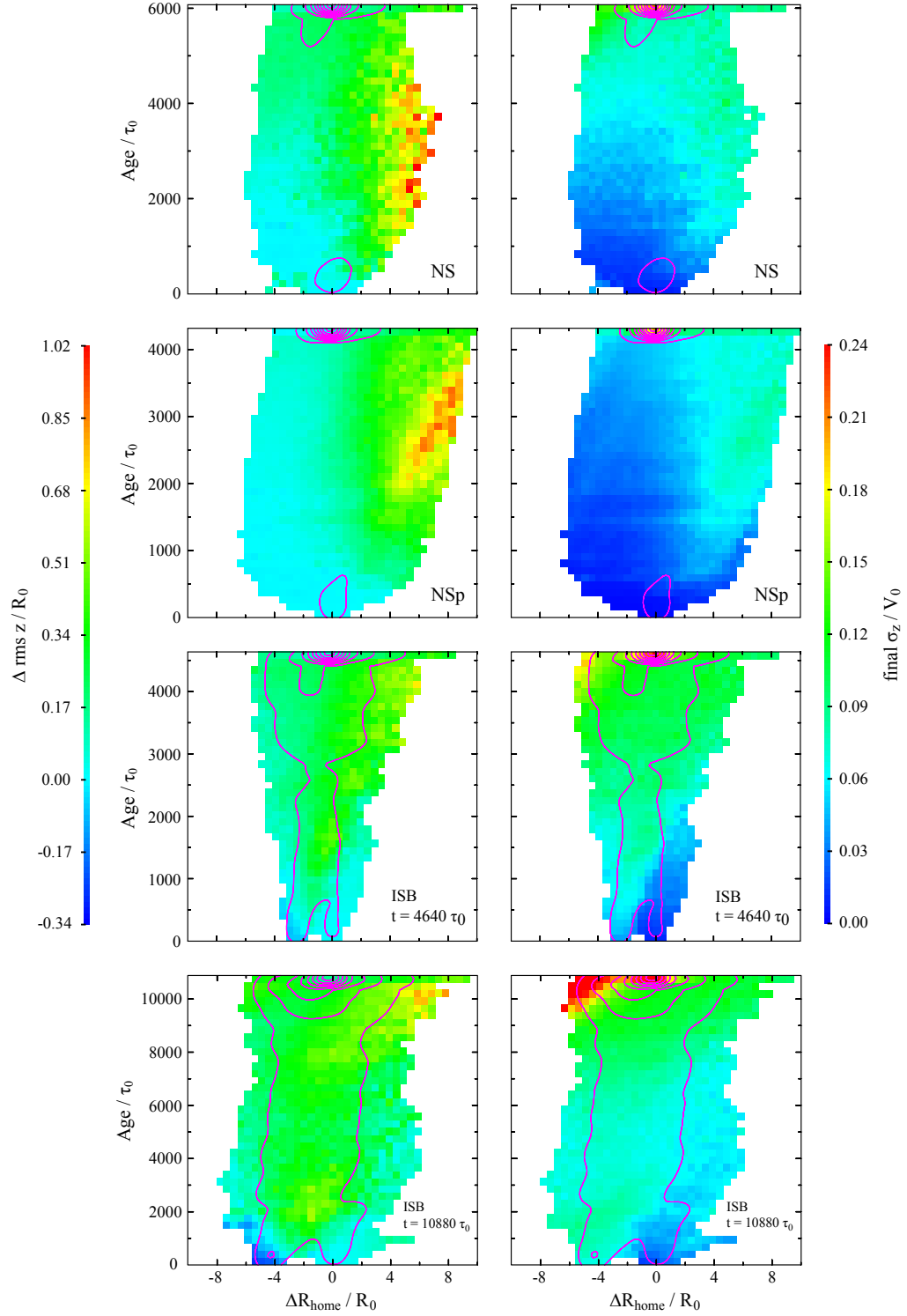Figure 4.8 The left column shows changes in rms z and the right one final σ_z as color gradients of bins in particle ages and changes in home radii for simulations NS (top row), NSp (second row), ISB at time $4{,}640\tau_0$ just before the bar forms (third row), and ISB at the final time $10{,}880\tau_0$ well after the bar has formed (bottom row). Magenta contours denote particle number density as in Fig. 4.5.

a single transient $m = 2$ spiral, in the bottom left plots of Figs. 4.5 & 4.6 in order to test for hints of vertical heating due to vertical resonances.

In Fig. 4.5, first of all, note that outwards migrating particles with intermediate initial R_{home} around corotation have slightly positive Δ rms z (some yellow bins), whereas the inwards migrating particles in that region have slightly negative vertical changes (some cyan bins) as one would expect to be caused by churning. Yet, the greatest increases in rms z, which are much greater than the rest, occur in two small groups of bins that we also identified in §2.3.3 for its simulation M2 in its figure 9.

The first is for bins with the greatest increases in R_{home} outside of the outer Lindblad resonance. The outer $m = 2$ vertical resonance lies at initial $R_{\text{home}} \approx 17R_0$, which we mark with a red dashed vertical line in Fig. 4.5. This is outside of this group of vertically heated particles. However, the actual vertical frequency of particles with non-small initial vertical amplitudes is smaller than ν that is measured in the midplane, which moves the outer vertical resonance inwards closer to the outer radial Lindblad one for these particles. Also, a single transient spiral wave does not have an exact fixed pattern speed Ω_p. A small spread in the pattern speed leads to a spread in the location of the resonances. So, these particles may be vertically resonating with the wave. Yet, why do the rest of the particles with smaller ΔR_{home} at these initial home radii not heat vertically? This thickening for only the greatest ΔR_{home} particles might still be just related to them experiencing weaker vertical restoring forces at the greater radii to which their guiding centers move at the outer edge of the disk.

The second group is for particles with negative ΔR_{home} that begin just outside of the inner Lindblad resonance. Due to the inner hole of the Mestel disk, the inner surface density is reduced making the vertical frequency comparable to the radial one and thus placing the inner $m = 2$ vertical resonance just slightly inside of the inner Lindblad one. Some of this vertical thickening and the fact that it is for inwards migrators is probably due to this inner hole as discussed above. However, the facts that the inwards migrators just inside the inner $m = 2$ vertical resonance do not thicken, and that there is an accompanying group of highly negative changes in rms z for the outwards migrators that start just inside this resonance point toward some other vertical heating mechanism, which perhaps is the inner vertical

resonance. The σ_z counterparts in Fig. 4.6 for these two groups of excessive vertical heating do not show any structure that stands out. No matter what the explanations for these two groups are, such regions probably exist for every transient spiral and add this localized disk thickening in addition to the affect of radial migration.

Yet what is responsible for vertical heating in the rest of the disk? Sellwood (2013a) recently found evidence suggesting that all disk simulations with moderate numbers of particles as ours suffer from relaxation due to two-body scattering, which thickens the disk over time; meaning that they are really not collisionless. He found that the amount of heating decreases for a greater number of particles. To test whether this is true in our simulations, we present the two simulations MSp and NSp that are similar to MS and NS, but contain an order of magnitude more particles. For NSp, we also increase the number of particles added per adding step by the same factor. As seen in Table 4.4, rms z for all the migrations increases less in MSp and NSp compared to their MS and NS counterparts even though the spirals have similar strengths (Fig. 4.2). Both greatest increases in rms z and greatest final σ_z encompass greater regions in Fig. 4.8 for NS than for NSp, while their characteristic trends are somewhat similar. Thus, vertical heating due to two-body scattering is present in our simulations as Sellwood (2013a) suspected. This effect is also likely present in the simulations of Roškar et al. (2013) and is not negligible since they use a similar number of particles to our simulation NSp.

This effect is milder in simulation M2p, because it only has forces calculated from the $m = 0$ and $m = 2$ sectoral harmonics, which essentially smooth the potential due to each particle making it less sharp. Hence, M2p is a good test of vertical heating mechanisms other than two-body relaxation.

Although this effect does not exist or is very weak in realistic galaxies, which have many more stars, scattering by giant molecular clouds yields noticeable vertical heating in them, which we do not account for in our simulations. So compensating for this real effect to some degree by having a false vertical heating mechanism at all radii is somewhat realistic. However, the two effects likely do not yield equal heating. Sellwood (2013a) suggested that were a population of extra-heavy particles mimicking GMCs to be included, then two-body scattering yields roughly the correct velocity ellipsoid in simulations with moderate numbers

of particles. Our simulations do not contain extra heavy particles.

4.5   Vertical profiles

We now wish to analyze the vertical profiles of the disks in our simulations, and check whether they suggest the presence of thicker disk populations in addition to the thin at final times.

For each of our disks, we construct one vertical profile averaged over the entire disk and separate profiles at varying radial annuli averaged over all azimuths at both the initial and final times. We find that the vertical profiles vary in a complex way with increasing radius between four different types of profiles. Fig. 4.9 illustrates these four types: single exponential ($\rho(|z|) = C_1 \cdot \exp(-|z|/h_1)$), sum of two different exponentials ($\rho(|z|) = C_1 \cdot \exp(-|z|/h_1) + C_2 \cdot \exp(-|z|/h_2)$), sum of a single exponential and a positive constant ($\rho(|z|) = C_1 \cdot \exp(-|z|/h_1) + C_2$), and the sum of a single exponential and a negative constant, in which C_1, C_2, h_1, and h_2 are all positive constants except C_2 is a negative constant in the last case.

We determine the best fits to the vertical profiles using the so called total-least-squares method: minimizing the sum of the squares of the minimum (perpendicular) distances from the points to the model. We omit the few points within $|z| < 0.2R_0$ for the exponential disk simulations and $|z| < 0.4R_0$ for the Mestel disk ones that depart down from the thin exponential term reflecting the $\mathrm{sech}^2 z$ nature of our disks' initial rounded-off exponential vertical profiles (eq. 2.5). We also omit bins with less than a hundred contributing particles. The profiles for the exponential disks include added particles. We weight each square vertical distance component by the number of particles contributing to the $|z|$ bin and by the reciprocal of the model ρ value at the mean $|z|$ of the particles in the bin in order to give all the points on the log $\rho(|z|)$ scale equal fitting importance. We also weight each square horizontal distance component by the reciprocal of the variance in $|z|$ of the particles in the bin. The simpler least-squares-vertical-distance method performs almost as well, but yields slightly larger errors.

We use bootstrapping with a thousand realizations to calculate 16 and 84 percentile
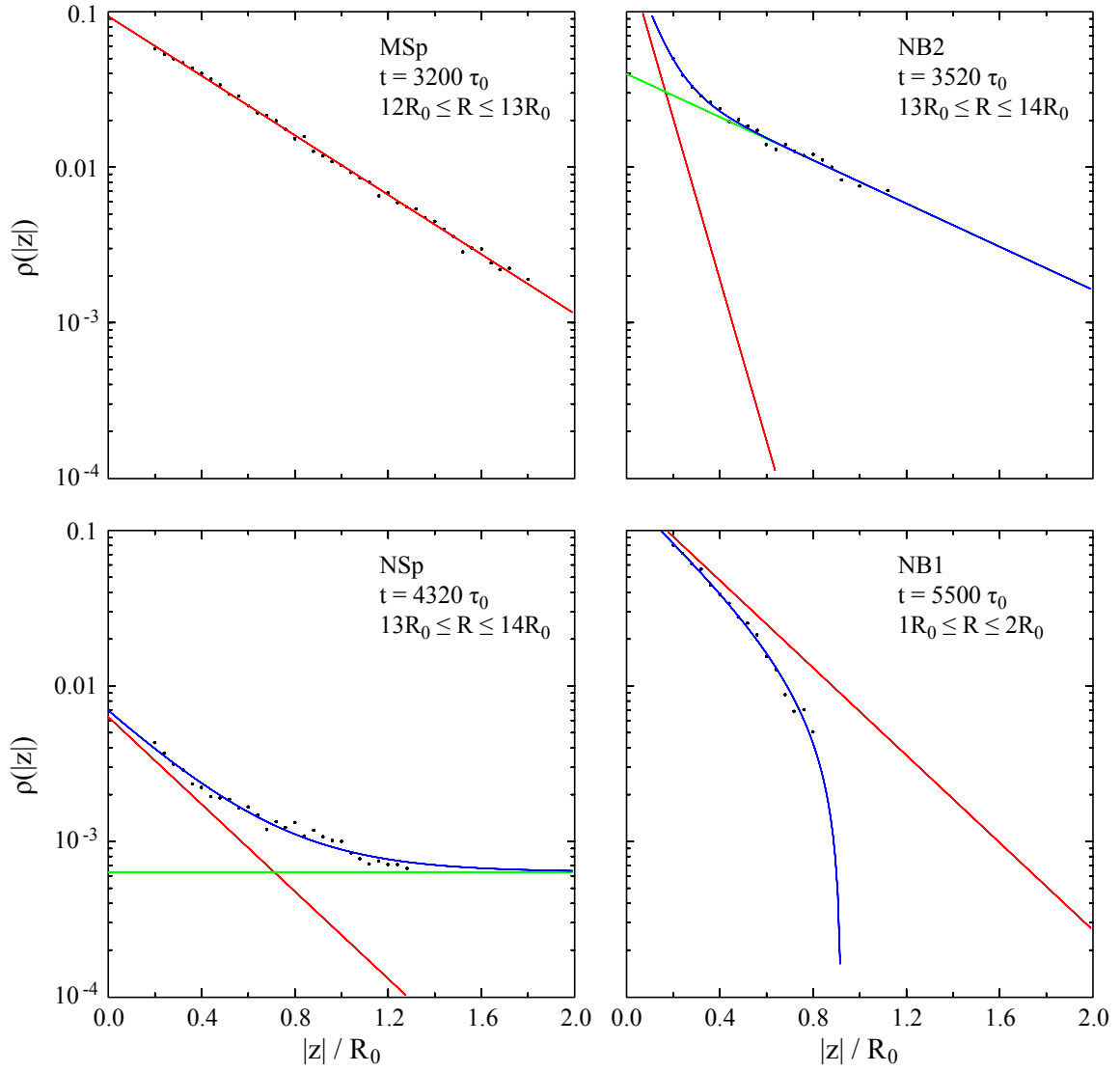
Figure 4.9 The four different types of vertical profiles seen in various radial annuli of our disks: single exponential (top left), double exponential (top right), exponential plus positive constant term (bottom left), and exponential plus negative constant term (bottom right). These particular examples are from the simulations, final times, and radial annuli listed at the top right corners of each panel. Each point corresponds to a small bin in $|z|$. We normalize the profiles by the total number of contributing particles. Red lines show the first exponential component of the best fit, green lines show the second component whether exponential or a positive constant, and the blue curves show the total best fit model. The negative constant term of the fourth profile type of course cannot be shown on the log plot; it has a value of $-0.0071 \pm^{0.0018}_{-0.0026} R_0$.

errors on the constants C_2, h_1, and h_2 of the best fit models and on the $|z|$ at equal density of the two components for the double exponential and positive constant second component profile types, which roughly marks the turnover height above which the thicker component dominates. This value is also roughly a proxy for whether the thinner or thicker component dominates the profile by mass fraction. For radial annuli not at the very edge of the disk, a $|z|$ at equal density of about $0.4R_0$ and less occurs for profiles with thicker dominant components, such as in the top right plot of Fig. 4.9, whereas values greater than this correspond to profiles with the thinner component dominating (bottom left plot of Fig. 4.9). Many of our profiles have dominant thicker components with mass fraction contributions sometimes as high as 80%.

The second constant component profiles are surprising, especially ones with negative constants, which obviously cannot be fit with a sum of two exponentials. Such negative constant second component profiles only appear in three barred simulations at a small radial annulus within the bar.

Trying to fit the positive constant second component profiles with double exponential profiles sometimes yields best-fit thick component scale heights on the order of $500R_0$, which is unreasonably high, and at other times gives reasonable scale heights, but with very large errors (also on the order of $500R_0$) or with skewed errors: both 16 and 84 percentiles are positive or both negative making the best fit parameters lie outside of them and far from the mean of the distribution. In the former case, the positive constant second component model is truly the better fit. But in the case of unrealistic errors, the double exponential profile is usually the better fit with a smaller minimum sum of total squares. Furthermore, visually, double exponentials should fit all of these profiles well. The problem likely relates to the fact that the double exponential has one extra fitting parameter compared to the positive constant second term profile, which allows for too much freedom resulting in many different double exponentials fitting the same vertical profile well. Thus, we report these cases as our model fitter finds to be of the positive constant term profile type, but keep in mind that they could also likely be fit well with a second exponential.

In principle, a sum of more than two exponential components could also fit these profiles well. Such models would portray the continuum of mono-abundance sub-populations picture

found by Bovy et al. (2012a). We do not try to fit our profiles with these more complicated models, since finding the best fit with just two components is already quite complicated, and our goal is to strictly determine whether any thicker populations exist in addition to the thinnest.

Figs. 4.10 & 4.11 show the best fit model parameters and how they vary with radius for the disks of every simulation. The profiles at initial times are all as expected: single exponentials with scale heights equaling z_0 as we set up. Deviations for simulations NS, NSp, and ISB occur when we increase the inner Toomre's Q by the procedure described in §4.2.2. All the simulations exhibit growth in the scale height of the thinnest component over time. The middle region annuli have thicker second components at final time in all the exponential disk simulations except NS and the barred simulation NB1, but exhibit single exponential vertical profiles in the Mestel disk simulations. These latter simulations have weaker spirals, which may be responsible for the absence of thicker second components.

The over-all-radii profiles of MS, MSp, and NS, which only have single exponentials at every annulus, show a second thicker component. So, when averaged over larger annuli, the profiles contain multiple populations, and we see this pattern in all of our simulations. The scale height of the single component in NS remains fairly constant with radius, so why is its over-all-radii profile a double exponential? The analogue NSp with ten times more particles, on the other hand, mostly contains profiles with second components at final time. The difference arises due to the better particle resolution and our cutoff of $|z|$-bins with less than hundred contributing particles, which mostly cuts off the greater $|z|$ tail in NS that thicker populations dominate. When averaged over all radii, more particles contribute to each $|z|$-bin in NS, and so the overall profile shows presence of the thicker populations. We confirmed that lowering the cutoff number of particles (twenty instead of hundred) brings up the second components in the middle radial annuli, but we report the profiles with the hundred particle cutoff for good statistics. This also likely affects the middle disk region of NB1 and the outermost few annuli in all the simulations, which contain less particles and therefore have single exponential profiles. These outermost annuli show some degree of outer-disk flaring in most of the simulations.

There is no single pattern of how the parameters of these double component profiles
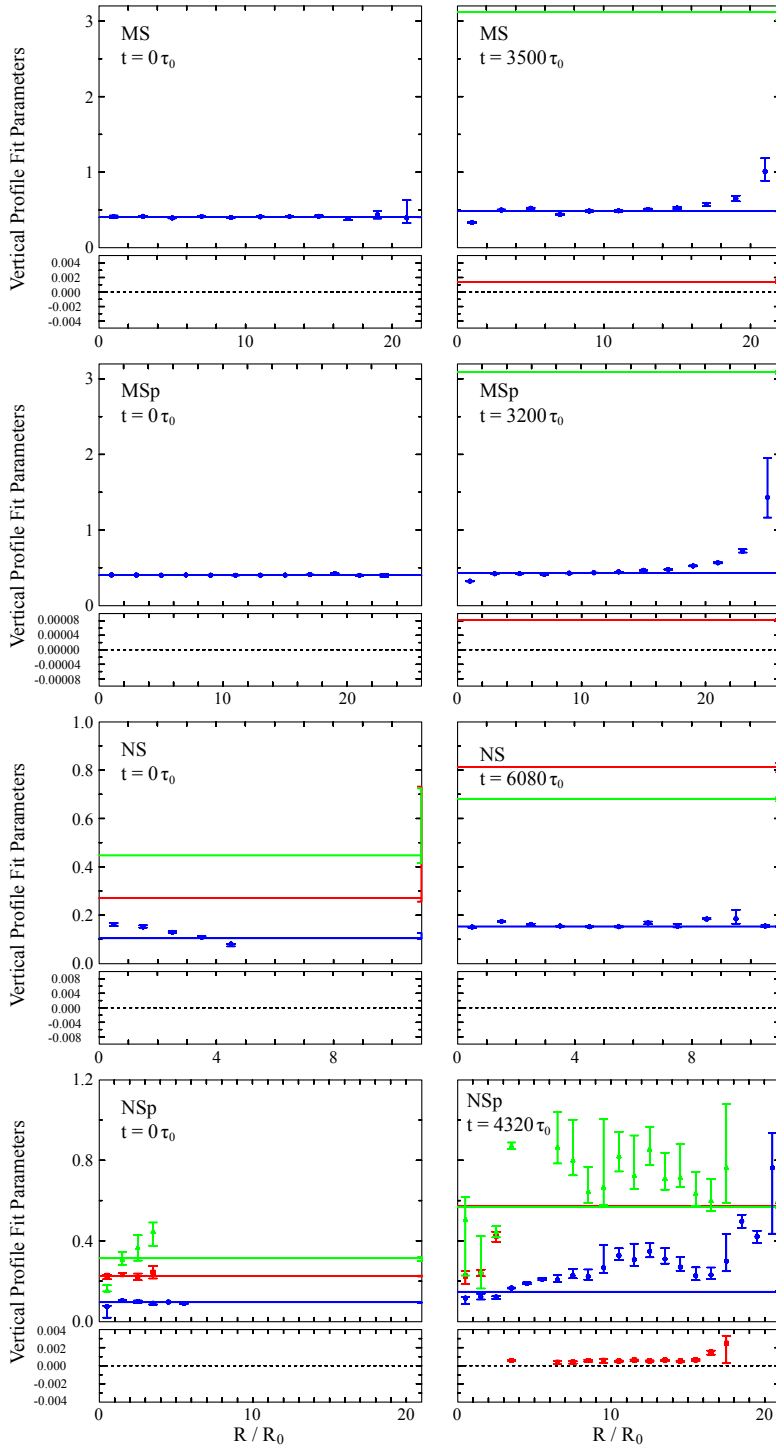
Figure 4.10 Best fit model parameters to the vertical profiles at different radial annuli of the disks of the spirals-only simulations MS, MSp, NS, and NSp at the listed times. Blue open circles show h_1, red open squares h_2 for double exponentials or C_2 for the second constant term, and green open triangles show the value of $|z|$ at equal density of the two components. Thus, if a radial bin only has a blue circle, its vertical profile is a single exponential, if the red square is above the blue circle, it is a double exponential, and if the red square appears below or in the bottom zoomed-in-around-zero panel, it has an either positive or negative constant second component. Also, negative constant term profiles do not have a green triangle. Horizontal blue, red, and green lines represent similar values of the best fit model to the entire disk averaged over all radii. Vertical error bars show 16 and 84 percentile bootstrap errors. Ones for the overall-radii fits appear at the right edges of the horizontal lines. The radial annuli have widths of $1R_0$ for the exponential disk simulations and $2R_0$ for the Mestel ones. Note that the scales on both axes differ between each simulation.

Figure 4.11 Same as Fig. 4.10 but for the barred simulations ISB, MB, NB1, NB2, and IB.

vary with radius between the simulations: in ISB the thin component scale height dips, in NSp and NB2 it form a hump, and in IB it remains fairly constant in the middle region. The main point, however, is that thicker populations form by the end of most of our more realistic exponential disk simulations.
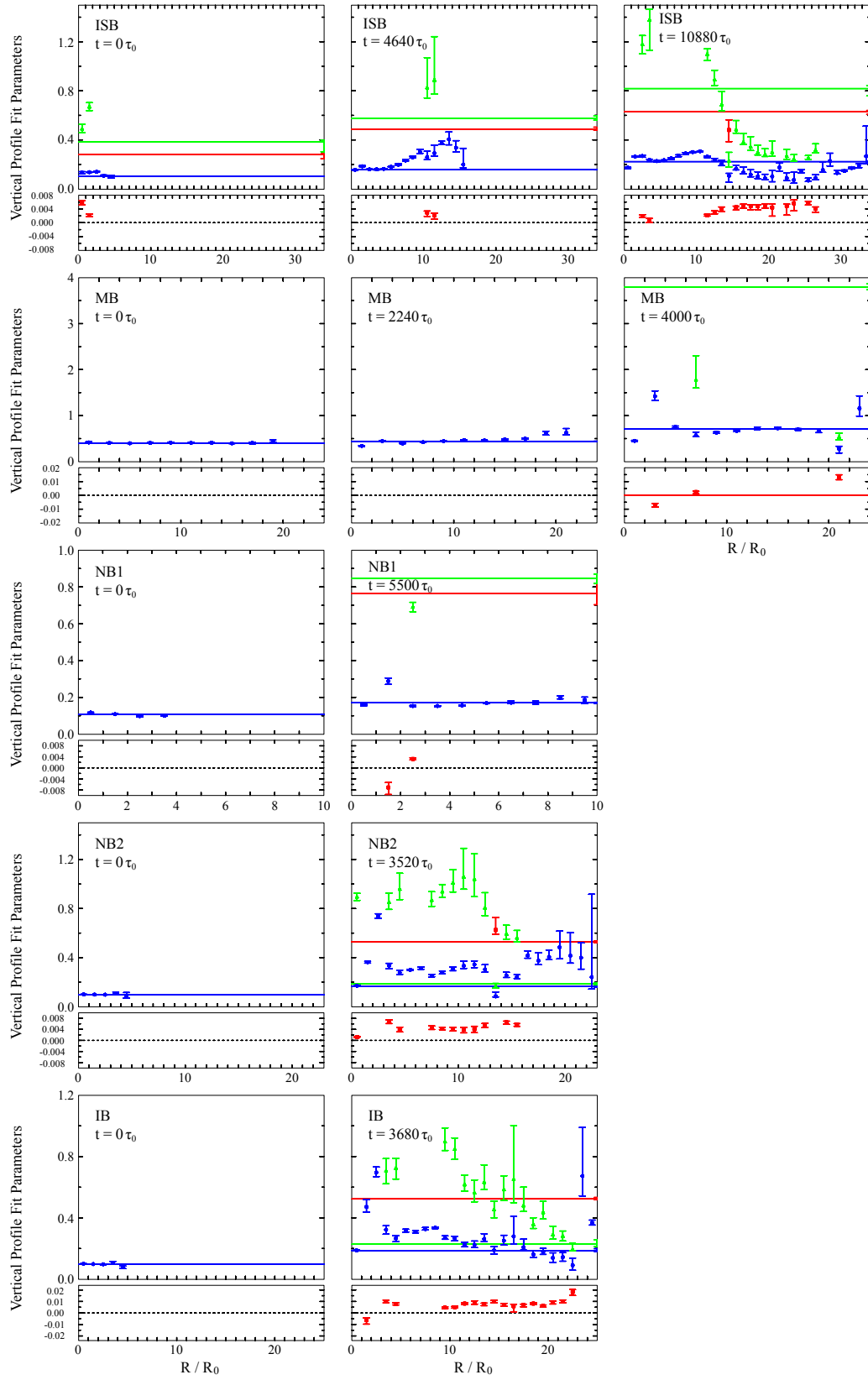
4.5.1 Formation radii of particles that constitute the thicker populations

Yet, only a small fraction of particles that compose these thicker populations migrate outwards from the inner region ($R \leq 5R_0$). The top left plot of Fig. 4.12 shows changes in home radii versus initial home radii of such particles for the radial annulus $[13R_0, 14R_0]$ of simulation NSp (corresponds to the bottom left plot of Fig. 4.9). Most of these particles migrate outwards, but only about 5% of the particles have initial home radii within $5R_0$. The same is true for the other middle region annuli of NSp with vertical profiles that contain thicker second components.

The story is a little different at the final time of simulation ISB: the bottom left plot of Fig. 4.12 shows that many more of the particles migrate inwards to the $[13R_0, 14R_0]$ radial annulus to build the thicker population compared to that in NSp. Accordingly, the fraction of those particles that migrate outwards from within $5R_0$ is smaller at about 2%. This is likely due to the fact that ISB has weaker spirals than NSp.

Thus, the thicker disk populations in our spirals-only simulations are mostly composed of particles that originate in the middle and outer regions, not in the inner one. The formation of thicker disks through radial migration outwards from the inner disk exists, but yields a minor negligible contribution, just as we found through other means in §4.3.

The middle two plots of Fig. 4.12 show changes in the maximum vertical extents $z_{\max}$ versus changes in home radii of these particles just discussed. The solid green mean and dashed blue median curves of the top plot for NSp have positive slope, which shows the effect of outwards radial migration. The slope of these curves for ISB in the bottom middle plot, however, is effectively zero. So, given the context of §4.3.5, the rate at which added particles increase the vertical restoring force in the middle region of the ISB disk is such that the vertical amplitudes of outwards migrating particles do not change due to radial migration. In both simulations, the average $\Delta z_{\max}$ are positive, so vertical heating is present.
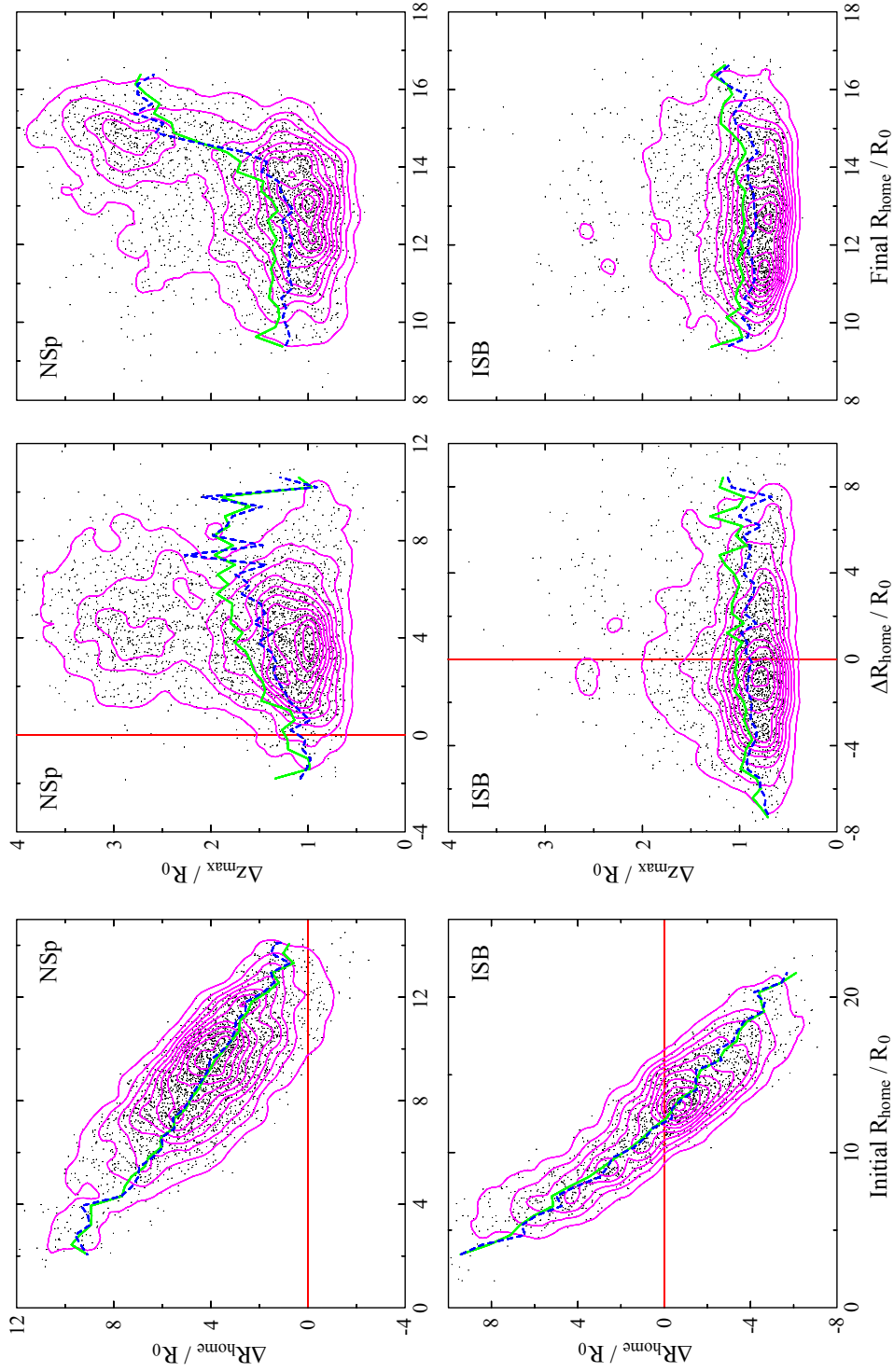
Figure 4.12 Changes versus initial R_{home} (left) and Δz_{max} versus ΔR_{home} (middle) and final R_{home} (right) of particles that lie in $|z|$ bins of the thicker component of the vertical profile for the radial annulus $[13R_0, 14R_0]$ of the final disk in NSp (top) and ISB (bottom). The smallest such $|z|$ bin for NSp is at height $0.6R_0$, and for ISB at $0.5R_0$. Green solid curves show the mean, blue dashed ones the median, magenta contours show linear number density at 95%, 85%, and so on, and the red lines marks zero changes in R_{home}.

Interestingly, the top middle plot of NSp shows two main groups of particles: ones with smaller and ones with bigger changes in z_{max}. Both experience similar positive ΔR_{home}, but the top right plot of Fig. 4.12 reveals that the group with greater Δz_{max} has greater final R_{home}. The particles lie in the radial annulus $[13R_0, 14R_0]$ based upon their instantaneous final radii, but they compose a larger range of final home radii, as the top right plot shows. These two groups are not distinct in the ages of particles: both contain particles from the entire range of ages (zero to the duration of the simulation). The top right plot shows that they are roughly separated by the final home radius value of $14R_0$, which is close to the break radius $13.7R_0$ between the middle and outer declining exponential parts of the radial surface density profile of the NSp disk at final time (Table 4.3). Furthermore, this break radius lies in the $[13R_0, 14R_0]$ annulus of final instantaneous radii of these particles. Therefore, the group with the greater Δz_{max} primarily corresponds to those particles that migrate outwards and cross this break radius, thus ending up experiencing a much weaker vertical restoring force due to the much steeper declining outer exponential part of the surface density. In the case of ISB, the final break radius lies at $27.7R_0$, which is well outside of $[13R_0, 14R_0]$. Hence, the bottom middle and right similar plots of Fig. 4.12 do not contain a second group of particles with greater vertical amplitude increases.

4.5.2 Variation of vertical profiles with age

Finally, we study how the vertical profiles vary with age to see if their scale heights increase with age as Bovy et al. (2012c), Bird et al. (2013), and Stinson et al. (2013) found. Populations of increasing age automatically have decreasing radial length scales in our simulations due to our inside-out prescription of adding particles. We do this analysis only for simulation NSp, in which the number of particles is high enough. Fig. 4.13 shows plots of best fit vertical profile parameters similar to Figs. 4.10 & 4.11 for four different age groups of particles in NSp at varying radial annuli of widths $3R_0$. The four age groups are $0-1{,}320\tau_0$, $1{,}320-2{,}320\tau_0$, $2{,}320-3{,}320\tau_0$, and $3{,}320-4{,}320\tau_0$. With our suggested scaling to physical units, each $1{,}000\tau_0$ duration equals 3 Gyr. The last group includes the original particles all of whose age is $4{,}320\tau_0$.

The plots do show evidence of older populations having greater scale heights, but it is not
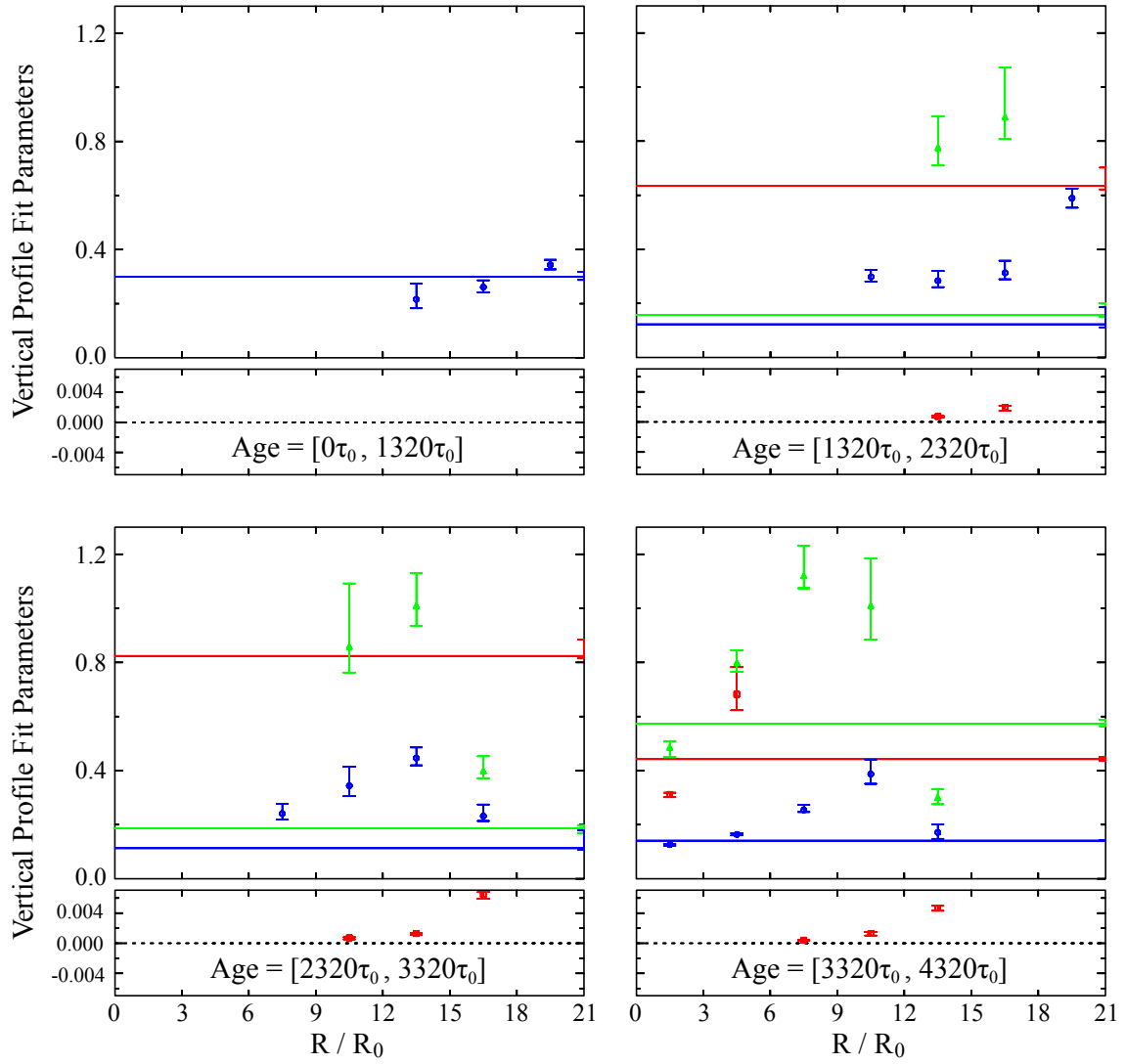
Figure 4.13 Same as Fig. 4.10 but for the four different age groups $0 - 1{,}320\tau_0$ (top left), $1{,}320 - 2{,}320\tau_0$ (top right), $2{,}320 - 3{,}320\tau_0$ (bottom left), and $3{,}320 - 4{,}320\tau_0$ (bottom right) of simulation NSp at radial annuli of width $3R_0$.

directly obvious and requires an explanation. The total profiles averaged over all radii do not show this trend. Comparing the different age groups at a given radial annulus, however, shows an increase in the dominant component's scale height with increasing age. For most annuli, the dominant component is the thinner one. The exceptions are the outermost annuli of the two oldest groups, in which the scale height of the thin component is smaller, but that of the thick component is considerably bigger, and the thick component dominates the vertical profile by mass fraction substantially.

It is interesting that, in each age group, the scale height of the dominant component increases with radius, which one might argue shows the opposite trend since due to our inside-out addition of new particles greater radii might contain more younger particles. However, radial migration mixes the formation radii making this reasoning incorrect.

Another interesting feature revealed in these plots is that the youngest age group is composed only of single exponential profiles, whereas in the older groups, thicker second components prevail. We find that this trend of older populations having greater scale heights does not come about from an upside-down vertical formation as Bird et al. (2013) suggested. In our simulations, we explicitly placed every new particle in the midplane of the disk. Hence, the secular evolution and dynamics cause the older populations to thicken more over time and give rise to this trend observed by Bovy et al. (2012c) in the Milky Way.

4.6 Summary of whether radial migration produces thick disks in our simulations

We showed that, in our N-body simulations of Mestel and more realistic exponential disks that only have spirals and no bar, about $15 - 20\%$ of particles that begin in the inner disk region (about one final disk scale length from the galactic center) manage to migrate out of it by the end of the simulations. So, outwards radial migration from the very inner region exists.

However, very few ($\lesssim 0.05\%$) of the particles that begin in the inner region migrate out to beyond two final disk scale lengths (our rough analogue of the inner boundary of the

solar neighborhood). Thus, radial migration is not powerful enough in producing thick disk components at the middle and outer disk regions in our simulations. Indeed, the majority of the particles that make up the thicker disk in these regions by the end of our simulations are ones that begin in those regions. Also, our exponential disk simulation, in which we add new particles, do not produce thick enough populations that would correspond to the Galactic thick disk in the solar neighborhood.

We attribute both problems to the strengthening of the vertical restoring force in the middle and outer regions of the exponential disks caused by our addition of particles in the midplane at those regions while not adding new particles in the inner region.

Just as Roškar et al. (2013), we found that both radial migration and vertical heating due to spiral vertical resonances and more so two-body relaxation (Sellwood 2013a) contribute to the increase in the vertical amplitudes of the particles. There is no clear cut answer to how much each contributes, and it varies between the simulations. We ran similar simulations with an order of magnitude more particles, but found no significant decrease of vertical heating in them.

We observed the initial and final vertical profiles of the disks, both averaged over all radii and separately in varying radial annuli. We fitted them with single exponential, double exponential, or single exponential plus a constant term functions depending on which one fit each profile best. The profiles exhibit a complex structure and a nontrivial variation with radius. Nevertheless, they do contain or show evidence for second thicker components by final time. We tracked the particles contributing to the thicker populations in the middle and outer annuli, and confirmed the same result that the majority did not migrate from the inner disk regions. We also found, like Bovy et al. (2012c), Bird et al. (2013), and Stinson et al. (2013), that older populations tend to have greater scale heights, although in our simulations it is not as clear cut.

We caution that the whole business of fitting profiles with double exponentials is cumbersome, and it is not easy to get meaningful values of scale heights. This is mainly due to the fact that, often, a big range of scale heights and normalization coefficients can fit a single profile. Nonetheless, one can easily tell, even by eye, whether a profile is more than just a single exponential and compare whether two profiles have similar scale heights or

which one is greater. Also, a good double exponential fit does not imply that the profile is a sum of two disks: one thin and the other thick. A sum of three or more exponential components could probably fit it just as well if not better due to the finer tuning possible from the extra parameters. Hence, our results neither favor nor oppose the decomposition of the Milky Way stars into a continuum of mono-abundance sub-populations found by Bovy et al. (2012a,c,b).

We suspect there are not enough extreme migrators from the inner region in our simulations because the spirals are not strong enough. Also, they do not occur long enough at small radii. Furthermore, we believe that including the production of new stars in the inner region in our simulations, where most of the star formation in real disk galaxies actually happens, would raise the fraction of extreme migrators from the galactic center. Adding mass in the inner region would also increase these particles' final vertical amplitudes after outwards migration, because the inner disk would remain significantly denser than the outer regions allowing these particles to experience significant decreases in the vertical restoring force. We omitted such additions because our main task was to test the ability of bars to suppress outwards radial migration from the inner region, adding particles inside the bar is not trivial, and we put up spirals-only simulations as similar to the barred ones as possible for fair comparison. Likely, the simulations of other groups, such as Loebman et al. (2011), that do produce realistic thick disks through radial migration manage to do so because of the presence of stronger spirals and the inclusion of this central star formation.

We are continuing to try to generate simulations with stronger spirals that do not form a bar and have longer periods of spiral activity at smaller radii in order to see whether the fraction of extreme outwards migrators from the inner disk region is noticeably greater under such conditions. Also, we are considering simulations with a secondary addition of particles in the inner region, so that the vertical restoring force increases there too. Finally, we are running simulations with even more particles than NSp to check whether vertical two-body relaxation heating decreases in them.

Chapter 5

Suppression of outwards radial migration capable of producing thick disks by bar formation

In our simulations, outwards radial migrators from the inner region do not make up the majority of thick disk particles in the middle and outer regions at the end of the simulations, and more importantly our more realistic exponential disk simulations do not form realistically thick enough disks in the solar neighborhood compared to the Milky Way. Yet, other groups' simulations manage to form thick disk populations through outwards radial migration that resemble the Milky Way thick disk (*e.g.* Loebman et al. 2011; Brook et al. 2012) even though they also contain vertical heating (Roškar et al. 2013). Although Loebman et al. (2011) and Brook et al. (2012) reproduced the metallicity and circular velocity trends with height observed in the Milky Way, the age trend resulting from their simulations, which do not contain a long-lived bar, implies a younger mean age with a broader 2σ envelope for the thick disk than is observed (*e.g.* Bensby et al. 2003; Haywood et al. 2013). So, whether bar formation can suppress this migration from the inner region and yield a thick disk with no stars younger than the bar, is still interesting. It could also explain the metal-poor dominated outer disk observed by Haywood et al. (2013).

Theoretically, stars should not migrate out of a steady bar, because a bar is not a transient feature and traps stars about its Lagrange points. Stars that are at the outer tip of the bar should keep oscillating about its corotation endlessly, and on average come back to their initial radii due to the long, if not indefinite, lifetime of the steady bar. Transient spirals cannot penetrate into the bar, because the bar is a much stronger amplitude feature. Yet, they could pick up stars found outside of the bar's corotation and scatter them further outwards. The important point, however, is that many of the other stars within the bar should never cross corotation, because the potential well of the bar traps those stars that do not have enough energy to escape it. This includes new stars that are born within the bar. Real and simulated bars are not steady, but evolve slowly.

Hence, we proceed by defining inner and outer regions in our barred simulations similar to the ones in §4.3.1, and track how many of the particles that are inside the inner bar region just shortly after the bar forms manage to migrate out of it by final time.

5.1 Particles in a rotating potential

In a steadily rotating potential (BT08, §3.3.2), such as that of a bar, the effective potential (BT08, eq. 3.114) in the frame rotating with the bar offers a natural definition of the inner and outer regions. The Lagrange points L_1 and L_2, which lie along the bar and the long axis of the potential at corotation, are saddle points (Fig. 1.8; BT08, Fig. 3.14). The equipotential contour they lie on bounds particles. The green curve in Fig. 5.1 shows the effective potential Φ_{eff} as a function of radius at the azimuth along L_1 averaged with that along L_2. The two halves differ very little, but we average them anyways. This effective potential achieves a maximum Φ_{crt} at $R_{L_{1,2}}$ due to the repulsive centrifugal term overtaking the gravitational potential at larger radii.

Particles conserve neither their energies nor their angular momenta in this potential, but they do conserve their Jacobi integrals $E_J = E - \mathbf{\Omega_b} \cdot \mathbf{L}$. They are forbidden to reside in the area under the Φ_{eff} surface. Ones with $E_J < \Phi_{\mathrm{crt}}$ cannot cross $R_{L_{1,2}}$ and remain trapped either within $R_{L_{1,2}}$ or outside of it, whereas particles with $E_J \geq \Phi_{\mathrm{crt}}$ are not bound and can in principle move through $R_{L_{1,2}}$. The latter ones are not guaranteed to escape, however, because the Coriolis force does not allow particles to accelerate steadily in the $-\bigtriangledown\Phi_{\mathrm{eff}}$ direction. Thus, $R_{L_{1,2}}$ and Φ_{crt} naturally mark the boundary of the four quadrants shown in Fig. 5.1 in red.

However, just as before, we want to assign particles to a region not based upon instantaneous radii at the analysis time, but based upon the minimum and maximum radial excursions of their orbits so as to ensure that they completely remain in their quadrant. This time, we integrate their orbits for about hundred full radial periods in the frozen potential of the analysis time rotating steadily at the pattern speed of the bar measured at that time. During these integrations, the Jacobi Integrals of our particles remain very well conserved. We define the following six regions, and assign particles to them based upon their Jacobi integrals and radial extrema:

I	$E_J \geq \Phi_{\mathrm{crt}}$ and $R_{\min} \geq R_{L_{1,2}}$
II	$E_J \geq \Phi_{\mathrm{crt}}$ and $R_{\max} < R_{L_{1,2}}$
III	$E_J < \Phi_{\mathrm{crt}}$ and $R_{\max} < R_{L_{1,2}}$
IV	$E_J < \Phi_{\mathrm{crt}}$ and $R_{\min} \geq R_{L_{1,2}}$
V	$E_J \geq \Phi_{\mathrm{crt}}$ and $R_{\min} < R_{L_{1,2}}$ but $R_{\max} \geq R_{L_{1,2}}$
VI	$E_J < \Phi_{\mathrm{crt}}$ and $R_{\min} < R_{L_{1,2}}$ but $R_{\max} \geq R_{L_{1,2}}$.

Theoretically, there should be no particles in region VI for a steady bar. We find very small numbers residing in it, which is due to slow variations of our bars. Therefore, from here on, we do not report any results about region VI. We find that, at all times, region III contains roughly 35% of all the particles in MB and between 50% and 60% of all the original particles in the exponential disk simulations.

In Fig. 5.1, we plot the particles' Jacobi integrals versus their instantaneous radii shortly after the bar forms at time $480\tau_0$ in simulation NB1. Agreeing with theory within our approximations, very few particles lie below the green Φ_{eff} curve.

We focus on the original particles in our analysis, and do not include any new added particles in the exponential disk simulations except ISB. As we mentioned earlier, our particle adding prescription intentionally avoids placing new particles within the bar. In all the exponential disk simulation except ISB, the bars form early, which yields a small number of new particles added from start till bar formation. In ISB, we include all the particles added before each initial analysis time.

5.2   Fraction of particles remaining trapped by the bar

Our task now is to track in which region each particle ends up in at the final time. We do not use the same regions as at the bar formation time, but redefine the six regions in the same way based upon the new effective potential, bar pattern speed, and bar phase at the final time. This is important because the bar parameters change slowly during the simulations, which we discuss in more detail in the next section.
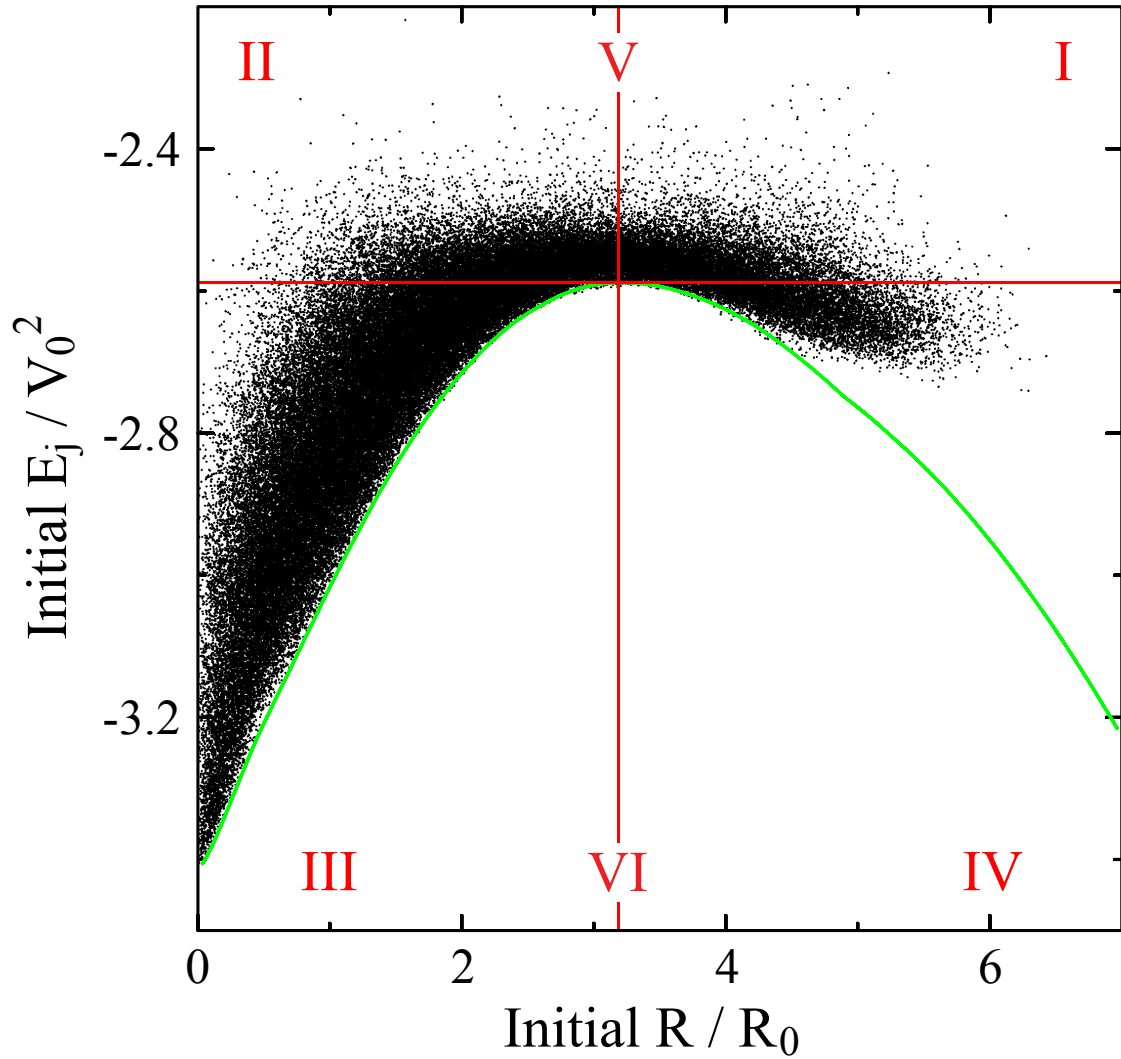
Figure 5.1 Specific Jacobi integrals versus instantaneous radii of the particles in NB1 shortly after the bar forms at $t = 480\tau_0$. The green curve shows the effective potential in the frame rotating at the bar pattern speed averaged between the two azimuths of the arms of the bar along its major axis as a function of radius. Red horizontal and vertical lines intersect at the maximum point of the effective potential and show the boundaries defining the six regions labeled in red.

We are interested in what happens to the particles in region III, the ones trapped within the bar, especially those deep in the bar's potential well with small Jacobi integrals. When the bar forms, particles in region II and V that are within the bar but not trapped by it are free to continue migrating outwards and populating the thick disk, but they are all at least as old as the bar, so they will not make the thick disk younger. We also expect a small number of particles closest to $R_{L_{1,2}}$ with greatest E_J to escape from region III due to fluctuations in the bar potential. However, ones in the inner bar region that are deep in the potential well should not escape at all. New stars that form later in the central galactic region within the bar, which is the region dense enough to produce the 10%-mass contributing Galactic thick disk through radial migration, will belong to this trapped group. If our hypothesis is correct, these stars will remain trapped by the bar till present time never migrating to populate the thick disk, which would explain why the Galactic thick disk is old, given that thick disk populations form primarily through outwards radial migration when only spirals are present, and not through vertical heating or non-secular mechanisms.

The third column in Table 5.1 shows our findings that in the exponential disk simulations $\sim 13\%$ and in MB 7% of particles originally in region III escape it by the final time over the entire duration from shortly after the bar forms till the end of each simulation. We also calculate this percentage over intermediate interesting sections during which the bar amplitude behaves differently. As expected, we find that the percentage is lower than over the entire bar duration, and, overall, more particles escape region III during longer durations in a given simulation.

As seen in Fig. 4.2, in MB, the bar amplitude oscillates a lot most likely due to beating with the outer spirals. In ISB, it first remains constant for some time, and then at about $6{,}720\tau_0$ begins to oscillate up and down, but at a time scale much longer for the oscillations to be caused by beating with spirals. Less particles escape region III during the first rise of the amplitude from $6{,}720\tau_0$ to $7{,}040\tau_0$ than during the preceding constant-amplitude interval from $6{,}080\tau_0$ to $6{,}720\tau_0$ and the succeeding decreasing amplitude between $7{,}040\tau_0$ and $7{,}520\tau_0$, as one would expect. In NB1, the amplitude remains somewhat constant, and then at time $\sim 3{,}850\tau_0$ begins to grow eventually asymptoting to a greater constant value by the end of the simulation. Again there are fewer escapers during this amplitude growth.

Table 5.1 Percentage of migrators from the trapped region III within the bar

Sim.	RG.	% of migrators from III between times $t_i/\tau_0 \to t_f/\tau_0$				
MB		2,560→4,000				
	I	0.0%				
	II	4.1%				
	III	93.2%				
	IV	0.2%				
	V	1.9%				
NB1		480→5,500	480→3,840	3,840→5,500		
	I	0.7%	0.5%	0.1%		
	II	4.0%	3.8%	2.9%		
	III	86.9%	87.7%	95.6%		
	IV	1.8%	1.5%	0.1%		
	V	6.0%	5.9%	1.4%		
NB2		320→3,520	320→1,120	1,120→1,200	1,200→3,520	
	I	0.1%	0.1%	0.0%	0.0%	
	II	7.0%	5.2%	2.3%	5.8%	
	III	87.8%	92.2%	97.6%	91.8%	
	IV	0.4%	0.3%	0.0%	0.0%	
	V	3.0%	2.2%	0.1%	1.5%	
IB		160→3,680	160→262.4	262.4→368	368→3,680	
	I	0.2%	0.0%	0.0%	0.0%	
	II	7.0%	3.4%	3.1%	6.3%	
	III	87.6%	95.3%	96.3%	91.2%	
	IV	0.4%	0.1%	0.0%	0.1%	
	V	3.2%	1.1%	0.6%	1.9%	
ISB		6,080→10,880	6,080→6,720	6,720→7,040	7,040→7,520	7,520→10,880
	I	0.2%	0.0%	0.0%	0.0%	0.1%
	II	10.2%	4.5%	1.9%	3.7%	8.6%
	III	86.0%	94.8%	98.0%	95.9%	89.1%
	IV	0.1%	0.0%	0.0%	0.0%	0.1%
	V	3.4%	0.6%	0.1%	0.3%	2.1%

Each entry in columns three through seven in the second through sixth rows of each simulation, which is listed in the first row, give the percentage of particles originally in region III at time t_i that end up in the region listed in the second column at time t_f. The first row of each new simulation lists these initial and final times. The third column is for the entire duration from just after the bar forms till the end of the simulation, whereas the rest are for interesting intermediate sections. Note that the percentages in each column of each simulation do not always add up to 100% due to a very small number of particles that escape the grid, mostly vertically, either during the simulation or during the orbit integration in the rotating frozen potential at final time.

IB and especially NB2 are the most interesting with amplitudes dropping drastically in a very short duration at times $\sim 300\tau_0$ and $\sim 1{,}150\tau_0$ respectively. We checked that, surprisingly, these drops are not at all associated with buckling of the bar, but rather with an unfortunate combined orientation with a very strong outer spiral mode. The spiral arms originate just ahead of the bar in phase, and gradually switch to trailing it. Sellwood (2013b) suggests that in this scenario, the gravitational stresses of the spirals onto the bar cause the bar to gain angular momentum from the spirals making the bar weaker, which is likely what causes the bars to weaken abruptly in IB and NB2. Yet, during these drastic amplitude drops, the percentage of particles that remain trapped in region III is very high at $\sim 97\%$, which is likely because these are such short duration changes.

Of the particles originally in region III that escape it by final time, which is at most 14%, the majority end up in region II which is still within the bar, and only about 4% actually migrate outside of the bar to regions I, IV, and V. Simulation NB1 is the only exception with 8.5% of the escapers ending up in these three outer regions, but even of these, 6% are in region V having pericenters inside $R_{L_{1,2}}$. The top row of Fig. 5.2 shows that, in NB1, most of these escapers have borderline Jacobi integrals close to the Φ_{crt} value and home radii close to $R_{L_{1,2}}$ initially at time $480\tau_0$. Even though tails of intermediate E_J and R_{home} within the bar exist, the main point is that none of the particles in region III with small Jacobi integrals and small inner home radii escape the bar potential. This holds true for the escapers in the other barred simulations too. Therefore, bar formation does stop the outwards radial migration of future forming stars from the dense central galactic region necessary to form thick disk populations in the middle and outer galactic regions.

Our bars remain intact till the end of the simulations and likely would exist forever were we to run the simulations further. Once a bar forms, it is very hard to destroy it in isolated disks. Also, the fraction of barred galaxies has increased by roughly a factor of 2 for intermediate stellar mass galaxies and stayed the same for massive ones ($M > 10^{11} M_\odot$) since $z \sim 1$ (Elmegreen et al. 2004; Jogee et al. 2004; Sheth et al. 2008; Barazza et al. 2009; Nair & Abraham 2010; Cameron et al. 2010), but has surely not gone down. Hence, outwards radial migration from the inner region never resumes after a bar forms and shuts it off.
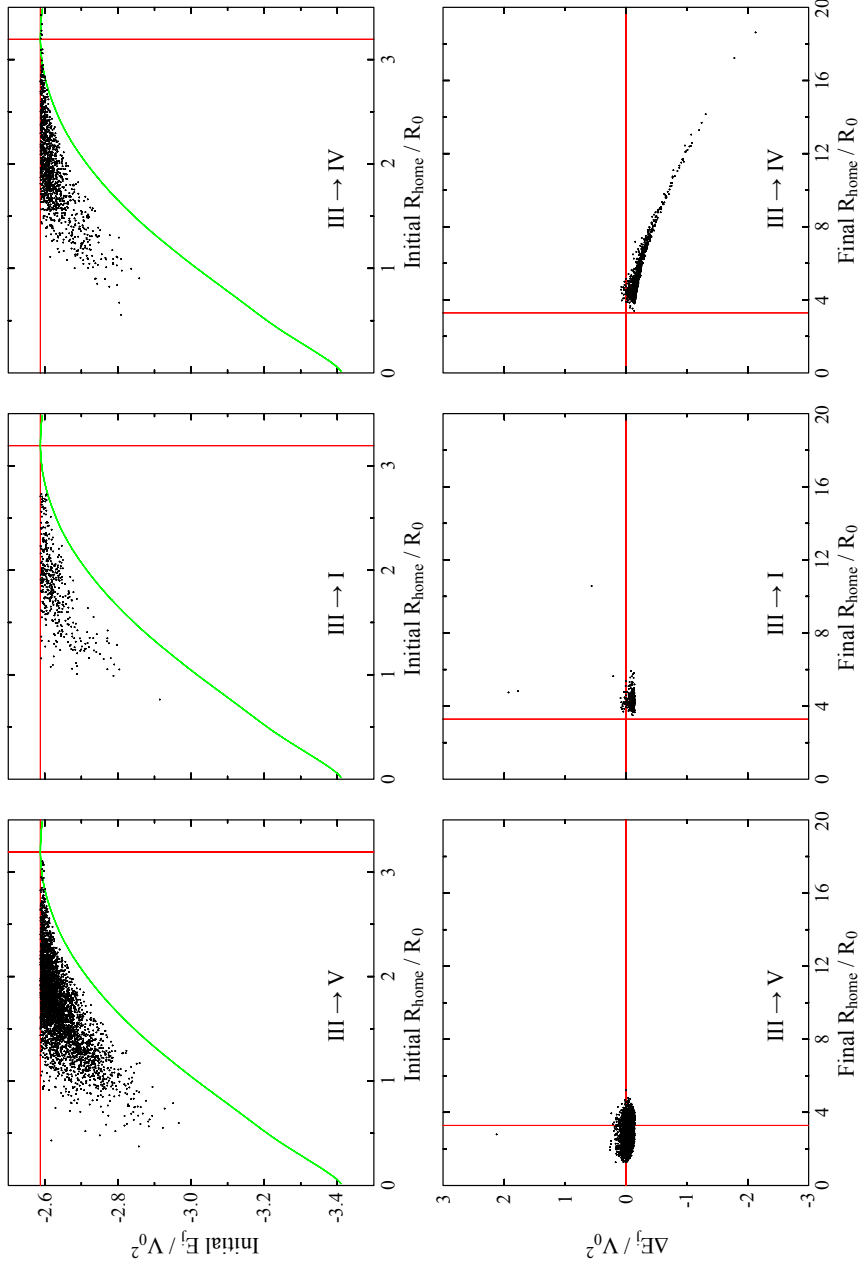
Figure 5.2 Top plots show initial E_J versus initial R_{home} measured shortly after the bar forms at $480\tau_0$ in simulation NB1 for the particles that are in region III at this initial time, but escape it to the regions specified at the bottom of the plots by the end of the simulation. Red horizontal and vertical lines mark the location of Φ_{crt}, and the green curve shows Φ_{eff}. Note that these plots differ from Fig. 5.1 in that they show home radii and not instantaneous ones. The bottom row shows changes in E_J between these two times versus final R_{home} for these particles and corresponding migrations from region III. In these plots, the red horizontal lines mark zero changes in E_J and the vertical ones the location of $R_{L_{1,2}}$ at final time, which barely changes from the initial one. Note also that here we use enlarged dots to represent the particle data compared to in Fig. 5.1 so that the fewer dots remain visible.

The bottom row of Fig. 5.2 shows where the escapers from region III end up and how their Jacobi integrals change. The ones that migrate to regions V and I remain near the bar corotation and their E_J are mostly conserved, except for a few particles whose Jacobi integrals increase a lot. As for those that migrate to region IV, they form a tail of outwards migrators with decreasing E_J, but barely populate the thick disk beyond radius $12R_0$: only $\sim 0.02\%$ of particles originally in region III escape and migrate outwards to within and beyond the solar neighborhood. Once these particles escape the bar potential, they get scattered by spirals and gain angular momentum by radially migrating outwards, which decreases they Jacobi integral in the frame steadily rotating with the bar.

5.3   Changes in bar parameters over time

Why do the bars allow some particles in region III to escape? As time goes on, bars undergo changes that cause Φ_{crt} to increase or decrease and $R_{L_{1,2}}$ to move about slightly. When Φ_{crt} drops, particles with initially borderline E_J become free to escape the bar potential if $E_J \geq \Phi_{\mathrm{crt}}$. Also, when $R_{L_{1,2}}$ decreases, particles near their apocenters with apocenters just less than the original $R_{L_{1,2}}$ can end up outside of region III.

Fig. 5.3 shows how the bar pattern speed Ω_b, Φ_{crt}, $R_{L_{1,2}}$, corotation radius, and the bar semi-major axis vary with time for all the barred simulations. We measure the bar pattern speeds and corotations using the method described in Sellwood & Athanassoula (1986). Bar phases, which we use to get the effective potential along the bar major axis and thus Φ_{crt} and $R_{L_{1,2}}$, we get by calculating the arctangent of the ratio of the imaginary part to the real part of the $m = 2$ density Fourier coefficients: $\arctan[\Im(A_2)/\Re(A_2)]$. We also calculate the pattern speeds with a second method of linearly fitting the phases as a function of time over short local periods of time. The two methods agree very well with each other. Finally, the lengths of the semi-major axes, we estimate from where the amplitude departs from a linear decline similarly to how Debattista & Sellwood (2000) did. We do not report bar lengths measured by where the phase departs from being constant since this method yields very poor results muddled by the phases of the spirals that coincide with that of the bar from time to time. As seen in Fig. 5.3, the amplitude method also does not always give solid results. We find, as Debattista & Sellwood (2000) did, that the amplitude method

tends to underestimate the visual bar length slightly most of the time, but also sometimes overestimates it as seen by spikes in NB2 and IB.

The value of Φ_{crt} does not change much during the simulations, but exhibits some noticeable gradual declines and increases and fluctuations in the case of MB. $R_{L_{1,2}}$ fluctuates more in MB, and increases in NB1 when the bar amplitude increases after time $3{,}840\tau_0$, but only undergoes small changes in the other three simulations. Φ_{crt} mostly declines gradually in NB1, NB2, IB, and ISB, but gradually increases in MB modulo the small fluctuations. Accordingly, from Table 5.1, the percentage of escapers from region III in MB is smaller than in the four declining Φ_{crt} simulations. Also, in NB1, the percentage is smaller for when Φ_{crt} and $R_{L_{1,2}}$ increase during the amplitude increase after $3{,}840\tau_0$ compared to before this time when Φ_{crt} decreases. These results somewhat agree with our expectations that more escapers escape region III during declines in Φ_{crt}, although there is still the fact that the greatest percentage of escapers corresponds to the longest durations we test. We do not have a clear declining $R_{L_{1,2}}$ case to test whether there are more escapers during it than when $R_{L_{1,2}}$ grows or remains constant.

The bottom row of Fig. 5.3 shows that our simulations both have small and large and fast and slow bars. The ratios of $R_{L_{1,2}}$ to the bar semi-major axis just when the bars form are 1.3, 1.4, 1.4, 1.1, and 2.0 for MB, NB1, NB2, IB, and ISB respectively, and change with time according to the plots. Ratios between 1 and 1.4 are more realistic (Contopoulos 1980; Athanassoula 1992; Weiner & Sellwood 1999; Debattista et al. 2002; Aguerri et al. 2003; Corsini 2008), but very slow bars also exist (Chemin & Hernandez 2009). Our halos are rigid, so we are ignoring dynamical friction between the bar and the halo, which would slow the bars down (Debattista & Sellwood 2000). We also omit gas and thus ignore inner flows of gas along the bar that could speed it up by transferring angular momentum to it.

Thus, no matter how the bar amplitude and Φ_{crt} behave, whether in a Mestel or exponential disk, with an NFW or isothermal halo, whether with a weak or strong, large or small, or fast or slow bar, whether with a bar that forms right away from a vigorous bar instability or later by growing from particle noise, and whether with weak or strong outer spirals, our results agree with theory that the bar is efficient at keeping particles trapped at the galactic center and deep in its potential well of region III.
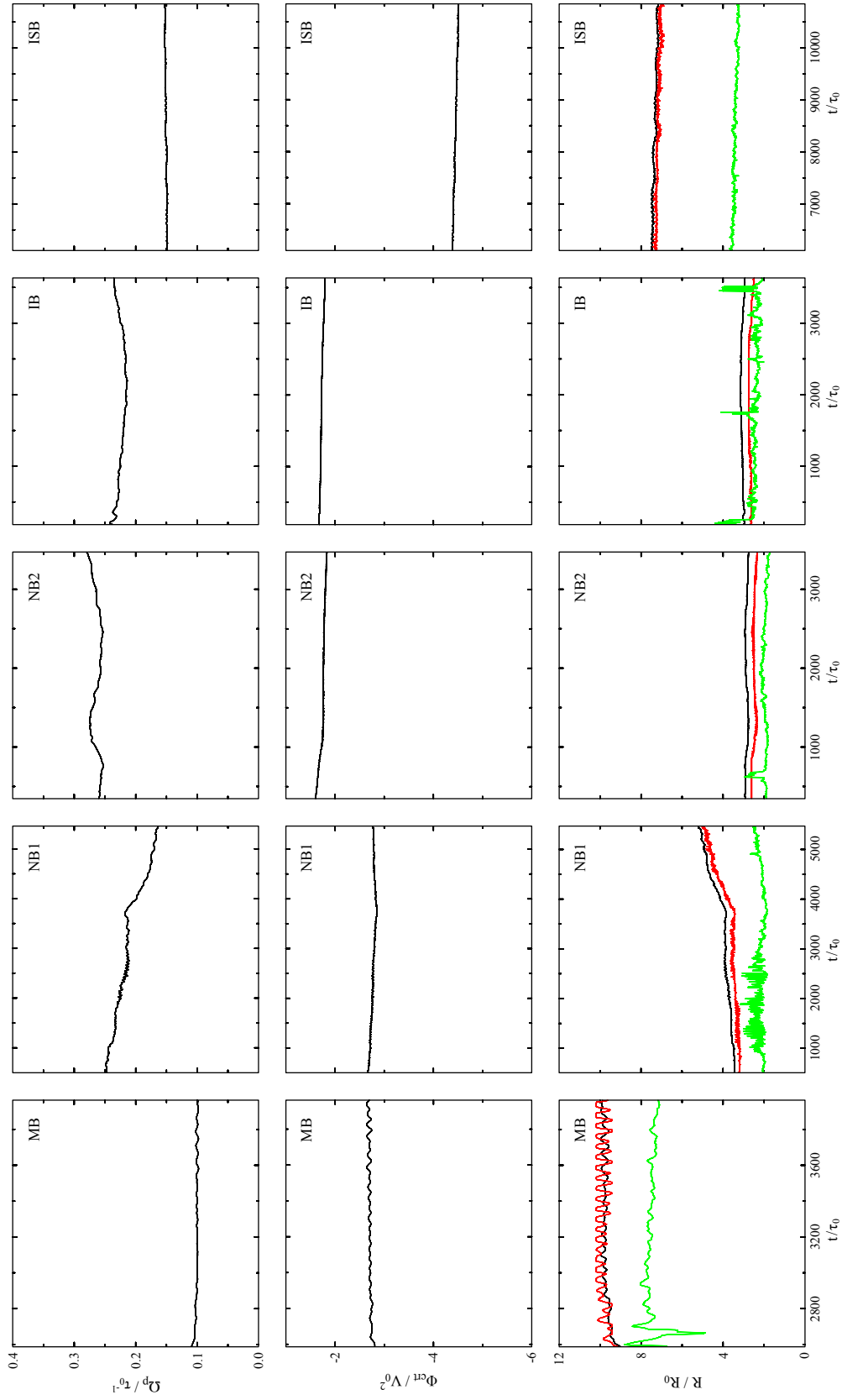
Figure 5.3 Temporal variation of the bar pattern speed (left column), $\Phi_{\rm crt}$ (middle column), $R_{L_{1,2}}$ (red curve in right column), corotation radius (black curve in right column), and the bar semi-major axis (green curve in right column) in simulations MB, NB1, NB2, IB, and ISB from top to bottom respectively.

5.4 Summary of the suppression of outwards radial migration by bar formation

We find that bars do trap particles and reduce the outwards radial migration from them. Even in the weak bar case of simulation ISB, at most 14% of particles escape the inner region trapped by the bar by final time. The majority of these escapers, however, remain within the bar, and manage to end up with Jacobi integrals $E_J = E - \Omega_b L_z$ slightly greater that the peak of the effective potential well of the bar Φ_{crt} due to fluctuations of that peak with time. At most 6% end up on non-trapped orbits that oscillate in and out of the inner bar region defined by the radius of the bar's effective potential peak $R_{L_{1,2}}$. And only $\lesssim 2\%$ of the initially trapped particles escape the bar completely. Their Jacobi integrals decrease for further outwards migrators (bottom plots of Fig. 5.2), which favors the most plausible scenario of their escape: first they managed to escape the bar potential well, but kept oscillating in and out of it until, at some point, they got scattered out by outer spiral waves to larger radii through radial migration, while their Jacobi integrals in the bar's rotating frame decreased due to their gain of angular momentum. Most importantly, we find that only 0.02% of the initially trapped particles make it out to the inner edge of the solar neighborhood and beyond.

Furthermore, the top plots of Fig. 5.2 show that the majority of these escapers have initial Jacobi integrals and radii close to the initial location of the peak of the bar's effective potential. We attribute all escapers to the temporal variations and fluctuations of the bars' pattern speeds, values of their effective potential peaks, radii of these peaks, and the bar's amplitudes, which we show in Fig. 5.3.

Initially, there are many particles in the inner region, $\approx 6\%$ within $R_{L_{1,2}}$ and $\approx 20\%$ with orbits that cross $R_{L_{1,2}}$ of all the particles, that are not trapped by the bar due to their high Jacobi integrals. They are free to get picked up by outer spirals and migrate out of the inner galactic region while the bar exists. The important point, however, is that all of them are at least as old as the bar. Whereas younger stars that form within the bar are born trapped deep in the bar's potential well. And so, the region of interest for checking whether younger stars can migrate out of the bar and populate the thick disk by present

time is the trapped region within the bar.

Although we do not add new particles in this region, our results of very few escapers tested with the original particles over durations ~ 10 Gyr while the bars exist suffices. In fact, it is more than necessary since younger stars would have had less time to be able to escape the bar. As seen in Table 5.1, less particles manage to escape during shorter intermediate durations than during the whole age of the bar. Even in the interesting cases in simulations NB2 and IB of the bar amplitude dropping abruptly to a much lower value, at most 5% of the trapped particles become non-trapped or escape.

Lastly, in order to contribute to the thickest disk populations in the solar neighborhood at present, stars would have had to migrate outwards as far as possible in order to experience the greatest decrease in the vertical restoring force. Therefore, the most interesting stars are ones that would have formed after the bar with initial home radii deep within the bar very close to the disk center. The top plots of Fig. 5.2 show that there almost no escapers that have such small home radii when the bar forms.

Thus, we find that bar formation is successful at stopping outwards radial migration from the inner galactic region that is capable of producing the thickest disk populations at the solar neighborhood and beyond. This explains why the Milky Way thick disk in the solar neighborhood has no young stars. Once the Milky Way bar formed, very few new stars that formed within it managed to escape and migrate outwards far.

This scenario suggests that the youngest observed thick disk stars correspond to the age of the Milky Way bar, given that the thick disk did mostly form through radial migration. The only other way to date the bar we are aware of was done by Cole & Weinberg (2002), who used carbon stars to estimate an upper bound of ~ 6 Gyr on its age.

It would be interesting to collect statistics of disk galaxies that have thick disk populations, and see whether all the ones that contain only old thick disk stars also contain a bar, and whether all those that have young thick disk stars do not harbor bars. This would be a true observational test of this scenario. Hopefully, this will be possible to do in the future, when telescopes become powerful enough to resolve stars in more nearby external disk galaxies than just Andromeda. In doing this project, one would have to overcome the problem that observations of thick disks and bars are somewhat disjoint: the former are best

detected in edge-on galaxies, whereas the latter are best detected in face-on ones. A couple of remedies are detecting the presence of bars in edge-on disks as elongated pseudobulges, since bars tend to buckle and develop a boxy peanut vertical shape (*e.g.* Martinez-Valpuesta et al. 2006), and also from the characteristic non-circular kinematic features seen edge-on caused by the elongated streams of gas along the bars (Bureau & Freeman 1999).

Chapter 6

Conclusions

It has recently become clear that the "churning" effect discovered by Sellwood & Binney (2002), under which stars migrate radially without increases in their orbits' eccentricities, plays an important role in the secular evolution of spiral disk galaxies. Theoretically, every transient spiral wave should generate it (Sellwood & Binney 2002). Simulations confirm this (*e.g.* Sellwood & Binney 2002; Roškar et al. 2008a; Loebman et al. 2011; Minchev et al. 2012c), and observations of stellar metallicity gradients in the solar neighborhood suggest its presence (*e.g.* Haywood 2008; Lee et al. 2011; Yu et al. 2012).

Radial migration is important, because it mixes stellar formation environments and erases the history of the galaxy over time. Each spiral wave scatters stars by an average distance of ~ 1 kpc radially, and affects a ~ 2 kpc-wide annulus centered at the corotation resonance of the spiral. Transient spirals recur on a timescale of roughly 200 Myr, and, usually, multiple modes coexist simultaneously. Since different waves normally have corotations at different radii, stars essentially end up random walking in radius, and a single one can migrate almost the entire disk radius in a Gyr.

Earlier studies mainly focused on thoroughly testing radial migration in thin galactic disks. Yet, many galaxies, including the Milky Way, also contain thick disks. Schönrich & Binney (2009a,b) assumed that radial migration affects thick populations equally as the thin, and prescribed it in their Galactic chemical evolution model, which naturally formed a realistic thick disk through outwards radial migration. Thus, it became important to test this effect in thick disks.

We have carried out the first detailed study of churning in thick disks using N-body simulations, and published it in Solway et al. (2012) presented in this thesis in §2. We found that radial migration weakens with increasing disk thickness, but gradually, and the maximum angular momentum changes remain almost as great as in thin disks. Thus, this effect occurs and is still important in thick disks as thick as that of the Milky Way.

We also found that radial migration is weaker in hotter disks (greater velocity dispersion), and under spirals of smaller spatial scale, *i.e.* weaker spiral amplitude and/or greater number of arms. In simulations that form a bar, it is slightly more enhanced than in ones without a bar. However, the cumulative effect of multiple transient spirals still dominates the middle and outer regions of the disk.

In §3, we sought a quantity of a star's motion that remains conserved while it undergoes radial migration. We found that, on average, the vertical action, and not the vertical energy, is conserved. This should be used in prescribing vertical motion changes caused by radial migration in chemo-dynamic models of disk galaxy evolution.

As stars migrate outwards, they experience weaker vertical restoring forces, because the density of mass declines with radius in disks. This, along with the fact that their vertical actions remain conserved, implies that their vertical amplitudes increase as they migrate outwards, and vise versa when they migrate inwards. We confirmed this in our simulations in §§2 & 4.

This is how a thick disk formed in the chemical evolution model of Schönrich & Binney (2009b). They proposed that thick galactic disks can form by outwards migration of stars that originate in the inner region of a galaxy, which is an internal quiescent formation mechanism unlike the previously suggested violent ones that require external perturbers or sources. Loebman et al. (2011); Brook et al. (2012) also found that a realistic thick disk formed through this mechanism in their N-body simulations. However, the simulations of Minchev et al. (2012a,b); Bird et al. (2012, 2013) did not produce thick disks, and so this mechanism remains debated.

We tested it in our simulations as well, and, in §4, found that they do not produce thick enough disks. We attribute this result to not strong enough spiral activity and our addition of new particles, which omits the realistic star formation at the galactic center. Thus, our results on this matter are inconclusive, and we are continuing to try to generate more realistic simulations with stronger spirals, but no bar.

A major problem of the outwards radial migration scenario for thick disk formation is its inability to explain on its own why the Galactic thick disk does not contain young stars in the solar neighborhood. Theoretically, the formation of the Milky Way bar offers a natural explanation since bars are non-transient features that trap orbits within them. Younger stars that formed in the inner Galactic region, which are the only ones capable of building a thick disk in the outer regions, likely have remained trapped by the bar, and therefore have not populated the thick disk.

We set out to test this hypothesis in our simulations, and in §5 showed evidence in its

support. We found that bar formation significantly reduces outwards migration from the trapped region. However, it does not shut it off entirely, because the height of the bar potential well, size of the trapped region, the bar pattern speed, and amplitude tend to fluctuate and vary with time. Although this happens slowly, some stars with greater Jacobi integrals manage to escape, and can get picked up by outer spirals that can scatter them further outwards by churning. Yet, only a mere 0.02% of the initially trapped particles make it to within the solar neighborhood and beyond after ~ 10 Gyr while the bar exists. Nevertheless, the important point is that new stars that would form within the bar would be deep in its potential well, and our analysis suggests that they would definitely remain trapped.

The best test to prove whether the old Galactic thick disk could have formed through outwards radial migration followed by its suppression due to the formation of the Galactic bar, would use a simulation that would include star formation in the inner disk in addition to the moving-outwards outer one, and that would begin with strong spiral activity for about 3 Gyr, and then form a realistic bar that would survive for the remaining ~ 10 Gyr duration of the simulation. We did not test such a simulation yet.

The scenario of bar formation closing off the supply of younger stars to the thick disk suggest that one can date the Galactic bar by associating its age with that of the youngest observed thick disk stars.

In the future, when instruments become capable of resolving individual stars in more nearby external disk galaxies, astrophysicists will be able to test this scenario observationally by seeing whether every galaxy that contains an old thick disk also contains a bar, and whether ones with young thick disks are not barred.

Appendix A

Numerical estimate of vertical action

Fig. A.1 illustrates the SoS for five different energies, all for $L_z = 7$. Each invariant curve is generated by a test particle in the initial potential of M2. All the particles in one panel have the same energy and angular momentum (noted in the top right corner), but differ in the extent of their vertical motion. The zero-velocity curve, where a particle's radial velocity must be zero for the L_z and E values adopted is the outer most green curve. We see that most of phase space is regular, but not all consequents mark out simple closed invariant curves; some significant fraction of phase space is affected by islands in the SoS that surround multiply periodic orbits. Chaotic motion, in which consequents fill an area rather than lie on a closed curve in the SoS, is extensive only for the greatest energy.

The paths in the meridional plane of three multiply periodic orbits are shown in Fig. A.2. They correspond to the bold red invariant curves in the second, fourth, and fifth SoS panels of Fig. A.1. The last orbit has almost equal radial and vertical periods and circulates only clockwise in the meridional plane. Since we plot only when the particle passes R_{home} with $\dot{R} > 0V_0$, the consequents lie only in the first quadrant of the $(z, \dot{z})$ plane. Were we to plot the other crossing instead, where $\dot{R} < 0V_0$, the invariant curve would be a reflected image in the second quadrant. Also, had we chosen the negative root for initial radial velocity, the particle would have circulated only counterclockwise and yielded a 180°-rotationally symmetric invariant curve in the third quadrant. This accounts for the skewness of the invariant curves in the SoS, which diminishes for particles of lower energy.

The area in the SoS enclosed by only those orbits having a simple invariant curve yields a numerical estimate of the vertical action J_z.[I] We find all the consequents for a particle as its motion advances over 7×10^4 dynamical times from its position in the frozen, azimuthally averaged, potential, and make a numerical estimate of the area integral (eq. 3.2).

We repeat this exercise at both the initial and final times in the simulation.

[I]A regular orbit trapped about a resonant island has a different set of actions that are not of interest here.
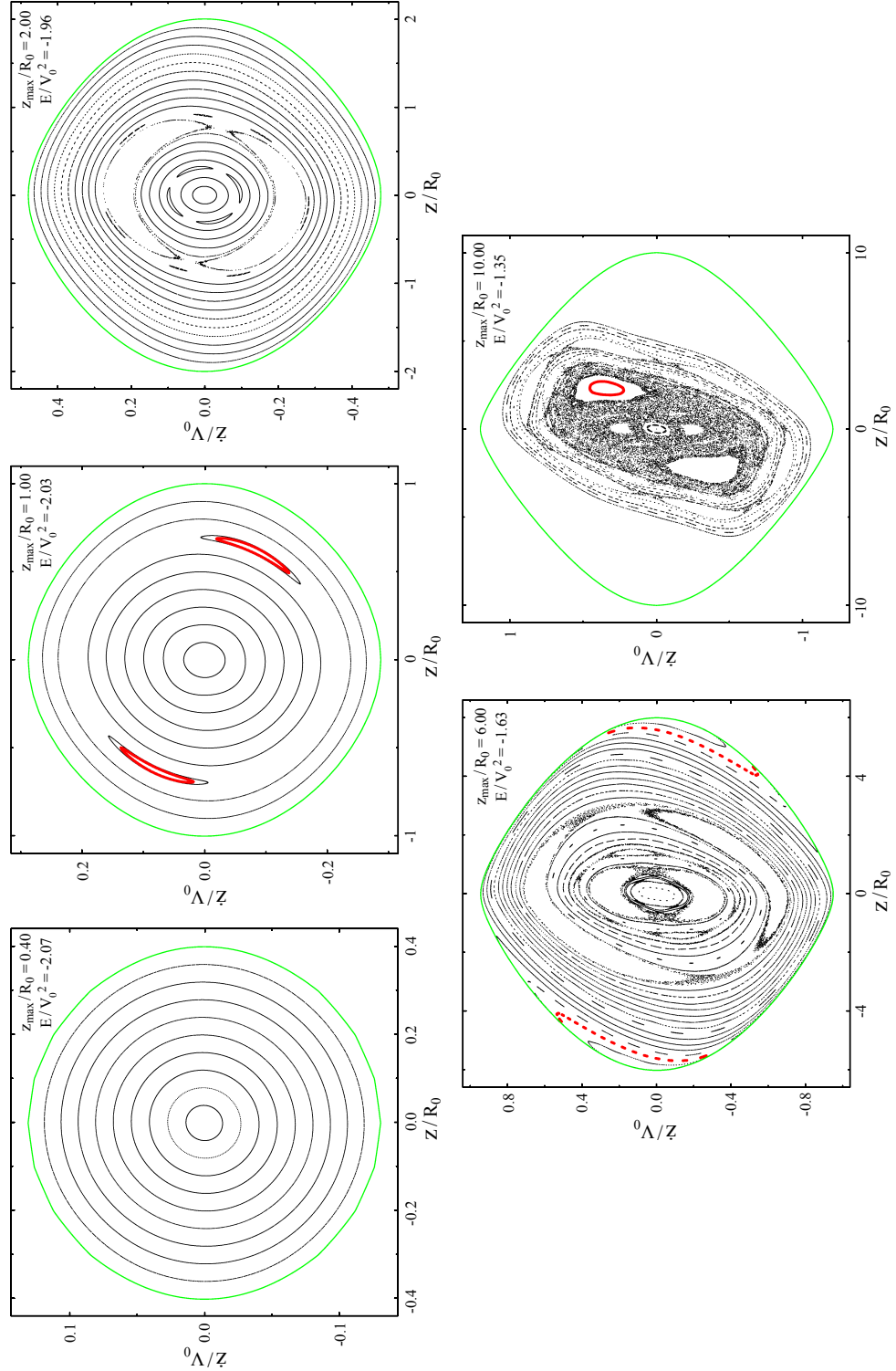
Figure A.1 Surfaces of section in the $(z, \dot{z})$ plane, when $R = R_{\text{home}}$ and $\dot{R} > 0V_0$, for test particles in the initial potential of simulation M2. All particles in each panel have the same total energy and corresponding z_{max}, which are noted in the top right corner. The outer most green curves mark the zero-velocity curves, at which $\dot{R} = 0V_0$ for the given z, L_z and E. Finally, the bold red curves are from the three orbits shown in Fig. A.2.
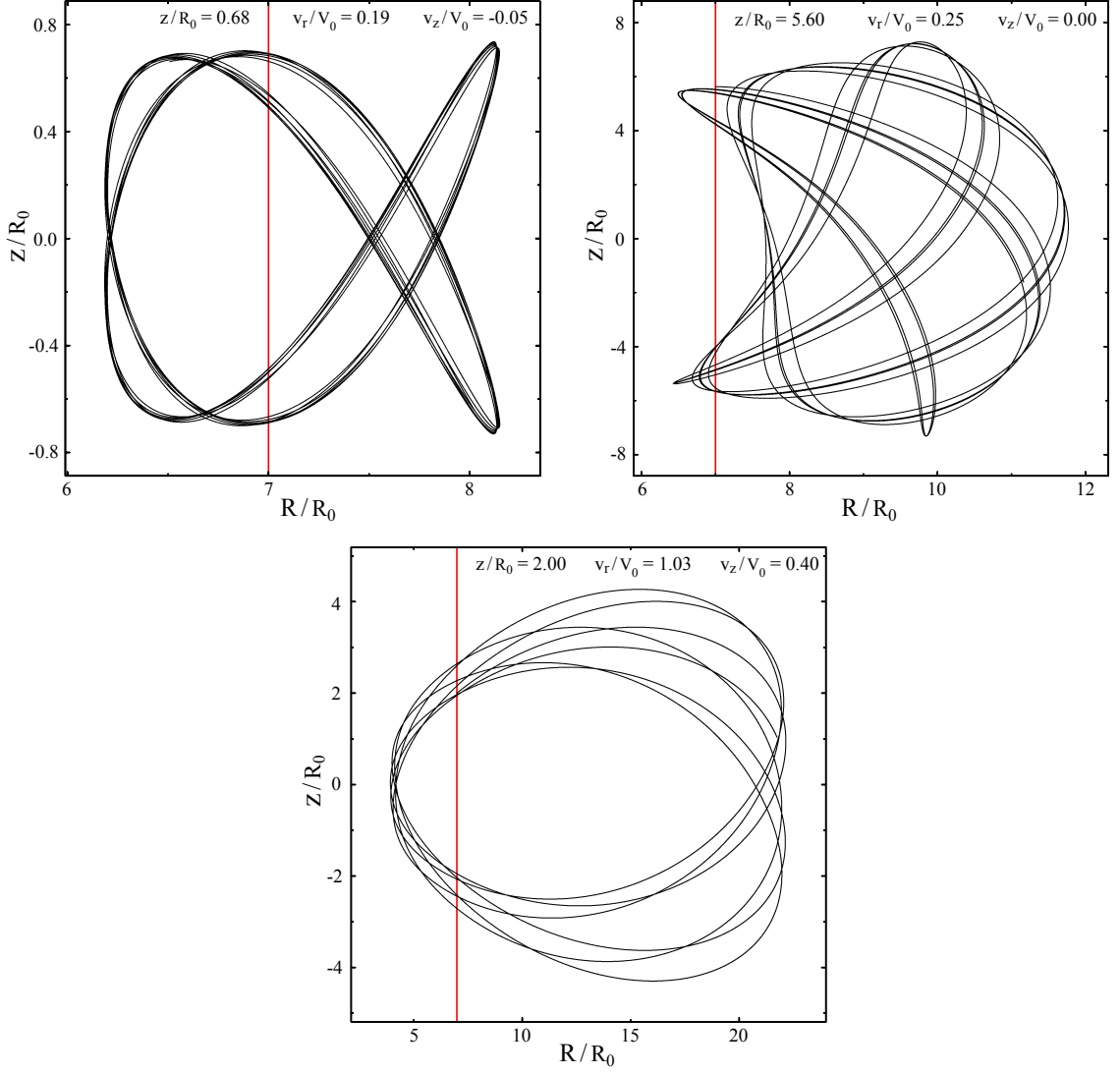
Figure A.2 Orbits in the meridional plane of the three test particles drawn in bold red in the second, fourth and fifth panels of Fig. A.1. Note that we show only a small fraction of the full orbit used to produce the invariant curves in the $(z, \dot{z})$ plane. The vertical red lines mark R_{home} at which the SoS is constructed. The initial vertical position and radial and vertical velocities of each of these three particles are noted.

Bibliography

Abadi, M. G., Navarro, J. F., Steinmetz, M., & Eke, V. R. 2003, ApJ, **597**, 21

Adibekyan, V. Z., Figueira, P., Santos, N. C., et al. 2013, A&A, **554**, A44

Aguerri, J. A. L., Debattista, V. P., & Corsini, E. M. 2003, MNRAS, **338**, 465

Aguerri, J. A. L., Méndez-Abreu, J., & Corsini, E. M. 2009, A&A, **495**, 491

Alves-Brito, A., Meléndez, J., Asplund, M., Ramírez, I., & Yong, D. 2010, A&A, **513**, A35

Araki, S. 1985, PhD thesis, MASSACHUSETTS INSTITUTE OF TECHNOLOGY.

Assmann, P., Fellhauer, M., Kroupa, P., Brüns, R. C., & Smith, R. 2011, MNRAS, **415**, 1280

Athanassoula, E. 1984, Phys. Rep., **114**, 319

—. 1992, MNRAS, **259**, 345

—. 2005, MNRAS, **358**, 1477

Athanassoula, E., & Beaton, R. L. 2006, MNRAS, **370**, 1499

Athanassoula, E., & Bosma, A. 2003, Ap&SS, **284**, 491

Athanassoula, E., Bosma, A., Creze, M., & Schwarz, M. P. 1982, A&A, **107**, 101

Babcock, H. W. 1939, Lick Observatory Bulletin, **19**, 41

Bahcall, J. N., & Soneira, R. M. 1984, ApJS, **55**, 67

Barazza, F. D., Jogee, S., & Marinova, I. 2008, ApJ, **675**, 1194

Barazza, F. D., Jablonka, P., Desai, V., et al. 2009, A&A, **497**, 713

Barmby, P., & Huchra, J. P. 2001, AJ, **122**, 2458

Barnes, J. 1996, in IAU Symposium, Vol. 171, New Light on Galaxy Evolution, ed. R. Bender & R. L. Davies, 191

Barnes, J. E. 1986, in Lecture Notes in Physics, Berlin Springer Verlag, Vol. 267, The Use of Supercomputers in Stellar Dynamics, ed. P. Hut & S. L. W. McMillan, 175

Beaton, R. L., Majewski, S. R., Guhathakurta, P., et al. 2007, ApJ, **658**, L91

Beck, R., Brandenburg, A., Moss, D., Shukurov, A., & Sokoloff, D. 1996, ARA&A, **34**, 155

Becker, R. H., Fan, X., White, R. L., et al. 2001, AJ, **122**, 2850

Beers, T. C., Flynn, K., & Gebhardt, K. 1990, AJ, **100**, 32

Benedict, G. F., Howell, D. A., Jørgensen, I., Kenney, J. D. P., & Smith, B. J. 2002, AJ, **123**, 1411

Benjamin, R. A., Churchwell, E., Babler, B. L., et al. 2005, ApJ, **630**, L149

Bennett, C. L., Larson, D., Weiland, J. L., et al. 2012, ArXiv

Bensby, T., & Feltzing, S. 2012, in European Physical Journal Web of Conferences, Vol. 19, European Physical Journal Web of Conferences, 4001

Bensby, T., Feltzing, S., & Lundström, I. 2003, A&A, **410**, 527

Bensby, T., Feltzing, S., Lundström, I., & Ilyin, I. 2005, A&A, **433**, 185

Bensby, T., Oey, M. S., Feltzing, S., & Gustafsson, B. 2007a, ApJ, **655**, L89

Bensby, T., Zenn, A. R., Oey, M. S., & Feltzing, S. 2007b, ApJ, **663**, L13

Bertin, G., & Lin, C. C. 1996, Spiral structure in galaxies a density wave theory (Cambridge, MA: MIT Press)

Bertin, G., Lin, C. C., Lowe, S. A., & Thurstans, R. P. 1989a, ApJ, **338**, 78

—. 1989b, ApJ, **338**, 104

Binney, J. 2010, MNRAS, **401**, 2318

Binney, J., & Merrifield, M. 1998, Galactic Astronomy (Princeton, NJ: Princeton Univ. Press) **(BM98)**

Binney, J., & Tremaine, S. 2008, Galactic Dynamics (Princeton, NJ: Princeton Univ. Press) **(BT08)**

Binney, J. J., & Lacey, C. G. 1988, MNRAS, **230**, 597

Bird, J. C., Kazantzidis, S., & Weinberg, D. H. 2012, MNRAS, **420**, 913

Bird, J. C., Kazantzidis, S., Weinberg, D. H., et al. 2013, ApJ, **773**, 43

Birnboim, Y., & Dekel, A. 2003, MNRAS, **345**, 349

Bissantz, N., & Gerhard, O. 2002, MNRAS, **330**, 591

Bland-Hawthorn, J., Vlajić, M., Freeman, K. C., & Draine, B. T. 2005, ApJ, **629**, 239

Boeche, C., Chiappini, C., Minchev, I., et al. 2013, A&A, **553**, A19

Bond, N. A., Ivezić, Ž., Sesar, B., et al. 2010, ApJ, **716**, 1

Boroson, T. 1981, ApJS, **46**, 177

Bosma, A. 1978, PhD thesis, Groningen Univ., Groningen, Netherlands

Bosma, A. 1996, in Lecture Notes in Physics, Berlin Springer Verlag, Vol. 474, Lecture Notes in Physics, Berlin Springer Verlag, ed. A. Sandqvist & P. O. Lindblad, 67

Bournaud, F., & Combes, F. 2002, A&A, **392**, 83

Bournaud, F., Elmegreen, B. G., & Martig, M. 2009, ApJ, **707**, L1

Bouwens, R. J., Illingworth, G. D., Labbe, I., et al. 2011, Nature, **469**, 504

Bovy, J., & Hogg, D. W. 2010, ApJ, **717**, 617

Bovy, J., Hogg, D. W., & Roweis, S. T. 2009, ApJ, **700**, 1794

Bovy, J., Rix, H.-W., & Hogg, D. W. 2012a, ApJ, **751**, 131

Bovy, J., Rix, H.-W., Hogg, D. W., et al. 2012b, ApJ, **755**, 115

Bovy, J., Rix, H.-W., Liu, C., et al. 2012c, ApJ, **753**, 148

Brook, C. B., Kawata, D., Gibson, B. K., & Freeman, K. C. 2004, ApJ, **612**, 894

Brook, C. B., Stinson, G. S., Gibson, B. K., et al. 2012, MNRAS, **426**, 690

Brooks, A. M., Governato, F., Quinn, T., Brook, C. B., & Wadsley, J. 2009, ApJ, **694**, 396

Brunetti, M., Chiappini, C., & Pfenniger, D. 2011, A&A, **534**, A75

Bureau, M., & Freeman, K. C. 1999, AJ, **118**, 126

Burkert, A., Brodie, J., & Larsen, S. 2005, ApJ, **628**, 231

Burstein, D. 1979, ApJ, **234**, 829

Buta, R. 1986, ApJS, **61**, 609

—. 1990, ApJ, **356**, 87

Buta, R. 1991, in IAU Symposium, Vol. 146, Dynamics of Galaxies and Their Molecular Cloud Distributions, ed. F. Combes & F. Casoli, 251

—. 1995, ApJS, **96**, 39

Buta, R., & Combes, F. 1996, Fund. Cosmic Phys., **17**, 95

Buta, R., Crocker, D. A., & Byrd, G. G. 1992, AJ, **103**, 1526

Buta, R. J., Byrd, G. G., & Freeman, T. 2003, AJ, **125**, 634

Buta, R. J., Corwin, H. G., & Odewahn, S. C. 2007, The de Vaucouleurs Altlas of Galaxies

Buta, R. J., Knapen, J. H., Elmegreen, B. G., et al. 2009, AJ, **137**, 4487

Cabrera-Lavers, A., Bilir, S., Ak, S., Yaz, E., & López-Corredoira, M. 2007, A&A, **464**, 565

Cabrera-Lavers, A., González-Fernández, C., Garzón, F., Hammersley, P. L., & López-Corredoira, M. 2008, A&A, **491**, 781

Caffau, E., Bonifacio, P., François, P., et al. 2011, Nature, **477**, 67

Calbet, X., Mahoney, T., Garzon, F., & Hammersley, P. L. 1995, MNRAS, **276**, 301

Caldwell, N., Rose, J. A., Sharples, R. M., Ellis, R. S., & Bower, R. G. 1993, AJ, **106**, 473

Cameron, E., Carollo, C. M., Oesch, P., et al. 2010, MNRAS, **409**, 346

Camm, G. L. 1950, MNRAS, **110**, 305

Carlberg, R. G., & Freedman, W. L. 1985, ApJ, **298**, 486

Carney, B. W. 1979, ApJ, **233**, 211

Carollo, D., Beers, T. C., Chiba, M., et al. 2010, ApJ, **712**, 692

Casagrande, L., Schönrich, R., Asplund, M., et al. 2011, A&A, Volume = 530, Pages = A138

Casetti-Dinescu, D. I., Girard, T. M., Korchagin, V. I., & van Altena, W. F. 2011, ApJ, **728**, 7

Chemin, L., & Hernandez, O. 2009, A&A, **499**, L25

Cheng, J. Y., Rockosi, C. M., Morrison, H. L., et al. 2012, ApJ, **752**, 51

Chiba, M., & Beers, T. C. 2000, AJ, **119**, 2843

Cole, A. A., & Weinberg, M. D. 2002, ApJ, **574**, L43

Collins, M. L. M., Chapman, S. C., Ibata, R. A., et al. 2011, MNRAS, **413**, 1548

Combes, F., Debbasch, F., Friedli, D., & Pfenniger, D. 1990, A&A, **233**

Combes, F., & Elmegreen, B. G. 1993, A&A, **271**, 391

Combes, F., & Sanders, R. H. 1981, A&A, **96**, 164

Comerón, S., Knapen, J. H., Beckman, J. E., et al. 2010, MNRAS, **402**, 2462

Comerón, S., Elmegreen, B. G., Salo, H., et al. 2012, ApJ, **759**, 98

Contopoulos, G. 1980, A&A, **81**, 198

Contopoulos, G., & Grosbøl, P. 1989, A&A Rev., **1**, 261

Corsini, E. M. 2008, in IAU Symposium, Vol. 245, IAU Symposium, ed. M. Bureau, E. Athanassoula, & B. Barbuy, 125

Côté, S., Carignan, C., & Freeman, K. C. 2000, AJ, **120**, 3027

Courteau, S., Andersen, D. R., Bershady, M. A., MacArthur, L. A., & Rix, H.-W. 2003, ApJ, **594**, 208

Curir, A., Lattanzi, M. G., Spagna, A., et al. 2012, A&A, **545**, A133

Dalcanton, J. J., & Bernstein, R. A. 2002, AJ, **124**, 1328

de Blok, W. J. G., McGaugh, S. S., & van der Hulst, J. M. 1996, MNRAS, **283**, 18

de Grijs, R., Peletier, R. F., & van der Kruit, P. C. 1997, A&A, **327**, 966

de Jong, J. T. A., Yanny, B., Rix, H.-W., et al. 2010, ApJ, **714**, 663

de Jong, R. S. 1996, A&A, **313**, 45

de Jong, R. S., Seth, A. C., Radburn-Smith, D. J., et al. 2007, ApJ, **667**, L49

de Vaucouleurs, G. 1948, Annales d'Astrophysique, **11**, 247

—. 1959, Handbuch der Physik, **53**, 275

de Vaucouleurs, G. 1964, in IAU Symposium, Vol. 20, The Galaxy and the Magellanic Clouds, ed. F. J. Kerr, 195

de Vaucouleurs, G., de Vaucouleurs, A., Corwin, Jr., H. G., et al. 1991, Third Reference Catalogue of Bright Galaxies. Volume I: Explanations and references. Volume II: Data for galaxies between 0^h and 12^h. Volume III: Data for galaxies between 12^h and 24^h. (New York, NY: Springer)

de Vaucouleurs, G., & Freeman, K. C. 1972, Vistas in Astronomy, **14**, 163

Debattista, V. P., Corsini, E. M., & Aguerri, J. A. L. 2002, MNRAS, **332**, 65

Debattista, V. P., Mayer, L., Carollo, C. M., et al. 2006, ApJ, **645**, 209

Debattista, V. P., & Sellwood, J. A. 1998, ApJ, **493**, L5

—. 2000, ApJ, **543**, 704

Debattista, V. P., & Williams, T. B. 2004, ApJ, **605**, 714

Dekel, A., & Birnboim, Y. 2006, MNRAS, **368**, 2

Dekel, A., & Woo, J. 2003, MNRAS, **344**, 1131

Di Matteo, P., Haywood, M., Combes, F., Semelin, B., & Snaith, O. N. 2013, A&A, **553**, A102

Dieterich, S. B., Henry, T. J., Golimowski, D. A., Krist, J. E., & Tanner, A. M. 2012, AJ, **144**, 64

Djorgovski, S. 1993, in Astronomical Society of the Pacific Conference Series, Vol. 50, Structure and Dynamics of Globular Clusters, ed. S. G. Djorgovski & G. Meylan, 373

D'Onghia, E., Springel, V., Hernquist, L., & Kereš, D. 2010, ApJ, **709**, 1138

Donner, K. J., & Thomasson, M. 1994, A&A, **290**, 785

Dressler, A., Oemler, Jr., A., Couch, W. J., et al. 1997, ApJ, **490**, 577

Dubinski, J., Gauthier, J.-R., Widrow, L., & Nickerson, S. 2008, in Astronomical Society of the Pacific Conference Series, Vol. 396, Formation and Evolution of Galaxy Disks, ed. J. G. Funes & E. M. Corsini, 321

Edvardsson, B., Andersen, J., Gustafsson, B., et al. 1993, A&A, **275**, 101

Efstathiou, G., & Jones, B. J. T. 1980, Comments on Astrophysics, **8**, 169

Eggen, O. J., Lynden-Bell, D., & Sandage, A. R. 1962, ApJ, **136**, 748

Egusa, F., Kohno, K., Sofue, Y., Nakanishi, H., & Komugi, S. 2009, ApJ, **697**, 1870

Eisenhauer, F., Schödel, R., Genzel, R., et al. 2003, ApJ, **597**, L121

Elmegreen, B. G., Elmegreen, D. M., & Hirst, A. C. 2004, ApJ, **612**, 191

Elmegreen, B. G., & Thomasson, M. 1993, A&A, **272**, 37

Elmegreen, D. M. 1980, ApJS, **43**, 37

Elmegreen, D. M. 1996, in Astronomical Society of the Pacific Conference Series, Vol. 91, IAU Colloq. 157: Barred Galaxies, ed. R. Buta, D. A. Crocker, & B. G. Elmegreen, 23

Elmegreen, D. M., & Elmegreen, B. G. 1982, MNRAS, **201**, 1021

—. 1984, ApJS, **54**, 127

Erwin, P., Beckman, J. E., & Pohlen, M. 2005, ApJ, **626**, L81

Eskridge, P. B., Frogel, J. A., Pogge, R. W., et al. 2000, AJ, **119**, 536

—. 2002, ApJS, **143**, 73

Evans, N. W., & Read, J. C. A. 1998, MNRAS, **300**, 106

Fall, S. M., & Efstathiou, G. 1980, MNRAS, **193**, 189

Famaey, B., Pont, F., Luri, X., et al. 2007, A&A, **461**, 957

Feltzing, S., & Gonzalez, G. 2001, A&A, **367**, 253

Fletcher, A., Beck, R., Shukurov, A., Berkhuijsen, E. M., & Horellou, C. 2011, MNRAS, **412**, 2396

Forbes, J., Krumholz, M., & Burkert, A. 2012, ApJ, **754**, 48

Förster Schreiber, N. M., Genzel, R., Bouché, N., et al. 2009, ApJ, **706**, 1364

Foyle, K., Rix, H.-W., Dobbs, C. L., Leroy, A. K., & Walter, F. 2011, ApJ, **735**, 101

Frebel, A., Christlieb, N., Norris, J. E., et al. 2007, ApJ, **660**, L117

Freeman, K. C. 1970, ApJ, **160**, 811

Fridman, A. M., & Poliachenko, V. L. 1984, Physics of gravitating systems. II - Nonlinear collective processes: Nonlinear waves, solitons, collisionless shocks, turbulence. Astrophysical applications

Friedli, D., Benz, W., & Kennicutt, R. 1994, ApJ, **430**, L105

Fuchs, B. 2001, A&A, **368**, 107

Fuchs, B., Dettbarn, C., & Tsuchiya, T. 2005, A&A, **444**, 1

Fuhrmann, K. 1998, A&A, **338**, 161

—. 2008, MNRAS, **384**, 173

Fukugita, M., & Peebles, P. J. E. 2004, ApJ, **616**, 643

Gadotti, D. A. 2011, MNRAS, **415**, 3308

Gallagher, III, J. S., & Hunter, D. A. 1984, ARA&A, **22**, 37

Garcia Gomez, C., & Athanassoula, E. 1993, A&AS, **100**, 431

Gerhard, O. 2002, in Astronomical Society of the Pacific Conference Series, Vol. 273, The Dynamics, Structure & History of Galaxies: A Workshop in Honour of Professor Ken Freeman, ed. G. S. Da Costa, E. M. Sadler, & H. Jerjen, 73

Gilmore, G., & Reid, N. 1983, MNRAS, **202**, 1025

Gilmore, G., & Wyse, R. F. G. 1985, AJ, **90**, 2015

Gilmore, G., Wyse, R. F. G., & Jones, J. B. 1995, AJ, **109**, 1095

Gilmore, G., Wyse, R. F. G., & Norris, J. E. 2002, ApJ, **574**, L39

Girard, T. M., Korchagin, V. I., Casetti-Dinescu, D. I., et al. 2006, AJ, **132**, 1768

Goldreich, P., & Lynden-Bell, D. 1965, MNRAS, **130**, 125

Goldreich, P., & Tremaine, S. 1978, ApJ, **222**, 850

—. 1981, ApJ, **243**, 1062

González-Fernández, C., López-Corredoira, M., Amôres, E. B., et al. 2012, A&A, **546**, A107

Gott, III, J. R., & Thuan, T. X. 1976, ApJ, **204**, 649

Governato, F., Willman, B., Mayer, L., et al. 2007, MNRAS, **374**, 1479

Gratton, R. G., Carretta, E., Matteucci, F., & Sneden, C. 2000, A&A, **358**, 671

Grenon, M. 1999, Ap&SS, **265**, 331

Grevesse, N., & Sauval, A. J. 1999, A&A, **347**, 348

Grosbøl, P., Patsis, P. A., & Pompei, E. 2004, A&A, **423**, 849

Hammersley, P. L., Garzon, F., Mahoney, T., & Calbet, X. 1994, MNRAS, **269**, 753

Hänninen, J., & Flynn, C. 2002, MNRAS, **337**, 731

Harris, W. E. 1996, AJ, **112**, 1487

Hasan, H., Sellwood, J. A., & Norman, C. A. 1993, in IAU Symposium, Vol. 153, Galactic Bulges, ed. H. Dejonghe & H. J. Habing, 385

Haywood, M. 2008, MNRAS, **388**, 1175

Haywood, M., Di Matteo, P., Lehnert, M., Katz, D., & Gomez, A. 2013, ArXiv (A&A, accepted)

Helmi, A., Navarro, J. F., Nordström, B., et al. 2006, MNRAS, **365**, 1309

Heyl, J. S., Hernquist, L., & Spergel, D. N. 1994, ApJ, **427**, 165

Hockney, R. W., & Brownrigg, D. R. K. 1974, MNRAS, **167**, 351

Hohl, F. 1971, ApJ, **168**, 343

Holmberg, J., Nordström, B., & Andersen, J. 2007, A&A, **475**, 519

Holwerda, B. W., Allen, R. J., de Blok, W. J. G., et al. 2013, Astronomische Nachrichten, **334**, 268

House, E. L., Brook, C. B., Gibson, B. K., et al. 2011, MNRAS, **415**, 2652

Hoyle, B., Masters, K. L., Nichol, R. C., et al. 2011, MNRAS, **415**, 3627

Hubble, E. 1943, ApJ, **97**, 112

Hubble, E. P. 1936, Realm of the Nebulae (New Haven, CT: Yale Univ. Press)

Humphreys, R. M., & Sandage, A. 1980, ApJS, **44**, 319

Hunter, D. 1997, PASP, **109**, 937

Ibata, R., Chapman, S., Ferguson, A. M. N., et al. 2005, ApJ, **634**, 287

Inagaki, S., Nishida, M. T., & Sellwood, J. A. 1984, MNRAS, **210**, 589

Ivezić, Ž., Sesar, B., Jurić, M., et al. 2008, AJ, **684**, 287

James, R. A., & Sellwood, J. A. 1978, MNRAS, **182**, 331

Jayaraman, A., Gilmore, G., Wyse, R. F. G., Norris, J. E., & Belokurov, V. 2013, MNRAS, **431**, 930

Jeans, J. H. 1902, Royal Society of London Philosophical Transactions Series A, **199**, 1

Jogee, S., Barazza, F. D., Rix, H.-W., et al. 2004, ApJ, **615**, L105

Johnson, H. M. 1957, AJ, **62**, 19

Jørgensen, B. R., & Lindegren, L. 2005, A&A, **436**, 127

Julian, W. H., & Toomre, A. 1966, ApJ, **146**, 810

Jurić, M., Ivezić, Ž., Brooks, A., et al. 2008, AJ, **673**, 864

Kalberla, P. M. W., & Kerp, J. 2009, ARA&A, **47**, 27

Kalnajs, A. J. 1971, ApJ, **166**, 275

—. 1973, Proceedings of the Astronomical Society of Australia, **2**, 174

—. 1977, ApJ, **212**, 637

Kalnajs, A. J. 1978, in IAU Symposium, Vol. 77, Structure and Properties of Nearby Galaxies, ed. E. M. Berkhuijsen & R. Wielebinski, 113

Kalnajs, A. J. 1991, in Dynamics of Disc Galaxies, ed. B. Sundelius, 323

Karaali, S., Bilir, S., Ak, S., Yaz, E., & Coşkunoğlu, B. 2011, PASA, **28**, 95

Karaali, S., Bilir, S., & Hamzaoğlu, E. 2004, MNRAS, **355**, 307

Kaufman, M., Bash, F. N., Hine, B., et al. 1989, ApJ, **345**, 674

Kaufmann, D. E., & Contopoulos, G. 1996, A&A, **309**, 381

Kazantzidis, S., Bullock, J. S., Zentner, A. R., Kravtsov, A. V., & Moustakas, L. A. 2008, ApJ, **688**, 254

Kennicutt, Jr., R. C., Armus, L., Bendo, G., et al. 2003, PASP, **115**, 928

Kereš, D., Katz, N., Weinberg, D. H., & Davé, R. 2005, MNRAS, **363**, 2

Kerr, F. J. 1967, in IAU Symposium, Vol. 31, Radio Astronomy and the Galactic System, ed. H. van Woerden, 239

Kirk, J. M., Gear, W. K., Fritz, J., et al. 2013, ArXiv (ApJsubmitted)

Knapen, J. H. 1999, in Astronomical Society of the Pacific Conference Series, Vol. 187, The Evolution of Galaxies on Cosmological Timescales, ed. J. E. Beckman & T. J. Mahoney, 72

Knapen, J. H. 2005, A&A, **429**, 141

Knapen, J. H., & Beckman, J. E. 1996, MNRAS, **283**, 251

Kormendy, J. 1979, ApJ, **227**, 714

Kormendy, J. 1981, in Structure and Evolution of Normal Galaxies, ed. S. M. Fall & D. Lynden-Bell, 85

Kormendy, J., & Kennicutt, R. C. 2004, ARA&A, **42**, 603

Kormendy, J., & Norman, C. 1979, ApJ, **233**, 539

Kregel, M., van der Kruit, P. C., & de Grijs, R. 2002, MNRAS, **334**, 646

Kroupa, P. 2002, MNRAS, **330**, 707

Kuijken, K., & Merrifield, M. R. 1995, ApJ, **443**, L13

Larsen, S. S. 2011, ArXiv

Launhardt, R., Zylka, R., & Mezger, P. G. 2002, A&A, **384**, 112

Laurikainen, E., Salo, H., Buta, R., & Knapen, J. H. 2009, ApJ, **692**, L34

Lee, Y. S., Beers, T. C., An, D., et al. 2011, ApJ, **738**, 187

Lépine, J. R. D., Acharova, I. A., & Mishurov, Y. N. 2003, ApJ, **589**, 210

Lin, C. C., & Shu, F. H. 1964, ApJ, **140**, 646

—. 1966, Proceedings of the National Academy of Science, **55**, 229

Lindblad, B. 1962, in IAU Symposium, Vol. 15, Problems of Extra-Galactic Research, ed. G. C. McVittie, 146

Lindblad, B. 1963, Stockholms Observatoriums Annaler, **22**, 5

Liu, C., & van de Ven, G. 2012, MNRAS, **425**, 2144

Loebman, S. R., Roškar, R., Debattista, V. P., et al. 2011, ApJ, **737**, 8

López-Corredoira, M., Cabrera-Lavers, A., Mahoney, T. J., et al. 2007, AJ, **133**, 154

Lovelace, R. V. E., & Hohlfeld, R. G. 1978, ApJ, **221**, 51

Lynden-Bell, D. 1979, MNRAS, **187**, 101

Lynden-Bell, D., & Kalnajs, A. J. 1972, MNRAS, **157**, 1

Lynden-Bell, D., & Pringle, J. E. 1974, MNRAS, **168**, 603

Lynds, B. T. 1970, in IAU Symposium, Vol. 38, The Spiral Structure of our Galaxy, ed. W. Becker & G. I. Kontopoulos, 26

Ma, J. 2002, A&A, **388**, 389

Majewski, S. R. 1993, ARA&A, **31**, 575

Manos, T., & Athanassoula, E. 2011, MNRAS, **415**, 629

Mark, J. W.-K. 1976, ApJ, **205**, 363

—. 1977, ApJ, **212**, 645

Martínez-García, E. E., & González-Lópezlira, R. A. 2013, ApJ, **765**, 105

Martinez-Valpuesta, I., Shlosman, I., & Heller, C. 2006, ApJ, **637**, 214

Martini, P., Regan, M. W., Mulchaey, J. S., & Pogge, R. W. 2003, ApJ, **589**, 774

Masters, K. L., Nichol, R. C., Hoyle, B., et al. 2011, MNRAS, **411**, 2026

Mathewson, D. S., & Ford, V. L. 1996, ApJS, **107**, 97

Matteucci, F., & Francois, P. 1989, MNRAS, **239**, 885

McGaugh, S. S., Rubin, V. C., & de Blok, W. J. G. 2001, AJ, **122**, 2381

McMillan, P. J. 2011, MNRAS, **414**, 2446

Meidt, S. E., Rand, R. J., & Merrifield, M. R. 2009, ApJ, **702**, 277

Meidt, S. E., Rand, R. J., Merrifield, M. R., Debattista, V. P., & Shen, J. 2008, ApJ, **676**, 899

Menéndez-Delmestre, K., Sheth, K., Schinnerer, E., Jarrett, T. H., & Scoville, N. Z. 2007, ApJ, **657**, 790

Merrifield, M. R. 2004, in Astronomical Society of the Pacific Conference Series, Vol. 317, Milky Way Surveys: The Structure and Evolution of our Galaxy, ed. D. Clemens, R. Shah, & T. Brainerd, 289

Merrifield, M. R., & Kuijken, K. 1995, MNRAS, **274**, 933

Merritt, D., & Hernquist, L. 1991, ApJ, **376**, 439

Mestel, L. 1963, MNRAS, **126**, 553

Miller, R. H., Prendergast, K. H., & Quirk, W. J. 1970, ApJ, **161**, 903

Minchev, I., & Famaey, B. 2010, ApJ, **722**, 112

Minchev, I., Famaey, B., Combes, F., et al. 2011, A&A, **527**, A147

Minchev, I., Famaey, B., Quillen, A. C., & Dehnen, W. 2012a, in European Physical Journal Web of Conferences, Vol. 19, European Physical Journal Web of Conferences, 7002

Minchev, I., Famaey, B., Quillen, A. C., et al. 2012b, A&A, **548**, A127

—. 2012c, A&A, **548**, A126

Monaghan, J. J. 1992, ARA&A, **30**, 543

Moni Bidin, C., Carraro, G., & Méndez, R. A. 2012, ApJ, **747**, 101

Moni Bidin, C., Girard, T. M., Carraro, G., et al. 2009, in Revista Mexicana de Astronomia y Astrofisica Conference Series, Vol. 35, Revista Mexicana de Astronomia y Astrofisica Conference Series, 109

Moore, B. 1994, Nature, **370**, 629

Morgan, W. W., Keenan, P. C., & Kellerman, E. 1943, An Atlas of Stellar Spectra (Chicago, IL: Chicago Univ. Press)

Munn, J. A., Monet, D. G., Levine, S. E., et al. 2004, AJ, **127**, 3034

Nair, P. B., & Abraham, R. G. 2010, ApJ, **714**, L260

Nakai, N. 1992, PASJ, **44**, L27

Navarro, J. F., Abadi, M. G., Venn, K. A., & Freeman, K. C. 2011, MNRAS, **412**, 1203

Navarro, J. F., Frenk, C. S., & White, S. D. M. 1997, ApJ, **490**, 493

Noguchi, M. 2004, in Astrophysics and Space Science Library, Vol. 319, Penetrating Bars Through Masks of Cosmic Dust, ed. D. L. Block, I. Puerari, K. C. Freeman, R. Groess, & E. K. Block, 231

Nordström, B., Mayor, M., Andersen, J., et al. 2004, A&A, **418**, 989

Ocvirk, P., Pichon, C., & Teyssier, R. 2008, MNRAS, **390**, 1326

Ohta, K., Hamabe, M., & Wakamatsu, K.-I. 1990, ApJ, **357**, 71

Ostriker, J. P., & Peebles, P. J. E. 1973, ApJ, **186**, 467

Pasetto, S., Grebel, E. K., Zwitter, T., et al. 2012, A&A, **547**, A70

Pasha, I. I. 1985, Soviet Astronomy Letters, **11**, 1

Patsis, P. A. 2006, MNRAS, **369**, L56

Patsis, P. A., Skokos, C., & Athanassoula, E. 2003, MNRAS, **346**, 1031

Peacock, M. B., Maccarone, T. J., Knigge, C., et al. 2010, MNRAS, **402**, 803

Peletier, R. F., Balcells, M., Davies, R. L., et al. 1999, MNRAS, **310**, 703

Pérez-Ramírez, D., Knapen, J. H., Peletier, R. F., et al. 2000, MNRAS, **317**, 234

Persic, M., Salucci, P., & Stel, F. 1996, MNRAS, **281**, 27

Petitpas, G. R., Peck, A. B., Iono, D., et al. 2005, in Bulletin of the American Astronomical Society, Vol. 37, American Astronomical Society Meeting Abstracts, 1258

Pettini, M., Shapley, A. E., Steidel, C. C., et al. 2001, ApJ, **554**, 981

Pineda, J. L., Langer, W. D., Velusamy, T., & Goldsmith, P. F. 2013, A&A, **554**, A103

Planck Collaboration, Ade, P. A. R., Aghanim, N., et al. 2013, ArXiv (A&Asubmitted)

Pohlen, M., Dettmar, R.-J., Lütticke, R., & Aronica, G. 2002, A&A, **392**, 807

Pryor, C., & Meylan, G. 1993, in Astronomical Society of the Pacific Conference Series, Vol. 50, Structure and Dynamics of Globular Clusters, ed. S. G. Djorgovski & G. Meylan, 357

Quillen, A. C., Minchev, I., Bland-Hawthorn, J., & Haywood, M. 2009, MNRAS, **397**, 1599

Quinn, P. J., Hernquist, L., & Fullagar, D. P. 1993, ApJ, **403**, 74

Raboud, D., Grenon, M., Martinet, L., Fux, R., & Udry, S. 1998, A&A, **335**, L61

Radburn-Smith, D. J., Roškar, R., Debattista, V. P., et al. 2012, ApJ, **753**, 138

Raha, N., Sellwood, J. A., James, R. A., & Kahn, F. D. 1991, Nature, **352**, 411

Rand, R. J., & Kulkarni, S. R. 1990, ApJ, **349**, L43

Reddy, B. E., Lambert, D. L., & Allende Prieto, C. 2006, MNRAS, **367**, 1329

Regan, M. W., & Mulchaey, J. S. 1999, AJ, **117**, 2676

Regan, M. W., Sheth, K., Teuben, P. J., & Vogel, S. N. 2002, ApJ, **574**, 126

Regan, M. W., & Teuben, P. J. 2003, ApJ, **582**, 723

—. 2004, ApJ, **600**, 595

Regan, M. W., Thornley, M. D., Helfer, T. T., et al. 2001, ApJ, **561**, 218

Rix, H.-W., & Rieke, M. J. 1993, ApJ, **418**, 123

Rix, H.-W., & Zaritsky, D. 1995, ApJ, **447**, 82

Roman, N. G. 1955, ApJS, **2**, 195

Rose, J. A. 1985, AJ, **90**, 787

Rots, A. H., Bosma, A., van der Hulst, J. M., Athanassoula, E., & Crane, P. C. 1990, AJ, **100**, 387

Roškar, R., Debattista, V. P., & Loebman, S. R. 2013, MNRAS, **433**, 976

Roškar, R., Debattista, V. P., Loebman, S. R., Ivezić, Z., & Quinn, T. R. 2011, in Astronomical Society of the Pacific Conference Series, Vol. 448, 16th Cambridge Workshop on Cool Stars, Stellar Systems, and the Sun, ed. C. Johns-Krull, M. K. Browning, & A. A. West, 371

Roškar, R., Debattista, V. P., Quinn, T. R., Stinson, G. S., & Wadsley, J. 2008a, ApJ, **684**, L79

Roškar, R., Debattista, V. P., Quinn, T. R., & Wadsley, J. 2012, MNRAS, **426**, 2089

Roškar, R., Debattista, V. P., Stinson, G. S., et al. 2008b, ApJ, **675**, L65

Roškar, R., Debattista, V. P., Stinson, G. S., et al. 2008c, in Astronomical Society of the Pacific Conference Series, Vol. 396, Formation and Evolution of Galaxy Disks, ed. J. G. Funes & E. M. Corsini, 217

Rubin, V. C., Ford, J., & K., W. 1970, ApJ, **159**, 379

Ruchti, G. R., Fulbright, J. P., Wyse, R. F. G., et al. 2011, ApJ, **737**, 9

Rybicki, G. B. 1972, in Astrophysics and Space Science Library, Vol. 31, IAU Colloq. 10: Gravitational N-Body Problem, ed. M. Lecar, 22

Sakamoto, K., Okumura, S. K., Ishizuki, S., & Scoville, N. Z. 1999, ApJ, **525**, 691

Sales, L. V., Helmi, A., Abadi, M. G., et al. 2009, MNRAS, **400**, L336

Sánchez-Gil, M. C., Jones, D. H., Pérez, E., et al. 2011, MNRAS, **415**, 753

Sandage, A. R., & Eggen, O. J. 1959, MNRAS, **119**, 278

Scannapieco, C., White, S. D. M., Springel, V., & Tissera, P. B. 2011, MNRAS, **417**, 154

Schlesinger, K. J., Johnson, J. A., Rockosi, C. M., et al. 2012, ApJ, **761**, 160

Schönrich, R., & Binney, J. 2009a, MNRAS, **396**, 203

—. 2009b, MNRAS, **399**, 1145

—. 2012, MNRAS, **419**, 1546

Schruba, A., Leroy, A. K., Walter, F., & HERACLES Team. 2011, in Bulletin of the American Astronomical Society, Vol. 43, American Astronomical Society Meeting Abstracts #217, #133.04

Schuster, W. J., Moitinho, A., Márquez, A., Parrao, L., & Covarrubias, E. 2006, A&A, **445**, 939

Schwarz, M. P. 1981, ApJ, **247**, 77

Schwarzkopf, U., & Dettmar, R.-J. 2000, A&A, **361**, 451

Schweizer, F. 1976, ApJS, **31**, 313

Schweizer, F. 1998, in Saas-Fee Advanced Course 26: Galaxies: Interactions and Induced Star Formation, ed. J. Kennicutt, R. C., F. Schweizer, J. E. Barnes, D. Friedli, L. Martinet, & D. Pfenniger, 105

Seigar, M. S., Chorney, N. E., & James, P. A. 2003, MNRAS, **342**, 1

Sellwood, J. A. 1980, A&A, **89**, 296

—. 1981, A&A, **99**, 362

—. 1985, MNRAS, **217**, 127

—. 1987, ARA&A, **25**, 151

Sellwood, J. A. 1989, in Dynamics of Astrophysical Discs, ed. J. A. Sellwood, 155

—. 2000, Ap&SS, **272**, 31

—. 2010, MNRAS, **409**, 145

—. 2011, MNRAS, **410**, 1637

—. 2012, ApJ, **751**, 44

—. 2013a, ApJ, **769**, L24

—. 2013b, Dynamics of Disks and Warps, ed. T. D. Oswalt & G. Gilmore, 923

Sellwood, J. A., & Athanassoula, E. 1986, MNRAS, **221**, 195

Sellwood, J. A., & Binney, J. J. 2002, MNRAS, **336**, 785 **(SB02)**

Sellwood, J. A., & Carlberg, R. G. 1984, ApJ, **282**, 61

Sellwood, J. A., & Debattista, V. P. 2009, MNRAS, **398**, 1279

Sellwood, J. A., & Kahn, F. D. 1991, MNRAS, **250**, 278

Sellwood, J. A., & Lin, D. N. C. 1989, MNRAS, **240**, 991

Sellwood, J. A., & Moore, E. M. 1999, ApJ, **510**, 125

Sellwood, J. A., & Sparke, L. S. 1988, MNRAS, **231**, 25P

Sellwood, J. A., & Valluri, M. 1997, MNRAS, **287**, 124

Sellwood, J. A., & Wilkinson, A. 1993, Reports on Progress in Physics, **56**, 173

Seth, A. C., Dalcanton, J. J., & de Jong, R. S. 2005, AJ, **130**, 1574

Shen, J., & Sellwood, J. A. 2004, ApJ, **604**, 614

Sheth, K., Elmegreen, D. M., Elmegreen, B. G., et al. 2008, ApJ, **675**, 1141

Shetty, R., Vogel, S. N., Ostriker, E. C., & Teuben, P. J. 2007, ApJ, **665**, 1138

Shu, F. H. 1970, ApJ, **160**, 89

Skokos, C., Patsis, P. A., & Athanassoula, E. 2002, MNRAS, **333**, 847

Solway, M., Sellwood, J. A., & Schönrich, R. 2012, MNRAS, **422**, 1363 (**S12**)

Spano, M., Marcelin, M., Amram, P., et al. 2008, MNRAS, **383**, 297

Sparke, L. S., & Sellwood, J. A. 1987, MNRAS, **225**, 653

Spitzer, L. 1942, ApJ, **95**, 329

Spitzer, L., & Schwarzschild, M. 1953, ApJ, **118**, 106

Stark, A. A., & Lee, Y. 2006, ApJ, **641**, L113

Stewart, K. R., Brooks, A. M., Bullock, J. S., et al. 2013, ApJ, **769**, 74

Stinson, G. S., Bovy, J., Rix, H.-W., et al. 2013, ArXiv

Strickland, D. K., Heckman, T. M., Colbert, E. J. M., Hoopes, C. G., & Weaver, K. A. 2004, ApJ, **606**, 829

Strom, S. E., Strom, K. M., & Jensen, E. B. 1976, ApJ, **206**, L11

Strom, S. E., Strom, K. M., Wells, D. C., et al. 1981, ApJ, **245**, 416

Subramaniam, A., & Subramanian, S. 2009, ApJ, **703**, L37

Sygnet, J. F., Tagger, M., Athanassoula, E., & Pellat, R. 1988, MNRAS, **232**, 733

Tamburro, D., Rix, H.-W., Walter, F., et al. 2008, AJ, **136**, 2872

Thomasson, M., Elmegreen, B. G., Donner, K. J., & Sundelius, B. 1990, ApJ, **356**, L9

Thornley, M. D. 1996, ApJ, **469**, L45

Tilanus, R. P. J., & Allen, R. J. 1989, ApJ, **339**, L57

Toomre, A. 1966, 111

—. 1969, ApJ, **158**, 899

—. 1977a, ARA&A, **15**, 437

Toomre, A. 1977b, in Evolution of Galaxies and Stellar Populations, ed. B. M. Tinsley, D. Larson, & R. B. G. Campbell, 401

Toomre, A. 1981, in Structure and Evolution of Normal Galaxies, ed. S. M. Fall & D. Lynden-Bell, 111

—. 1982, ApJ, **259**, 535

Toomre, A. 1989, in Dynamics of Astrophysical Discs, ed. J. A. Sellwood, 153

—. 1990, Gas-hungry Sc spirals., ed. R. Wielen, 292

Toomre, A., & Toomre, J. 1972, ApJ, **178**, 623

Tremaine, S., & Weinberg, M. D. 1984, ApJ, **282**, L5

Trinchieri, G. 2012, in EAS Publications Series, Vol. 56, EAS Publications Series, ed. M. A. de Avillez, 231

Tsoutsis, P., Kalapotharakos, C., Efthymiopoulos, C., & Contopoulos, G. 2009, A&A, **495**, 743

Vallenari, A., Pasetto, S., Bertelli, G., et al. 2006, A&A, **451**, 125

van den Bergh, S. 2009, ApJ, **702**, 1502

van der Kruit, P. C. 1979, A&AS, **38**, 15

—. 1987, A&A, **173**, 59

van der Kruit, P. C., & Freeman, K. C. 2011, ARA&A, **49**, 301

van der Kruit, P. C., & Searle, L. 1981, A&A, **95**, 105

van Gorkom, J. H. 2004, Clusters of Galaxies: Probes of Cosmological Structure and Galaxy Evolution, 305

van Loon, J. T., Gilmore, G. F., Omont, A., et al. 2003, MNRAS, **338**, 857

Villalobos, A., & A., H. 2008, MNRAS, **391**, 1806

Walcher, C. J., van der Marel, R. P., McLaughlin, D., et al. 2005, ApJ, **618**, 237

Wallerstein, G. 1962, ApJS, **6**, 407

Wang, Y., & Zhao, G. 2013, ApJ, **769**, 4

Weinberg, M. D. 1985, MNRAS, **213**, 451

—. 1998, MNRAS, **297**, 101

Weiner, B. J., & Sellwood, J. A. 1999, ApJ, **524**, 112

Weiner, B. J., Sellwood, J. A., & Williams, T. B. 2001, ApJ, **546**, 931

White, S. D. M., & Rees, M. J. 1978, MNRAS, **183**, 341

Wilson, M. L., Helmi, A., Morrison, H. L., et al. 2011, MNRAS, **413**, 2235

Wolfe, A. M., Gawiser, E., & Prochaska, J. X. 2005, ARA&A, **43**, 861

Wright, E. L. 2006, PASP, **118**, 1711

Wyse, R. F. G. 2009, in IAU Symposium, Vol. 254, IAU Symposium, ed. J. Andersen, B. Nordström, & J. Bland-Hawthorn, 179

Wyse, R. F. G., & Gilmore, G. 1986, AJ, **91**, 855

Xue, X. X., Rix, H. W., Zhao, G., et al. 2008, ApJ, **684**, 1143

Yamauchi, C., & Goto, T. 2004, MNRAS, **352**, 815

Yoachim, P., & Dalcanton, J. J. 2006, AJ, **131**, 226

—. 2008a, ApJ, **682**, 1004

—. 2008b, ApJ, **683**, 707

Yoachim, P., Roškar, R., & Debattista, V. P. 2012, ApJ, **752**, 97

York, D. G., Adelman, J., Anderson, Jr., J. E., et al. 2000, AJ, **120**, 1579

Young, J. S., & Scoville, N. Z. 1991, ARA&A, **29**, 581

Yu, J., Sellwood, J. A., Pryor, C., Chen, L., & Hou, J. 2012, ApJ, **754**, 124

Yun, M. S., Ho, P. T. P., & Lo, K. Y. 1994, Nature, **372**, 530

Zang, T. A. 1976, PhD thesis, Massachussetts Institute of Technology, Cambrigde, MA

Zhang, X. 1996, ApJ, **457**, 125

—. 1998, ApJ, **499**, 93

Zibetti, S., Charlot, S., & Rix, H.-W. 2009, MNRAS, **400**, 1181

Zoccali, M., Renzini, A., Ortolani, S., et al. 2003, A&A, **399**, 931

Zwicky, F. 1955, PASP, **67**, 232